

Search for the Supersymmetric Partner to the Top Quark Using Recoils Against Strong Initial State Radiation

a dissertation presented
by
Siyuan Sun
to
The Department of Physics

in partial fulfillment of the requirements
for the degree of
Doctor of Philosophy
in the subject of
Physics

Harvard University
Cambridge, Massachusetts
May 2017

©2017 – Siyuan Sun
all rights reserved.

Search for the Supersymmetric Partner to the Top Quark Using Recoils Against Strong Initial State Radiation

Abstract

The ATLAS experiment at Large Hadron Collider (LHC) searches for experimental evidence of beyond the standard model physics at the TeV scale. As we collect more data at the LHC we continue to extend our sensitivity to these new phenomena, probing for the existence of increasingly massive particles. Despite this progress there are still regions of parameter space where constraints remain weak. One common region where we lack sensitivity is when the new BSM particle has a very small mass splitting between it and its decay products. The BSM particle then has little energy left over to give momenta to its decay products and the low momenta decay products are difficult to experimentally detect. These regions of small mass splitting are called compressed regions. We are able to gain sensitivity to these difficult regions by searching for new particles produced in conjunction with hard initial state radiation (ISR). The hard ISR boosts the new particle's decay products and gives them momentum.

This thesis covers the search for the supersymmetric partner to the top quark, called the stop, in the region when the stop and its decay products are nearly de-

generate in mass. No searches prior to 2016 were sensitive to this region. We were able to exclude stops up to a mass of 600 GeV in this region using 36.07 fb^{-1} of $\sqrt{s} = 13 \text{ TeV}$ LHC proton-proton collision data. This data was collected by the ATLAS experiment during 2015 and 2016. We introduce a new and more accurate technique for identifying whole ISR systems composed of multiple ISR jets as part of this analysis. The methods demonstrated in this analysis are completely generalizable and can be used in many other BSM searches and precision SM model measurements of the ISR p_T spectrum.

Contents

0	Introduction	1
1	Theoretical Motivation	16
1.1	The Standard Model	16
1.2	Introduction to Supersymmetry	19
1.2.1	R-Parity Conservation	24
2	General Analysis Strategy	26
2.1	R-Parity Conserving SUSY Searches in Regions with Large Mass Splittings	26
2.2	R-Parity Conserving SUSY Searches in Compressed Regions	30
3	Experimental Apparatus	39
3.1	The ATLAS Detector	42
3.1.1	Inner Detector	46
3.1.2	The Calorimeter	51
3.1.3	The Muon Spectrometer	57
4	Object Reconstruction at ATLAS	62
4.1	Inner Detector Track Reconstruction	63
4.2	Vertex Reconstruction	64
4.3	Hadronic Jets	67
4.3.1	Hadronic Jet Reconstruction	67
4.3.2	Jet Calibration and Systematics	70
4.3.3	Pile-up Jet Rejection and Jet Vertex Tagger	72
4.3.4	Jet Quality and Jet Cleaning	73
4.3.5	Identifying Jets Originating from Heavy Flavor Hadrons	76
4.4	Electron and Photons	78
4.4.1	Electron and Photon Reconstruction	78
4.4.2	Electron Identification and Quality	80
4.4.3	Photon Identification and Quality	82
4.4.4	Electron and Photon Energy Calibration	83
4.5	Muons	85
4.5.1	Muon Inner Detector and Muon Spectrometer Track Reconstruction	85

4.5.2	Muon Combined Reconstruction	87
4.5.3	Muon Quality	88
4.5.4	Muon Reconstruction Efficiency and Momentum Calibration .	91
4.6	Missing Transverse Momentum	92
4.6.1	E_T^{miss} Reconstruction	93
4.6.2	Track E_T^{miss} Reconstruction	95
4.6.3	E_T^{miss} Performance	96
5	Trigger	98
5.1	Level 1 E_T^{miss} trigger	100
5.2	HLT E_T^{miss} trigger	101
5.3	Improvements to the E_T^{miss} Trigger in Run 2	103
6	Physics Object Definitions	106
6.1	Baseline and Signal Electron Definition	108
6.2	Baseline and Signal Muon Definition	109
6.3	Baseline and Signal Jet Definitions	110
6.3.1	Calorimeter Jets	110
6.3.2	<i>b</i> -tagged Jets	112
6.4	Baseline and Signal Photon Definition	113
6.5	E_T^{miss} Definitions	114
6.5.1	Calorimeter-based E_T^{miss}	114
6.5.2	Track-based E_T^{miss}	115
6.6	Resolving overlapping objects	115
7	Monte Carlo Simulation of Physics Processes at ATLAS	117
7.1	Detector Simulation	119
7.2	Pile-Up Simulation	120
7.3	Signal Monte Carlo Generation	121
7.4	SM Background Monte Carlo Generation	124
7.4.1	Standard Model $t\bar{t}$ Monte Carlo Generation	124
7.4.2	Standard Model Single-Top Monte Carlo Generation	126
7.4.3	Standard Model $W + \text{jets}$ and $Z + \text{jets}$ Monte Carlo Generation	128
7.4.4	Standard Model $t\bar{t} + V$ Monte Carlo Generation	129
7.4.5	Standard Model $t\bar{t} + \gamma$ Monte Carlo Generation	129
7.4.6	Standard Model Diboson Monte Carlo Generation	130
8	Recursive Jigsaw Reconstruction	131
8.1	Recursive Jigsaw Method of Identifying Initial State Radiation	133
8.2	Performance of Initial State Radiation Identification Algorithm	135
8.3	Kinematic Variables of Initial State Radiation and Sparticle Systems . .	137

9	Collision Data Samples	139
9.1	Data Periods and Good Run List	139
10	Event Preselection	142
10.1	zero-lepton Preselection	144
10.2	One-Lepton Preselection	146
11	Signal Region Definition	150
11.1	Physical Intuition on how Signal Region Selections Reject Background	151
11.2	Order of Magnitude Estimation of how Signal Region Selections Improve Signal over Background Ratio	159
11.3	Signal Region Kinematic Selection	162
11.4	Signal Region Expected Yields and Kinematic Distributions	169
12	Standard Model Backgrounds	174
12.1	Signal Region Background Composition	174
12.2	Using Control and Validation Regions to Estimate Background in the Signal Region	175
12.3	Dominant Background: Standard Model $t\bar{t}$	177
12.3.1	Two Kinematically Distinct Populations of $t\bar{t}$	177
12.3.2	Predicting the amount of $t\bar{t}$ in Signal Region using a One-Lepton Control Region	180
12.3.3	Validating $t\bar{t}$ Predictions in Signal Region using a Zero-Lepton Validation Region	192
12.4	Subdominant Backgrounds	196
12.4.1	Standard Model W+Jets	196
12.4.2	Standard Model Single-Top	202
12.4.3	Standard Model $t\bar{t}+Z$	207
12.4.4	Standard Model Z+Jets	211
12.4.5	Standard Model Diboson	212
12.4.6	Standard Model QCD Multijet	213
13	Statistical Analysis	222
13.1	Introduction to Log Likelihood Fitting	222
13.2	Overview of Fitting to Control Regions and Signal Regions	225
13.3	Parameterization of Systematics as Gaussian Constraints	228
13.4	Background Only Fit and Background Estimation	229
13.5	Exclusion Fit and Exclusion Limit Calculation	230
13.6	Discovery Fit and Discovery Significance Calculation	231

14 Systematic Uncertainties	233
14.1 Experimental Uncertainties	235
14.1.1 Uncertainties on the Jet Energy Scale and Jet Energy Resolution	235
14.1.2 Uncertainty on <i>b</i> -tagging Efficiency	238
14.1.3 Uncertainty on the E_T^{miss} Soft Term	240
14.1.4 Uncertainties on Lepton Reconstruction and Resolution	245
14.1.5 Pile-up Uncertainty	245
14.2 Theoretical Uncertainties	245
14.2.1 $t\bar{t}$ Theoretical Uncertainty	247
14.2.2 $W + \text{jets}$ Theoretical Uncertainty	250
14.2.3 Single-top Theoretical Uncertainty	251
14.2.4 $t\bar{t} + W/Z$ Theoretical Uncertainty	253
14.2.5 Dibosons Theoretical Uncertainty	255
14.2.6 $Z+\text{jets}$ Theoretical Uncertainty	255
15 Results and Conclusion	256
15.1 Interpretation of Results on Different Stop Models	260
15.2 Broader Applications of the ISR Identification Algorithm	263
References	274

Listing of figures

1	Diagram of SM particles and their respective superpartners	3
2	Feynman diagram for the production and decay of stops at the LHC .	4
3	Stop signal with $m_{\tilde{t}} - m_{\tilde{\chi}_1^0} \gg m_t$ and SM background E_T^{miss} distribution after loose preliminary selections for $E_T^{\text{miss}} > 250\text{GeV}$, zero leptons and at least four jets	6
4	Stop signal with $m_{\tilde{t}} - m_{\tilde{\chi}_1^0} \sim m_t$ and SM background E_T^{miss} distribution after loose preliminary selections for $E_T^{\text{miss}} > 250\text{GeV}$, zero leptons and at least four jets	7
5	95% confidence limits on stop parameter space from various analysis on ATLAS $\sqrt{s} = 7 + 8\text{TeV}$ data	8
6	95% confidence limits on stop parameter space from various analysis on CMS $\sqrt{s} = 7 + 8\text{TeV}$ data	9
7	Correlation between the $E_T^{\text{miss}}/p_T^{\text{ISR}}$ ratio in simulation for stop samples with $m_{\tilde{t}} - m_{\tilde{\chi}_1^0} = m_t$	10
8	Schematic depictions of stop plus hard initial state radiation event kinematics	12
9	Distributions of the reconstructed ISR p_T over true ISR p_T ratio for stop signal and $t\bar{t}$ background in simulation	13
1.1	List of standard model elementary particles	17
1.2	One-loop corrections to the Higgs mass due to (a) a Dirac fermion f and (b) a scalar \tilde{f} to the Higgs mass parameter m_H^2	20
1.3	Diagram of SM particles and their respective superpartners	21
2.1	Stop signal with $m_{\tilde{t}} - m_{\tilde{\chi}_1^0} \gg m_t$ and SM background E_T^{miss} distribution after loose preliminary selections for $E_T^{\text{miss}} > 250\text{GeV}$, zero leptons and at least four jets	28
2.2	Stop signal with $m_{\tilde{t}} - m_{\tilde{\chi}_1^0} \gg m_t$ and SM background $m_T^{b,\text{max}}$ distribution after loose preliminary selections for $E_T^{\text{miss}} > 250\text{GeV}$, zero leptons and at least four jets	29
2.3	Gluino signal with large mass splittings and SM background m_{eff} distribution after loose preliminary selections for $E_T^{\text{miss}} > 250\text{GeV}$, zero leptons and at least six jets	29

2.4	$R_{\text{ISR}} = E_{\text{T}}^{\text{miss}} / p_{\text{T}}^{\text{ISR}}$ distributions for stop signals with $m_{\tilde{t}} - m_{\tilde{\chi}_1^0} \sim m_t$ in MC simulation	33
2.5	Schematic depictions of stop+hard ISR event kinematics	34
2.6	N_{jet}^S and m_{T}^S distributions for stop signal and SM background after loose selections for $E_{\text{T}}^{\text{miss}} > 250\text{GeV}$, zero leptons and at least four jets	35
2.7	Schematic depictions of the kinematics of a $t\bar{t}$ event with the top recoiling against the anti-top in a back-to-back manner and a stop+hard ISR event	36
2.8	Schematic diagram demonstrating the use of control regions to estimate background rates in the signal region	37
3.1	The Large Hadron Collider complex. ⁵¹	41
3.2	Cutaway view of the ATLAS detector with different sub-detector systems labeled.	42
3.3	Artistic representation of different detector signatures left by particles in ATLAS.	43
3.4	Radial and Cutaway view of the ATLAS inner detector	48
3.5	Schematic of the ATLAS Insertable B-Layer (IBL)	49
3.6	Layout of the ATLAS calorimeter	52
3.7	Schematic depiction of the ATLAS electromagnetic calorimeter module and cells	54
3.8	The tile calorimeter module with steel absorber, tile scintillators and photomultiplier readout	55
3.9	Cutaway view of the ATLAS Muon Spectrometer	58
3.10	Geometry of the ATLAS barrel and endcap toroid magnets	58
3.11	Schematic Representation of MDT tubes	60
3.12	Schematic Representation of CSC chambers	60
3.13	Schematic of the ATLAS muon trigger system	61
4.1	Flow chart of the steps involved in jet calibration	71
4.2	Jet p_{T} resolution for $ \eta < 0.8$ and $0.8 < \eta < 1.2$ jets as a function of jet p_{T} in the 8 TeV ATLAS dataset	73
4.3	The distribution of the jet vertex tagger efficiency as a function of jet p_{T} in 2015+2016 data.	74
4.4	Distribution of the MV20c10 multivariate discriminant used for tagging b-jets	79
4.5	Schematic representation of the electron reconstruction algorithm	81
4.6	Electron identification efficiency in 2016 data as a function of E_{t} and η for different electron qualities	82
4.7	Photon identification efficiency in 2016 data as a function of E_{t} for converted and unconverted photons	83

4.8	Flow chart of the steps involved in the calibration of the energy response of electrons and photons	84
4.9	The muon reconstruction efficiency distribution for Loose and Medium muons	92
4.10	Dimuon invariant mass before and after muon momenta calibration in data and MC	93
4.11	Distribution of the E_T^{miss} track soft term (TST) resolution in $Z \rightarrow \mu\mu$ events	97
5.1	Schematic representation of the ATLAS trigger system and information flow	100
5.2	ATLAS trigger turn on curves for E_T^{miss} triggers with several different thresh- olds.	103
5.3	Improvement to the L1_XE50 rate with new dynamic pedestal correction for out-of-time pile-up	104
7.1	The decay topologies of the signal models considered in this analysis. The decay mode depends on the mass splitting between stop (\tilde{t}) and neutralino ($\tilde{\chi}_1^0$). If the mass splitting is larger than m_t , then a real top maybe produced in (a) the 2 body decay $\tilde{t} \rightarrow t\tilde{\chi}_1^0$. If the mass splitting is too small then a stop may decay through (b) a virtual top to $\tilde{t} \rightarrow bW\tilde{\chi}_1^0$. The stop de- caying into b-quark plus chargino ($\tilde{\chi}_1^\pm$) channel shown in (c) is also con- sidered in mixed decay interpretations.	122
8.1	The distribution of the ratio of reconstructed vs true ISR p_T for the 350 GeV stop mass and 172 GeV neutralino mass signal sample. Only simu- lations with fully hadronic stop decays and at least 400 GeV of true ISR p_T are accepted. The red distribution is formed when the whole ISR sys- tem is equated to just the highest p_T jet. The blue distribution uses the thrust based ISR identification system.	136
9.1	Distribution of the amount of data delivered by the LHC and recorded by ATLAS vs time in 2015 (a) and 2016 (b)	140
9.2	Distribution of the mean number of interactions per bunch crossing weighted by integrated luminosity for 2015 and 2016 ATLAS data taking.	141
10.1	Kinematic variable distributions after the zero-lepton preselection.	149
11.1	Pie chart of the branching fractions for different $t\bar{t}$ decay channels.	152
11.2	The E_T^{miss} distribution after zero-lepton preselection for stop signal and SM background	153
11.3	The $R_{\text{ISR}} = E_T^{\text{miss}} / p_T^{\text{ISR}}$ distribution after zero-lepton preselection for stop signal and SM background	154

11.4	Schematic depiction of the kinematics of the $t\bar{t}$ back-to-back $t\bar{t}$ population and the $t\bar{t}$ +hard ISR population that exists after the zero-lepton preselection	155
11.5	Schematic depiction of example events from the $t\bar{t}$ back-to-back population, the $t\bar{t}$ +hard ISR population, and the stop+hard ISR signal after the zero-lepton preselection	157
11.6	The selection efficiency for $t\bar{t}$ as a function of ISR p_T for $t\bar{t}$ after the zero-lepton preselection and after all signal region selections	158
11.7	Distribution of true ISR p_T for $t\bar{t}$ after the zero-lepton preselection and after all signal region selections	159
11.8	Normalized $t\bar{t}$ differential cross section as a function of $p_T^{t\bar{t}}$	161
11.9	R_{ISR} distribution for signal and background after preselection plus $p_T^{ISR} > 400\text{GeV}$, $N_{jet}^S \geq 5$, and $N_{b-jet}^S \geq 1$ selections	165
11.10	m_T^S , $p_T^{4,S}$, and $p_{T,b}^{0,S}$ distributions for signal and background after preselection plus $p_T^{ISR} > 400\text{GeV}$, $N_{jet}^S \geq 5$, and $N_{b-jet}^S \geq 1$ selections	167
11.11	$\Delta\phi_{ISR, E_T^{\text{miss}}}$ distribution after the zero-lepton preselection, $p_T^{ISR} > 400\text{ GeV}$, sparticle hemisphere jet multiplicity and sparticle hemisphere energy requirements	168
11.12	R_{ISR} distribution after signal region selection corresponding to 36.07 fb^{-1} of data	169
11.13	Distributions of kinematic variable after the signal region selection	172
11.14	Distributions of kinematic variable after the signal region selection	173
12.1	The $t\bar{t}$ production and decay Feynman diagram	178
12.2	Schematic depiction of the $t\bar{t}$ two tops back-to-back population and the $t\bar{t}$ +hard ISR population after the zero-lepton preselection	179
12.3	Distribution of true ISR p_T for $t\bar{t}$ after the zero-lepton preselection and after all signal region selections	181
12.4	The true ISR p_T distribution for $t\bar{t}$ events after signal region and $t\bar{t}$ control region (CRTopC) selections	185
12.5	One-lepton $t\bar{t}$ control region (CRCTop) distributions for 36.07 fb^{-1} of data	189
12.6	One-lepton $t\bar{t}$ control region (CRTopC) distributions for 36.07 fb^{-1} of data	190
12.7	Distribution of select variables in the zero-lepton $t\bar{t}$ validation region	194
12.8	Distribution of select variables in the zero-lepton $t\bar{t}$ validation region	195
12.9	Kinematic distributions in the $W + \text{jets}$ control region after the background only fit to 36.07 fb^{-1} of data	200
12.10	Kinematic distributions in the $W + \text{jets}$ control region after the background only fit to 36.07 fb^{-1} of data	201
12.11	Single-top control region distributions for 36.07 fb^{-1} of data after a simultaneous fit to all control regions	205

12.12 Single-top control region distributions for 36.07 fb^{-1} of data after a simultaneous fit to all control regions.	206
12.13 γ and $Z p_T$ distributions in MC simulation with no detector resolution effects	210
12.14 Distributions of select kinematic variables in the $t\bar{t} + \gamma$ control region	212
12.15 Schematic diagram demonstrating the Jet Smearing method of estimating QCD background	214
12.16 p_T^{ISR} , $\Delta\phi_{\text{ISR}, E_T^{\text{miss}}}$ and m_T^S distributions in the QCD control region	219
12.17 R_{ISR} and $\Delta\phi_{\text{ISR}, E_T^{\text{miss}}}$ distributions in the QCD validation regions	219
 13.1 Schematic representation of the relationship between control, validation and signal regions	227
 14.1 Post-fit pull plot for the background-only fit	237
14.2 The fractional uncertainty on the jet energy scale vs jet p_T	239
14.3 The fractional uncertainty on the jet energy scale vs jet η	240
14.4 The fractional uncertainty on the jet energy resolution vs jet p_T	241
14.5 The fractional uncertainty on the jet energy resolution vs jet η	242
14.6 Ratio of b-tagging efficiency in data and MC between data and MC. .	243
14.7 Uncertainty on the E_T^{miss} track soft term as a function the number of reconstructed vertexes.	244
14.8 Single top production Feynman diagram for the Wt channel.	252
 15.1 Unblinded R_{ISR} distributions for SRC1-5 for 36.07 fb^{-1}	257
15.2 95% confidence limit curves in the stop, neutralino parameter space for the compressed stop analysis	261
15.3 95% confidence limit curves in the stop, neutralino mass parameter space for the compressed stop analysis and the bulk region stop 0L analysis .	264
15.4 Observed 95% confidence limits in the stop, neutralino mass plane for different branching ratios between the $\tilde{t} \rightarrow t\tilde{\chi}_1^0$ decay channel and the $\tilde{t} \rightarrow b\tilde{\chi}_1^\pm$ channel	267

Acknowledgments

I'd first like to say thank you to my Ph.D. advisor Professor Melissa Franklin without whom this project would not have been possible. Thank you for all the opportunities that you have given me and pushing me to accomplish my very best. Thank you for the faith that you had in me when I doubted myself and thank you for taking the long, often frustrating, hours to teach me the skills that I need to succeed.

Also thank you my undergraduate advisor, Professor Ashutosh Kotwal, for introducing me to the field of particle physics and giving the opportunity to advance to the place I am today.

Thank you Professor Matt Reece for first giving me the idea for this project. Thank you Professor Joao Guimaraes da Costa, Professor Masahiro Morii, and Professor John Huth for all the guidance you have given me all these years at Harvard.

Thank you Kerim Suruliz, Chris Rogan, and Matthias Saimpert. It has been a pleasure working side-by-side with all of you on the compressed stop search. Thank you, Kerim and Chris for all the long explanations and teaching me the knowledge necessary to perform an analysis from start to finish. Without your tireless contributions,

this analysis definitely would not have made it to publication.

Thank you to members of the ATLAS 3rd Generation SUSY group and the Stop Zero-Lepton Group including Walter Hopkins, Vasiliki Kouskoura, Professor Iacopo Vivarelli, Fabrizio Miano, Professor George Redlinger, Andrea Rodriguez, and Calum Macdonald. It was a pleasure to work with you and thank you for all the support.

Laura Jeanty, Giovanni Zevi Della Porta, Pierluigi Catastini, and William Spearman it was great fun completing various projects with you during the years and thank you for all the things that you taught me when I was a young graduate student.

Thank you Professor Ludo Pontecorvo, Professor Enrico Pasqualucci, and Professor Roberto Ferrari. It was a pleasure to work on the ATLAS muon spectrometer with you over these many years. Thank you Ludo for your faith in my abilities.

Thank you my fellow graduate students and post-docs in the Harvard ATLAS group: Alex Tuna, Stefano Zambino, Tomo Lazovich, Emma Tolley, Karri DiPetrillo, Tony Tong, Stephen Chan, Julia Gonski, and Jennifer Roloff. Thank you especially, Ann Wang for suffering through my many grammar mistakes and helping me edit this thesis.

Thank you Lisa Cacciabuado and Carol Davis, you two have always been great support for all Harvard Graduate students. Thank you, Barbara Drauschke for reading almost the entirety of this thesis on such short notice.

To all the friends who I made a long the way on this long journey, David Dodsworth, Amar Doshi, Kelsey O'Connor, Natalie Fisher, Nick Langellier, Edlyn Levine, Katya

Kosheleva, Manuel Olmedo, Zach Corse, Jenna Molnar, Bijan Haney, Anna Duncan, Nicola Abraham, Michael Fenton, Duncan Leggat, Cameron Dean, Harry Moss, Rose Ardell, Emma Buchanan, Rebecca Pickles, Xanthe Hoad, Stephen Jiggins, Rob Hard-ing, Ellis Kay, Will Madden, Chloe Gray, David Lack, Elliot Reynolds, Laura Dodd, Murdo Trail, Sarah Charley, Max Hutinet, and Oliver Lantwin, may we always have fond memories to look back upon.

My middle school teacher, Mrs. Randolph, thank you for faith in me at a time when I had very little to show for. Without your push, I may have never realized my potential. My third grade teacher, Mrs. Ryan, and my English as a second language teacher, Mrs. Estes thank you for the care and attention that you gave me when I first came to America.

Lastly, thank you to my family in both America and China for the support that you given me over the years.

Sister Zhao Yue, you will always be in my memories.

0

Introduction

The Standard Model of Elementary Particles (SM) provides a concrete description of the interactions and dynamics of all known elementary particles with the exception of gravity.^{66,48} In the SM, matter is composed of three generations of fermions with spin 1/2 while interactions are governed by gauge symmetries and mediated by spin 1 gauge bosons.

The last piece of the SM, the Higgs boson, was discovered in 2012 at the Large Hadron Collider.^{2,43} The complex scalar Higgs field spontaneously breaks the electroweak (EW) symmetry by acquiring a vacuum expectation value (VEV).^{47,55,49,56} This process of electroweak symmetry breaking (EWSB) gives mass to the W and Z gauge bosons. The fermions also acquire their mass through Yukawa interactions between the Higgs and fermion fields.

Although the Brout-Englert-Higgs mechanism^{55,49,56} ensures that the SM theory will remain viable as a perturbative physical theory up to the Planck scale, current experimental evidence suggests that the SM is not a complete theory of nature. The SM leaves several important fundamental questions unanswered. These open questions include but are not limited to the nature of Dark Matter (DM), the apparent matter/anti-matter asymmetry in the universe, the reason behind the SM mass spectrum, the potential unification of EW and strong interactions at high energy scales, the nature of neutrino masses, and the hierarchy problem regarding the naturalness of the Higgs mass. The answers to these questions are at the frontier of physics research and form the major goals of many different physics experiments across multiple disciplines.

One proposed solution to many of these questions is the introduction of a new spacetime symmetry called supersymmetry.⁶⁴ Supersymmetry imposes a new symmetry between fermions and bosons allowing one to transform into the other. In this way, the supersymmetric extension to the SM (SUSY) predicts the existence of

a yet undiscovered superpartner to every known SM particle. The SM particles and their respective superpartners are shown in Figure 1.

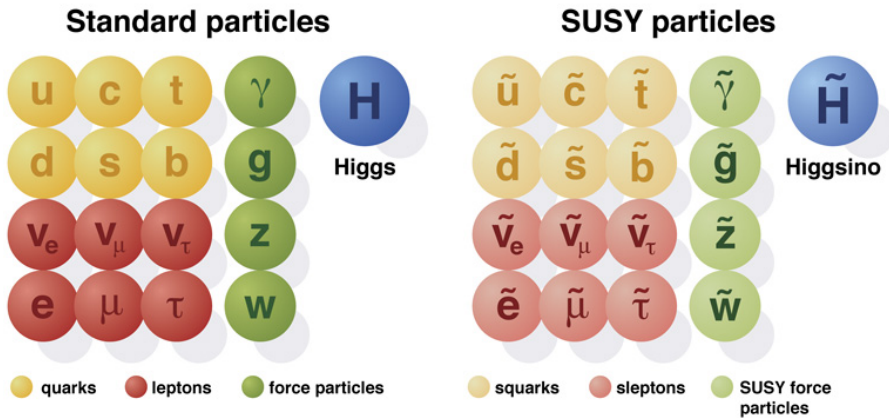


Figure 1: Diagram of SM particles and their respective superpartners.

SUSY gives one possible solution to the hierarchy problem of the Higgs as large contributions to the Higgs potential are canceled out between SM particles and their superpartners. Some supersymmetric models also unify the strong and electroweak force at high energies, provide more CP violation to generate matter/antimatter asymmetry and produce plausible dark matter candidates.

No previous high energy experiments including the Tevatron and LEP have detected the existence of superpartners.^{24,53} Therefore, if SUSY exists in nature then it must be a spontaneously broken symmetry. Many different SUSY symmetry-breaking mechanisms have been proposed but they all make the superpartners more massive than their SM counterparts.

A major goal of the Large Hadron Collider (LHC) experiment is to search for the predicted superpartners at an unprecedented energy scale. If SUSY is the solution to the hierarchy problem and restores naturalness to the Higgs mechanism, then the superpartner to the top quark, called the stop, is expected to be no heavier than a few TeV. The stop mass is strongly constrained due to the large coupling between the SM top quark and the Higgs with $\lambda_t \sim 0.94$. As such, searches for the stop at the LHC are especially interesting because the stop mass may be low enough for it to be directly produced at the energy scale of the LHC.

This thesis concerns the search for stops in an experimentally difficult region. One expected stop decay channel produces a top quark along with the superpartner to a neutral electroweak boson, the neutralino ($\tilde{\chi}_1^0$). The Feynman diagram for stop production and decay is shown in Figure 2.

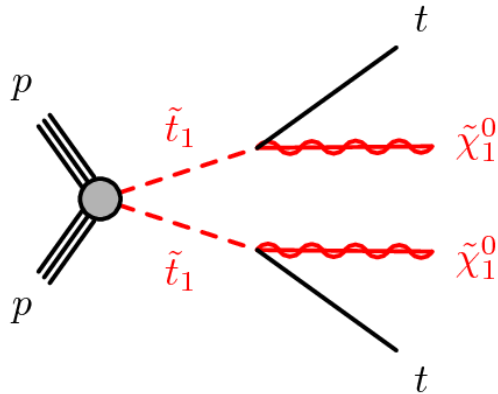


Figure 2: Feynman diagram for the $pp \rightarrow \tilde{t}\tilde{t} \rightarrow t\tilde{\chi}_1^0 t\tilde{\chi}_1^0$ process. This process is one of the expected stop production and decay channels at the LHC. The $\tilde{t} \rightarrow t\tilde{\chi}_1^0$ decay channel can have large branching fractions if the lightest stop is mainly right-handed or the lightest supersymmetric particle is a bino. The exact branching fraction depends on the sparticle masses in the SUSY model and whether the lightest stop is mainly right or left-handed.

One popular search strategy for stops targets the experimental signatures of neutralinos as they are unique to SUSY. This involves searching for events with large missing transverse energy (E_T^{miss}), the experimental signature of high momentum neutralinos. This search strategy can effectively detect stops if there is a large mass splitting between $m_{\tilde{t}}$ and $m_{\tilde{\chi}_1^0}$. The heavy stop can impart large amounts of momentum onto its decay products in this region of phase space. Monte Carlo simulation of the E_T^{miss} distribution for the $m_{\tilde{t}} = 1000$ GeV and $m_{\tilde{\chi}_1^0} = 1$ GeV signal is shown as the dashed yellow histogram in Figure 3. The E_T^{miss} distribution for SM backgrounds can also be seen in the solid stacked histogram.

The E_T^{miss} distribution for the $m_{\tilde{t}} = 600$ GeV and $m_{\tilde{\chi}_1^0} = 300$ GeV signal is shown in Figure 3 as the dashed purple histogram. The smaller mass splitting between stop and neutralino in the (600 GeV, 300 GeV) sample means the stop has less energy to boost the heavy neutralino. This leads to a softer E_T^{miss} distribution and less separation power between signal and background.

When the stop mass is nearly degenerate to $m_t + m_{\tilde{\chi}_1^0}$, the stop has just enough energy to produce the top and neutralino. The resulting stop decay products gain little momenta from the stop decay. The low p_T neutralinos in turn generate very little E_T^{miss} . The E_T^{miss} distribution for $(m_{\tilde{t}}, m_{\tilde{\chi}_1^0}) = (250 \text{ GeV}, 77 \text{ GeV}), (300 \text{ GeV}, 127 \text{ GeV})$ and $(400 \text{ GeV}, 227 \text{ GeV})$ signal samples is given in Figure 4. As we can see, the E_T^{miss} variable provides little separation power between signal and background in this region of phase space.

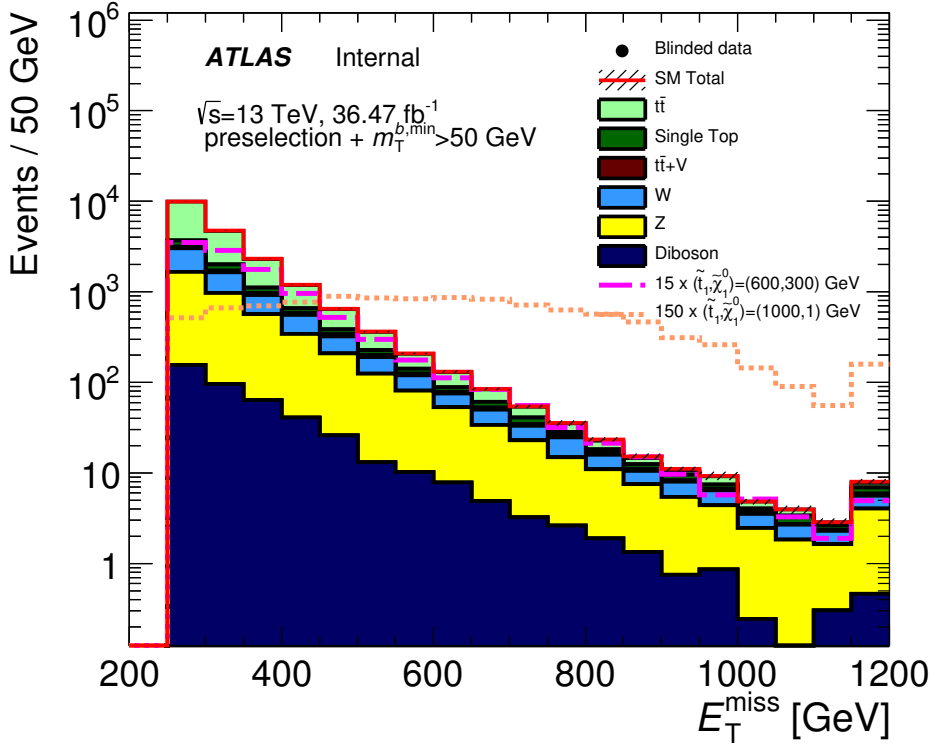


Figure 3: E_T^{miss} distribution for $(m_{\tilde{t}}, m_{\tilde{\chi}_1^0}) = (1000 \text{ GeV}, 1 \text{ GeV})$ and $(600 \text{ GeV}, 300 \text{ GeV})$ stop signal and expected SM background. The signal cross section has been scaled up by 150 and 15 respectively for better visibility. Basic selections ensuring well reconstructed E_T^{miss} , no leptons, and at least four jets are applied. Details on selections can be found in reference [21]

The only other observables in the event are the visible tops which are also produced in SM top/anti-top pair ($t\bar{t}$) production. This inability to distinguish SM $t\bar{t}$ from stop signal greatly hampers the search sensitivity in this region because SM $t\bar{t}$ production cross section is $50\times$ to $300\times$ that of the stop if the stop mass is between 250 and 400 GeV.

BSM particles only generating low p_T decay products present an experimental

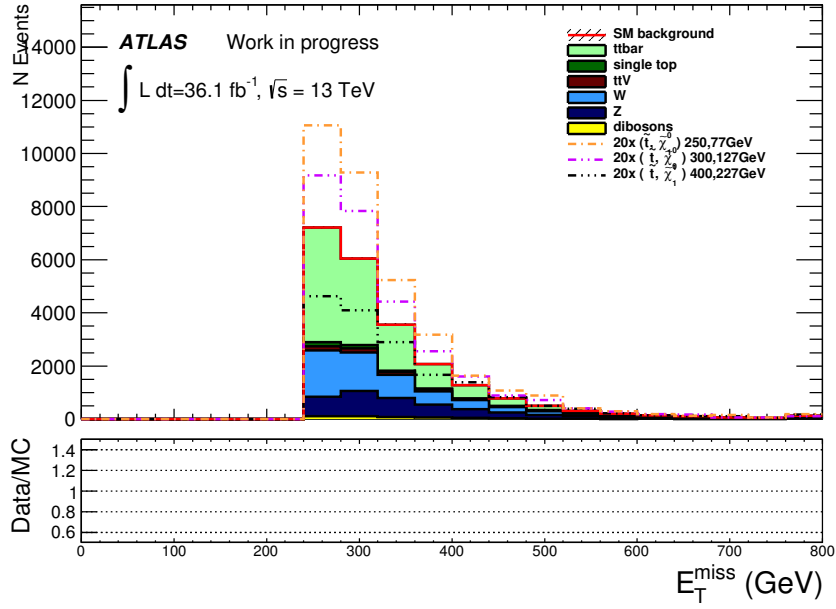


Figure 4: E_T^{miss} distribution for $(m_{\tilde{t}}, m_{\tilde{\chi}_1^0}) = (250 \text{ GeV}, 77 \text{ GeV})$, $(300 \text{ GeV}, 127 \text{ GeV})$ and $(400 \text{ GeV}, 227 \text{ GeV})$ stop signal and expected SM background. All three signal samples have $m_{\tilde{t}} - m_{\tilde{\chi}_1^0} \sim m_t$. The signal cross section has also been scaled up by a factor of 20 for better visibility. Basic selections ensuring well reconstructed E_T^{miss} , no leptons, and minimal jet multiplicity requirements are applied. Preselections are defined in chapter 10.

problem that is ubiquitous to all regions of phase space that have small mass splittings. Many ATLAS searches in SUSY including charginos, Higgsinos, sbottom, sleptons, etc. all have some region of phase space with a compressed mass spectra. In general, such regions of phase space are called compressed regions.

The ATLAS Run 1 stop search results are summarized in Figure 5. Shaded regions have been excluded by ATLAS Run 1 searches to 95% confidence level. The different colored regions correspond to different searches.

Searches targeting high E_T^{miss} are sensitive to stop signals with large mass split-

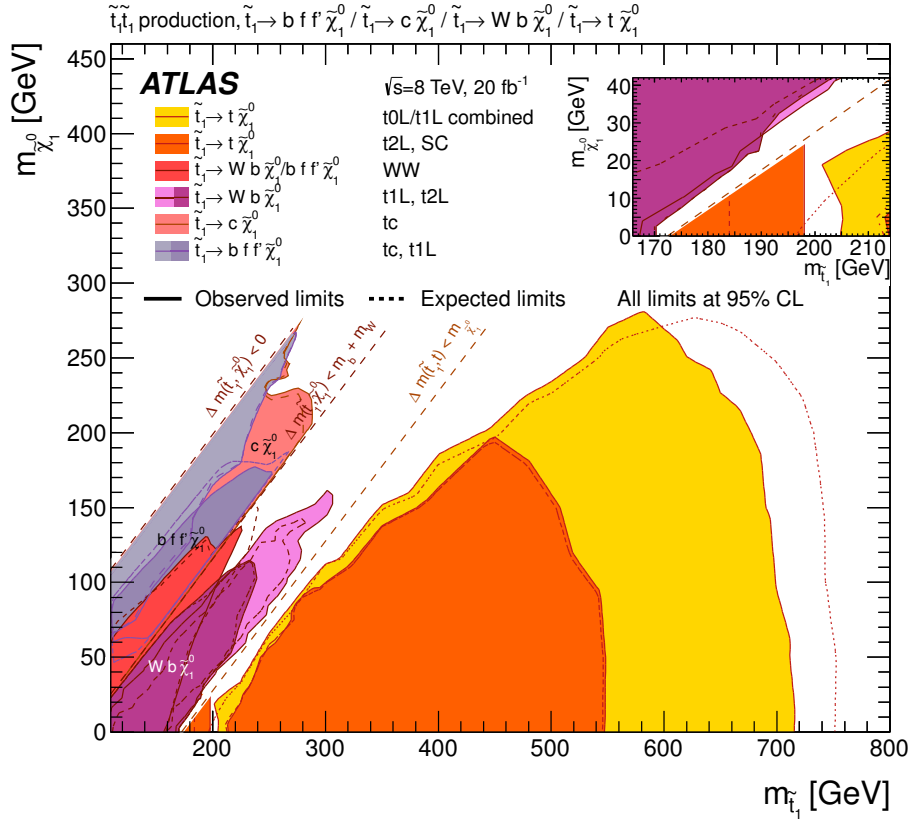


Figure 5: 95% confidence limits on stop parameter space from various analysis on ATLAS $\sqrt{s} = 7 + 8$ TeV data. Shaded regions have been excluded by ATLAS Run 1 searches. Different colored regions correspond to different search strategies including different experimental signatures. The $m_{\tilde{t}} - m_{\tilde{\chi}_1^0} = m_t$ remains unconstrained for all stop masses.

tings at the bottom right corner. Searches targeting off shell top decays are sensitive to regions with mass splittings smaller than the top mass ($m_{\tilde{t}} - m_{\tilde{\chi}_1^0} < m_t$). These searches are able to rule out the purple, red and gray regions above the $m_{\tilde{t}} - m_{\tilde{\chi}_1^0} = m_t$ diagonal line. However, the corridor near $m_{\tilde{t}} - m_{\tilde{\chi}_1^0} = m_t$ remains unconstrained even at low stop masses. The same features can be seen in Run 1 CMS results shown in Figure 6.

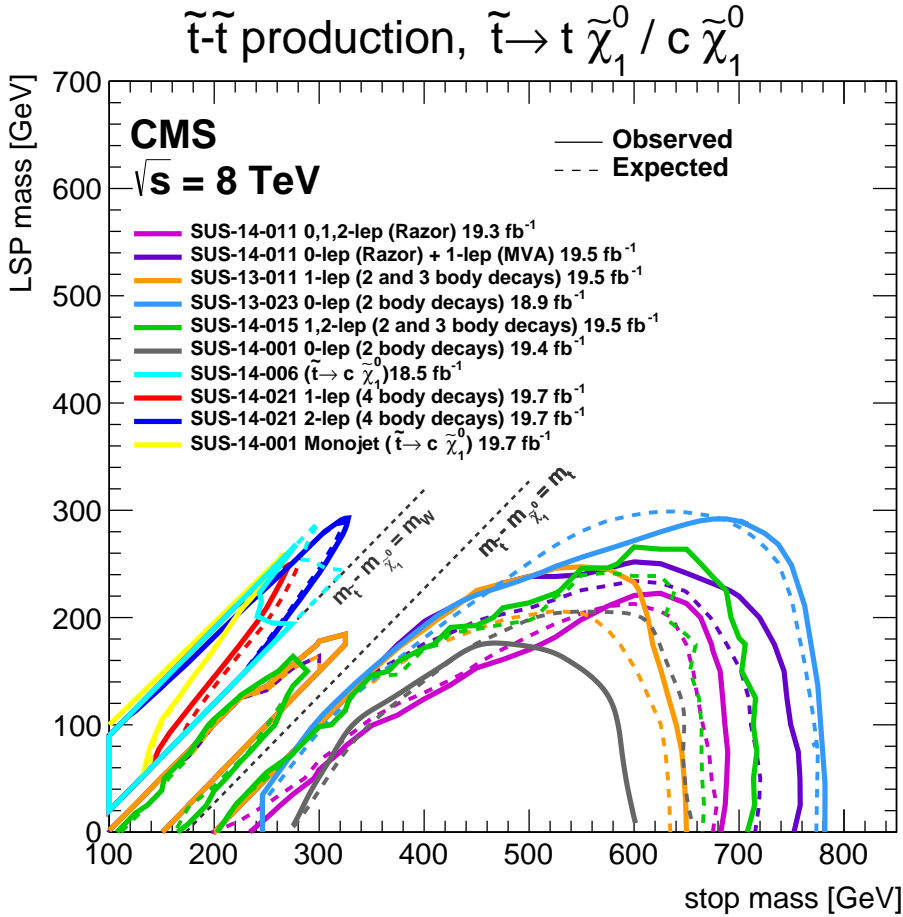


Figure 6: 95% confidence limits on stop parameter space from various analysis on CMS $\sqrt{s} = 7 + 8$ TeV data. Regions below colored curves have been excluded by CMS Run 1 searches. Different colored curves correspond to different search strategies including different experimental signatures. The $m_{\tilde{t}} - m_{\tilde{\chi}_1^0} = m_t$ line remains unconstrained for all stop masses.

This thesis demonstrates a new method of searching for stops in the $m_{\tilde{t}} - m_{\tilde{\chi}_1^0} = m_t$ compressed region by isolating events with hard initial state radiation (ISR). The ISR boosts the stops and gives additional momentum to the stop decay products. The correlation between ISR p_T and stop decay product p_T tends to be extremely

strong in this region precisely because the stop decay products gain little momentum from the stop decays. Specifically, there exists a strong correlation between ISR and neutralino systems in both direction and p_T .

The neutralinos will inherit a fraction of the original ISR p_T proportional to $m_{\tilde{\chi}_1^0}/m_{\tilde{t}}$ and the ISR and neutralinos should be back-to-back to one another. The $E_T^{\text{miss}}/p_T^{\text{ISR}}$ ratio distribution can be seen in Figure 7. The two stop signals both have $m_{\tilde{t}} - m_{\tilde{\chi}_1^0} = m_t$. Their $E_T^{\text{miss}}/p_T^{\text{ISR}}$ ratios peak sharply at $m_{\tilde{\chi}_1^0}/m_{\tilde{t}}$ according to their respective stop and neutralino masses.

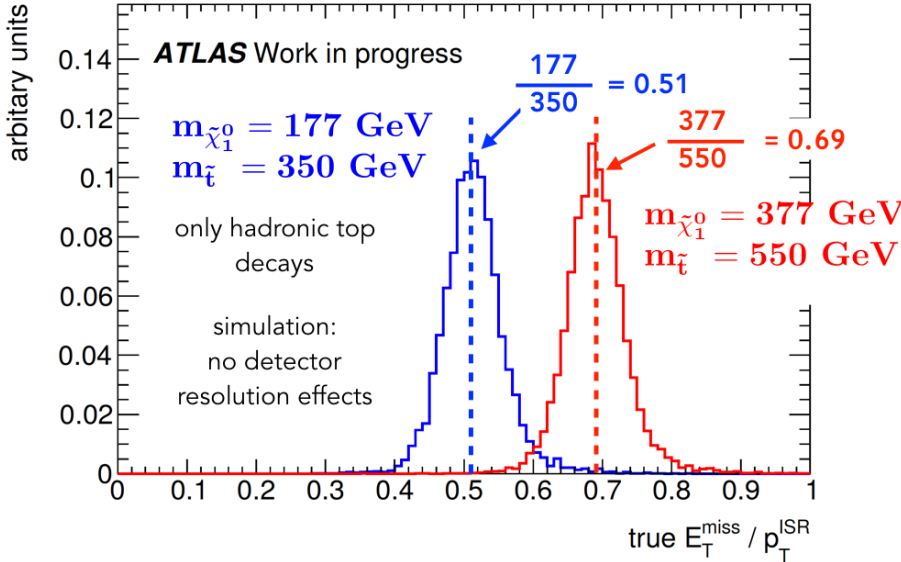


Figure 7: Correlation between the $E_T^{\text{miss}}/p_T^{\text{ISR}}$ ratio in simulation for two stop samples with $m_{\tilde{t}} - m_{\tilde{\chi}_1^0} = m_t$. Both stop samples peak sharply at $m_{\tilde{\chi}_1^0}/m_{\tilde{t}}$ with only a gaussian width of 4%. Deviation from the preferred ratio is limited by the top width, as the top must be pulled off-shell to generate phase space. No detector resolution effects are included and only the all hadronic decay channel is considered.

These correlations between ISR and E_T^{miss} allow us to separate signal from $t\bar{t}$ background and overcome the difference in production cross section in this experimentally difficult region.

In order to capitalize on these sharply peaking variables, we developed a new, accurate ISR identification system. The algorithm works by first finding the axis that maximizes the amount of back-to-back p_T along it, called the thrust axis. In events with hard ISR, the ISR and sparticle back-to-back recoil represents the single largest back-to-back kick in the event. The thrust axis should mimic the axis of back-to-back recoil between the ISR and sparticle systems.

A schematic representation of the thrust axis in stop+hard ISR events can be seen in Figure 2.5.

We then divide the event into two hemispheres according to the thrust axis. All objects in the same hemisphere as the E_T^{miss} are considered to have originated from a stop decay because we expect the neutralinos to travel in approximately the same direction as the original stops. All objects in the hemisphere opposite the E_T^{miss} are considered to have originated from ISR. In this way, the thrust-based algorithm is able to identify entire ISR systems composed of multiple jets.

The ISR identification algorithm is completely general and can be used to identify ISR for SM processes as well as other BSM searches. The performance of the ISR identification algorithm in stop and SM $t\bar{t}$ events can be seen in Figure 9. In summary, the algorithm can achieve a 9% uncertainty on the reconstructed ISR p_T in

$pp \rightarrow \tilde{t}\tilde{t} + j + j$ event

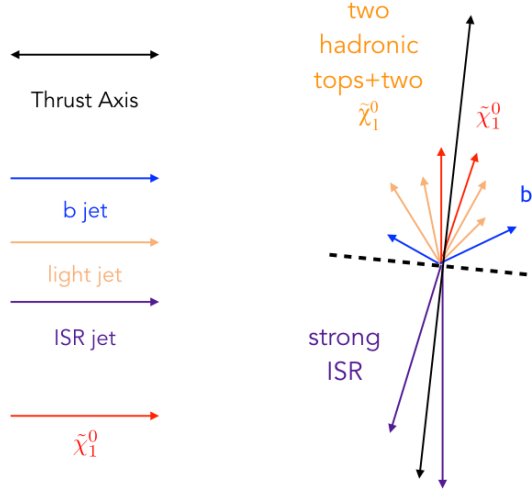


Figure 8: Schematic depictions of stop+hard ISR event kinematics. The thrust axis approximates the direction of back-to-back boost between ISR and stop decay products. The hemisphere containing E_T^{miss} also contains most of the other stop decay products. The hemisphere opposite the E_T^{miss} contains the energetic ISR jets.

stop and $t\bar{t}$ events with at least 400 GeV of true ISR p_T . This uncertainty includes any detector uncertainties due to the reconstruction of jets, E_T^{miss} and other physics objects.

The methods demonstrated in this thesis can be applied to other compressed region searches and searches involving ISR such as dark matter searches. The accurate ISR identification algorithm can also directly measure the amount of ISR produced in conjunction with SM particles. Potential applications include measuring the SM $t\bar{t}$ ISR p_T spectrum.

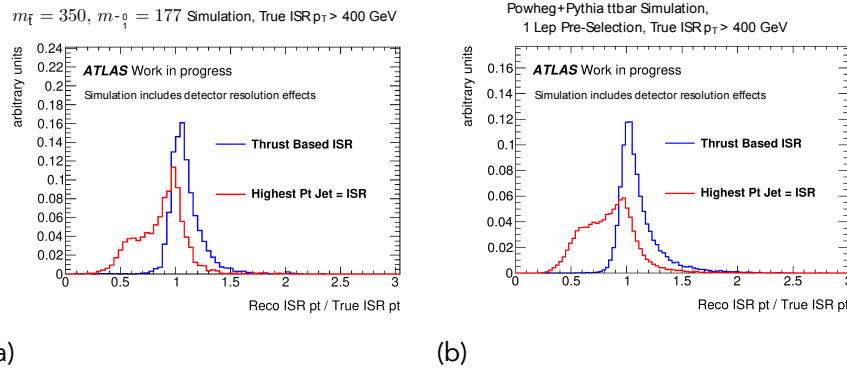


Figure 9: Distributions of the reconstructed ISR p_T over true ISR p_T ratio for stop signal and $t\bar{t}$ background in simulation. Only events with at least 400 GeV of true ISR p_T are accepted. The red distribution is formed when the whole ISR system is equated to just the highest p_T jet. The blue distribution uses the thrust based ISR identification system. Detector resolution effects are included in the simulation.

The increase in center-of-mass energy from 8 to 13 TeV translates to approximately an order of magnitude increase in the production cross section of heavy sparticles with hard ISR. The 13 TeV dataset presents a golden opportunity to search for many experimentally difficult physics processes that need a boost from hard ISR in order to be detected. This ISR based approach allowed us to finally make a definitive statement on the existence of stops in a region with no previous exclusion sensitivity.

The thesis is organized as follows. Chapter 1 presents an overview of the standard model and theoretical motivations for supersymmetry. Chapter 2 concerns the general strategy used in SUSY searches targeting regions with large mass splittings and the general strategy of using ISR to separate signal from background in compressed regions.

Chapter 3 describes the experimental setup of the LHC accelerator and ATLAS detector. Chapter 4 and chapter 5 details the reconstruction and calibration of physics objects at ATLAS the ATLAS trigger system.

The physics objects used in the analysis are defined in chapter 6. The Monte Carlo simulations of stop signal and SM background are described in chapter 7.

We present the new thrust based ISR identification algorithm in chapter 8. The algorithm is explained in the context of a more general set of algorithms that uses extremizations to classify objects called Recursive Jigsaw reconstruction. The performance of the ISR identification algorithm is also demonstrated on both signal and background.

Chapters 9 - 11 describes the 2015 and 2016 LHC dataset that is used for this analysis and the kinematic selections used to define the signal region. The chapters develop physical intuition on each signal region selection and explain how they reject different backgrounds.

The SM backgrounds in the signal region are described in detail in chapter 12. This chapter explains the use of control regions to directly estimate the expected background rates in the signal region. The control regions are designed to mimic the background kinematics in the signal region but are orthogonal to the signal region. The control regions are also dominated by background and have a low expected signal rate. We directly measure the background rate in the control regions using data. Then, we use Monte Carlo simulations to predict the background rate in

the signal region.

A large portion of chapter 12 is devoted to building intuition on the unique kinematic properties of each background, especially for the dominant background SM $t\bar{t}$. This physical intuition is used to explain the control region design and how the control regions are able to accurately estimate the background rate and minimize systematic uncertainties.

Chapter 13 summarizes the statistical methods used to extract the signal strength. Chapter 14 describe each of the experimental and theoretical systematics associated with signal and background. Systematic uncertainty is divided into two categories: experimental uncertainties due to limitations on detector resolution and theoretical uncertainties on the Monte Carlo simulations.

Finally chapter 15 shows the results with 36.07 fb^{-1} of $\sqrt{s} = 13 \text{ TeV}$ data and give an interpretation of the results on select signal models.

1

Theoretical Motivation

1.1 The Standard Model

The standard model (SM) describes our current understanding of the interactions of all known elementary particles. SM is composed of 3 parts; fermions with spin 1/2 that make up the visible matter in our universe; vector bosons with spin 1 that mediate the interactions between the fermions; and a scalar spin 0 Higgs boson that

gives mass to the massive fermions and the W and Z vector bosons. The fermions are organized in two groups, the quarks and leptons, with three families of increasing mass. The force mediators, the photon, W/Z boson, and gluon are respectively responsible for the electromagnetic, weak, and strong interactions. A diagram displaying the SM particles is shown in Figure 1.1.

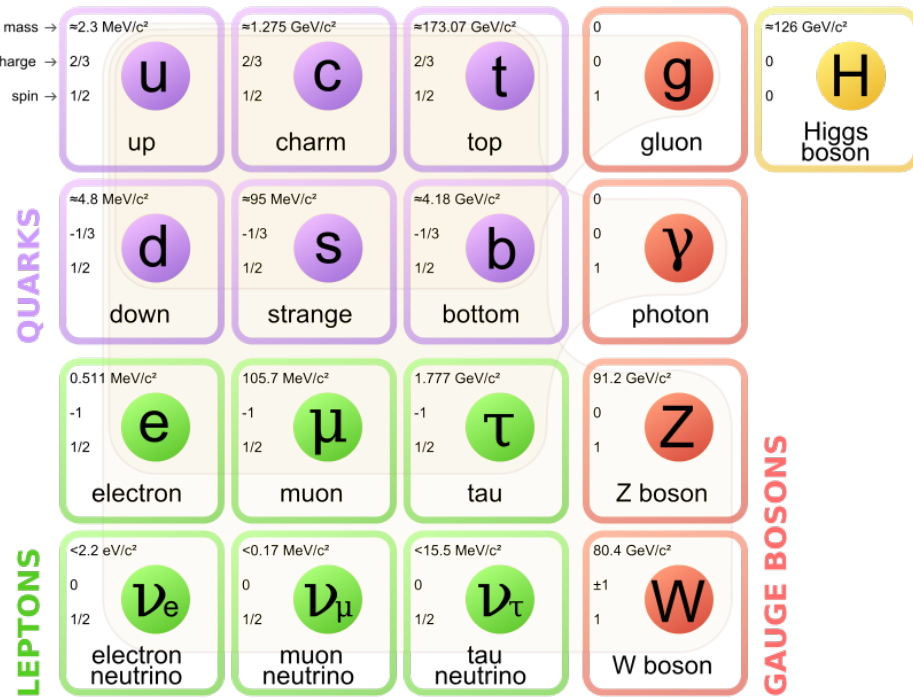


Figure 1.1: List of standard model elementary particles

Interactions in the SM are described by non-abelian Yang-Mills gauge theory with the gauge group $SU(3)_C \times SU(2)_L \times U(1)_Y$ where $SU(3)_C$ corresponds to the strong interaction and $SU(2)_L \times U(1)_Y$ corresponds to the electroweak interactions.

The quarks can interact via the strong interaction described by the $SU(3)_C$ sym-

metry. These quarks carry color charge in addition to their electromagnetic charges. The gluons mediate the strong interactions but unlike electrically neutral photons, gluons carry color charge. The self-interaction of the gluon causes the coupling strength of the strong coupling constant α_s to diverge at low energies. This phenomenon, called confinement, ensures that quarks are confined to be within composite color singlet states in the form of hadrons. At the same time, the running of α_s approaches zero at high energy, forming a phenomenon known as asymptotic freedom.

For energetic particles like those produced in proton-proton collisions at the LHC, colored partons will recursively radiate collinear gluons and quark/anti-quark pairs in a parton shower. These partons eventually form color-singlet hadrons once the energy scale is lower than the IR-cutoff scale due to confinement. The result is a jet of color-neutral baryons and mesons localized in a narrow cone in the direction of the initial colored parton.

Both quarks and leptons also interact via the weak interaction. Specifically, the left handed components of the fermions form an $SU(2)_L$ doublet while the right handed components form an $SU(2)_L$ singlet. Therefore, only the left handed components of SM fermions carry weak charge and interact via the weak interaction.

The generators of the gauge groups correspond to the massless spin one vector bosons. The W^\pm and Z bosons acquire mass through spontaneous electroweak symmetry breaking using the Higgs mechanism. This is accomplished using an addi-

tional $SU(2)_L$ doublet of complex spin zero fields, the Higgs field. The Higgs has a nonzero vacuum expectation value (VEV) at the minimum of its quadratic potential, shown in equation 1.1. When $\lambda > 0$ and $m_H^2 < 0$, $\langle H \rangle = \sqrt{-m_H^2/2\lambda}$.

$$V(H) = m_H^2|H|^2 + \lambda|H|^4 \quad (1.1)$$

This breaks the $SU(2)_L \times U(1)_Y$ electroweak symmetry and leaves only the $U(1)_{em}$ electromagnetism invariant. Meanwhile, the other gauge bosons from $SU(2)_L \times U(1)_Y$ gain a longitudinal degree of freedom from degrees of freedom associated with the Higgs doublet and thereby gaining mass. The photon, W^\pm and Z bosons are therefore linear combinations of the original $SU(2)_L$ and $U(1)_Y$ generators. The Higgs boson also gives fermions their mass through Yukawa couplings.

After symmetry breaking, only one neutral scalar component of the Higgs doublet is left. This is the massive Higgs boson observed in July 2012 at the LHC.

1.2 Introduction to Supersymmetry

Theoretical calculations of the self interaction of the Higgs field give enormous quantum corrections to m_H^2 .⁶⁴ For example, the correction to m_H^2 from a loop containing a Dirac fermion f with mass m_f is given in equation 1.3. The Feynman diagram associated with the fermion loop is shown in Figure 1.2a.

$$\Delta m_H^2 = -\frac{|\lambda_f|^2}{8\pi^2} \Lambda_{UV}^2 + \dots \quad (1.2)$$

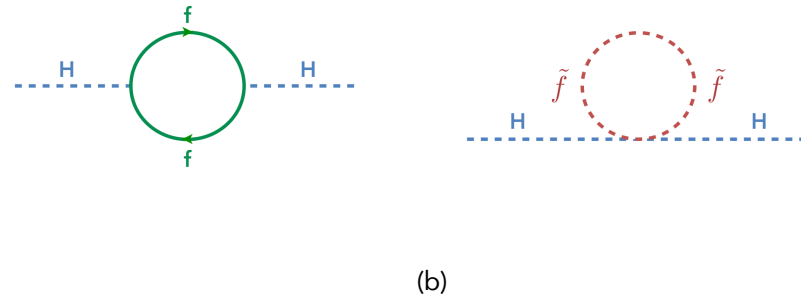


Figure 1.2: One-loop corrections to the Higgs mass due to (a) a Dirac fermion f and (b) a scalar \tilde{f} to the Higgs mass parameter m_H^2

λ_f is the Yukawa coupling between the fermion and the Higgs, and Λ_{UV} is the ultraviolet cutoff used to regulate the loop integral. Λ_{UV} can be interpreted as around the energy scale of new physics. Since the scale of new physics may be orders of magnitudes larger than the electroweak scale, the quadratic dependence of m_H^2 on Λ_{UV} makes the Higgs potential extremely sensitive to new physics. This sensitivity to high mass scales for the Higgs potential is referred to as the hierarchy problem.

Supersymmetry (SUSY) solves this problem by proposing that there exists a new space-time symmetry with respect to the transformation Q that transforms fermions into bosons and bosons into fermions.

$$Q|Boson\rangle = |Fermion\rangle \quad Q|Fermion\rangle = |Boson\rangle \quad (1.3)$$

The supersymmetric Lagrangian is invariant under transformations of Q and Q^\dagger .

In order for this to be satisfied, SUSY proposes the existence of a supersymmetric partner (superpartner) to every known SM particle. SM particles and their superpartners are related to each other by the Q transformation and differ from each other by spin 1/2. A diagram of SM particles and their respective superpartners can be seen in Figure 1.3.

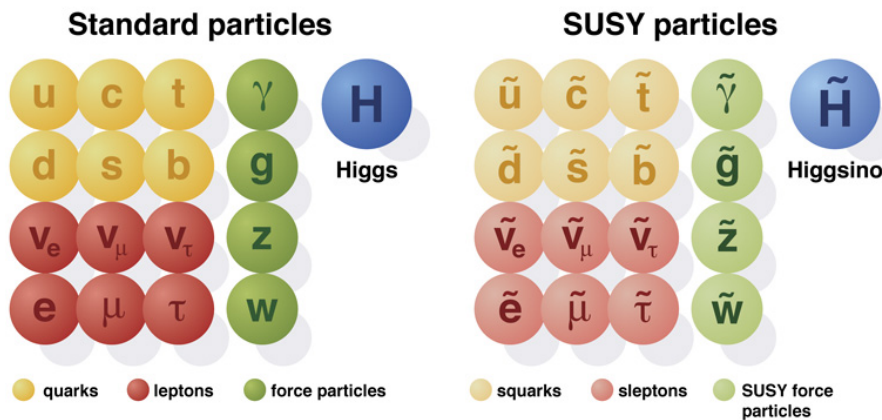


Figure 1.3: Diagram of SM particles and their respective superpartners.

If SUSY were an exact symmetry, then the SM particle and its superpartner would have the same mass. However, we have yet to discover even a single superpartner to the SM at collider experiments. Therefore, SUSY must be broken at low energies and the superpartners must have significantly more mass than their SM counter

parts.

Supersymmetry breaking can occur in many ways; the details of which are beyond the scope of this thesis. More details on SUSY symmetry breaking can be found in reference [64]. A brief summary of one example of supersymmetry breaking called gauge-mediated supersymmetry breaking will be given here. In gauge-mediated supersymmetry breaking, some scalar fields in the SUSY Lagrangian gain a vacuum expectation value due to their potential energy shape. This symmetry breaking gives mass to some fermions and their super-partners called messengers. Both the scalars and the messengers are too heavy to be directly detectable and are not the SM superpartners.

Instead, the messengers contribute effective mass to the superpartners of SM particles via loop interactions. Gauge symmetry ensures that the loop corrections to the SM gauge bosons are zero to all orders, but the same protection is not afforded to their spin 1/2 superpartners, the gauginos. These gauginos gain effective mass through one-loop diagrams involving virtual messenger particles. In a similar fashion, the scalar partners to SM fermions gain effective mass through two-loop diagrams involving virtual messengers and SM gauge bosons. In this way, gauge mediated symmetry breaking leads to heavier superpartners relative to their SM counterparts.

In general, if a complex scalar sparticle \tilde{f} with mass $m_{\tilde{f}}$ exists and couples to the Higgs according to the term $-\lambda_S |H|^2 |\tilde{f}|^2$, then correction to the Higgs mass due to the loop diagram in Figure 1.2b is given in equation 1.4.

$$\Delta m_H^2 = \frac{\lambda_s}{16\pi^2} [\Lambda_{UV}^2 - 2m_f^2 \ln \Lambda_{UV}/m_f + \dots] \quad (1.4)$$

This correction also contains a quadratically divergent term that has an opposite sign to equation 1.3. The two quadratic contributions to m_H^2 will cancel if $|\lambda_f|^2 = \lambda_s$ and we are left with only a term that is proportional to $\ln \Lambda_{UV}/m_f$. If supersymmetry exists, then the cancellation of quadratically divergent terms will occur not only for the one loop case, but for all loop orders in perturbation theory.

The term that remains after cancellation is proportional to equation 1.5. While the correction is now only logarithmically dependent on Λ_{UV} , the correction term is also directly proportional to m_f^2 . This implies that the superpartners masses cannot be too large, otherwise the correction to m_H^2 is again too large relative to the Higgs mass. If we set Λ_{UV} to approximately the Planck scale M_P and $\lambda_s \sim 1$, we find that m_f for the lightest supersymmetric particle should not be heavier than the TeV scale if we want to avoid any unphysical fine-tuning on the Higgs mass.⁶⁴

$$\Delta m_H^2 \sim m_f^2 \left[\frac{\lambda_s}{16\pi^2} \ln \Lambda_{UV}/m_f \right] \quad (1.5)$$

In particular, we know that the superpartner to the top quark has a coupling to the Higgs of order 1 due to $\lambda_S = |\lambda_f|^2 \sim 0.94^2$. This makes searches for the stop especially interesting as stop production is potentially within reach of the energy of the LHC.

1.2.1 R-Parity Conservation

Supersymmetry introduces many new interactions not found in the SM. Some of these interactions directly violate total lepton and baryon numbers. If such interactions exist then the half-life of a proton may be only a tiny fraction of a second. However, proton decay experiments have shown that the proton half-life exceeds 10^{32} years. A new discrete symmetry, called R-parity, is introduced to remove these B and L violating terms from the supersymmetric Lagrangian.

If R-parity is conserved, then the quantity P_R , defined in equation 1.6, must multiply to 1 in all interaction vertices.

$$P_R = (-1)^{3(B-L)+2s} \quad (1.6)$$

R-parity conservation has several important phenomenological consequences. P_R equals 1 for all SM particles and equals -1 for all superpartners. This means in R-parity respecting SUSY, superpartners are always produced in pairs. Superpartners must always decay into other superpartners forming a long decay chain of SUSY particle to SUSY particle that ultimately ends in the lightest supersymmetric particle (LSP) which is absolutely stable. If the LSP is electrically and color neutral, then it is an attractive dark matter candidate.

In this search, we assume R-parity is conserved and the LSP is a weakly interacting

neutralino.

2

General Analysis Strategy

2.1 R-Parity Conserving SUSY Searches in Regions with Large Mass Splittings

In R-parity conserving SUSY searches, the sought-after supersymmetric particles are produced in pairs. Each particle decays via a chain that ends in a stable, lightest super-symmetric particle (LSP). If the LSP is weakly interacting, it can not be directly

detectable by the ATLAS detector and must be inferred from transverse momentum conservation as E_T^{miss} . The rest of the products from the decay chain will be a series of SM particles.

All searches must distinguish between signal SUSY processes and background SM processes that mimic the signal detector signature. Most search methods often place a special emphasis on identifying the LSP as this is the one decay product that is unique to SUSY events. Practically this generally means searching for events with large amount of E_T^{miss} .

In regions with a large mass splitting between the sparticle and the LSP, the decay of the original sparticle generates large amounts of momentum for the LSP. Searches targeting high sparticle masses with large mass splittings therefore target the large amount of E_T^{miss} generated by the LSP as a method to separate signal from background. The E_T^{miss} distributions for stop signals with $(m_{\tilde{t}}, m_{\tilde{\chi}_1^0}) = (1000 \text{ GeV}, 1 \text{ GeV})$ and $(600 \text{ GeV}, 300 \text{ GeV})$ are shown in Figure 2.1.

Searches often use other kinematic variables that also depend on E_T^{miss} . Some examples include the $m_T^{b,\text{max}}$ and m_{eff} defined in equations 2.1 and 2.2.

$$m_T^{b,\text{max}} = \sqrt{(E_{T,b} + E_T^{\text{miss}})^2 - (\vec{p}_{T,b} + \vec{E}_T^{\text{miss}})^2} \quad (2.1)$$

$$m_{\text{eff}} = E_T^{\text{miss}} + \sum_{\text{visible objects}} p_T \quad (2.2)$$

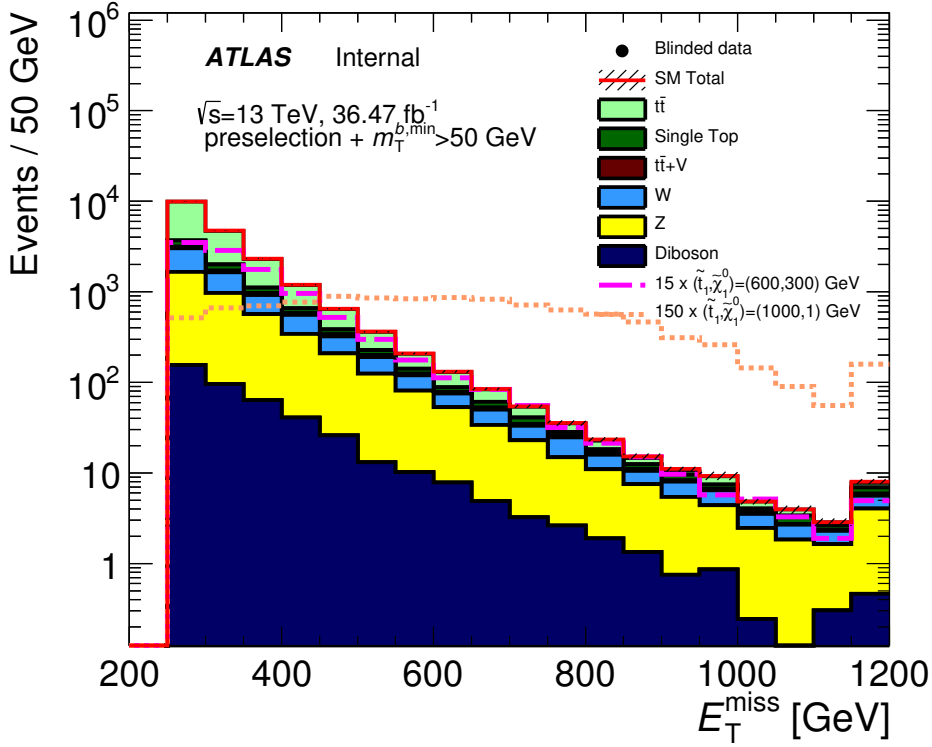


Figure 2.1: E_T^{miss} distribution for $(m_{\tilde{t}}, m_{\tilde{\chi}_1^0}) = (1000 \text{ GeV}, 1 \text{ GeV})$ and $(600 \text{ GeV}, 300 \text{ GeV})$ stop signal and expected SM background. The signal cross section has been scaled up by 150 and 15 respectively for better visibility. Basic selections ensuring well reconstructed E_T^{miss} , no leptons, and minimal jet multiplicity requirements are applied. Details on selections can be found in reference [21].

$m_T^{b,\text{max}}$ is the transverse mass between E_T^{miss} and the b-jet that is furthest away in ϕ from E_T^{miss} . m_{eff} is the scalar sum of all visible objects' p_T plus the E_T^{miss} . While both variables capture additional kinematic information, both are strongly correlated with the total magnitude of E_T^{miss} . The $m_T^{b,\text{max}}$ distribution for $(m_{\tilde{t}}, m_{\tilde{\chi}_1^0}) = (1000 \text{ GeV}, 1 \text{ GeV})$ and $(600 \text{ GeV}, 300 \text{ GeV})$ stop samples is shown in Figure 2.2. The m_{eff} distribution for gluinos is shown in Figure 2.3. SM backgrounds correspond to

the solid stacked histograms.

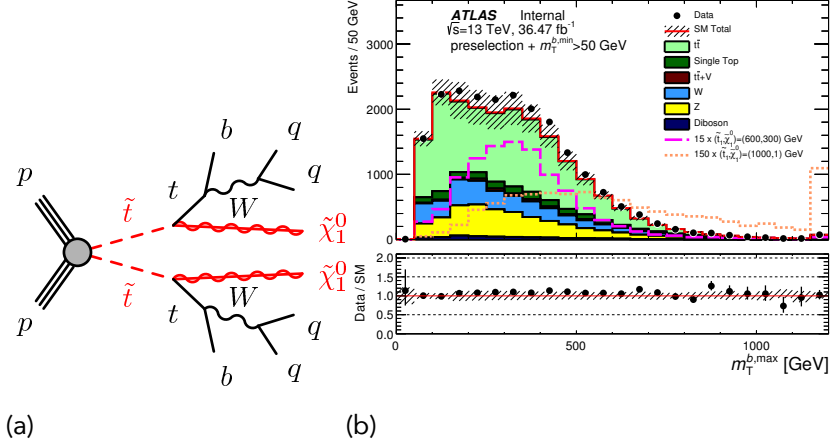


Figure 2.2: (a) Feynman diagram for stop production and decay. (b) $m_T^{b,\text{max}}$ distribution for $(m_{\tilde{t}}, m_{\tilde{\chi}_1^0}) = (1000 \text{ GeV}, 1 \text{ GeV})$ and $(600 \text{ GeV}, 300 \text{ GeV})$ samples after loose selections for $E_T^{\text{miss}} > 250 \text{ GeV}$, zero leptons and at least four jets.²¹

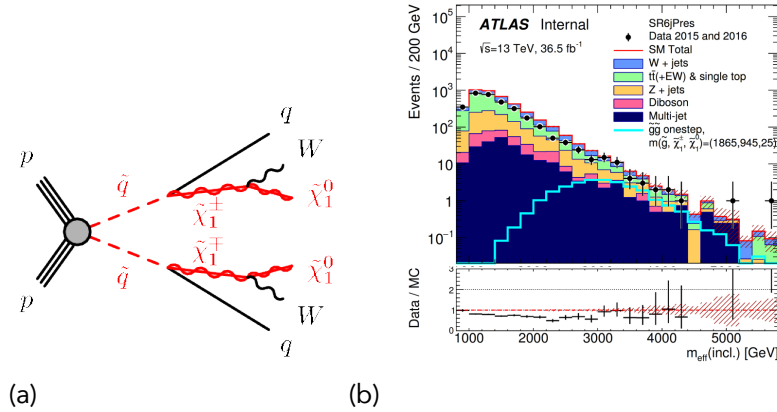


Figure 2.3: (a) Feynman diagram for gluino production and decay. (b) m_{eff} distribution for gluino $(m_{\tilde{g}}, m_{\tilde{\chi}_1^\pm}, m_{\tilde{\chi}_1^0}) = (1865 \text{ GeV}, 945 \text{ GeV}, 25 \text{ GeV})$ after loose selections for $E_T^{\text{miss}} > 250 \text{ GeV}$, zero leptons and at least six jets.²²

Both distributions have large separation power between signal and SM background.

grounds. By making kinematic selections on these sensitive variables, ATLAS and CMS searches are able to gain sensitivity to high sparticle masses with small production cross sections. For example, current ATLAS and CMS searches can exclude stops to upwards of 1 TeV.

2.2 R-Parity Conserving SUSY Searches in Compressed Regions

When the mass splitting between the original sparticle and its decay products becomes small, the sparticle has little energy to generate momenta in its decay products. The result is LSPs with low momenta. The traditional strategy of searching for events with large amount of E_T^{miss} therefore fails in this region of parameter space. This problem is ubiquitous to all regions with small mass splittings. We refer to all such regions as compressed regions.

In our analysis, the super-partner of the top, the stop, is expected to decay into a neutralino and top. When the stop mass is close to that of the top mass plus the neutralino mass, both the top and neutralino gain very little momenta from the decay. The invisible neutralinos in turn generate very little missing transverse energy. This leaves only the visible tops, which are mimicked by SM $t\bar{t}$.

Search methods that depend on variables that are highly correlated with the total magnitude of E_T^{miss} , such as $m_T^{b,\text{max}}$ and m_{eff} , fail to separate stops from SM $t\bar{t}$. This plus the fact that the $t\bar{t}$ production cross section is $50 - 300 \times$ the production cross

section of stops for stop masses between 250 and 400 GeV means these search methods have little sensitivity to the compressed parameter space.

However, the soft decay products can gain additional momenta if the entire system is boosted by hard initial state radiation (ISR). The goal of the traditional searches has always been to identify the presence of the LSPs and use their presence to distinguish between signal and background. Instead of targeting events with large amount of E_T^{miss} , we use the correlations between the LSP momenta and any ISR jets to identify LSPs in compressed regions.^{63,29} Because LSPs gain little momenta from stop decays, the correlation between ISR and LSPs in compressed regions tend to be extremely strong. By targeting the correlations between ISR and E_T^{miss} instead of the total magnitude of E_T^{miss} , we effectively turn a weakness of the compressed region into a strength.

For the $p p \rightarrow \tilde{t} \bar{\tilde{t}} \rightarrow t \tilde{\chi}_1^0 \bar{t} \tilde{\chi}_1^0$ process, the relationship is given by equation 2.4. This ratio between the invisible decay products and the total ISR p_T is called R_{ISR} .

$$E_T^{\text{miss}} \equiv p_{\tilde{\chi}_1^0 \tilde{\chi}_1^0, T}^{\text{lab}} \sim \gamma_{\tilde{t} \bar{\tilde{t}}}^{\text{lab}} \beta_{\tilde{t} \bar{\tilde{t}}}^{\text{lab}} E_{\tilde{\chi}_1^0 \tilde{\chi}_1^0}^{\tilde{t} \bar{\tilde{t}}} \sim \frac{p_T^{\text{ISR}}}{m_{\tilde{t} \bar{\tilde{t}}}} 2\gamma_{\tilde{t}}^{\tilde{t} \bar{\tilde{t}}} m_{\tilde{\chi}} \sim p_T^{\text{ISR}} \frac{2\gamma_{\tilde{t}}^{\tilde{t} \bar{\tilde{t}}} m_{\tilde{\chi}}}{2\gamma_{\tilde{t}}^{\tilde{t} \bar{\tilde{t}}} m_{\tilde{t}}} \sim p_T^{\text{ISR}} \frac{m_{\tilde{\chi}_1^0}}{m_{\tilde{t}}} \implies \quad (2.3)$$

$$R_{\text{ISR}} \equiv \frac{E_T^{\text{miss}}}{p_T^{\text{ISR}}} \sim \frac{m_{\tilde{\chi}_1^0}}{m_{\tilde{t}}} , \quad (2.4)$$

The ratio between E_T^{miss} and ISR p_T is proportional to the ratio between the mass of the LSP and the original sparticle. It is interesting to note that the back-to-back

boost between the two original stops does not affect the correlation between the observable E_T^{miss} and ISR p_T . Although the LSPs can individually gain momenta from the sparticles boosting against one another, the back-to-back momenta will exactly cancel resulting in zero measurable E_T^{miss} .

The di-LSP system only gains p_T by inheriting it from the boost by the ISR system on the two sparticles. The fraction of the momenta that is inherited by the di-LSP system is exactly $\frac{m_{LSP}}{m_{\text{sparticle}}}$ if the sparticle decay gives no additional momentum to the LSP.

Figure 2.4 shows the distribution of the R_{ISR} ratio in $pp \rightarrow \tilde{t}\bar{t} \rightarrow t\tilde{\chi}_1^0\bar{t}\tilde{\chi}_1^0$ simulation for two different stop masses (350 and 550 GeV). In both cases, the $\Delta m = m_{\tilde{t}} - m_{\tilde{\chi}_1^0}$ is 173 GeV, only 500 MeV from the $m_t = 172.5$ GeV. Both stop samples sharply peak at exactly $m_{\tilde{\chi}_1^0}/m_{\tilde{t}}$ just as equation 2.4 predicted. The gaussian width of each peak has a width of only $\sim 4\%$. No detector resolution effects were included in the simulation and only the all hadronic decay channel was considered.

The ISR and E_T^{miss} correlations also exist in direction. ISR and E_T^{miss} are necessarily back-to-back, because the neutralinos recoil in the opposite direction as the ISR.

The relationship between the decay products and ISR also has an additional benefit of being model independent. This correlation is dictated solely by relativistic kinematics rather than the underlying QFT of any particular model. The decay products' momentum and direction are determined mostly by two things: how heavy the decay products are and how hard they are kicked by the ISR.

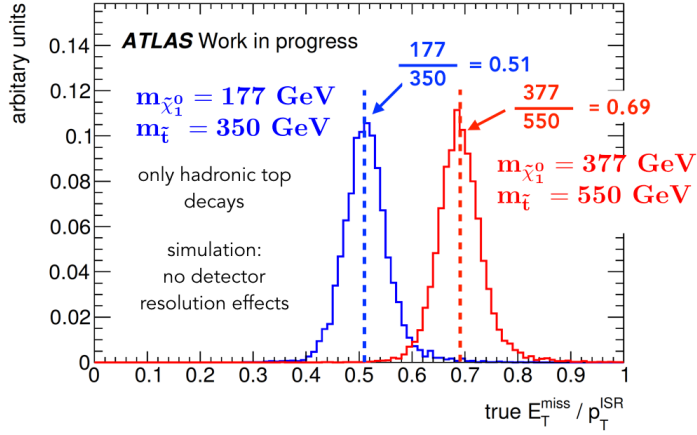


Figure 2.4: The $R_{\text{ISR}} = E_{\text{T}}^{\text{miss}} / p_{\text{T}}^{\text{ISR}}$ distribution for two different stop samples both with $m_{\tilde{t}} - m_{\tilde{\chi}_1^0} \sim m_t$. Both stop MC samples peak sharply at $m_{\tilde{\chi}_1^0}/m_{\tilde{t}}$ with only a gaussian width of 4%. Deviation from the preferred ratio is limited by the top width, as the top must be pulled off shell to generate phase space. No detector resolution effects were included and only the all hadronic decay channel was considered.

We identify ISR by finding the axis of maximum back-to-back p_{T} , called the thrust axis. The thrust axis should mimic the axis of back-to-back boost between the ISR and sparticle systems because the back-to-back boost between the ISR and sparticle systems represents the single largest back-to-back kick in events with hard ISR.

A schematic representation of the roles of the thrust axis in stop+hard ISR events can be seen in Figure 2.5.

We divide the event into two hemispheres according to the thrust axis. The hemisphere with $E_{\text{T}}^{\text{miss}}$, called the sparticle hemisphere, is expected to contain mostly stop decay products. The hemisphere opposite the $E_{\text{T}}^{\text{miss}}$ should contain the energetic ISR jets. The accurate ISR identification algorithm preserves the sharp correla-

$pp \rightarrow \tilde{t}\tilde{t} + j + j$ event

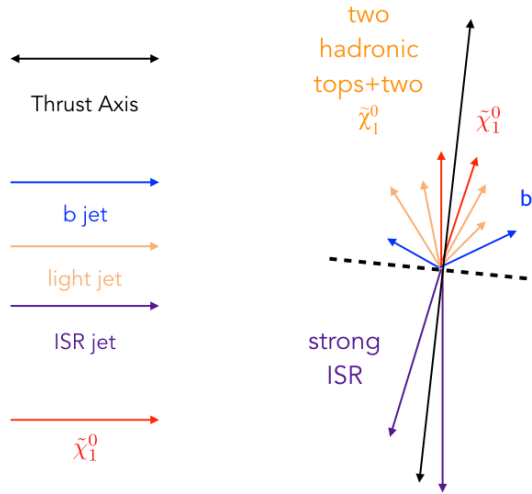


Figure 2.5: Schematic depictions of stop+hard ISR event kinematics. The thrust axis approximates the direction of back-to-back boost between ISR and stop decay products. The hemisphere containing E_T^{miss} also contains most of the other stop decay products. The hemisphere opposite the E_T^{miss} contains the energetic ISR jets.

tions between ISR and E_T^{miss} .

Other kinematic properties of the two hemispheres can also be used to separate signal from background. For example, the number of jets in the sparticle system N_{jet}^S and the total transverse mass m_T^S of the sparticle hemisphere are both expected to be larger in signal. The N_{jet}^S and m_T^S distributions for signal and SM backgrounds are shown in Figure 2.6.

In the stop signal, the six partons from the two top decays are also boosted by the ISR and tend to go in the same direction as the two neutralinos. In comparison,

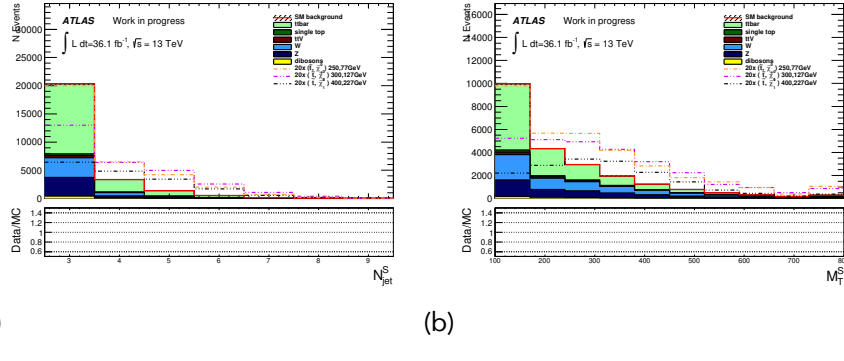


Figure 2.6: (a) N_{jet}^S distribution for stop signal and SM background after loose selections for $E_T^{\text{miss}} > 250$ GeV, zero leptons and at least 4 jets. (b) m_T^S distribution for stop signal and SM background after loose selections for $E_T^{\text{miss}} > 250$ GeV, zero leptons and at least four jets. Details on preliminary selections can be found in chapter 10

the dominant $t\bar{t}$ background tends to have the top and anti-top recoil against one another in a back-to-back fashion. Therefore, only one set of top decay products are in the same hemisphere at the E_T^{miss} . The result is the signal tends to have higher jet multiplicities and total energy in the hemisphere containing E_T^{miss} . Figure 2.7 illustrates this difference between signal and $t\bar{t}$ background kinematics.

Chapter 8 defines the kinematic variables on the sparticle and ISR hemispheres and explains the ISR identification algorithm in greater detail.

Selections are made on these sensitive variables forming a signal region (SR) that is optimized to maximize signal sensitivity. The expected background rates in the signal region are predicted using a combination of MC and data driven techniques. One common technique involves making kinematically similar control regions (CR) and validation regions (VR). All expected background rates in the signal region have

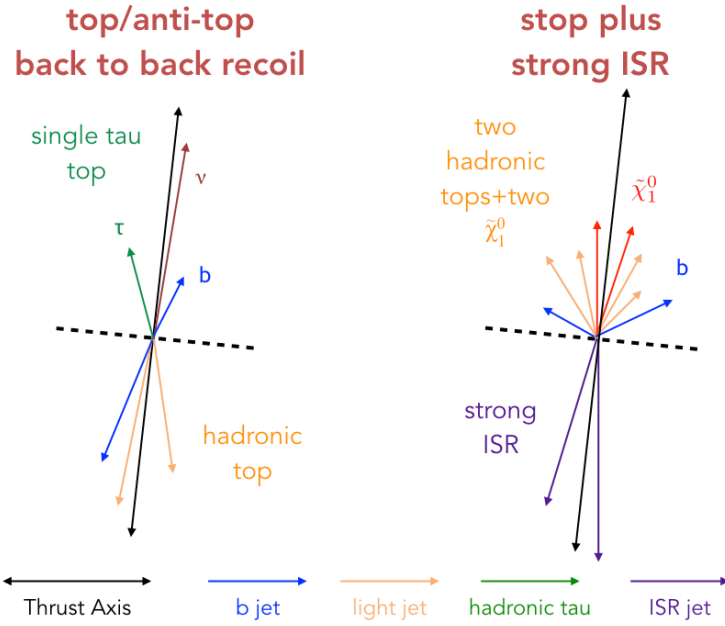


Figure 2.7: Schematic depictions of the kinematics of a $t\bar{t}$ event with the top recoiling against the anti-top in a back-to-back manner and a stop+hard ISR event. The thrust axis approximates the direction of back-to-back boost between ISR and stop decay products in signal and the back-to-back boost between the top and anti-top in the $t\bar{t}$ background. This leads to the hemisphere containing E_T^{miss} has greater jet multiplicity N_{jet}^S and total transverse mass m_T^S in signal.

been normalized to control regions defined in chapter 12. The control regions are designed to mimic the background kinematics in the signal region but are orthogonal to the signal region and have low expected signal rate. We directly measure the background rate using data in the control regions and use simulation to extrapolate background predictions from the control region to the signal region. The validation regions are even closer in kinematic selections to the signal and form an independent cross check on the extrapolation between the control and signal regions.

The relationship between control, validation, and signal regions is graphically depicted in Figure 2.8. Details on signal region selections can be found in chapter 11. Details on background estimation, control regions and validation regions can be found in chapter 12.

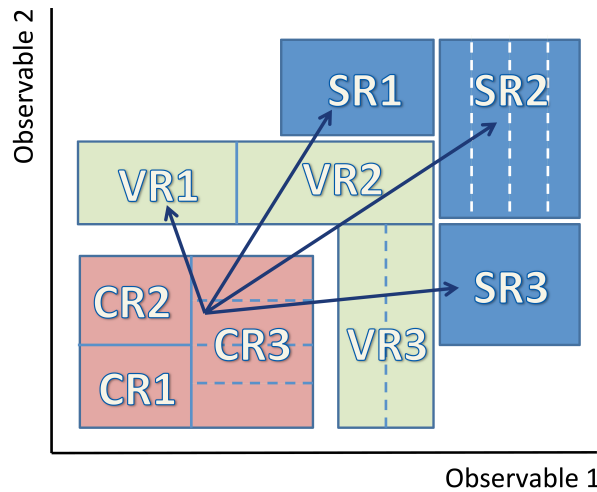


Figure 2.8: Schematic diagram demonstrating the use of control regions (CR) to estimate background rates in the signal region (SR). Control regions are dominated by background and have few expected signal events. We can estimate the amount of background we expect in the signal region by measuring the amount of background in the control region and extrapolating to the signal region using MC predictions. Validation regions exist between control regions and signal regions and serve as an independent region to validate background predictions.

The data in the signal region is originally blinded to avoid any bias for or against discovery. We unblind the signal region only after we decide the background prediction in the signal region is well understood based on observations in the control regions and validation regions.

If an excess of data is found in the signal region after unblinding then a simulta-

neous fit to all the control regions and the signal region is performed to calculate the statistical significance of any potential excess. If no excess is found, then a simultaneous fit to all the control regions and the signal region is also performed to quantify the smallest signal cross section that can be excluded.

3

Experimental Apparatus

The study of standard model (SM) physics at the TeV scale and search for potentially new physics beyond the standard model (BSM) is one of the highlights of current physics programs at the Large Hadron Collider (LHC). The LHC is a circular superconducting particle accelerator capable of accelerating and colliding both protons and lead ions. The LHC is built in the 27km LEP tunnel between 45 to 170m under-

ground near the city of Geneva. The entire LHC accelerator complex, shown in Figure 3.1 is operated by the Organization for European Nuclear Research or CERN. More details on the LHC machine and the CERN accelerator complex can be found in reference [⁵¹].

During 2015 to 2016, the LHC collided protons with a center of mass energy of 13 TeV. During 2016, the LHC surpassed its design by reaching peak instantaneous luminosities of $1.34 \times 10^{34} \text{ cm}^{-2} \text{ sec}^{-1}$.

The LHC uses four major particle detectors located at four interaction points at different locations in the ring to study the result of these collisions. Two of these, ATLAS and CMS, are hermetic 4π general-purpose detectors that study a wide variety of SM and BSM physics including SUSY. ATLAS and CMS are located at the opposite ends of the ring to ensure equal integrated luminosity. The two detectors are sensitive to the same physics processes and serve as validations to one another. The ALICE detector specializes in the collision of heavy ions and LHCb specializes in physics involving the bottom quark.

In addition to the 4 major particle detectors, three smaller experiments, TOTEM, MoEDAL and LHCf, study proton-proton scattering cross sections, diffractive processes, and cosmic ray physics.

This analysis uses data collected by the ATLAS detector in 2015 and 2016. A summary of the ATLAS detector is given in section 3.1.

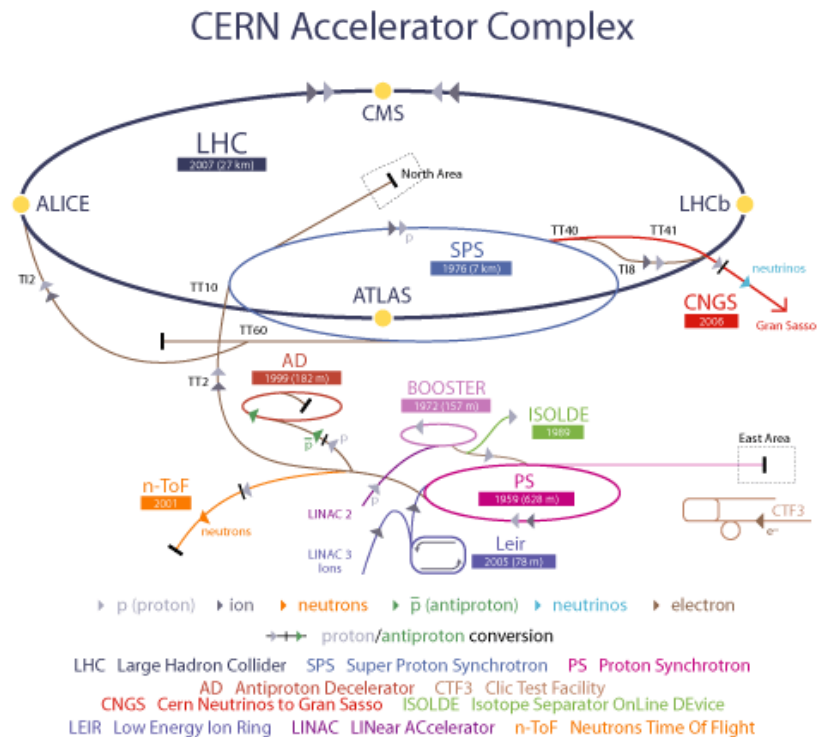


Figure 3.1: The Large Hadron Collider complex.⁵¹

3.1 The ATLAS Detector

The ATLAS Detector is a general purpose detector designed to search for new physics at the TeV scale and precisely measure SM parameters. The ATLAS detector is composed of several subdetectors arranged in concentric cylinders surrounding the interaction point. The hermetic detector covers nearly the entire 4π solid angle around the interaction point. A cutaway view of the ATLAS detector can be seen in Figure 3.2. For more details on the ATLAS detector design and specifications see reference [44].

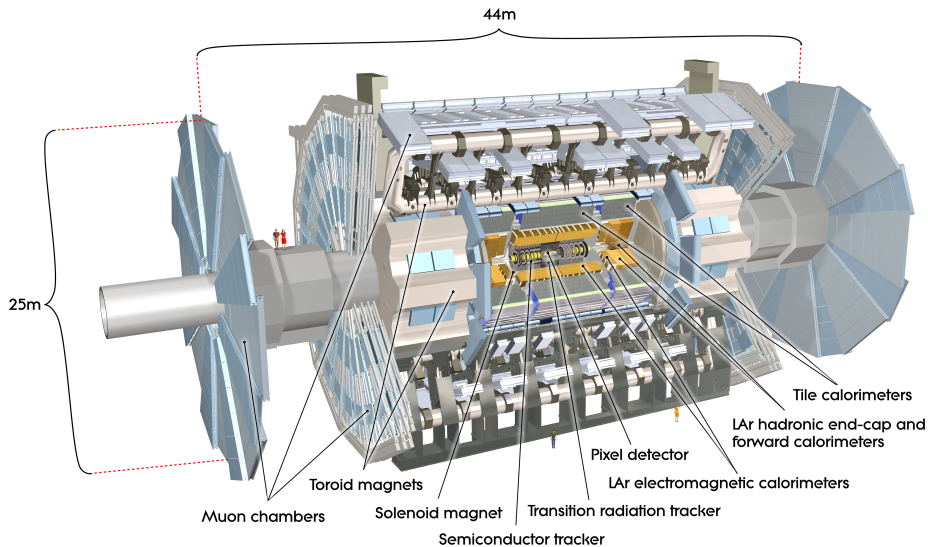


Figure 3.2: Cutaway view of the ATLAS detector with different sub-detector systems labeled.

A coordinate system is defined with the nominal interaction point as the origin. The x-axis points to the center of the LHC ring and the y-axis points upwards. The

z -axis points along the beam line. The A-side of the detector is defined to be the half with positive z and the C-side of the detector is the half with negative z . The azimuthal angle ϕ is defined to be around the beam axis in the x - y plane and the polar angle θ is defined to be from the z -axis. The pseudorapidity, $\eta = -\ln \tan(\theta/2)$, is often used instead of the coordinate θ .

The detector can be divided into the inner detector, the electromagnetic calorimeter, the hadronic calorimeter and the muon spectrometer. The detector signatures left by different particles can be seen in Figure 3.3.

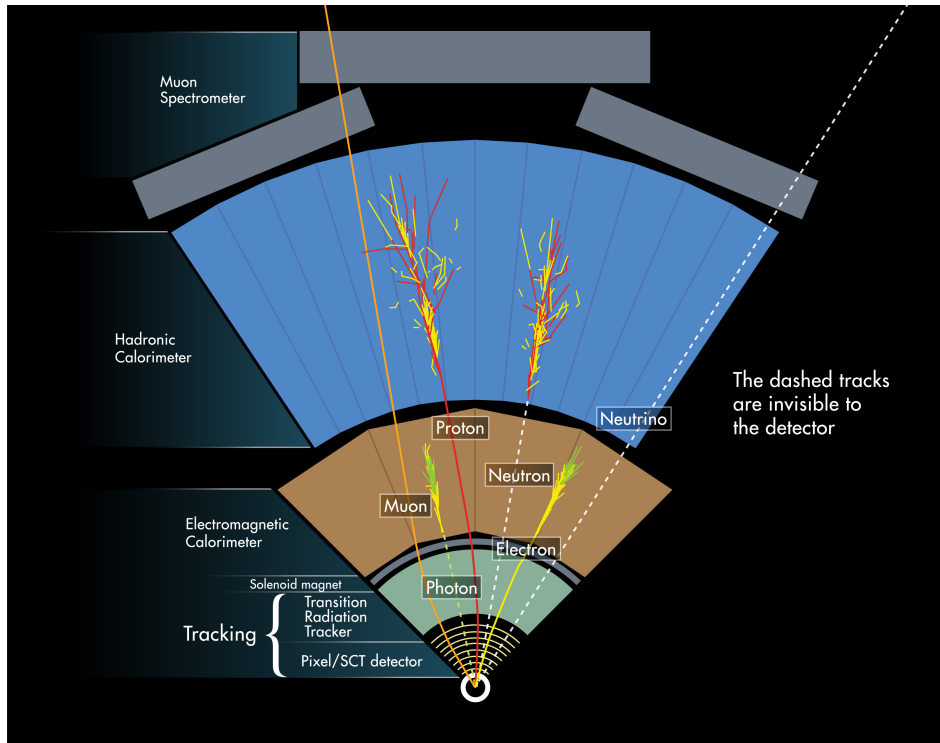


Figure 3.3: Artistic representation of different detector signatures left by particles in ATLAS.

Details on the reconstruction of physics objects can be found in chapter 4. A brief

description of detector signatures will be given here in order to motivate the purpose of each subdetector system.

The inner detector provides the position of charged particles as they fly through the detector. These position measurements are then connected to form a track along the flight path of the charged particle. A central superconducting solenoid magnet provides a 2 Tesla axial magnetic field that bathes the entire inner detector volume. The magnetic field bends charged particles in ϕ thereby allowing for the measurement of momentum as a function of track curvature.

The calorimeters sample the energy of all charged and neutral particles that interact via the electromagnetic and strong force. The ATLAS calorimeter is a sampling calorimeter that alternates between absorber and active material layers. Electromagnetically charged particles such as electrons and photons interact with the dense absorber material mainly through bremsstrahlung, ionization and electron pair production. An EM particle shower develops until the particles within the shower no longer have the energy necessary to pair produce. Hadronic particles that interact via the strong force will also form analogous hadronic showers. The shower particles deposit energy in the active material layers within the calorimeter inducing a signal.

We can measure the longitudinal and lateral shower shape and shower depth by combining signals from different calorimeter layers. Showers from EM objects such as photons and electrons form denser narrow profiles while showers from strongly interacting particles form broad showers that penetrate deep into the hadronic

calorimeter.

The muon is the only charged SM particle that is expected to be able to fully penetrate the entire calorimeter intact. Muons in turn leave tracks in the muon spectrometer (MS). This track can be matched to the inner detector track forming a combined muon track that traverses the entire detector. Barrel and endcap superconducting toroid magnets provide a magnetic field to the MS volume and allow the momentum measurement. Field strength varies depending on location but on average an integrated field of $2.5 \text{ T}\cdot\text{m}$ and $4 \text{ T}\cdot\text{m}$ are expected for muons traversing through the barrel and endcap respectively.

A combination of these different detector signatures is used to identify and reconstruct the different particles produced in a particle collision. Electrons leave an electromagnetic shower in the calorimeter with an associated track. Unconverted photons leave an electromagnetic shower without an associated track. Colored partons fragment into jets and leave a hadronic shower in the calorimeter with a number of associated inner detector (ID) tracks. Muons are reconstructed from a combined ID and MS track with limited energy deposited in the calorimeter. Tau leptons either decay leptonically via $\tau \rightarrow \nu\mu\nu$ or $\tau \rightarrow \nu e\nu$ or decay hadronically to pions and leave a narrow hadronic shower in the calorimeter. Particles that only interact via the weak force, i.e. neutrinos, do not interact with the ATLAS detector. These weakly interacting particles escape the detector completely and their presence can be inferred through the conservation of transverse momenta as E_T^{miss} .

The following subsections are dedicated to covering each subdetector in further detail.

3.1.1 Inner Detector

The inner detector consists of three independent sub-detectors. All 3 sub-detectors are immersed in a 2 T axial magnetic field produced by a solenoidal superconducting magnet. Two silicon semiconductor detectors, the Pixel detector and the Semiconductor Tracker (SCT), form the inner part of the tracking volume and the Transition Radiation Tracker (TRT) covers the outer part. The three independent sub-detectors together provide a precise and robust pattern recognition system used to reconstruct charged particle tracks and measure charged particle momentum. The ID also provides precise impact parameter measurements of tracks and primary and secondary vertex reconstruction.

The layout of the inner detector can be seen in Figure 3.4. A summary of the geometry and coverage of each ID subdetector is given in Table 3.1.

More detail on each ID sub-detector technology is given below.

Pixel Detector and the Insertable B-Layer

The Pixel detector consists of three layers of high resolution pixel silicon sensors in the cylindrical barrel and three wheels of pixel sensors in the endcap. The innermost layer of pixel sensors, called the Insertable B-Layer (IBL), was added in the first long

Table 3.1: Main specifications of each subdetector in the ATLAS inner detector including the intrinsic accuracy of single sensor elements.

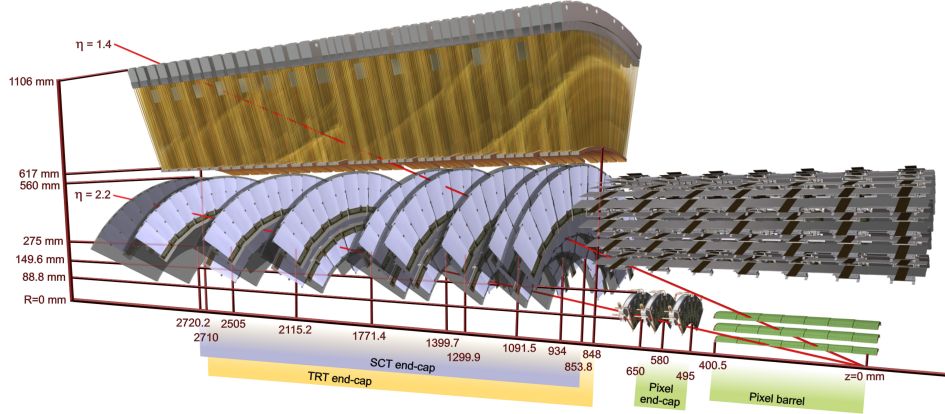
Detector	Sensor Element Size	Avg. num. of hits per barrel track	η coverage
IBL	$50 \times 240 \mu\text{m}^2$	1	3.0
Pixel	$50 \times 400 \mu\text{m}^2$	3	2.5
SCT	$80 \mu\text{m}$	4	2.5
TRT	4 mm	36	2.0

shutdown between 2012 and 2015 along with a new beryllium beam pipe. The new beam pipe decreases the amount of multiple scattering before the inner tracker.

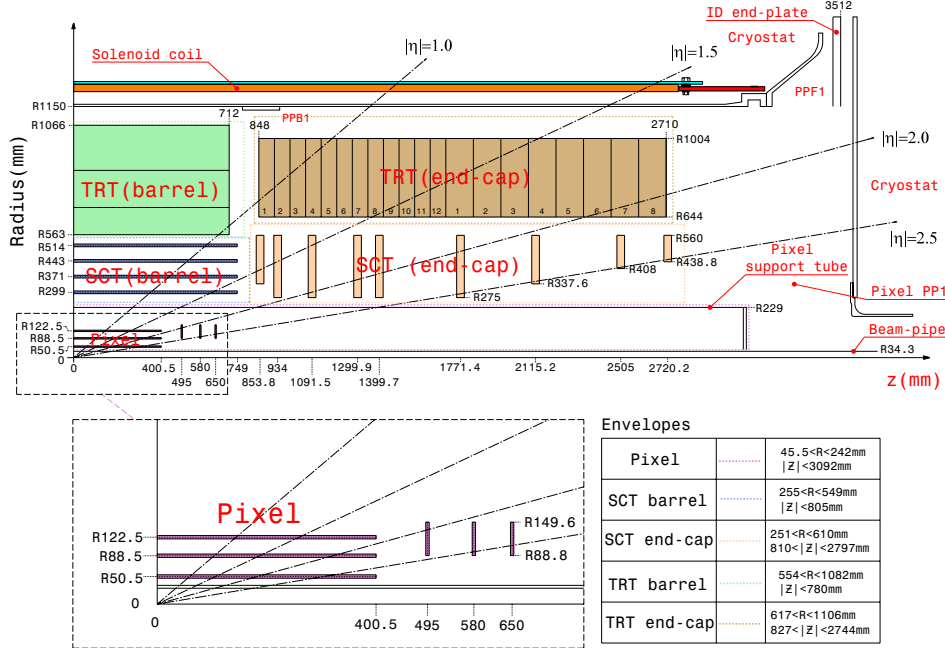
The original 3 layer Pixel detector comprises 80.4 million readout channels spread over 1744 Pixel modules. Each module houses a sensor tile with an area of $63.4 \times 25.4 \text{ mm}^2$. The sensors are composed of $250 \mu\text{m}$ thick n-type silicon wafer pixels with a size of $50 \times 400 \mu\text{m}^2$. The modules are read out by 16 front-end electronic chips, each with 2880 read out channels.

The pixels have an intrinsic accuracy of $10 \mu\text{m}$ in the bending ϕ direction and $115 \mu\text{m}$ accuracy in the non-bending z direction in the barrel and ϕ direction in the end-cap.

Installed in 2014, the Insertable B-Layer (IBL) contributes another 12 million channels to the Pixel system in Run 2.^{58,38} Located directly on top of the beam pipe at 3.3 cm from the beam axis, the IBL is the new most inner layer of the Pixel detector (the previous innermost B-Layer was at 5 cm). A schematic representation of IBL



(a)



(b)

Figure 3.4: (a) Cutaway view of the ATLAS inner detector. (b) Radial View of the ATLAS inner detector.⁴⁴

stave relative to the beam pipe can be seen in Figure 3.5.

The IBL is composed of 14 staves tilted at 14° in ϕ . Each stave is equipped with

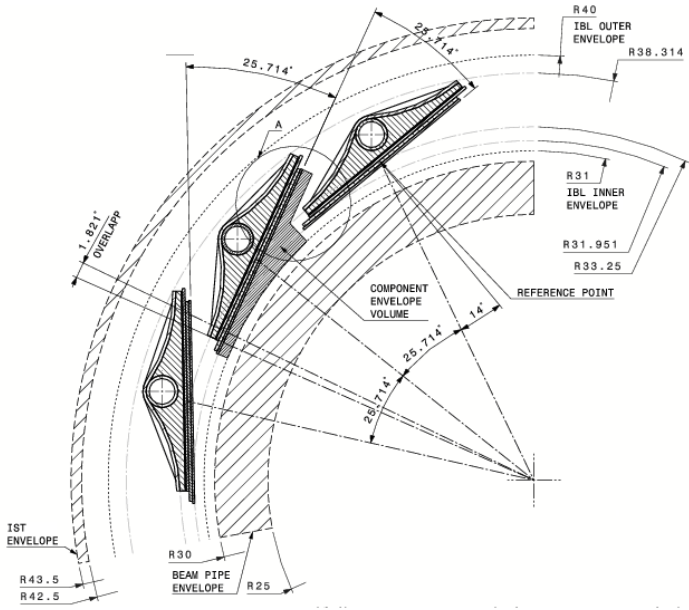


Figure 3.5: Schematic of the ATLAS Insertable B-Layer (IBL).⁵⁸

32 FE-I4 front-end chips bonded to silicon sensors. Each FE-I4 chip contains 26880 pixel cells with $50 \times 240 \mu\text{m}^2$ pitch.

The IBL improves both the tracking lever arm and track spatial resolution. The combined improvements translate to a factor of ~ 2 improvement in the impact parameter resolution and a factor of ~ 4 improvement in the b-tagging light jet rejection power.

Semiconductor Tracker

The SCT is composed of 4 coaxial layers of concentric cylinders in the barrel and 9 disks in each endcap and contributes at least 4 additional layers of high precision

position measurements to tracks. The entire SCT consists of approximately 6.3 million readout channels spread over 4088 modules. A barrel module is equipped with $64.0 \times 63.6 \text{ mm}^2$ sensors orientated in the transverse plane. Barrel sensors are made of $285 \mu\text{m}$ thick silicon wafers and contain 768 strips, achieving a barrel strip-pitch of $80 \mu\text{m}$. The endcap modules contain sensors that are trapezoidal in shape with strip pitch that vary from $54 \mu\text{m}$ to $90 \mu\text{m}$.

The sensors are mounted in a back-to-back fashion at angle of 40 mrad relative to one another. This allows the measurement of non-bending direction along with improved spatial resolution in the bending ϕ direction. The intrinsic accuracy per SCT module, dictated by the strip pitch, is $17 \mu\text{m}$ in the bending ϕ direction and $580 \mu\text{m}$ in the non-bending direction.

Transition Radiation Tracker

The TRT is the outermost component of the ID and contributes approximately 351000 readout channels. Each channel corresponds to a 4 mm diameter polyimide straw drift tube with a $31 \mu\text{m}$ gold plated tungsten anode wire, providing an intrinsic accuracy of $130 \mu\text{m}$. The total channel number is low compared to the silicon detectors but the TRT is able to compensate for this by providing a long lever arm and high hit multiplicity.

In the barrel region, TRT straws are 144 cm long and arranged parallel to the beam axis in 73 layers. In the end-cap region, straws are 37 cm long and arranged

in wheels with 160 radial layers. A typical barrel track will traverse 36 straws because the tubes are arranged in a matrix with layers offset from one another.

The dielectric material used to interweave the straws induces transition radiation in traversing charged particles. The Xenon-based gas mixture in the straws absorbs the low energy transition radiation photons. The transition radiation thereby induces a much larger signal amplitude than a minimum-ionizing charged particle. The large signal can then be used to distinguish electrons from charged pions.

In 2015 and 2016, approximately 1/3 to 2/3 of the TRT barrel and 1/7 of the TRT endcap were filled with an Argon gas mixture instead of Xenon due to leakages. This decreased electron identification efficiency by a few percent during 2015 and 2016. This decrease in electron identification efficiency is taken into account by a scale factor in the simulation.

3.1.2 The Calorimeter

The ATLAS calorimeter provides near full solid angle coverage of the interaction point up to an $|\eta| < 4.9$. The calorimeter system is composed of two parts; the electromagnetic calorimeter (ECAL) and hadronic calorimeter (HCAL). Both ECAL and HCAL are sampling calorimeters with different absorber material depending on the detector region. The ECAL uses liquid argon (LAr) as the active material and HCAL uses both scintillating tiles and liquid argon (LAr) as active materials.

The cutaway view of the ATLAS calorimeter can be seen in Figure 3.6.

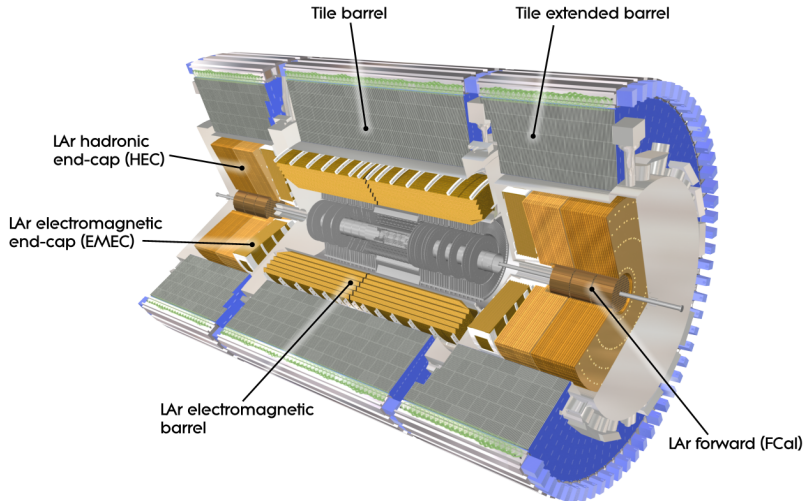


Figure 3.6: Layout of the ATLAS calorimeter.⁴⁴

The design EM resolution is $\sigma_E/E = 10\%/\sqrt{E} \oplus 0.2\%$. The design hadronic energy resolution varies from $\sigma_E/E = (56.4 \pm 0.4)/\sqrt{E} \oplus (5.4 \pm 0.1)\%$ in the barrel region to $\sigma_E/E = (94.2 \pm 1.6)/\sqrt{E} \oplus (7.5 \pm 0.4)\%$ in the forward regions.

Electromagnetic Calorimeter

The ATLAS ECAL is sampling calorimeter with lead absorber plates and LAr active material arranged in an accordion geometry. The ECAL provides coverage up to an $|\eta| < 3.2$ and the accordion design gives full crack-less coverage in ϕ .

The ECAL is split into a barrel and two endcap components with a transition region of $1.37 < |\eta| < 1.52$ in between. The barrel component is divided into two 3.2 m long half-barrel sections with an inner and outer radius of 2.8 m and 4 m re-

spectively. The endcap is divided into two coaxial wheels each 63 cm thick with an outer wheel covering the $1.375 < |\eta| < 2.5$ region and an inner wheel covering the $2.5 < |\eta| < 3.2$ region.

The barrel ECAL is segmented longitudinally into 3 layers with an additional presampler layer in front of certain regions. The presampler is composed of a thin liquid-argon layer 11mm in depth and is designed to determine the energy loss from material upstream of the calorimeter. The first layer after the presampler has a depth of 4.3 radiation length (X_0) and a fine granularity with $\Delta\eta \times \Delta\phi = 0.003 \times 0.1$. The high granularity allows for precision measurement of EM showers and can distinguish between the shower shape of electron/photons from those of $\pi^0 \rightarrow \gamma\gamma$ decays. The middle layer absorbs most of the energy in the EM shower and is made up of cells with $\Delta\eta \times \Delta\phi = 0.025 \times 0.025$ and a depth of $16X_0$. The back layer is designed to collect the tails of the EM showers and to distinguish between EM and hadronic showers. The back layer has cell sizes of $\Delta\eta \times \Delta\phi = 0.05 \times 0.025$ and a depth of $2X_0$.

The endcap ECAL is also divided into three longitudinal layers that perform the functions as the layers in the barrel. The front layer has a depth of $4.4 X_0$ and varies in cell size from $\Delta\eta \times \Delta\phi = 0.003 \times 0.1$ to $\Delta\eta \times \Delta\phi = 0.006 \times 0.1$. The middle layer has cells with the same size as the barrel at $\Delta\eta \times \Delta\phi = 0.025 \times 0.025$ and a similar depth. The back layer also has a $\Delta\eta \times \Delta\phi$ of 0.05×0.25 . A presampler also exists for the endcap with each presampler module consisting of two 2mm thick LAr layers.

The ATLAS ECAL segmentation can be seen in Figure 3.7.

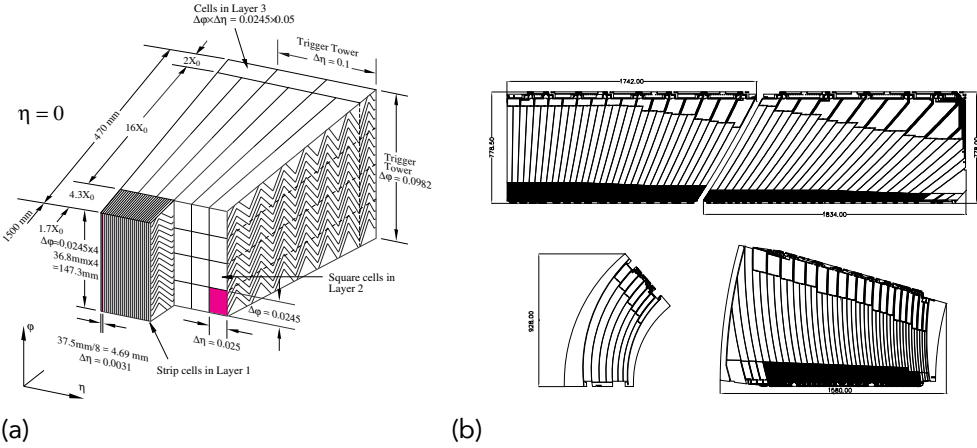


Figure 3.7: Schematic depiction of the ATLAS electromagnetic calorimeter (a) The three layers of the EM calorimeter module with the accordion geometry shown. (b) Orientation of EM calorimeter cells in the barrel and endcap relative to the IP.⁴⁴

The total thickness of the ECAL is at least $22X_0$ in the barrel and $24X_0$ in the endcap for electrons and photons and approximately 1.5 nuclear interaction length for hadronic objects.

Hadronic Calorimeter

The ATLAS HCAL is directly outside the ECAL and is responsible for containing and measuring the energy of hadronic showers. The HCAL consists of 3 separate detectors covering different η regions. The tile calorimeter covers the central region with $|\eta| < 1.7$. The LAr endcap calorimeter (HEC) covers the endcap region with $1.5 < |\eta| < 3.2$ and the LAr forward calorimeter (FCal) covers the forward region to upwards of $|\eta| < 4.9$.

The tile calorimeter is a sampling calorimeter using steel absorbers and scintillating tiles as active material. Two separate photomultiplier tubes read out the two sides of the scintillating tiles.

The barrel tile calorimeter covers an η range of $|\eta| < 1.0$ and two extended barrel tile calorimeters cover the $0.8 < |\eta| < 1.7$ region. Both barrel and extend barrel calorimeters are divided into 64 modules orientated along the ϕ direction. Each module covers a ϕ region of $\Delta\phi = 0.1$. The module is segmented in the radial direction into 3 longitudinal layers. The 3 layers have an approximate thickness of 1.5, 4.1 and 1.8 nuclear interaction lengths (λ) in the barrel and 1.5, 2.6, and 3.3 λ in the extended barrel.

A Schematic view of a tile calorimeter module can be seen in Figure 3.8

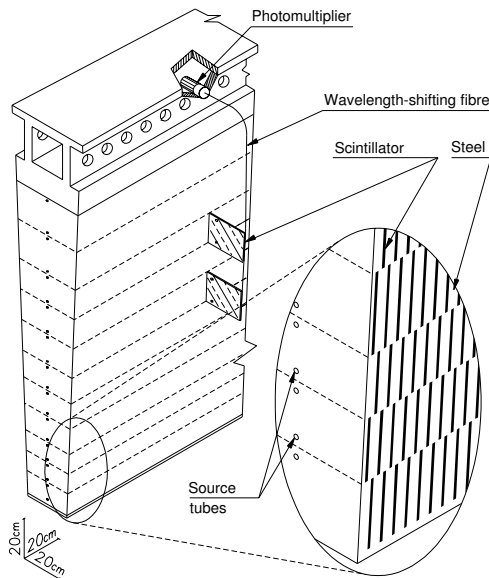


Figure 3.8: The tile calorimeter module with steel absorber, tile scintillators and photomultiplier readout.⁴⁴

The HEC uses LAr as the active material and copper as the absorber with copper plates interwoven between the LAr gaps. The HEC is located directly behind the ECAL endcap and two calorimeters share a single cryostat. The HEC covers an η range of $1.5 < |\eta| < 3.2$ and overlaps slightly with the tile calorimeter and FCAL in order to minimize any drop in material density.

Geometrically the HEC consists of two independent wheels per endcap with each wheel subdivided into 32 wedge shaped ϕ modules. Each HEC module is composed of cells with a size of $\Delta\eta \times \Delta\phi = 0.1 \times 0.1$ for the $|\eta| < 2.5$ region and $\Delta\eta \times \Delta\phi = 0.2 \times 0.2$ in higher eta regions. The HEC module is also segmented longitudinally into 2 layers making a total of 4 longitudinal layers in the 2 wheels. The combined depth of all 4 layers is approximately 10 interaction lengths.

The FCal is an LAr sampling calorimeter that extends the η coverage of the HCAL up to $|\eta| < 4.9$. A compact design with very small LAr gaps is chosen for this high flux region. The FCal is segmented in the longitudinal direction with 3 distinct modules. The absorber material is copper for the first module and tungsten in the last two. The copper absorber is optimized for EM measurements while the tungsten is predominantly designed for hadronic interactions. The 3 modules combined achieve a depth of 10 nuclear interaction length.

3.1.3 The Muon Spectrometer

The muon spectrometer (MS) consists of three layers of precision tracking chambers to track the path of muons in the bending η direction. The precision tracking chambers mainly consists of Monitored Drift Tube (MDT) detectors but also includes Cathode Strip Chambers (CSC) in the forward region. Complementing the precision trackers are fast trigger chambers, the Resistive Plate Chambers (RPC) in the barrel and the Thin Gap Chambers (TGC) in the endcap.

The MS is designed to be able to detect muon candidates with a wide range of momenta from 3 GeV to 3 TeV with standalone muon momentum resolution of $\sigma_{p_T}/p_T = 10\%$ at a p_T of 1 TeV. The configuration of the MS is shown in Figure 3.9. The open design of the MS minimizes multiple scattering after the calorimeter and gives a large lever arm for high momentum resolution.

Eight air core superconducting toroid magnets in the barrel and eight additional magnets in each endcap provide a $1.0 \text{ T} \cdot \text{m}$ to $7.5 \text{ T} \cdot \text{m}$ of bending power in the MS volume. The configuration of the magnets is shown in Figure 3.10

The barrel magnets cover an $|\eta|$ range up to 1.4 and the endcap magnets cover an $|\eta|$ range from 1.6 to 2.7. The area between $1.4 < |\eta| < 1.6$, called the transition region, has a mixed magnetic field from both the barrel and endcap. The endcap magnets are offset from the barrel magnets by 22.5 degrees in ϕ to allow a smoother magnetic field in the transition region.

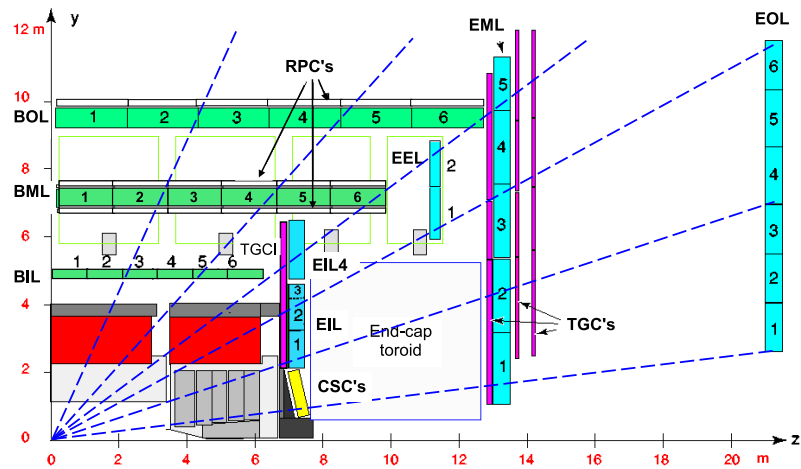


Figure 3.9: Cutaway view of the ATLAS Muon Spectrometer.⁴⁴

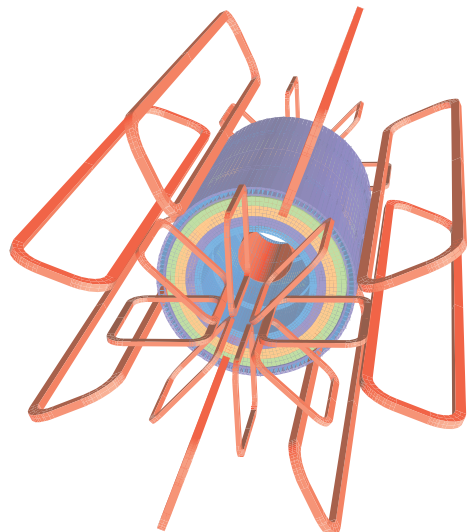


Figure 3.10: Geometry of the ATLAS barrel and endcap toroid magnets. The cylinder represents the calorimeter.⁴⁴

Muon Precision Tracking

The ATLAS MS system consists of 3 stations of muon precision tracking chambers at approximately 5 m, 7.5 m and 10 m radii in the barrel and 7.4 m, 14 m and 21.5 m in z in the endcap. This provides precision tracking coverage up to an $|\eta| < 2.7$. Most precision tracking chambers use Monitored Drift Tube (MDT) technology with 3 to 8 layers of MDT tubes each. The only exception to this is the very high rate forward region with $2.0 < |\eta| < 2.7$ which uses CSC technology.

MDT tubes are 3cm diameter aluminum tubes filled with Ar/CO₂ gas mixture with a tungsten-rhenium anode wire. Each tube has an intrinsic resolution of 80 μm corresponding to a resolution of 35 μm per chamber and offers position measurements in the bending η direction.

The CSCs are multiwire proportional chambers with one layer of anode wires in the bending plane and two layers of cathode strips. The position measurement is obtained by interpolating the signal on neighboring cathode strips. The strips are perpendicular to one another with 5.31mm (5.56mm) pitch in the bending plane and 12.5 mm (21.0 mm) in the non-bending plane for small (large) chambers. This results in a 60 μm resolution per plane in the bending plane and about 5 mm resolution in the non-bending plane.

The structure of MDT tubes and CSC chambers can be seen in Figures 3.12 and 3.12 .

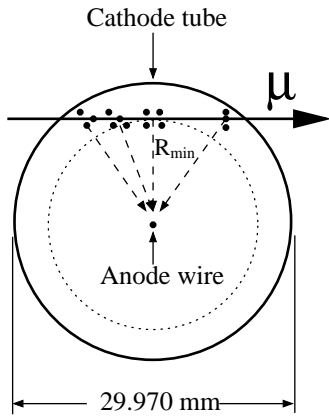


Figure 3.11: Schematic Representation of MDT tubes.⁴⁴

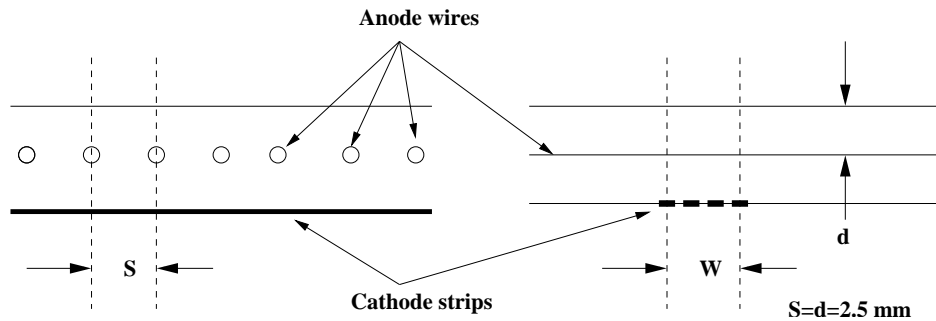


Figure 3.12: Schematic Representation of CSC chambers.⁴⁴

Muon Trigger Chambers

The ATLAS MS also features a system of fast trigger chambers consisting of three stations of Resistive Plate Chambers (RPC) in the barrel and 4 stations of Thin Gap Chambers (TGC) in the endcap. The MS triggering system provides triggering coverage up to an $|\eta|$ of 2.4. The RPCs are placed below and above the middle MDT station and outside the outer MDT barrel station. The TGC stations are arranged with one station in front of the inner endcap precision tracking wheel and 3 stations

split in front and behind the middle endcap MDT wheel.

In Run 2, muon triggers in the endcap also require coincidences in the inner-most layer of the TGC to reduce fake trigger rates due to particles interacting with beam shielding in the forward region.

A schematic of the muon trigger system is given in Figure 3.13. The trigger searches for fast coincidences between the layers along the expected trajectory of a muon. Different maximum deviation from the straight infinite momentum path is allowed for triggers with different p_T thresholds. High p_T tracks are straighter and lie closer to the infinite momentum straight track than a low p_T track.

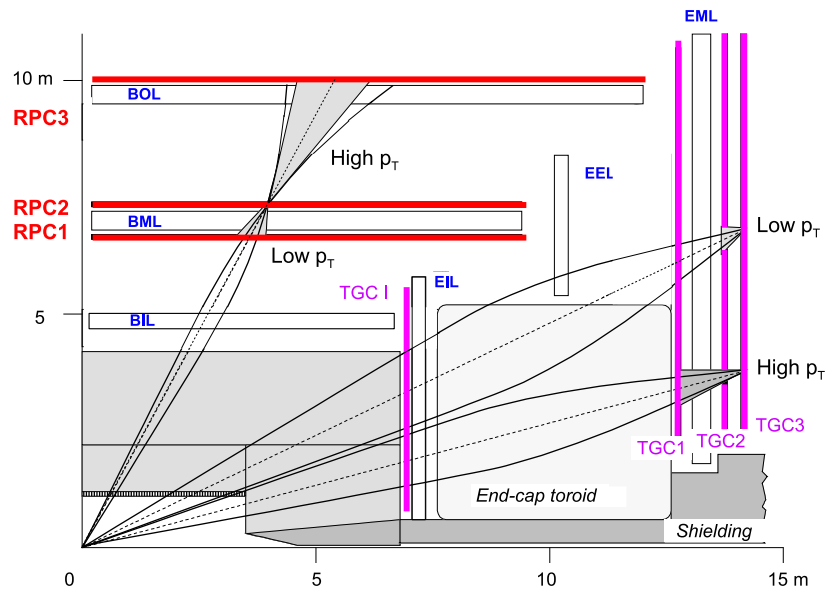


Figure 3.13: Schematic of the ATLAS muon trigger system. The coincidence windows for muons of different p_T is shown.⁴⁴ The trigger searches for fast coincidences between the layers along the expected trajectory of a muon. Different maximum deviation from the straight infinite momentum path is allowed for triggers with different p_T thresholds. High p_T tracks are straighter and lie closer to the infinite momentum straight track than a low p_T track.

4

Object Reconstruction at ATLAS

The subject of object reconstruction and calibration at ATLAS can easily fill a document that is multiple times the size of the thesis. The following sections give a brief summary of each object reconstruction algorithm. Section 4.1 covers the reconstruction of inner detector tracks. Section 4.2 covers the reconstruction of vertices. Section 4.3 summarizes the reconstruction and calibration of hadronic jets. Sections

4.4 and 4.5 describe the reconstruction and calibration of electrons, photons and muons. Lastly, section 4.6 discusses the reconstruction of missing transverse momentum (E_T^{miss}). Greater detail on each subject can be found in the references cited in each section.

4.1 Inner Detector Track Reconstruction

Many reconstructed physics objects depend on tracking information in the inner detector (ID). ID tracks are combined with the EM calorimeter and muon spectrometer information to identify and measure the momentum of electrons and muons.

Hadronic jets use ID tracks to determine if the jet originated from a heavy flavored hadron containing b-quarks or only light flavored hadrons. ID tracks are also crucial to identifying whether objects originate from the interesting hard scattering interaction or a less interesting pile-up interaction.

Two types of inner detector tracks are reconstructed, primary tracks and secondary tracks. Primary tracks originate from the interaction point (IP) and are meant to reconstruct the trajectories of charged particles originating directly from the proton-proton collisions. Secondary tracks target charged particles originating in the ID from secondary decays and interactions such as $\gamma \rightarrow e^+e^-$ conversions.

Primary tracks are reconstructed using the NEWT algorithm. The NEWT algorithm starts from seed segments in the inner silicon detectors and extended outwards to-

wards the TRT. Greater details can be found in reference [45]. A brief summary of the track reconstruction algorithm will be given here.

First, seed segments are created from three space point measurements in silicon detectors. Each pixel cluster corresponds to a single space point measurement since a single pixel sensor provides 3D position information. Two SCT clusters from the same SCT layer must be combined to form a single space point measurement because each SCT strip only provides 2D position information.

Seed segments can be formed out of all pixel (PPP), all SCT (SSS) or two pixel and one SCT (PPS) space points. PSS space points are rejected due to high fake rates.

Starting from the original seed segment, track reconstruction is extrapolated layer by layer through the inner detector. Hits are added to the track one layer at a time. If multiple tracks share a hit, then the shared hit is assigned to the most precise track.

In contrast, secondary tracks are reconstructed from the TRT and extrapolated inwards towards the direction of the beam line. Segments are reconstructed in the TRT and then extended inwards by adding silicon hits.

4.2 Vertex Reconstruction

On average around 25 proton-proton interactions occur in every beam crossing in Run 2. These p-p interactions are spread out in the Z coordinate due to the finite

bunch length at the LHC. We are able to reconstruct the original interaction vertex (primary vertex) by tracing back charged particle tracks to the beam line. We are able to differentiate objects from the interesting hard scattering p-p interaction from other pile-up interactions by reconstructing vertices. A brief summary of the primary vertex reconstruction algorithm is given in this section. Greater detail can be found in references [15,52].

A subset of reconstructed ID tracks are used to reconstruct the primary vertices.

In Run 2 tracks must satisfy:

$$p_T > 400 \text{ MeV}$$

$$|\eta| < 2.5$$

number of silicon hits ≥ 9 if $|\eta| \leq 1.65$ or ≥ 11 if $|\eta| > 1.65$

IBL hits + B Layer hits ≥ 1

maximum 1 shared module (1 shared pixel hit or 2 shared SCT hits)

pixel holes = 0 (holes exist when a hit is expected in a layer of sensors given the fitted trajectory of the track but none is found)

SCT holes ≤ 1

A vertex seed is found by searching for the global maximum in the Z coordinate of reconstructed tracks. The vertex position is fitted using an algorithm that is robust to additional noise and outlier tracks called the adaptive vertex fitting algorithm. 15,52

Adaptive fitting determines the vertex position by fitting to ID tracks according to the least squares fitting method. Tracks far from the vertex center, called outlier

tracks, have lower weights in the fit than tracks close to the vertex center. The simple least squares fitting method is sensitive to outliers tracks far from the vertex center. Outlier tracks have a high probability of being noise tracks that don't actually originate from the vertex we are trying to reconstruct. By weighting outlier tracks less in the fit, the adaptive fitting algorithm is able to decrease sensitivity to these noise tracks.

A-priori, we don't know the true position of the vertex center and which tracks are outliers. Therefore, the vertex is fitted iteratively. Initially, all tracks have high weights. This allows all tracks, including outlier tracks, to influence the position of the fitted vertex center. The weight of the outlier tracks decreases with each fit iteration and more weight is given to a core set of tracks near the fitted vertex center. In this way, the adaptive fitting algorithm determines both the vertex center and which tracks are outliers with increasing accuracy after each iteration. This process is repeated until the fitted vertex center no longer changes.

After a vertex is found, tracks incompatible with the vertex form a new vertex seed. The vertex reconstruction process is repeated until all tracks have been clustered into vertices or no additional vertices can be found.

The primary vertex with the highest total p_T summed over all associated tracks is identified as the vertex of the hard scattering interaction. All other primary vertices are referred to as pile-up vertices.

4.3 Hadronic Jets

Energetic partons carrying color charge produced in the initial hard scattering will quickly fragment into multiple hadrons. The result is a shower of charged and neutral hadrons referred to as a parton shower. The parton shower leaves a roughly conical energy deposit in the electromagnetic and hadronic calorimeter and multiple associated tracks in the inner tracker. Some energy may even be deposited in the muon spectrometer if the initial colored parton is energetic enough. This detector signature is referred to as a jet.

Identification and reconstruction of hadronic jets is very important for this analysis. This analysis specifically targets the $p p \rightarrow \tilde{t}\tilde{t} \rightarrow bqq\tilde{\chi}_1^0 + \bar{b}\bar{q}\bar{q}\tilde{\chi}_1^0$ channel where all the visible decay products from the two stops are quarks.

Of key importance is the correct reconstruction of the initial colored parton's energy. Also important is the rejection of jets resulting from pile-up interactions and identifying jets resulting from b-quarks. Jet reconstruction and energy calibration are described in sections 4.3.1 and 4.3.2. Jet vertex tagging and b-jet tagging are described in section 4.3.3 and 4.3.5.

4.3.1 Hadronic Jet Reconstruction

Hadronic jets are reconstructed by clustering energy deposits in the calorimeter. First, calorimeter cells are clustered into topological clusters (topo-clusters). A brief

summary of topo-cluster formation is given here. More details can be found in references [1, 13].

A topo-cluster starts as a single calorimeter cell that passes a 4σ signal above noise threshold called a seed cell. Cells neighboring the cluster are added to the cluster if they pass a 2σ signal over noise threshold. Each time a cell is added to the cluster, cells neighboring the newly added cell are also considered to be neighbors of the cluster. The cluster grows until no neighboring cells pass the 2σ signal over noise threshold. At this stage, one last round of neighboring cells is added regardless of the amount of signal to noise ratio in those cells.

Topo-clusters are then grouped into jets using the anti- k_t algorithm. The anti- k_t algorithm is explained in great detail in reference [36] and only a brief phenomenological description of the algorithm is given here.

The anti- k_t algorithm groups two objects (i,j) together into a single object according to the distance measure d_{ij} defined in equation 4.1. In this case the objects being grouped together are topo-clusters. If the two objects (i,j) have $d_{ij} < \min(k_{Ti}^{2p}, k_{Tj}^{2p})$ then the two are grouped into a single object. k_{Ti} refers to the p_T of object i and the parameter p is set to -1 . $\Delta R = \sqrt{\Delta\eta_{ij}^2 + \Delta\phi_{ij}^2}$ corresponds to the separation between the two objects i and j in η and ϕ . Finally R is an input parameter into the algorithm.

$$d_{ij} = \min(k_{Ti}^{2p}, k_{Tj}^{2p}) \frac{\Delta R^2}{R^2} \quad (4.1)$$

The algorithm first groups the two objects with the lowest d_{ij} together into a single object. That is to say, the algorithm first groups the two objects with both highest p_T and the least amount of separation in ΔR . The algorithm runs iteratively, grouping objects with the lowest d_{ij} until no objects satisfies the $d_{ij} < \min(k_{Ti}^{2p}, k_{Tj}^{2p})$ requirement.

The algorithm can best be explained by examining example cases. If an energetic topo-cluster called 1 is surrounded by only less energetic topo-clusters j then the anti- k_t algorithm will group all the calorimeter energy cells within a $\Delta R < R$ cone of topo-cluster 1 into a single jet. If two energetic topo-clusters exist within $\Delta R < R$ of one another then the two topo-clusters will be grouped into a single jet. If two energetic topo-clusters exist within $R < \Delta R < 2R$ of one another, then two jets will be formed around the two energetic topo-clusters with the calorimeter energy cells are split between the two jets.

The anti- k_t algorithm is both infrared and collinear safe, meaning the algorithm is insensitive to the radiation of additional soft particles and the collinear splitting of initial partons. Additional soft partons do not change the shape of the jets but the jet shape is flexible to accommodate the presence of other hard radiation. Theorists and phenomenologists also prefer the anti- k_t algorithm over other jet reconstruc-

tion algorithms because the anti- k_t algorithm can be used to group the particles in a parton shower.

ID Tracks are associated with jets according to a ghost association procedure described in reference [37]. In summary, tracks are also grouped with jets according the anti- k_t algorithm.

4.3.2 Jet Calibration and Systematics

Both the electromagnetic and hadronic calorimeters at ATLAS are sampling calorimeters. The energy deposited in the absorber material is effectively lost because the absorber does not actively record a signal. Therefore the energy measured using the active material must be scaled up to compensate for this loss. For this reason and others including leakage of energy outside of the calorimeter edges and deposition of energy below the energy thresholds, reconstructed jets must be calibrated to determine the original hadron's energy.

A variety of MC based and data based methods are used to calibrate hadronic jets and documented in references [11,7,6]. Figure 4.1 shows the steps in jet calibration for Run 2.¹¹

First the individual topo-clusters in the jet are calibrated to the energy scale of EM showers using MC simulations.¹¹ It should be noted that this calibration to EM showers correctly calibrates the energy in EM showers but underestimates the amount of energy lost in hadronic showers. Additional corrections are applied in the follow-

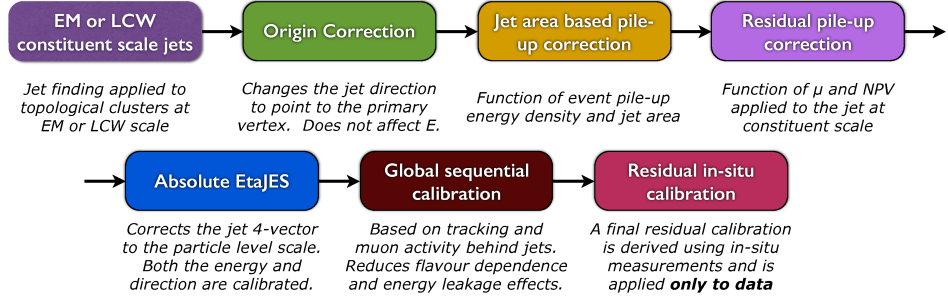


Figure 4.1: Flow chart of the steps involved in jet calibration.

ing steps to account for this difference.

A correction for energy deposited by pile-up interactions are applied.³ The correction is based on the measurement of average energy originating from pile-up multiplied by the jet area. The pile-up energy density is determined by measuring the median energy density around the central $|\eta| < 2.0$ part of the calorimeter.

In the next step, the jet energy scale is applied. The jet energy scale is a scale factor which relates the reconstructed jet energy with the true jet energy. The jet energy scale is derived from an inclusive jet MC after pile-up and origin corrections have been applied.¹¹

A residual difference between the energy responses of gluon and light quark jets remains after the jet energy scale calibration.¹¹ The difference is due to a number of reasons including the factor of 2 difference in color charge between quarks and gluons. A global sequential correction scheme uses information on the topology of energy deposits, associated inner detector tracks and activity in the muon spectrome-

ter behind the jet to account for this deference and correct for other detector-based issues. The global sequential correction scheme is described in detail in reference [¹⁰].

Lastly, further corrections to the jet energy response are obtained by measuring the balance between jets and some reference objects directly in data. The reference object can be a photon, a Z boson or other jets. The p_T balance between jets and the reference objects are measured in data and compared to the MC. A residual correction is applied to correct for any disagreements between data and MC. Systematic uncertainties on the jet energy responses including those on the jet energy scale and jet energy resolution are also derived using these data driven methods.

More details on the measurement of the jet energy response can be found in references [^{7,6}].

The jet p_T resolution after jet calibration for $|\eta| < 0.8$ and $0.8 < |\eta| < 1.2$ jets are shown in Figure 4.2.⁶

4.3.3 Pile-up Jet Rejection and Jet Vertex Tagger

It is imperative to be able to distinguish between jets originating from the hard scattering interaction (hard scattering jets) and those originating from other pile-up interactions (pile-up jets) in the high luminosity LHC environment. Pile-up jets may originate from the on average 25 additional p-p interactions in the same bunch crossing or from interactions in other beam crossings. We distinguish between the

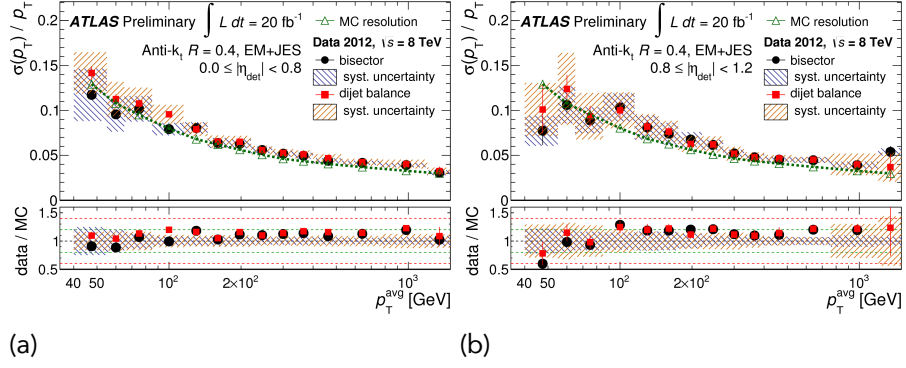


Figure 4.2: Jet p_T resolution for $|\eta| < 0.8$ and $0.8 < |\eta| < 1.2$ jets as a function of jet p_T in the 8 TeV ATLAS dataset.⁶

hard scattering jets and pile-up jets using a multivariate discriminant known as the jet vertex tagger (JVT). Reference [5] describes the jet vertex tagger in great detail.

For our analysis we require a jet vertex tagger value greater than 0.59. This corresponds to a 92 percent efficiency for jets originating from the hard scattering interaction and a 2 percent fake rate from pile-up jets, if the jet has $|\eta| < 2.4$ and $p_T < 60$ GeV. The JVT efficiency as a function of jet p_T is shown in Figure 4.3

4.3.4 Jet Quality and Jet Cleaning

Several variables are useful in discriminating between real hadronic jets and fake jets not coming from p-p interactions. The sources of fake jets include noise in the LAr and Tile calorimeters, beam induced backgrounds and cosmic ray showers. These variables can be divided into three broad categories: variables quantifying the EM and hadronic calorimeter energy ratio, ID track based variables and variables based

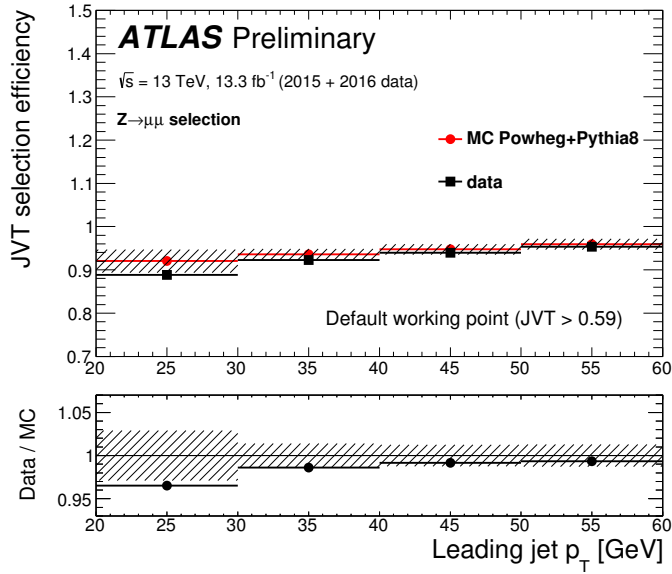


Figure 4.3: The distribution of the jet vertex tagger efficiency as a function of jet p_T in 2015+2016 data. Only jets balanced against a $Z \rightarrow \mu\mu$ boson are accepted. Details can be found in reference [5].

on the shape of the electronic signal pulse in the LAr calorimeters. Detailed descriptions of the procedure used to identify bad quality jets are found in reference [14] and a brief summary will be given here.

Energy ratio variables can reject calorimeter noise and beam induced backgrounds and energy deposited from cosmic rays. Jets originating from beam induced backgrounds tend to concentrate more energy in a few longitudinal layers compared with jets from p-p collisions. Multiple variables corresponding to the fraction of energy deposited in any one longitudinal section relative to the total energy deposited are useful in discriminating against fake jets.

Energy ratio variables include:

f_{EM} : ratio of EM calorimeter energy to total jet energy

f_{HEC} : ratio of hadronic endcap calorimeter (HEC) energy to total jet energy

f_{max} : maximum energy fraction in any single calorimeter layer

ID track based variables are useful because tracks can be matched to the primary vertex in good jets. Fake jets have low fraction of tracks that can be matched to the primary vertex.

Track based variables include:

f_{ch} : ratio of the scalar sum of ID track p_T where ID track must originate from the primary vertex to jet p_T . approximately the fraction of jet energy carried by charged particles.

f_{ch}/f_{max} : ratio of f_{ch} and f_{max} , the maximum energy fraction in any single calorimeter layer

The signal pulse shape in the LAr should be consistent with that of a particle shower in a good jet. A quality variable Q_{cell}^{LAr} distinguishes the quadratic difference between expected and actual pulse shapes in each LAr cell. Quality variables based on the fraction of cells in a jet with poor quality and the average quality is found to provide discrimination power against LAr noise.

The LAr pulse shape variables include:

$\langle Q \rangle$: weighted average of pulse quality of LAr cells (Q_{cell}^{LAr}) in a jet. Normalized to $0 < \langle Q \rangle < 1$.

f_Q^{LAr} : Fraction of energy in cells with poor quality pulse shapes in EM LAr Calorimeter

f_Q^{HEC} : Fraction of energy in cells with poor quality pulse shapes in hadronic endcap calorimeters (HEC) which also use LAr technology.

E_{neg} : total energy of all cells with negative energy

A jet satisfying any one of the following criteria is considered a BadLoose jet. The presence of a BadLoose jet can mean a noisy calorimeter or beam induced background. These problems can result in a misreconstructed E_T^{miss} . Therefore, if there are any BadLoose jets in the event then the entire event is rejected. This procedure is called jet cleaning.

A jet is considered a Loose jet if it is not identified as a BadLoose jet. Loose jets are used as signal jets in most ATLAS physics analysis including this one.

$$f_{EM} > 0.5 \text{ and } |f_Q^{HEC}| > 0.5 \text{ and } \langle Q \rangle > 0.8$$

$$E_{neg} > 60 \text{ GeV}$$

$$f_{EM} > 0.95 \text{ and } f_Q^{LAr} > 0.8 \text{ and } \langle Q \rangle > 0.8 \text{ and } |\eta| < 2.8$$

$$f_{max} > 0.99 \text{ and } |\eta| < 2.0$$

$$f_{EM} < 0.05 \text{ and } f_{ch} < 0.05 \text{ and } |\eta| < 2$$

$$f_{EM} < 0.05 \text{ and } |\eta| \geq 2$$

4.3.5 Identifying Jets Originating from Heavy Flavor Hadrons

Hadrons containing b-quarks with large p_T have long lifetimes, around 1.5 ps or a $c\tau$ of roughly 450 μm for a b-hadron with $p_T = 50$ GeV. The long flight distance allows

us to reconstruct ID tracks with large impact parameters and perhaps reconstruct secondary vertices.

Three separate algorithms are used to distinguish jets originating from b-hadrons (b-jets) from light hadrons and c-hadrons (c-jets). A brief description of each algorithm is given in this section. More details can be found in references [^{19,9}].

The first algorithm is based on track impact parameters for high quality tracks that are associated with jets. The discriminant is computed as a sum of the log likelihood ratio of each accepted track in the vertex or $\sum_i \ln(\frac{p_b}{p_{light}})$, where i sums over all accepted tracks in the jet and p_b is the track impact parameter probability density function (PDF) of a b-jet and p_{light} is the track impact parameter PDF of a light jet. The impact parameter PDF uses transverse and longitudinal impact parameters d_0 and z_0 as observables and is derived from MC simulation.

The second algorithm seeks to reconstruct the secondary vertex associated with the b-hadron decay. This algorithm has the advantage that if a secondary vertex is consistent with the decay of a long lived hadron that does not contain a b-quark, such as K_s or Λ or photon conversions, then the vertex may be rejected. Variables based on the secondary vertex location, energy, and mass can all be used to discriminant b-jets from light-jets and c-jets.

The third algorithm attempts to reconstruct the full b-hadron decay chain and is called the decay chain multi-vertex reconstruction algorithm. The algorithm uses a Kalman filter to the primary initial interaction vertex and the secondary bottom/charm

vertices.

The output of the three algorithms are all combined into a multivariate discriminant called MV2. MV2 uses a boosted decision tree (BDT) algorithm⁵⁷ to gain better separation power between different jet flavors. This analysis uses the MV20c10 discriminant to tag b-jets. MV20c10 is selected as it gives the best balance between light jets and c-jet rejection for a given b-tagging efficiency.

The b-tagging efficiencies and mis-tag rates have been calibrated by the ATLAS flavor tagging group. The distribution of the MV20c10 discriminant for light, charm and b-hadrons can be seen in Figure 4.4. We make a selection at $\text{MV2c10} > 0.6459$ which corresponds to approximately 77% b-tagging efficiency with a factor of 134 reject rate for light jets.

4.4 Electron and Photons

4.4.1 Electron and Photon Reconstruction

Both electron and photon reconstruction start from clusters of energy deposits in the electromagnetic calorimeter. The EM calorimeter is first divided into a grid of towers each with the size of $\Delta\eta \times \Delta\phi = 0.025 \times 0.025$. The energy from all longitudinal layers inside each tower is summed into the total tower energy.

The EM clusters are seeded by towers with energy above a certain threshold. A sliding-window algorithm groups energy towers near the seed into EM clusters.^{16,40}

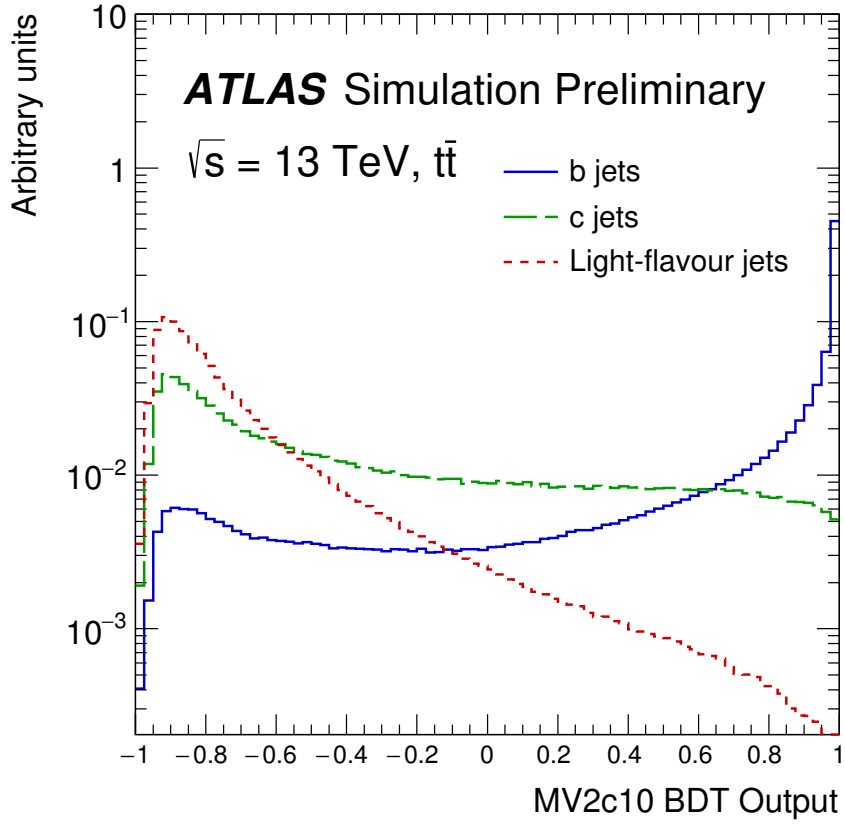


Figure 4.4: Distribution of the MV20c10 multivariate discriminant used for tagging b-jets.¹⁹

The window width is 3×7 towers in the barrel and 5×5 towers in the endcap. The reconstructed cluster therefore has a size of $\Delta\eta \times \Delta\phi = 0.075 \times 0.175$ in the barrel and 0.125×0.125 in the endcap. The same window size is used for electrons and photons to ensure better cancellation of systematics when using electrons to measure the photon response.¹⁶ The window position is adjusted so that the reconstructed cluster energy is the local maximum. The different cluster sizes were optimized for

the different energy distribution in the barrel and endcap calorimeters while minimizing pile-up and noise contributions.¹⁶

Identified clusters are then matched to reconstructed ID tracks using the track and cluster position. ID tracks are required to have a minimum number of pixel and silicon hits. Clusters are considered as an electron candidate if it has a single well-reconstructed associated ID track with an associated vertex. The cluster is considered an unconverted photon candidate if no associated tracks are found. The cluster is considered a converted photon candidate if two opposite signed collinear tracks which are consistent with electrons are associated with a secondary vertex. The cluster is also considered a converted photon if a single track is present but the track lacks hits in the IBL of the Pixel detector.

Furthermore, electron and photon candidates must satisfy a set of criteria. These variables include descriptions of the EM shower shapes, amount of hadronic activity behind the EM calorimeter and properties of associated tracks. More details on electron and photon identification are given in section 4.4.2 and 4.4.3.

A schematic of the electron reconstruction algorithm can be found in Figure 4.5.

4.4.2 Electron Identification and Quality

Electron identification in Run 2 is based on a likelihood algorithm that depends on a number of kinematics variables including EM shower shape, EM vs hadronic activity ratio, activity in the TRT and properties of the associated track. Reference [¹⁷] de-

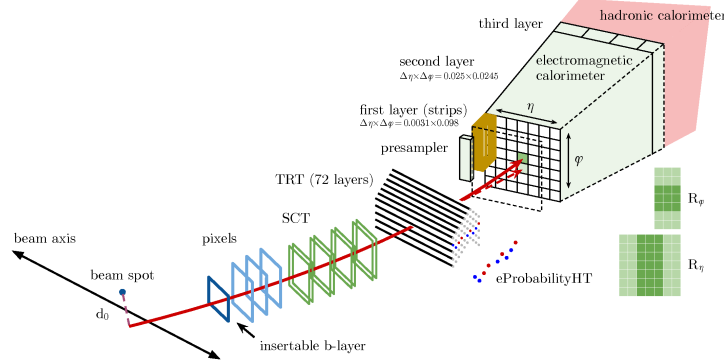


Figure 4.5: Schematic representation of the electron reconstruction algorithm.¹⁷

scribes the electron identification algorithm in greater detail. A brief summary of the different electron quality categories is given in this section.

Electron identification is split into categories Very Loose, Loose, Medium, and Tight. The tighter quality selections are a subset of loose quality selections. Because some shower shape distributions tend to broaden with the number of pile-up collisions, the cut on the likelihood discriminant is loosened as a function of the number of vertices. This is done to preserve the identification efficiency at high pile-up and does not drastically increase the amount of background.¹⁷

The electron identification efficiency for the different electron qualities are shown in Figure 4.6. 25 GeV Tight electrons have an efficiency of 78% and fake rate of 0.3%. 25 GeV Loose electrons have an efficiency of 90% and fake rate of 0.8. The efficiency increases with E_T while the fake rate decreases.¹⁷

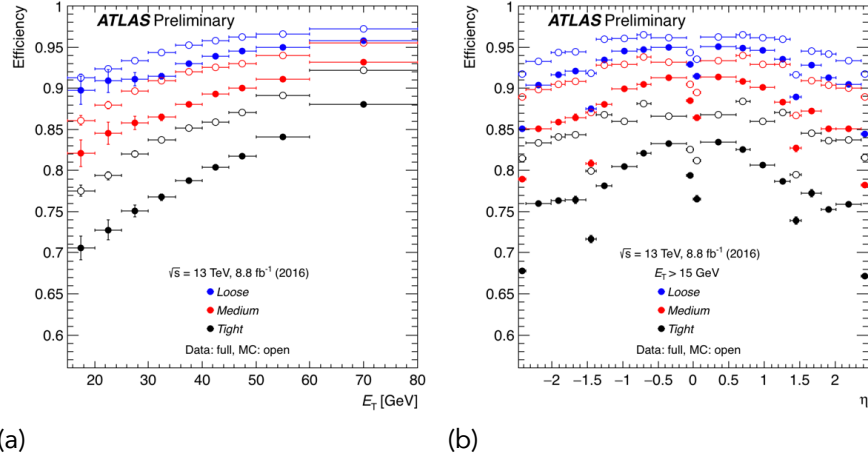


Figure 4.6: Electron identification efficiency in 2016 data as a function of E_T and η for different electron qualities.¹⁷

4.4.3 Photon Identification and Quality

Photon identification is based on the shower shape and the amount of hadronic activity behind the EM cluster. The energy deposited in the cells in the first and second layer of the EM calorimeter are important for distinguishing the EM shower originating from photons and those originating the neutral mesons such as π_0 . Further details on photon identification can be found in reference [20].

The requirements differ for converted and unconverted photon candidates to account for differences in the expected shower shapes of photons and pairs of electrons. The requirements also differ according to pseudorapidity intervals to account for the varying amount of material upstream of the calorimeter. These requirements were optimized using a multivariate technique.⁵⁷

Two photon quality categories exist: Loose photons and Tight photons. Loose photons are typically used for the triggering and for background studies. Tight photons are the ones generally recommended for physics analysis. This analysis uses Tight photons.

Distribution of photon identification efficiency for Tight photons are shown in Figure 4.7.

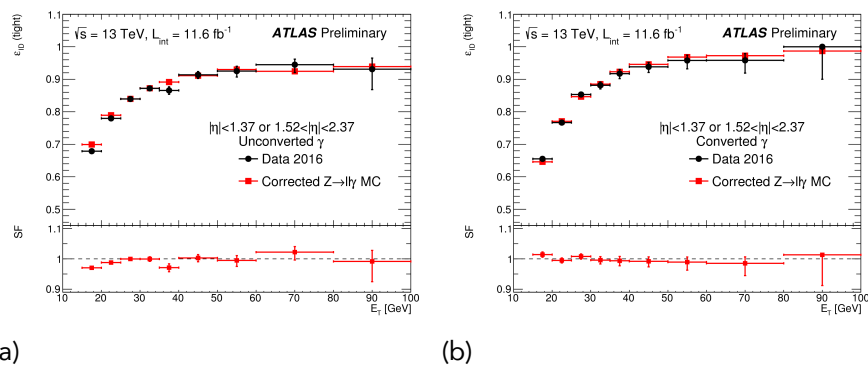


Figure 4.7: Photon identification efficiency in 2016 data as a function of E_t for converted and unconverted photons.¹⁶

4.4.4 Electron and Photon Energy Calibration

Typically a 100 GeV electron will deposit between a few percent to 20% of its energy before it reaches the calorimeter.¹⁶ Furthermore, $\sim 5\%$ of the electron energy may be deposited outside of the EM cluster. Electron and photon energy calibration account for all these effects to get an estimate of the true electron and photon energy. The calibration procedure follow the steps displayed in Figure 4.8.

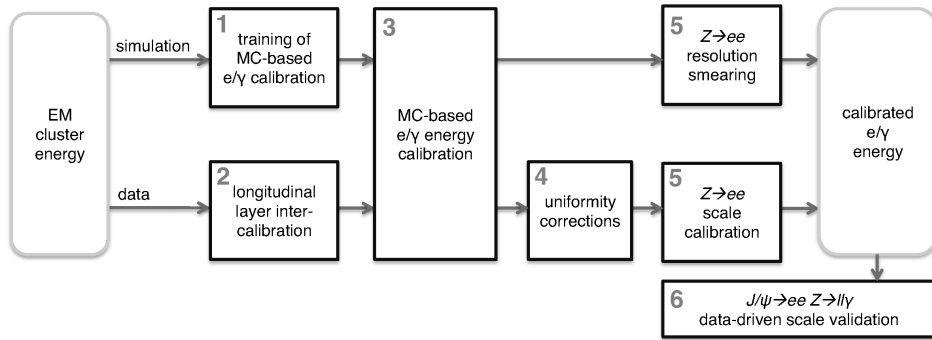


Figure 4.8: Flow chart of the steps involved in the calibration of the energy response of electrons and photons.⁴⁰

The EM clusters are first calibrated to the original electron or photon energy using a multivariate technique⁵⁷ based on MC simulations.^{16,40} The MC based calibration uses information on the EM cluster properties such as the longitudinal shower shape and information from any associated ID track. The response is different for electrons, converted photons and unconverted photons.

The longitudinal layers of the EM calorimeter must be calibrated relative to one another. Specifically, the relative energy response of the presampler and the first and second layer must be calibrated. These cannot be calibrated at the cluster level as clusters sum over all longitudinal layers. The intercalibration of the first and second layers of the EM calorimeter is performed with $Z \rightarrow \mu\mu$ decays.

A number of corrections are then applied to account for differences between simulation and data such as regions with non-optimal high voltage and geometrical effects. Finally a correction is applied to ensure that the $Z \rightarrow ee$ modeling in simula-

tion agrees with data. The same scale factors derived for electrons from $Z \rightarrow ee$ are applied to photons and additional photon-specific systematic uncertainties are also applied.

Cross-checks of the electron and photon calibration are performed with $J/\psi \rightarrow ee$ and $Z \rightarrow ll\gamma$ events in data after all energy corrections are applied.

4.5 Muons

4.5.1 Muon Inner Detector and Muon Spectrometer Track Reconstruction

Muons are first reconstructed independently in the inner detector (ID) and muon spectrometer (MS). Later information from the ID, MS and calorimeter are combined to form different types of reconstructed muons. The type of reconstructed muon formed depends on the type of information available.⁴¹

Muon tracks in the ID are reconstructed using the same algorithm for reconstructing all ID tracks summarized in section 4.1.

Muon tracks reconstructed in the MS start by forming segments in each individual muon chamber. A Hough transform is used to search for hits aligned in the bending η plane of the detector.⁵⁹ The MDT segments are reconstructed by performing a straight line fit. The RPC or TGC hits are associated with the MDT segment and measure the coordinate in the non-bending ϕ plane. Segments in the CSC are constructed using a combinatorial search in η and ϕ planes. Segment reconstruction

require that the segments are loosely compatible with a track originating from the collision point.

Muon spectrometer track candidates are built by fitting together the segments from different muon detector layers. The algorithm starts by identifying seed segments from the middle layer of the MS because the middle layer has more TGC and RPC hits available. The algorithm searches for other segments in the other layers by matching their relative positions and direction. Segments are added to the track candidate if they satisfy a set of criteria based on hit multiplicity and fit quality. After seed segments from the middle layer have been exhausted, segments in the inner and outer layers are also used as seeds to search for their own tracks.

At least two matching segments are required to build a track, except in the barrel to endcap transition region. In the transition region, a single high quality segment with both MDT and trigger hits can be considered a track.

At this point, the same segment can be in several track candidates. Overlap removal is then performed to either assign the segment to a single track or allow the segment to be shared between two tracks. Tracks that share two segments in the inner and middle layer are allowed if there are no shared hits in the outermost layer. This preserves the high efficiency of reconstructing two close by muons which can result from the two-body-decays of low-mass particles.

Once the track candidate is identified, the hits associated with each track candidate are fitted using a global χ^2 fit. Hits with a large contribution to χ^2 are removed

and the track is refitted without the outlier hits. Additional hits consistent with the track trajectory can also be added to the track. Again the track is refitted if any new hits are added. A track candidate is accepted if the fitted χ^2 satisfies the selection criteria.

4.5.2 Muon Combined Reconstruction

Four different types of muons are reconstructed by combining information from the ID, MS, and calorimeters. The four different types of muons are defined below based on what subdetector information is used to reconstruct them.

Combined muons: Combined muons combine reconstructed ID and MS tracks by performing a global refit that uses all the hits from the ID and MS tracks. MS hits may be added or removed from the track to improve the fit quality. The matching between MS and ID tracks are done mostly in an outside-in fashion. The MS track is extrapolated inwards and matched to an ID track with the energy loss in the calorimeter taken into account. The inside-out matching approach where the ID track is extrapolated outwards is also used as a complementary method.

Segment tagged muons: An ID track is combined with a MS segment in the MDT or CSC to form a segment tagged muon. The ID track is extrapolated to the MS to find matching segments. Segment tagged muons add reconstruction efficiency to muons that are either so low p_T that they pass only a single layer of muon detector or are in MS regions with gaps in coverage.

Calorimeter tagged muons (Calo-tagged): Calo-tagged muons are built by combining an ID track with calorimeter energy deposits that are consistent with a minimum ionizing particle. Calo-tagged muons has the lowest purity of all reconstructed muons. However it recovers some efficiency in regions with no or small MS coverage such as the central $|\eta| < 0.1$ region. The $|\eta| < 0.1$

region is occupied by cabling and servicing to the calorimeter and ID and only has partial MS coverage. The calo-tagged muon identification algorithm is optimized for the $|\eta| < 0.1$ region and a momentum range of $15 < p_T < 100$ GeV.

Extrapolated muons: In extrapolated muons the muon trajectory is reconstructed using only the MS track and a loose requirement of compatibility with the interaction point. Extrapolated muons are used mainly to extend acceptance past the ID coverage in the $2.5 < |\eta| < 2.7$ region.

4.5.3 Muon Quality

Reconstructed muons are flagged as Loose, Medium or Tight in terms of quality.

The quality selections identify prompt muons originating from the interaction point and attempt to reject backgrounds which include real muons originating from leptonic pion and kaon decays.

If a pion or kaon decays within the ID volume, then the decay will form a muon in the ID that then gets reconstructed as a track in the MS. The ID track of these muon will have a distinct kink topology. The resulting combined track will have both poor fit quality and poor matching between ID and MS track momenta. Therefore, combined muon use the following variables to distinguish between high and low quality muons:

q/p significance: q/p significance measures the compatibility of the ratio of charge and momentum (q/p) given by the ID and MS tracks. The quantity is normalized to the uncertainty on (q/p) from the two tracks.

ρ' : ρ' is the difference in p_T of the ID and MS tracks divided by the p_T of the combined track

fit χ^2 : The χ^2 of the fit to the combined track normalized to the degrees of freedom

Quality selections also set requirements on track hits to ensure a robust momentum measurement. Muon tracks have at least one Pixel hit and at least five SCT hits with fewer than three Pixel or SCT holes. If the track is located between η of 0.1 and 1.9, we also require at least 10% of TRT hits originally assigned to the track are still included in the final fit.

There are four muon quality four categories; Loose, Medium, Tight, and High- p_T . Loose, Medium and Tight muons are inclusive of one another. For example, all Tight muons are also included in the looser categories. Medium muons represent a good balance between momentum resolution and reconstruction efficiency. Most analyses, including this one, uses Medium muons to identify signal muons. We use signal muons in multiple one lepton control regions to estimate backgrounds. We use Loose muons to veto muons in the zero lepton signal and validation regions because of the higher muon reconstruction efficiency.

The High- p_T muon quality selections have stringent requirements in order to ensure good momentum resolution for muons with $p_T > 100$ GeV. Muons that pass the High- p_T quality requirements are used mainly for heavy resonances searches such as W' and Z' . We do not use high- p_T muons and will not discuss their identification in detail. Detailed description of the Loose, Medium and Tight muon categories

are given below.

Medium muons: Medium muons are considered the default muons used in physics analysis at ATLAS. The identification algorithm is designed to minimize systematic uncertainties on momentum measurement and reconstruction efficiency. Only combined and extrapolated muons are accepted. Combined muons must have ≥ 3 hits in at least two separate layers. The only exception is in the central $|\eta| < 0.1$ region where tracks can have at least one MDT layer but no more than one MDT hole is allowed. Extrapolated muons must have at least three MDT/CSC layers and are allowed only in the forward $2.5 < |\eta| < 2.7$ region which lies outside of ID coverage. q/p significance must be less than 7 in combined muons to ensure good agreement between ID and MS and reject decay-in-flight muons originating from hadrons.

Loose muons: Loose muon identification is designed to maximize reconstruction efficiency while still ensuring high quality tracks. All combined and extrapolated muons must satisfy the same requirements as the Medium muons. On top of this calo-tagged and segment tagged muons are also allowed in the $|\eta| < 0.1$ region in order to increase efficiency. The majority of Loose muons are still combined muons with approximately 97.5% of all Loose muons being combined muons in the $|\eta| < 2.5$ region. The rest consist of 1.5% calo-tagged and 1% segment tagged muons.

Tight muons: Tight muons are optimized to maximize muon purity but at the cost of reconstruction efficiency. Only combined muons with hits in at least two muon stations and satisfying the Medium definition are accepted. The combined track fit's normalized χ^2 must also be less than 8. A two dimensional cut in p_T and q/p significance is also applied. The 2D cut is tighter for low p_T muons to have better background rejection in a regime where misidentification probability is higher.

4.5.4 Muon Reconstruction Efficiency and Momentum Calibration

Muon reconstruction efficiency and muon momenta calibrations are determined by studying narrow resonances decaying into muon pairs in data. A brief summary is given below and more details can be found in reference [41].

Muon reconstruction efficiency is measured in data by using a tag and probe method using $J/\psi \rightarrow \mu\mu$ or $Z \rightarrow \mu\mu$ events. A well reconstructed muon that passes the Medium quality selection and fired the muon trigger is considered the tag. A bare ID track, a bare MS track, or a calo-tagged muon is considered the probe. Then we search to see if the probe is also reconstructed as a high quality combined muon.

The Run 2 muon reconstruction efficiency for Loose and Medium muons are shown in Figure 4.9.

Muon momentum is calibrated to $J/\psi \rightarrow \mu\mu$ or $Z \rightarrow \mu\mu$ events in data. The p_T of individual tracks are corrected to account for any inaccuracies in the detector description such as the magnetic field, dimensions of the detector and the amount of energy loss in the calorimeters. Correction parameters are extracted using a likelihood fit to data with templates derived from MC simulation. MS/ID alignment is also studied using special runs with no magnetic field. The correction parameters differ for different sections of η and ϕ regions because of the different amount of magnetic fields and independent alignment performed in each section.

On top of the total correction to the central value of the p_T , the momentum reso-

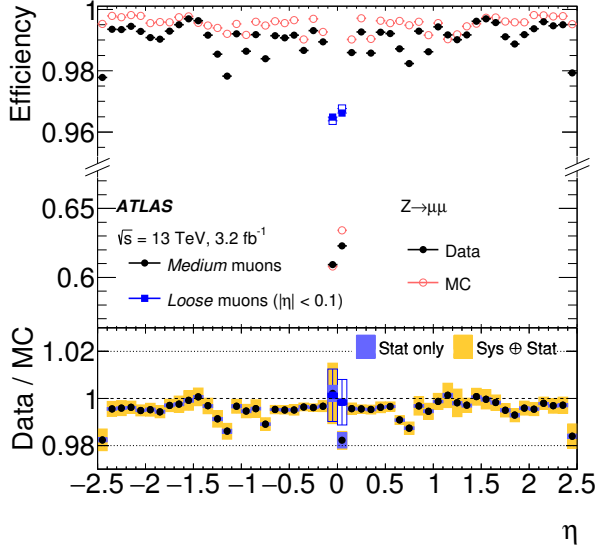


Figure 4.9: The distribution of muon reconstruction efficiency for Loose and Medium muons.⁴¹ Loose and Medium muons are identical except in the $|\eta| < 0.1$ region where Loose muons also accept calo-tagged and segment tagged muons to recover efficiency.

lution is also estimated using data. The MC is smeared such that the reconstructed di-muon mass peak agrees between data and MC. The effect of muon momenta calibration on the MC simulation of $J/\psi \rightarrow \mu\mu$ and $Z \rightarrow \mu\mu$ mass peaks can be seen in Figure 4.10. The dimuon mass distribution has better agreement with data after calibration.

4.6 Missing Transverse Momentum

Stable or metastable particles which only interact via the weak force and gravity cannot be directly detected at ATLAS. In SM, these particles correspond to neutrinos.

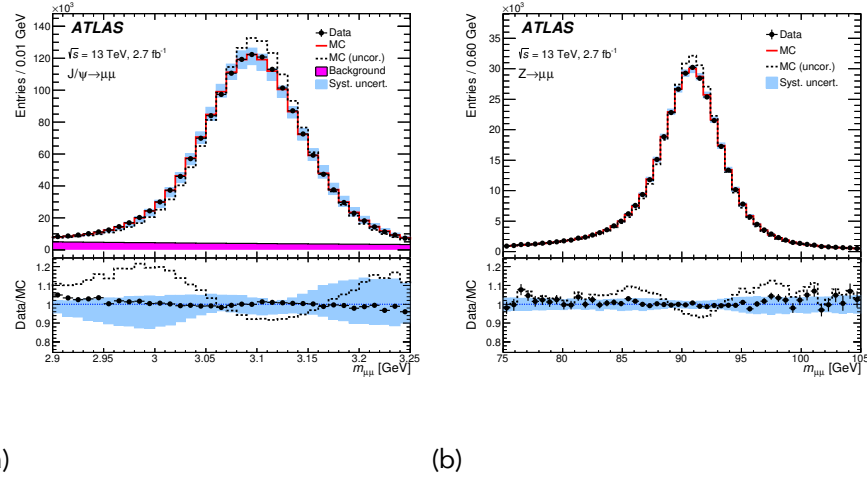


Figure 4.10: Dimuon invariant mass before and after muon momenta calibration in data and MC.⁴¹

nos. In BSM models, there maybe many other weakly interacting particles including WIMPs, gravitons, and a stable neutral SUSY LSP.

The presence of weakly interacting particles is inferred through conservation of transverse momentum. The total transverse momentum is zero in the initial colliding partons at the LHC. Therefore, any momentum imbalance in the transverse plane must be due to undetected particles in the final state.

4.6.1 E_T^{miss} Reconstruction

We reconstruct the E_T^{miss} according to equation 4.2. The first term is a negative vector sum of all hard fully calibrated objects and the second term represents the \vec{E}_t of all soft objects in the interaction.

$$E_T^{\text{miss}} = -\left(\sum_{\text{hard objects}} E_T + \sum_{\text{soft}} E_T \right) \quad (4.2)$$

Fully calibrated hard objects include muons, electrons, photons and jets that satisfy their respective Baseline selections. Baseline selections apply a loose set of p_T and quality requirements to ensure well reconstructed objects. Baseline object definitions can be found in chapter 6.

Hadronic taus are not independently reconstructed and calibrated. Therefore, hadronic taus will most likely be reconstructed as hadronic jets for our analysis. An overlap removal algorithm has been applied to the Baseline objects to remove any potential duplicate objects.

We use a track based method called Track Soft Term (TST)⁸ to reconstruct the contribution from soft objects. The TST algorithm builds the E_T^{miss} that is not associated with any hard objects by summing the p_T of ID tracks.

The TST algorithm has the advantage of being relatively robust against pile-up interactions because the TST algorithm use ID tracks that are matched with the primary vertex. However, the TST algorithm cannot measure the contribution to E_T from neutral particles because neutral particles do not leave tracks in the ID. The TST algorithm is the standard method of estimating E_T^{miss} at ATLAS in Run 2 due to the high pile-up conditions.

Only tracks with $p_T > 400$ MeV are accepted and a number of track quality re-

uirements are applied. The track quality requirement follows recommendations from the ATLAS tracking performance group and includes a minimum of 7 silicon hits and a requirement on the track d_0 . Any tracks within a ΔR of 0.05 of any electron or photon cluster, the ID tracks of muons, and any ID tracks matched to jets are removed to avoid double counting. Further details on TST can be found in reference [8].

E_T^{miss} reconstructed using this method is the standard E_T^{miss} used throughout all signal, control and validation regions in this analysis and is simply referred to as E_T^{miss} . This method of reconstructing E_T^{miss} is also referred to as TST E_T^{miss} to distinguish it from an alternative method of reconstructed E_T^{miss} called track E_T^{miss} described in section 4.6.2.

4.6.2 Track E_T^{miss} Reconstruction

Track E_T^{miss} ($E_T^{\text{miss,track}}$) forms a complementary method of reconstructing missing transverse energy. $E_T^{\text{miss,track}}$, defined in equation 4.3, is reconstructed using a negative vector sum of all accepted ID tracks.

$$E_T^{\text{miss,track}} = - \sum_{\text{ID tracks}} p_T \quad (4.3)$$

ID tracks must pass the same requirements described in section 4.6.1 but no attempt is made at removing tracks that are associated with hard objects. The one ex-

ception to this is tracks associated with an electron. Because of the high number of interaction expected between an electron and the material in the ID, electron tracks are replaced with the electron calorimeter cluster instead.

Track E_T^{miss} is very robust against high pile-up conditions because ATLAS has a very good vertex resolution. However track E_T^{miss} neglects the presence of neutral particles. Track E_T^{miss} is also limited by η coverage of the ID which only extends to an $|\eta| < 2.5$. We use track E_T^{miss} as a cross check on the object based E_T^{miss} reconstruction described in 4.6.1. Both object based and track based E_T^{miss} must agree loosely in direction for our analysis.

4.6.3 E_T^{miss} Performance

E_T^{miss} performance may be measured using a number of processes including $Z \rightarrow ll$, $W \rightarrow l\nu$ and $t\bar{t}$. $Z \rightarrow ll$ produced with additional jets is considered the gold standard. Very little intrinsic E_T^{miss} is produced in the $Z \rightarrow ll$ plus jets process. This presents a good opportunity to study the effect of the E_T^{miss} soft term calculation since no hard invisible particles exist. The only variable intrinsic to E_T^{miss} reconstruction is the soft term. All other terms in E_T^{miss} reconstruction depend directly on the resolution of the respective reconstructed hard objects. $W \rightarrow l\nu$ is also used to study a topology with a high- p_T neutrino and therefore intrinsic E_T^{miss} and $t\bar{t}$ is used to study topologies with a large number of jets.

Results from $Z \rightarrow ll$ performance study will be summarized here. This study is de-

scribed in detail in reference [8]. The $W \rightarrow l\nu$ E_T^{miss} and $t\bar{t}$ study will not be covered here but further detail can also be found in reference [8].

$Z \rightarrow \mu\mu$ events are selected by requiring exactly two same flavor, opposite signed muons with $p_T > 25$ GeV. The dilepton invariant mass must be within 25 GeV of the Z mass.

Distribution of the E_T^{miss} resolution in $Z \rightarrow \mu\mu$ events , defined as the root-mean-squared (RMS) of the E_T^{miss} distribution is shown in Figure 4.11. The E_T^{miss} resolution degrades both with the total amount of E_T in the event and the number of reconstructed vertices.

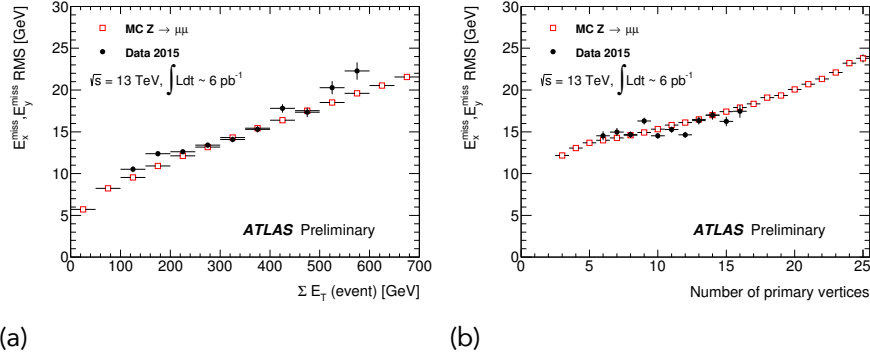


Figure 4.11: Distribution of the E_T^{miss} track soft term (TST) resolution in $Z \rightarrow \mu\mu$ events.⁸ (a) shows the E_T^{miss} TST resolution as a function of the total E_T of all reconstructed objects and (b) shows the TST E_T^{miss} resolution as a function of the number of reconstructed vertices in $Z \rightarrow \mu\mu$ events. The E_T^{miss} resolution degrades as E_T and pile-up increases.

5

Trigger

Due to the large volume of data produced at the LHC, an efficient and robust triggering system is essential for deciding which events are potentially interesting and should be recorded for later study. The ATLAS triggering system is composed of two levels in Run 2. The first-level trigger (Level1 or L1 trigger) is hardware based and uses a subset of detector information to quickly reduce the rate of accepted

events from the initial 40 MHz to 100 kHz. Afterwards, the software based high-level trigger (HLT) further reduces the event rate to 1 kHz. Any events passing the HLT are recorded by ATLAS for further reconstruction and offline analysis.

Object reconstruction at the HLT is done only to the precision required by the trigger algorithms. The online reconstruction algorithms tend to be less precise than the offline reconstruction algorithms described in chapter 4 but are significantly faster.

A schematic showing the different ATLAS trigger components is given in Figure 5.1. Only components relevant to the triggers used in this analysis will be discussed in detail. Further detail can be found in reference [42].

We use the lowest unprescaled E_T^{miss} trigger in this analysis. The lowest unprescaled trigger threshold increases multiple times between early 2015 to late 2016 to accommodate the increases in instantaneous luminosity during the same time period.

The lowest unprescaled triggers correspond to the HLT_xe70_mht_L1XE50 trigger in 2015, the HLT_xe90_mht_L1XE50 trigger for 2016 data taking period A-D3, the HLT_xe100_mht_L1XE50 trigger for the period D4-F1 and the HLT_xe110_mht_L1XE50 trigger for period F2 and onward. These triggers have a HLT E_T^{miss} threshold of 70, 90, 100, and 110 GeV respectively. All HLT triggers that we use are seeded by the L1_XE50 trigger which corresponds to the L1 E_T^{miss} threshold of 50 GeV.

A summary of the L1 and HLT E_T^{miss} triggers used in this analysis is given in sections 5.1 and 5.2.

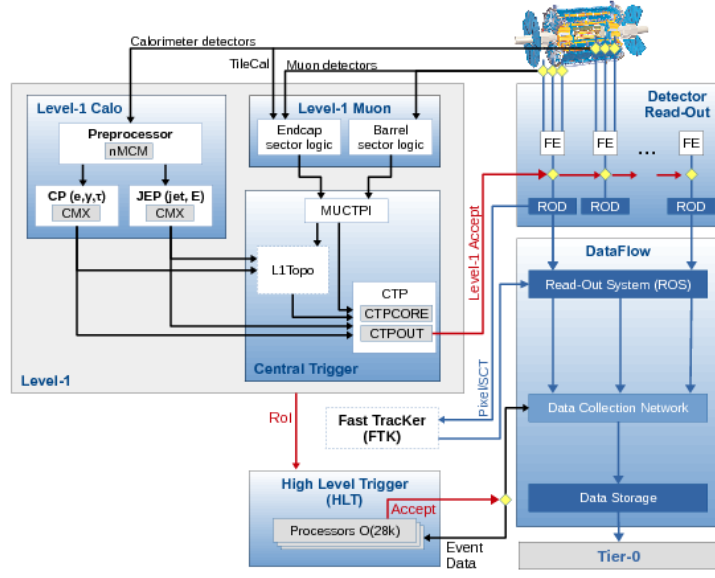


Figure 5.1: Schematic representation of the ATLAS trigger system and information flow.⁴²

5.1 Level 1 E_T^{miss} trigger

The L1 E_T^{miss} trigger is based on the vector sum of E_T in the calorimeter and is part of the L1Calo trigger system⁵⁰ shown in Figure 5.1. The process starts with trigger towers in the electromagnetic and hadronic calorimeters. Trigger towers are more coarse than those used in offline reconstruction; most are 0.1×0.1 in $\Delta\eta \times \Delta\phi$.

These trigger towers are then built into jet elements composed of 2×2 EM trigger towers and combined with the 2×2 hadronic trigger towers directly behind

the EM towers. The jet elements are then fed to the Jet/Energy-sum Processor (JEP).

The JEP calculates the global sums of E_t and E_T^{miss} by summing the scalar E_t and the vector $\langle E_x, E_y \rangle$ for all jet elements. If the total $E_T^{\text{miss}} = | - \sum_{\text{all jet elements}} \sqrt{E_x^2 + E_y^2} |$ is above a trigger threshold value then the event passes the E_T^{miss} trigger and is passed to the HLT. For instance, the L1_XE50 E_T^{miss} trigger has a 50 GeV threshold.

5.2 HLT E_T^{miss} trigger

The reconstruction of E_T^{miss} for the HLT also begins by identifying topo-clusters in the calorimeters, much like offline topo-clusters described in section 4.3.1. Seed cells that pass the 4σ signal over noise thresholds are first identified and neighboring cells that pass a 2σ signal over noise thresholds are added to the cluster. Neighboring cells that pass 2σ signal over noise thresholds are continually added to the cluster until no cells neighboring the cluster can pass the 2σ signal over noise threshold. At this point, one final round of neighboring cells are added regardless of their signal over noise thresholds.

Jet reconstruction and calibration are also similar to offline jet reconstruction described in section 4.3.1. Jets are reconstructed using the $\text{anti}-k_t$ algorithm from topo-clusters.¹ Jet calibration also follows the same basic offline procedure in section 4.3.2. However, HLT jet calibration and offline calibration procedures do differ in many ways including different pile-up corrections, track-based corrections and

certain in-situ corrections. Overall this leads to poorer jet resolutions at the HLT level. Some of these corrections were added in 2016 to further improve the agreement between online and offline jet reconstruction. Details can be found in the reference [23].

The trigger E_T^{miss} reconstruction algorithm, called the online E_T^{miss} reconstruction algorithm, defines the E_T^{miss} as the negative vector sum of the transverse momentum of all reconstructed jets. Only contributions from the calorimeter are taken into account in the E_T^{miss} calculation and muon tracks are not included. This method of calculating the E_T^{miss} from calibrated jets is referred to as missing H_T (MHT).

We apply a 70, 90, 100, or 110 GeV threshold to our HLT E_T^{miss} trigger depending on the data taking period. The trigger E_T^{miss} threshold increases over time because the instantaneous luminosity also increases.

Trigger turn on curves as a function of offline E_T^{miss} can be seen in Figure 5.2. If online E_T^{miss} reconstruction has the same E_T^{miss} resolution as the offline E_T^{miss} resolution then the trigger turn on curve would approach a step function. The poor online E_T^{miss} resolution compared to the offline E_T^{miss} resolution is the reason behind the gradual trigger turn on curve.

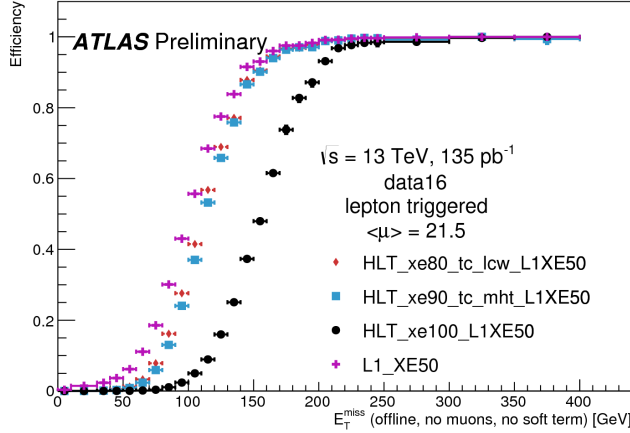


Figure 5.2: ATLAS trigger turn on curves for E_T^{miss} triggers with several different thresholds.²³ The E_T^{miss} reconstruction algorithm used in triggering defines the E_T^{miss} as the negative vector sum of the transverse momentum of all reconstructed jets. This method of calculating the E_T^{miss} from calibrated jets is referred to as missing H_T (MHT). Three HLT E_T^{miss} trigger thresholds of 80, 90, and 100 GeV are shown, correspond to HLT_xe80, HLT_xe90, and the HLT_xe100 triggers. The turn on curve for the L1_XE50 E_T^{miss} trigger with a L1 E_T^{miss} threshold of 50 GeV is also shown. All HLT triggers are seeded by the L1_XE50 trigger and therefore reach $\sim 100\%$ trigger efficiency at a higher offline E_T^{miss} than L1_XE50. The poorer online E_T^{miss} resolution compared to the offline E_T^{miss} resolution is the reason behind the gradual trigger turn on curve.

5.3 Improvements to the E_T^{miss} Trigger in Run 2

A significant improvement to pile-up mitigation was made to the L1Calo trigger system for Run 2.⁴² The ATLAS Liquid Argon Calorimeter integrates its signal over a time window of 600 ns. This long time window corresponds to 24 bunch crossings. Hence, energy deposition from collisions occurring in neighboring bunches (referred to as out-of-time pile-up) will be registered as signal. This results in a higher average signal amplitude, referred to as the pedestal, in collisions at the beginning of a

bunch train than those at the end of a bunch train.

The pedestal's dependence on bunch-crossing location was corrected offline but not at the trigger level in Run 1. However in Run 2, a dynamic bunch-by-bunch pedestal correction was implemented at the trigger level. This lead to a significant reduction in L1 E_T^{miss} trigger rate as shown in Figure 5.3.

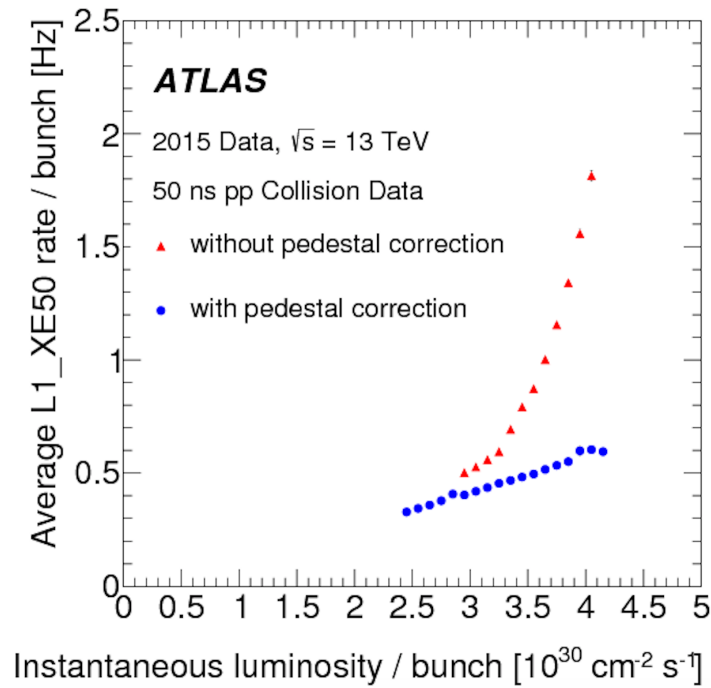


Figure 5.3: Improvement to the L1_XE50 rate with new dynamic pedestal correction for out-of-time pile-up.⁴² The L1 trigger rate with the liquid argon pedestal correction is significantly lower than the trigger rate without pedestal corrections at high instantaneous luminosities in 2015 data.

The pedestal correction to the LAr energy calibration also improves the jet energy calibration at the HLT level. This not only improves HLT E_T^{miss} trigger performance

but also improves the performance of other HLT calorimeter triggers such as those on total E_T .²³

6

Physics Object Definitions

We require a certain set of quality cuts for all reconstructed physics objects used in this analysis. In general, we have a looser set of requirements on `Baseline` objects and a tighter set of requirements on `Signal` objects. The object selection is inclusive meaning that the tighter `Signal` object requirements must also pass the looser `Baseline` object requirements.

Baseline objects have the loosest set of quality requirements and minimum p_T selection needed to maximize object reconstruction efficiency while limiting fake rates. In this analysis, Baseline objects are used to reconstruct E_T^{miss} and to veto events. These applications benefit the most from having a higher reconstruction efficiency. For example, the lepton momentum resolution is less important when we veto since we are not performing any measurements on the lepton except tagging their presence. The same is true for the E_T^{miss} reconstruction because even low quality calibrated objects tend to have better resolution than the E_T^{miss} soft term calculation.

In general, Signal objects are used in the analysis in places where we need to ensure robust energy/momentum reconstruction or just the presence of well reconstructed objects. For example, Signal electrons and muons are used in the one-lepton regions where the lepton momentum is used to calculate variables such as the transverse mass but Baseline electrons and muons are used to veto events for the zero-lepton regions.

Signal jets are used in the zero-lepton signal and validation regions and one-lepton control regions. Signal photons are used in the single photon control region used to estimate the ttV background.

Overlapping objects are resolved at the Baseline level using the algorithm described in section 6.6. The E_T^{miss} is reconstructed using Baseline objects that passed overlap removal according to the algorithm described in section 4.6.

All object definitions used follow the ATLAS performance group recommendations and the ATLAS SUSY working group standards. Details on each object is given below.

6.1 Baseline and Signal Electron Definition

Baseline electron candidates are selected using the `VeryLooseLH` quality definition. The `VeryLooseLH` quality definition is given in the electron reconstruction, calibration and quality section in 4.4.

The energy clusters associated with the electron are required to have an $E_T = E_{\text{cl}} / \cosh \eta > 7 \text{ GeV}$ and an η within $|\eta_{\text{cl}}| < 2.47$. Electrons in the transition region between EM barrel and endcap calorimeters ($1.37 < |\eta| < 1.52$), also called the crack region, are accepted as long as they satisfy the `VeryLooseLH` criteria.

We use the `Gradient Loose` criteria for electron isolation. The isolation parameter changes depending on the electron p_T in the gradient isolation scheme, ensuring a balance between efficiency and fake rate at all electron p_T values.

Table 6.1 summarizes the Baseline electron definition criteria.

Signal electrons require the tight likelihood `TightLH` quality requirement. The minimum p_T is also increased to 20 GeV. Table 6.2 summarizes the Signal electron definition.

Table 6.1: Summary of the Baseline electron selection criteria. The overlap removal is described in more detail in section 6.6.

Cut	Value
Acceptance	$p_T > 7 \text{ GeV}, \eta_{\text{clust}} < 2.47$
Quality	VeryLooseLH
Isolation	Gradient Loose
Overlap: e rejected if	$0.2 < \Delta R(e, \text{jet}) < 0.4$

Table 6.2: Summary of the Signal Electron selection criteria. The overlap removal is described in more detail in section 6.6.

Cut	Value
Acceptance	$p_T > 20 \text{ GeV}, \eta_{\text{clust}} < 2.47$
Quality	TightLH
Isolation	Gradient Loose
Overlap: e rejected if	$0.2 < \Delta R(e, \text{jet}) < 0.4$

6.2 Baseline and Signal Muon Definition

Baseline muon candidates must pass the Loose quality criteria. Baseline muons must also have a $p_T > 6 \text{ GeV}$ with $|\eta| < 2.7$. Muon reconstruction, calibration and quality definitions are described in more detail in section 4.5.

We use the Gradient Loose criteria for muon isolation. The isolation parameter changes depending on the muon p_T in the gradient isolation scheme, ensuring a balance between efficiency and fake rate at all muon p_T values.

Baseline muon selections are summarized in Table 6.3.

Table 6.3: Summary of the Baseline muon selection criteria. The overlap removal is described in more detail in section 6.6.

Cut	Value
Acceptance	$p_T > 6 \text{ GeV}, \eta < 2.7$
Quality	Loose
Isolation	Gradient Loose
Overlap: μ is rejected if	$\Delta R(\mu, \text{jet}) < 0.4$

Signal muon candidates must pass the Medium quality criteria. Signal muons must have a $p_T > 20 \text{ GeV}$, and be within $\eta < 2.7$. Signal muon selections are summarized in Table 6.4.

Table 6.4: Summary of the Signal muon selection criteria. The overlap removal is described in more detail in section 6.6.

Cut	Value
Acceptance	$p_T > 20 \text{ GeV}, \eta < 2.7$
Quality	Medium
Isolation	Gradient Loose
Overlap: μ is rejected if	$\Delta R(\mu, \text{jet}) < 0.4$

6.3 Baseline and Signal Jet Definitions

6.3.1 Calorimeter Jets

Jets are reconstructed from topological clusters using the $\text{anti} - k_t$ jet algorithm¹ with a distance parameter of $R = 0.4$. The jets are calibrated using the EM+JES

calibration scheme and global sequential calibration is enabled. Area-based pile-up corrections are also applied. More details on jet reconstruction and calibration can be found in section 4.3.

Baseline jets must have $p_T > 20 \text{ GeV}$ with no η requirement. A jet vertex tagger (JVT) value greater than 0.59 is also required to reject pile-up jets not originating from the hard scattering interaction for jets with $|\eta| < 2.4$ and $p_T < 60 \text{ GeV}$. The 0.59 JVT working point corresponds to a 92% efficiency for jets originating from the hard scattering interaction and a 2% fake rate from pile-up, if the jet has $|\eta| < 2.4$ and $p_T < 60 \text{ GeV}$. Jets that pass this loose selection are considered when resolving overlapping objects and building E_T^{miss} .

After overlap removal, if any Baseline jets are tagged as being BadLoose quality jets then the entire event is vetoed. This is because the presence of a bad quality jet probably also means poor E_T^{miss} reconstruction for the event. Details on jet quality can be found in section 4.3.4

Baseline jets are summarized in Table 6.5.

Table 6.5: Summary of the Baseline jet selection criteria.

Cut	Value
Acceptance	$p_T > 20 \text{ GeV}$, no η requirement
JVT	> 0.59 if $p_T < 60 \text{ GeV}$ and $ \eta < 2.4$ no requirement if $p_T > 60 \text{ GeV}$ or $ \eta > 2.4$
Quality	if any jet is BadLoose then veto whole event
Overlap	See section 6.6

Signal jets are required to have $p_T > 20$ GeV and $|\eta| < 2.8$ plus all selections applied to the Baseline jets. Jet quality must satisfy the Loose criteria defined in section 4.3.4.

The Signal jet selection criteria is summarized in Table 6.6.

Table 6.6: Summary of the Signal jet selection criteria.

Cut	Value
Acceptance	$p_T > 20$ GeV, $ \eta < 2.8$
JVT	> 0.59 if $p_T < 60$ GeV and $ \eta < 2.4$ no requirement if $p_T > 60$ GeV or $ \eta > 2.4$
Quality	Loose
Overlap	See section 6.6

6.3.2 b -tagged Jets

Some jets are identified as originating from a b-hadron using the MV2c10 b-tagging algorithm described in section 4.3.5. b-jet candidates must be within ID coverage with $|\eta| < 2.5$. Any jet with $\text{MV2c10} > 0.6459$ is a b-tagged jet. The selection chosen corresponds to approximately 77% b-tagging efficiency with a factor of 134 rejection rate for light jets and a factor of 6 rejection of c-jets.

6.4 Baseline and Signal Photon Definition

Baseline photons are used only for E_T^{miss} calculation. Baseline photons must have $p_T > 25 \text{ GeV}$ and $|\eta| < 2.37$ and pass the Tight quality selection. Photon reconstruction and calibration are summarized in section 4.4.

The photon definition is summarized in Table 6.7.

Table 6.7: Summary of Baseline photon selection criteria.

Cut	Value
Acceptance	$p_T > 25 \text{ GeV}, \eta < 2.37$
Quality	Tight

Signal photons are used only in the $t\bar{t}\gamma$ control region to model the ttV background. Signal photons must pass the requirements in Table 6.8.

Table 6.8: Summary of Signal photon selection criteria.

Cut	Value
Acceptance	$p_T > 130 \text{ GeV}, \eta < 2.37$
Quality	Tight
Isolation	FixCutLoose

6.5 E_T^{miss} Definitions

6.5.1 Calorimeter-based E_T^{miss}

The E_T^{miss} reconstruction uses Baseline muons, electrons, photons and jets after overlap removal to determine the total \vec{E}_t of all visible objects in the event. Specifically, the E_T^{miss} is calculated according to equation 14.1 as the negative vector sum of the E_t of all Baseline objects plus an extra “soft term.” The soft term accounts for energy in the event that is not associated with any Baseline objects. Because Baseline objects have some minimum p_T requirement, the soft term is designed to capture the energy from objects that are too soft to pass the Baseline selection criteria.

The soft term is calculated using inner detector tracks that are matched to the primary vertex but are not associated with a Baseline electron, muon, or jet. The E_T^{miss} soft term is relatively robust against the presence of additional pile-up interactions because inner detector tracks can be associated with the primary vertex. More details on the E_T^{miss} reconstruction algorithm can be found in section 4.6.

$$E_T^{\text{miss}} = -\left(\sum_{\text{baseline objects}} E_T + \sum_{\text{soft}} E_T \right) \quad (6.1)$$

6.5.2 Track-based E_T^{miss}

A complementary method of determining missing transverse energy uses mainly tracking information instead of calorimeter information. The track based E_T^{miss} , referred to as $E_T^{\text{miss,track}}$, is defined as the negative vector sum of the p_T of all ID tracks. $E_T^{\text{miss,track}}$ is very robust against pile-up but does not include the contribution to E_T from neutral particles such as photons and π^0 s. None the less, a loose agreement in direction between $E_T^{\text{miss,track}}$ and calorimeter-based E_T^{miss} was found to be an effective discriminant against multijet QCD background. Details on $E_T^{\text{miss,track}}$ reconstruction can be found in section 4.6.2.

6.6 Resolving overlapping objects

Overlap removal between accepted physics objects must be performed in order to avoid double counting of objects. For example, the same calorimeter energy can be assigned to a jet and an electron before overlap removal. The distance metric $\Delta R = \sqrt{\Delta\phi^2 + \Delta\eta^2}$ is used to define overlapping objects. Objects too close in ΔR are considered overlapping and all except one object will be removed. The following guidelines are used for removing overlapping objects.

- If an electron and jet are located with $\Delta R < 0.2$, then the object is considered an electron and the jet is removed, unless the jet is b-tagged using the 85% working point in which case the jet is kept and the electron is removed.
- If a muon and jet are located with $\Delta R < 0.4$, then the object is considered

a jet and the muon is removed, unless the jet has less than three tracks (with $p_T > 500$ MeV), in which case the jet is removed while the muon is kept.

- If an electron and jet are located with $0.2 \leq \Delta R < 0.4$, then the object is considered a jet and the electron is removed.

Overlap removal is performed on Baseline objects before E_T^{miss} reconstruction.

7

Monte Carlo Simulation of Physics Processes at ATLAS

Simulated Monte Carlo (MC) samples are used to model the signal and background processes in this analysis. In general, a MC generator program calculates the hard interaction matrix element up to a certain degree of accuracy (leading order (LO),

next-to-leading order (NLO), next-to-next leading order (NNLO), etc.) Another program simulates the formation of parton showers through the fragmentation and hadronization of colored partons at low energy scales. The matrix element calculation at high energy scales and the parton shower calculations at low energy scales are then matched to one another using a prescribed matching scheme.

A parton density function (PDF) is used to describe the internal structures of the colliding protons. An underlying event tune is used to describe the different parameters associated with the parton shower including the amount of ISR/FSR emitted and the amount of multiple parton interactions. Different scales such as the factorization and renormalization scales must also be set as input parameters.

Because the LHC is operating at such high instantaneous luminosities, there are around 25 proton-proton interactions per bunch crossing. Most of these pile-up interactions have low amounts of momentum transfer between the protons and are modeled by overlaying additional minimum-bias interactions on top of the hard scattering interaction. Further details on the modeling of pile-up interactions can be found in the section 7.2.

After MC generation, the ATLAS detector is simulated using the GEANT4 program.²⁵ The simulated detector response is then reconstructed into physics objects using ATLAS reconstruction algorithms described in chapter 4. Further details on detector simulation can be found in the section 7.1.

A summary of MC generation programs and parameters are given in Table 7.1.

Details on the MC generation process for each signal and background MC are covered in sections 7.3 - 7.4.6.

Table 7.1: Overview of the nominal simulated samples. Generator refers to the MC generator program used for the matrix element calculation. fragm./hadron. refers to the program that simulates the formation of parton showers through the fragmentation and hadronization of colored partons. PDF set is the parton distribution function used to model the internal structure of the proton. UE Tune describes the different parameters used in the modeling of the parton shower. The cross section order refers to the degree of accuracy the matrix element calculation is performed to.

Process	Generator	fragm./hadron.
Stop Signal	MadGraph5_aMC@NLO	Pythia 8
$t\bar{t}$	Powheg-Box v2	Pythia 6
Single-Top	Powheg-Box v2	Pythia 6
$W/Z+jets$	Sherpa 2.2.1	Sherpa
Diboson	Sherpa 2.2	Sherpa
$t\bar{t} + V$	MadGraph5_aMC@NLO	Pythia 8

Process	PDF set	UE Tune	Cross section order
stop signal	NNPDF2.3	A14	LO
$t\bar{t}$	CT10	Perugia 2012	NLO
single-top	CT10	Perugia 2012	NLO
$W/Z+jets$	NNPDF3.0 NNLO	Default	NLO
diboson	CT10	Default	LO
$t\bar{t} + V$	NNPDF3.0 NNLO	A14	NLO

7.1 Detector Simulation

Two types of detector simulations are used. GEANT4²⁵ is used to perform the detector simulation for all background samples. For signal MC, a fast simulation framework is used in the interest of reducing computing time.³³ In the fast simulation framework, the majority of the detector is still simulated with GEANT4 with the ex-

ception of jets in the electromagnetic and hadronic calorimeters. Instead of simulating individual particle showers in the calorimeters, a predetermined parameterized description of the showers are used. The fast simulation framework was validated against full GEANT4 simulation for several selected signal samples and found to agree in observed kinematics.

ATLAS performance groups which measure the detector and reconstruction performance may recommend reweighting different MC samples depending on better or worse than expected detector performance. The following variables are reweighted to account for known differences between data and simulation: the lepton trigger efficiency, lepton reconstruction efficiency, lepton momentum scale, lepton isolation, and the b-tagging efficiency.

7.2 Pile-Up Simulation

Because the LHC is operating at such high instantaneous luminosities, there are around 25 proton-proton interactions per bunch crossing. Most of these interactions have low amounts of momentum transfer between the protons but still deposit energy in the detector. In order to understand the properties of these additional interactions, ATLAS records inelastic p-p interactions, called minimum-bias interactions, with no particular bias to any one kind of event.

All ATLAS simulation is produced with a varying number of minimum-bias interac-

tions overlaid on top of the hard scattering interaction. The minimum bias interactions are supposed to mimic the pile-up interactions. The distribution of additional overlaid minimum bias interactions is reweighted so that the distribution of pile-up interactions matches in data and MC.

7.3 Signal Monte Carlo Generation

We use MadGraph5_aMC@NLO to calculate the matrix element of the stop signal MC to leading order accuracy (LO).²⁸ Up to two additional QCD partons are included in the matrix element calculation, making the total hard scattering process

$$pp \rightarrow \tilde{t}\bar{t} + j + j.$$

Stop decays are treated differently depending on the mass splitting between the stop and its decay products. The different stop decays considered in this analysis are shown in the Feynman diagrams in Figure 7.1.

If $m_{\tilde{t}} - m_{\tilde{\chi}_1^0} \geq m_t$, then the top can be produced on shell. PYTHIA 8⁶⁹ performs the 2 body $\tilde{t} \rightarrow t\tilde{\chi}_1^0$ decay and subsequent decays of the top. m_t is set to 172.5 GeV. This process has the advantage of being computationally much faster than including the stop decays as part of the matrix element calculation.

If $m_{\tilde{t}} - m_{\tilde{\chi}_1^0} < m_t$, then the top must be produced off shell. PYTHIA 8 cannot perform the 3 body $\tilde{t} \rightarrow bW\tilde{\chi}_1^0$ decay or the 4 body $\tilde{t} \rightarrow bff\tilde{\chi}_1^0$ decay where the f stands for any fermion that can result from a W decay. Instead we use MadSpin³⁰

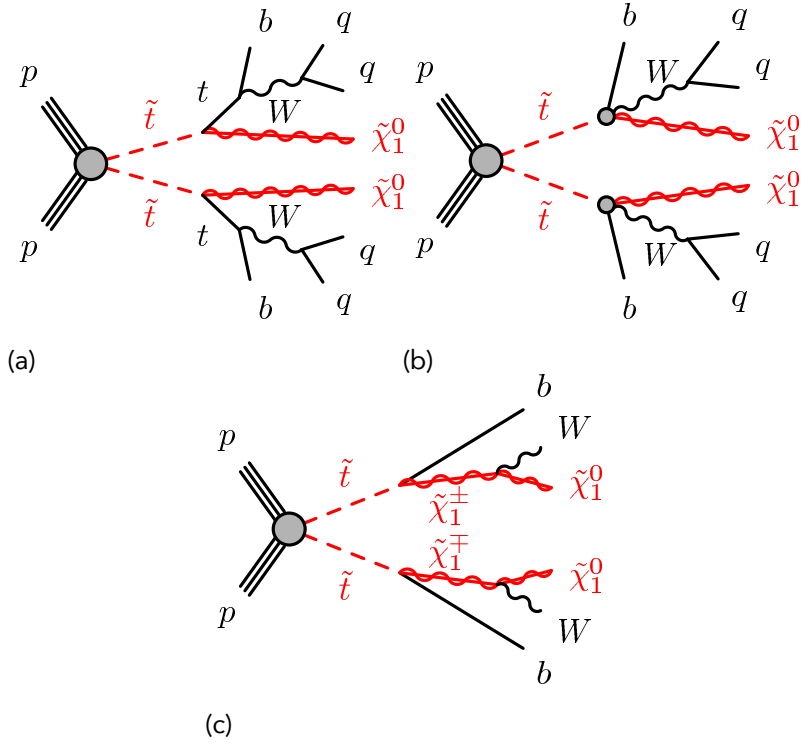


Figure 7.1: The decay topologies of the signal models considered in this analysis. The decay mode depends on the mass splitting between stop (\tilde{t}) and neutralino ($\tilde{\chi}_1^0$). If the mass splitting is larger than m_t , then a real top maybe produced in (a) the 2 body decay $\tilde{t} \rightarrow t\tilde{\chi}_1^0$. If the mass splitting is too small then a stop may decay through (b) a virtual top to $\tilde{t} \rightarrow bW\tilde{\chi}_1^0$. The stop decaying into b -quark plus chargino ($\tilde{\chi}_1^\pm$) channel shown in (c) is also considered in mixed decay interpretations.

to perform the $\tilde{t} \rightarrow bW\tilde{\chi}_1^0$ or $\tilde{t} \rightarrow bff\tilde{\chi}_1^0$ decay. MadSpin can perform 3 body and 4 body decays with off shell virtual particles as long as the decay are ultimately a series of 2 body decays. Decaying the stop using MadSpin also is also much faster then calculating the decay within the matrix element.

After the matrix element calculation and stop decays, the parton shower and hadronization of jets are simulated using PYTHIA 8 with the EvtGen v1.2.0 program

as an afterburner. The matching between the matrix element and parton shower jets is preformed with the CKKW-L prescription. The matching scale is set to 1/4 the mass of the stop.

The internal structure of the proton is modeled with the NNPDF3.0NNLO parton distribution function (PDF) set³² with A14 set as the underlying event (UE) tuning parameters⁴. The A14 tune optimizes over 10 parameters that vary the amount of ISR, FSR and multiple parton interactions. The variations are reduced to a 5 variable subset that is found to cover the uncertainty on experimental observables. Variable 1 mainly covers variation in the modeling of the underlying events. Variable 2 mainly covers variation in jet structure, and variables 3a, 3b and 3c cover different variations of ISR and FSR production. All 5 variations are used to quantify the theoretical uncertainties associated with parton shower and multiple parton interactions and are added in quadrature.

Signal cross sections are calculated to next-to-leading order in the strong coupling constant with the resummation of soft gluon emission added to next-to-leading-logarithmic accuracy (NLO+NLL).³⁵ An envelope of cross section predictions is produced using different PDF sets and factorization and renormalization scales. The nominal cross section and the uncertainty are then taken from the median and 1σ fluctuations around the median within the envelope.

Signal samples are generated to cover the entire stop and neutralino mass phase space that we may be sensitive to. Stop samples are generated at every 50 GeV

$m_{\tilde{t}}$ intervals for stop masses between 200 and 700 GeV. At each stop mass value, five samples with different $\Delta m = m_{\tilde{t}} - m_{\tilde{\chi}_1^0}$ are simulated to cover a wide corridor of phase space around Δm equals the top quark mass (m_t) line: $\Delta m = m_t - 82.5$ GeV, $m_t - 52.5$ GeV, $m_t - 22.5$ GeV, $m_t - 7.5$ GeV, $m_t + 0.5$ GeV, $m_t + 15.5$ GeV, $m_t + 27.5$ GeV. An extra row of $m_{\tilde{t}} = 225$ GeV samples is also produced to better estimate the 95% confidence limit at low stop masses.

7.4 SM Background Monte Carlo Generation

7.4.1 Standard Model $t\bar{t}$ Monte Carlo Generation

The nominal $t\bar{t}$ samples are generated using Powheg-Box v.2.²⁶ The matrix element calculation is computed to NLO accuracy and includes the $pp \rightarrow t\bar{t} + j$ process where the j represents an one additional emitted parton. The top quark mass is set to 172.5 GeV and the proton substructure is modeled by the CT10 NLO PDF set⁶² for the hard scattering process. The hard scattering renormalization and factorization scales are set to the generator default of $\sqrt{(m_t)^2 + (\rho_{Tt})^2}$.

PYTHIA 6 version 6.427 simulates the parton shower, hadronization and underlying event.⁷⁰ We use the Perugia 2012 tune⁷¹ and the corresponding leading order CTEQ6L1 PDF set⁶⁷ in PYTHIA 6. The resummation damping factor or h_{damp} , used by Powheg to control the matrix element and parton shower matching and the amount of high- ρ_T ISR/FSR, is set to m_t .

$t\bar{t}$ cross sections are calculated to NNLO accuracy in the strong coupling constant with the resummation of soft gluon emissions added to NNLL accuracy using the Top++v2.0 program.⁴⁶ Similar to the signal MC generation, an envelope of cross sections is produced for different PDF sets including MSTW2008NNLO, CT10 NNLO and NNPDF2.3 NNLO. Variations in the renormalization and factorization scales, strong coupling constant, and top quark mass are also included in the envelope. The median of envelope is taken as the nominal $t\bar{t}$ cross section and the 1σ variation in the envelope is taken as the $t\bar{t}$ cross section uncertainty.

In addition to the total cross section uncertainty, a number of $t\bar{t}$ samples are produced to study the variation in the shapes of $t\bar{t}$ kinematic distributions.

Two additional samples called radHi and radLo are produced to study the variation in the total amount of ISR/FSR. These samples have different renormalization and factorization scales than the nominal sample (x0.5 to radHi and x2 to radLo) in order to simulate $t\bar{t}$ with more/less ISR/FSR emissions. The radHi sample also increases the h_{damp} parameter, which controls the matching between the matrix element and parton shower calculations, from the nominal m_t to $2 \times m_t$.

We study the variation of the parton shower simulation using a Powheg+Herwigg++ $t\bar{t}$ sample. The hard scattering matrix element calculation is the same as the nominal Powheg+PYTHIA 6 sample. However the parton shower, fragmentation and hadronization is now performed with Herwigg++ program with the UE-EE-5 parameter tune.^{31,67}

Variations in the hard scattering matrix element calculation are studied by comparing the nominal to a sample generated using the SHERPA⁵⁴ program. SHERPA gives an alternative method to calculating both the matrix element and parton shower when compared to the nominal Powheg+PYTHIA 6 sample. The same CT10 NLO PDF set is used for SHERPA and the nominal sample. However SHERPA uses the default UE tune derived by the SHERPA team instead of the nominal Perugia 2012 UE tune.

Non-overlapping samples that are filtered in to E_T^{miss} are generated to increase statistics at high E_T^{miss} where our analysis resides. These samples are then merged after simulation to form a continuous E_T^{miss} distribution.

7.4.2 Standard Model Single-Top Monte Carlo Generation

Like the nominal $t\bar{t}$ sample, the nominal single-top samples are also simulated using Powheg-Box v.2^{27,68} with the PYTHIA 6 program being used for hadronization and parton showering. Similar to the $t\bar{t}$ sample, the single-top samples use the CT10 NLO PDF set and the Perugia 2012 set of UE tune parameters.

Unlike the $t\bar{t}$ samples, single-top samples are produced separately according to production channels. Three production channels exist, including the s-channel, t-channel and the Wt channel. The largest contribution to our analysis comes from the Wt channel.

The NLO calculation of the $pp \rightarrow Wt$ process includes contributions from $pp \rightarrow$

$t\bar{t} \rightarrow t + b + W$ process. However $pp \rightarrow t\bar{t} \rightarrow t + b + W$ is already included in our simulation of $t\bar{t}$ and including it here would be double counting. We can subtract out the $t\bar{t}$ contribution at either the amplitude level (DR scheme) or at the matrix element level (DS scheme). Subtracting at the matrix element level also remove any potential interference between the single-top $pp \rightarrow Wt$ process and the $pp \rightarrow t\bar{t} \rightarrow t + b + W$ process. Subtracting at the amplitude level does not remove those interferences. Both schemes violate formal gauge invariance and there isn't a consensus on the correct procedure. The nominal single-top sample is generated with the DR scheme and another sample is generated with the DS scheme. We compare the difference between the two samples to quantify the uncertainty due to the single-top and $t\bar{t}$ interference.

RadHi and radLo samples are also produced for single-top to study the variation in single-top ISR and FSR emissions. These samples are also produced with Powheg+PYTHIA6 but have different renormalization and factorization scales (x0.5 to radHi and x2 to radLo) to simulate more/less ISR/FSR emissions. The radHi sample also increase the h_{damp} parameter from the nominal m_t to $2 \times m_t$.

We study the variation of the parton shower simulation using Powheg+Herwig++ single-top samples. The hard scattering matrix element calculation has not changed from the nominal. The PDF used for the matrix element calculation is still CT10 NLO and the calculation is still performed with Powheg-Boxv.2 with the $h_{damp} = m_t$. However the parton shower, fragmentation and hadronization is now performed with

Herwig++ with the UE-EE-5 underlying event tune.⁶⁷

7.4.3 Standard Model $W + \text{jets}$ and $Z + \text{jets}$ Monte Carlo Generation

$W + \text{jets}$ and $Z + \text{jets}$ are generated with the SHERPAv2.2.1 program.⁵⁴ The matrix element are calculated for the vector boson plus 0, 1, and/or 2 additional partons at NLO accuracy and 3 and/or 4 additional partons at LO accuracy.

The matrix element calculation is merged with the SHERPA parton shower according to the MEPS@NLO prescription. The proton substructure is modeled with the NNPDF3.0 NNLO PDF set and the parton shower tuning defined by SHERPA.³²

We also generate additional samples that include 7 variations on the renormalization and factorization scales. These variations are used to quantify the theoretical uncertainty on our modeling of the $W + \text{jets}$ and $Z + \text{jets}$.

The $W + \text{jets}$ and $Z + \text{jets}$ samples are generated in multiple non-overlapping slices of vector boson p_T . The samples are further subdivided depending on the presence of b-jets and c-jets. These samples are merged after simulation to form a continuous distribution covering all phase space. This allows us to generate higher statistics in the region of phase space most relevant to our analysis, the region with high- p_T vector bosons and where b and/or c-jets are present.

7.4.4 Standard Model $t\bar{t} + V$ Monte Carlo Generation

$t\bar{t} + V$, where V is a W or Z boson, MC simulation are generated using the MadGraph5_aMC@NLO program with the NNPDF3.0 NLO PDF set.³² The matrix element calculation is performed to NLO accuracy. The parton shower, fragmentation, and hadronization are simulated using PYTHIA 8 with the A14 underlying event tune. Variations in the hard scattering matrix element calculation are studied by generating another sample using SHERPA and comparing its results to the nominal sample. Variation in renormalization and factorization scales are also produced.

7.4.5 Standard Model $t\bar{t} + \gamma$ Monte Carlo Generation

$t\bar{t} + \gamma$ samples are generated using the MadGraph5_aMC@NLO program with the NNPDF3.0 NLO PDF set.³² The matrix element calculation is performed to NLO accuracy. The parton shower, fragmentation, and hadronization are simulated using PYTHIA 8 with the A14 underlying event tune. The sample is filtered to only generate events at least one high p_T photon. This sample is then merged with the nominal $t\bar{t}$ sample to form the $t\bar{t} + \gamma$ sample. The events with high p_T photons in the nominal $t\bar{t}$ samples are removed to avoid double counting.

7.4.6 Standard Model Diboson Monte Carlo Generation

Dibosons samples are generated using the SHERPA v2.2 program with CT10 PDF set.

8

Recursive Jigsaw Reconstruction

Every search involving E_T^{miss} has to contend with the fact that information about the invisible system is lost. The E_T^{miss} reconstruction doesn't capture information on the invisible system's mass or the z component of the momentum. If multiple energetic weakly interacting particles exist in the event, we cannot directly determine how many energetic weakly interacting particles there are or how the E_T^{miss} should be

split among them. In summary, the question of how best to constrain these missing degrees of freedom is a problem ubiquitous to all analyses that use E_T^{miss} .

For the purpose of this analysis, we aim to separate the event into a sparticle system and an ISR system. The sparticle system contains objects that originate from stop decays and the ISR system contains ISR jets.

We cannot reconstruct the stops directly because we don't have the full four momenta of the two neutralinos. Therefore, features such as the stop mass peak are of limited use for determining if a jet originated from a stop decay. The high jet multiplicity also makes reconstructing tops very difficult. Furthermore, top reconstruction gives little separation power between signal and background since the dominant background, SM $t\bar{t}$, also has real tops.

Instead, we identify ISR by finding the axis of maximum back-to-back p_T , called the thrust axis. The thrust axis should mimic the axis of back-to-back boost between the ISR and sparticle systems because the back-to-back boost between the ISR and sparticle systems represents the single largest back-to-back kick in events with hard ISR.

We divide the event into two hemispheres according to the thrust axis. The hemisphere with the E_T^{miss} , called the sparticle hemisphere, is expected to contain most of the stop decay products. The 6 partons from the two top decays are also boosted by the ISR and tend to go in the same direction as the two neutralinos. The hemisphere opposite the E_T^{miss} should contain energetic ISR jets.

This method of separating objects into different categories by extremizing a metric is called the Recursive Jigsaw reconstruction method.^{60,61} In this case, the metric being maximized is the total back-to-back p_T of the ISR and sparticle systems.

In general, the Recursive Jigsaw reconstruction method gives a consistent way to constrain the missing degrees of freedom in invisible systems and reconstruct the full four momenta of multiple weakly interacting particles. We found that further subdividing the E_T^{miss} into the two neutralinos did not improve the search sensitivity because the important correlations for this analysis are between the ISR system and the dineutralino system as a whole.

Details on the ISR identification algorithm is covered in section 8.1 and the performance of the ISR identification algorithm is covered in section 8.2. More information on the Recursive Jigsaw reconstruction method can be found in references [^{60,61}].

8.1 Recursive Jigsaw Method of Identifying Initial State Radiation

In order to separate the event into an initial state radiation (ISR) system and a sparticle system, we first boost to the transverse center of mass frame of all accepted objects. The transverse center of mass frame has the useful property that when the entire event is divided into two systems, these two systems must have equal and

opposite transverse momenta. It's also important to note that the lab frame and the transverse center of mass frame only significantly differ in cases when an energetic object fails some quality selections. Therefore, the two frames differ significantly only when the E_T^{miss} has a high probability of being misreconstructed.

Once in the transverse center of mass frame, we find the thrust axis \vec{n} as defined in equation 8.1. The thrust axis \vec{n} represents the axis that maximizes the amount of back-to-back transverse momenta of all accepted objects, in this case all jets and E_T^{miss} . If hard ISR is present, then the back-to-back recoil between ISR and stops should represent the single largest back-to-back kick in the event. Therefore, the thrust axis should approximate the direction of the back-to-back recoil between the stops and ISR in events with hard ISR.

$$\vec{n} \equiv \max_{\text{jets, } E_T^{\text{miss}}} \sum_i |p_T^i \cdot \vec{n}| \quad (8.1)$$

We then divide the event into two hemispheres according to the thrust axis. The hemisphere containing the E_T^{miss} is identified as the sparticle hemisphere containing the decay products of the two stops. This is because we expect the sparticle hemisphere to contain the two neutralinos. The hemisphere opposite the direction of the E_T^{miss} is identified as the ISR hemisphere. All jets in the ISR hemisphere are considered to have originated from initial state radiation and all jets in the sparticle hemisphere are considered to have originated from one of the two stops.

The ISR identification algorithm can also be interpreted as an exclusive two jet clustering algorithm that seeks to simultaneously minimize the masses of both jets. This interpretation is a mathematically equivalent to the thrust axis interpretation. Since we are in the transverse center of mass frame, finding the thrust axis is the same as simultaneous maximizing the p_T of the sparticle ($p_T^{sparticle}$) and ISR systems (p_T^{ISR}). The total E_T of the event, shown in equation 8.2, is constant. Maximizing the p_T of the sparticle and ISR systems is identical to minimizing the masses of the sparticle ($m^{sparticle}$) and ISR systems (m^{ISR}). At the same time, the jet axes are guaranteed to be arranged in a back-to-back fashion because we in the transverse center of mass frame. The jet axis is therefore identical to the thrust axis.

$$E_T = \sqrt{(m^{ISR})^2 + (p_T^{ISR})^2} + \sqrt{(m^{sparticle})^2 + (p_T^{sparticle})^2} \quad (8.2)$$

8.2 Performance of Initial State Radiation Identification Algorithm

We can check the performance of the thrust based initial state radiation (ISR) identification algorithm by plotting the ratio of reconstructed over true ISR p_T in signal simulation. Figure 8.1 shows the distribution of the ratio of reconstructed vs true ISR p_T for 350 GeV stop mass and 172 GeV neutralino mass signal sample. Only events with fully hadronic stop decays and at least 400 GeV of true ISR p_T are accepted for this plot. Detector resolution effects on jets and E_T^{miss} are included when calculating

the reconstructed ISR p_T .

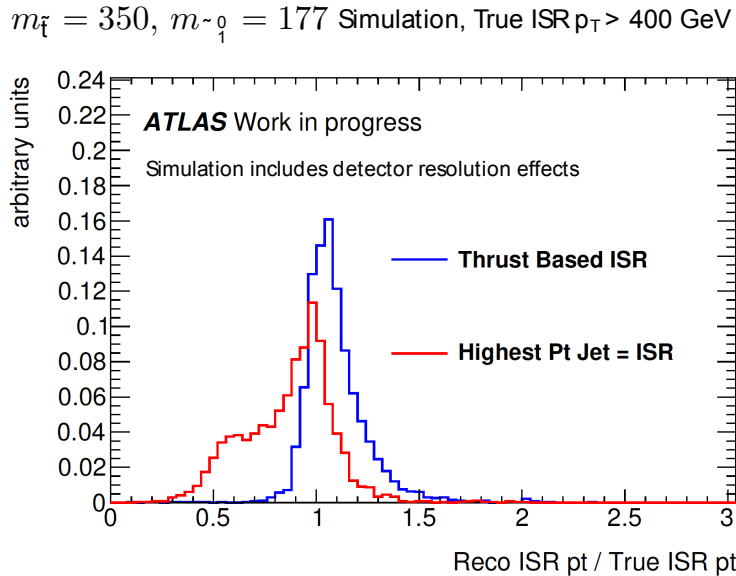


Figure 8.1: The distribution of the ratio of reconstructed vs true ISR p_T for the 350 GeV stop mass and 172 GeV neutralino mass signal sample. Only simulations with fully hadronic stop decays and at least 400 GeV of true ISR p_T are accepted. The red distribution is formed when the whole ISR system is equated to just the highest p_T jet. The blue distribution uses the thrust based ISR identification system.

A simple and currently popular form of ISR identification is simply the equating the highest p_T jet with the ISR system. The highest p_T jet algorithm is represented by the red distribution in Figure 8.1. The single jet algorithm loses 20-50% of the ISR energy in about 40% of events. This is because the ISR system energy is often split between multiple jets.

In comparison, the thrust based ISR identification system is able to capture the whole ISR system consisting of multiple jets. The fitted gaussian width of the blue peak is 9% and this uncertainty includes detector resolution effects. The gaussian

mean is centered about 1.05. The reason for this is because a jet originating from a stop will occasionally go in the opposite direction as the E_T^{miss} and be misidentified as an ISR jet. The p_T of the misidentified sparticle jet tend to be small when compared to the total p_T of the ISR system. Hence, this misidentification shows up as a 5% bias in the reconstructed ISR p_T . Optimization of the ISR identification algorithm shows that this small bias does not impact the sensitivity of the search.

The non-gaussian tail in the blue distribution that extends to a reconstructed over true ISR p_T ratio of 1.5 is due to energetic ISR jets that go in the same direction as the E_T^{miss} . In these cases, the ISR jets that are in the same direction as the E_T^{miss} are miss-reconstructed as having originated from a stop. Only the ISR jets going in an opposite direction to the E_T^{miss} are reconstructed as ISR jets. Therefore the reconstructed ISR system fail to partially cancel the p_T of the oppositely facing jets and the reconstructed ISR system has a larger p_T than the true ISR p_T . However, these cases are rare and the non-gaussian tail accounts for less than 15% of the events in blue distribution.

8.3 Kinematic Variables of Initial State Radiation and Sparticle Systems

Once we separated the event into two hemispheres according the thrust axis as described in section 8.1 we can construct a number of kinematic variables that captures different features of the two hemispheres. These variables are listed below.

$N_{\text{b-jet}}^S$: number of b-tagged jets associated with the sparticle hemisphere.

N_{jet}^S : number of jets associated with the sparticle hemisphere.

$p_{T,b}^{0,S}$: p_T of the leading b-tagged jet in the sparticle hemisphere.

$p_T^{4,S}$: p_T of the fourth highest p_T jet in the sparticle hemisphere.

m_T^S : transverse mass of the whole sparticle system and E_T^{miss} .

p_T^{ISR} : p_T of the ISR system.

$\Delta\phi_{\text{ISR}, E_T^{\text{miss}}}$: angular separation in ϕ of the ISR and the E_T^{miss} (evaluated in the transverse CM frame).

R_{ISR} : ratio between E_T^{miss} and p_T^{ISR} (evaluated in transverse CM frame).

N_{jet}^S and $N_{\text{b-jet}}^S$ quantify the jet multiplicity in the sparticle system. $p_{T,b}^{0,S}$, $p_T^{4,S}$, m_T^S and p_T^{ISR} quantify the amount of energy in the sparticle and ISR hemispheres. Finally, $\Delta\phi_{\text{ISR}, E_T^{\text{miss}}}$ and R_{ISR} describe the correlation between the ISR system and the E_T^{miss} in direction and magnitude. All of these variables will be used to separate signal from background in the signal region described in detail in chapter 11.

9

Collision Data Samples

9.1 Data Periods and Good Run List

This analysis uses the LHC proton-proton collision data at a centre-of-mass energy of $\sqrt{s}=13$ TeV that was collected by ATLAS in 2015 and 2016.

We select data where all relevant subdetector parts are running without defects and the quality of data is good. This is done by requiring the data pass a good run

list (GRL). The good run list is compiled from data that pass manual and automated checks on both detector hardware and the kinematics of reconstructed physics objects.

The GRLs used for the 2015 dataset is `data15_13TeV.periodAllYear_DetStatus-v79-repro20-02_DQDefects-00-02-02_PHYS_StandardGRL_All_Good_25ns.xml`.

The GRL for the 2016 data is `data16_13TeV.periodAllYear_DetStatus-v83-pro20-15_DQDefects-00-02-04_PHYS_StandardGRL_All_Good_25ns.xml`.

The dataset after GRL selection corresponds to a total integrated luminosity of $36.07 \pm 1.15 \text{ fb}^{-1}$. The total integrated luminosity as a function of time for 2015 and 2016 before the requirement of an GRL is shown in Figure 9.1.

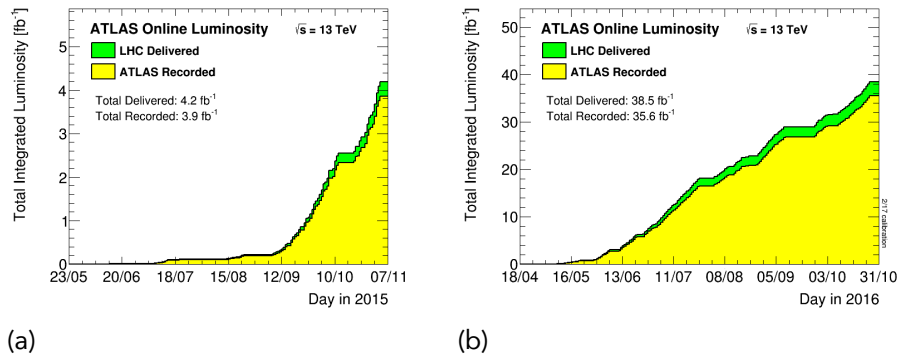


Figure 9.1: Distribution of the amount of data delivered by the LHC and recorded by ATLAS vs time in 2015 (a) and 2016 (b)

Peak luminosity reached $1.38 \times 10^{34} \text{ cm}^{-2} \text{ sec}^{-1}$ in 2016. Taking data at this high rate means we expect multiple p-p interactions in every bunch crossing. The average number of interactions per bunch crossing, $\langle \mu \rangle$, is 13.7 in 2015 and 23.2 in 2016.

The distribution of the mean number of interactions per bunch crossing is given in Figure 9.2.

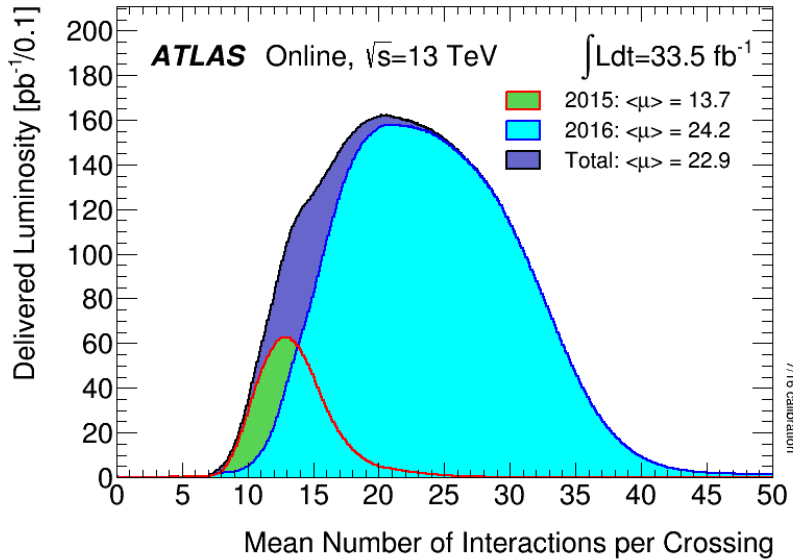


Figure 9.2: Distribution of the mean number of p-p interactions per bunch crossing weighted by integrated luminosity for 2015 and 2016 ATLAS data taking. On average 22.9 p-p interactions occur in every bunch crossing in the 2015+2016 ATLAS dataset.

In order to keep data flow to a manageable size, ATLAS only records events if a trigger is fired. The ATLAS trigger system is summarized in chapter 5. This analysis uses the lowest unprescaled E_T^{miss} trigger for each data taking period. This trigger threshold was set at 70 GeV to 110 GeV depending on the data taking period. The trigger efficiency curve as a function of offline E_T^{miss} for select E_T^{miss} triggers can be seen in Figure 5.2.

10

Event Preselection

We require that the event pass a few basic selections designed to reject non-collision backgrounds and events with large amounts of calorimeter noise. Together these basic selections are referred to as event cleaning and jet cleaning.

A brief description of the preselection requirements is given below: Details on all object definitions can be found in chapter 6.

Cut 1 Data events must satisfy the Good Runs List (GRL) requirement described in chapter 9.1. This ensures all relevant subdetectors of ATLAS are operating normally during data taking.

Cut 2 Remove events with noise bursts and possible incomplete events due to the TTC reset procedure from the data. Data events must have no errors flagged in the calorimeter and ID. The following error flags must be zero: larError == 0, tileError == 0, SCT error == 0, and coreFlags &0x4000 == 0.

Cut 4 Require that at least one reconstructed primary vertex exists.

Cut 5 Events must not contain any BadLoose jets with $p_T > 20$ GeV (at any η range). Bad quality jets indicate the presence of calorimeter noise or non-collision backgrounds. Both can lead to poor E_T^{miss} reconstruction. Hence, the whole event is rejected. BadLoose jets are defined in jet quality selection in section 4.3.4.

Cut 6 The event must not contain any cosmic muons. Cosmic muons are identified as muons with large impact parameters ($|z_0| > 1$ mm and $|d_0| > 0.2$ mm). Only Baseline muons after overlap removal are considered in cosmic muon identification.

Cut 7 The event must not contain any Baseline muons with $|\sigma(q/p)/|(q/p)| > 0.2$. Muons with large fractional uncertainty often result from kaon decays

or poorly reconstructed inner detector tracks that are incorrectly matched to muon spectrometer segments. These muons may result in misreconstructed E_T^{miss} so the whole event is rejected.

10.1 zero-lepton Preselection

All zero-lepton regions require the following set of preselections given in Table 10.1. We require exactly zero Baseline leptons to veto events containing electrons and muons.

All zero-lepton regions trigger on E_T^{miss} using the lowest unprescaled E_T^{miss} trigger for that data period. An offline selection of $E_T^{\text{miss}} > 250 \text{ GeV}$ is required to ensure that all accepted events are on the trigger efficiency plateau. The trigger efficiency curve as a function of offline E_T^{miss} for select E_T^{miss} triggers can be seen in Figure 5.2.

Table 10.1: The zero-lepton preselection criteria common to all zero-lepton regions.

GRL, Event Cleaning and Jet Cleaning	
	E_T^{miss} Trigger
E_T^{miss}	$> 250 \text{ GeV}$
$N_{\text{Baseline lep}}$	0
anti- k_t $R = 0.4$ Signal jets	≥ 4 , $p_T > 80, 80, 40, 40 \text{ GeV}$
b-tagged Signal jets	≥ 1
$ \Delta\phi(\text{jet}^{0,1}, E_T^{\text{miss}}) $	> 0.4
$E_T^{\text{miss,track}}$	$> 30 \text{ GeV}$
$ \Delta\phi(E_T^{\text{miss}}, E_T^{\text{miss,track}}) $	$< \pi/3$

We also require at least four Signal jets with a minimum p_T of (80, 80, 40, 40) GeV in the event. At least one Signal jet must be b-tagged at the 77% working point. These jet energy and multiplicity requirements are loose and will be superseded by more stringent selections.

We also include a number of selections aimed specifically at rejecting QCD multijet background. The primary reason that QCD multijet background can pass the $E_T^{\text{miss}} > 250$ GeV requirement is due to misreconstructed jets. QCD multijet processes produce little intrinsic E_T^{miss} but multijet background can have large reconstructed E_T^{miss} if any of the energetic jets are mismeasured. For example, an extremely energetic jet may punch through the calorimeter and deposit part of its energy outside the calorimeter. This lost E_T may be reconstructed as E_T^{miss} .

The $|\Delta\phi(\text{jet}^{0,1}, E_T^{\text{miss}})| > 0.4$ requirement ensures that the E_T^{miss} is not collinear with either of the two most energetic jets in the event. $|\Delta\phi(\text{jet}^{0,1}, E_T^{\text{miss}})|$ is defined in equation 12.4.

$$|\Delta\phi(\text{jet}^{0,1}, E_T^{\text{miss}})| = \min_{2 \text{ highest } p_T \text{ jets}} |\Delta\phi(\text{jet}, E_T^{\text{miss}})| \quad (10.1)$$

This provides strong rejection against fake E_T^{miss} resulting from a single misreconstructed energetic jet.

In addition, we require a loose agreement between two methods of reconstructing missing transverse energy, E_T^{miss} and $E_T^{\text{miss,track}}$. $E_T^{\text{miss,track}}$, defined in equation

4.3, is reconstructed using a negative vector sum of all accepted ID tracks. Track E_T^{miss} is very robust against pile-up conditions as ID tracks can be matched to a primary vertex but $E_T^{\text{miss,track}}$ neglects the presence of neutral particles. We found that a loose requirement of $E_T^{\text{miss,track}} > 30 \text{ GeV}$ and a loose agreement between E_T^{miss} and $E_T^{\text{miss,track}}$ in ϕ form an efficient discriminant against QCD multijet background.

Distributions of select kinematic variables after the zero-lepton preselection can be seen in Figure 10.1. The signal and background have similar E_T^{miss} distributions. This demonstrates that E_T^{miss} variable provides little separation power between the signal and background.

10.2 One-Lepton Preselection

We use one-lepton regions as control regions to estimate the background in the zero-lepton signal region. The MC is normalized to data in the control region through a combined fit to all control regions. This normalization is also applied to the background MC in the signal region. In this way, we directly measure the amount of background in the control region using data and only rely on simulation to extrapolate between the control region and the signal region. As such, the one-lepton control regions are designed to be kinematically similar to the zero-lepton signal region. This minimizes the extrapolation between the two regions and minimizes the uncertainty on the expected background rates in the signal region.

For this reason, the preselection for one-lepton regions is similar to the zero-lepton preselection. Both zero and one-lepton regions trigger using the E_T^{miss} triggers defined in chapter 5. We also require $E_T^{\text{miss}} > 250 \text{ GeV}$ to ensure that we are on the trigger efficiency plateau.

The one-lepton selections use **Signal** leptons instead of the **Baseline** leptons used in zero-lepton regions. The one-lepton regions use lepton momentum information and therefore require higher quality leptons.

The one-lepton preselection is summarized in Table 10.2.

Table 10.2: The one-lepton preselection criteria common to all one-lepton regions.

GRL, Event Cleaning and Jet Cleaning	
E_T^{miss} Trigger	
E_T^{miss}	$> 250 \text{ GeV}$
$N_{\text{Signal lep}}$	1
N_{jets}	≥ 4
b -tagged Signal jets	≥ 1
$ \Delta\phi(\text{jet}^{0,1}, E_T^{\text{miss}}) $	> 0.4

The lepton veto rejects single electron and single muon $t\bar{t}$ decays and the all hadronic $t\bar{t}$ decay produces little E_T^{miss} . For this reason, the biggest background in the signal region comes from SM $t\bar{t}$ where one top decays via the hadronic tau channel and the other top decays via the hadronic channel. The W from $W+\text{jets}$ and single-top backgrounds in the signal region also decays predominantly through the hadronic tau channel. For this reason, the majority of SM backgrounds in the signal

region contains a hadronic tau.

We expect many parallels between the electron and muon decay channels and the tau decay channel because of lepton universality. Therefore, we use the electron or muon in the one-lepton channel to mimic the hadronic tau in the signal region. Since we do not distinguish between hadronic tau jets and other jets in the signal region, both Signal leptons and Signal jets are counted as “jets” in one-lepton regions.

The $E_T^{\text{miss,track}} > 30 \text{ GeV}$ and $|\Delta\phi(E_T^{\text{miss}}, E_T^{\text{miss,track}})| < \pi/3$ requirements are removed because the QCD multijet contribution to one-lepton regions is negligible. The $|\Delta\phi(\text{jet}^{0,1}, E_T^{\text{miss}})| > 0.4$ selection is kept because it provides a closer modeling of the phase space in the signal region.

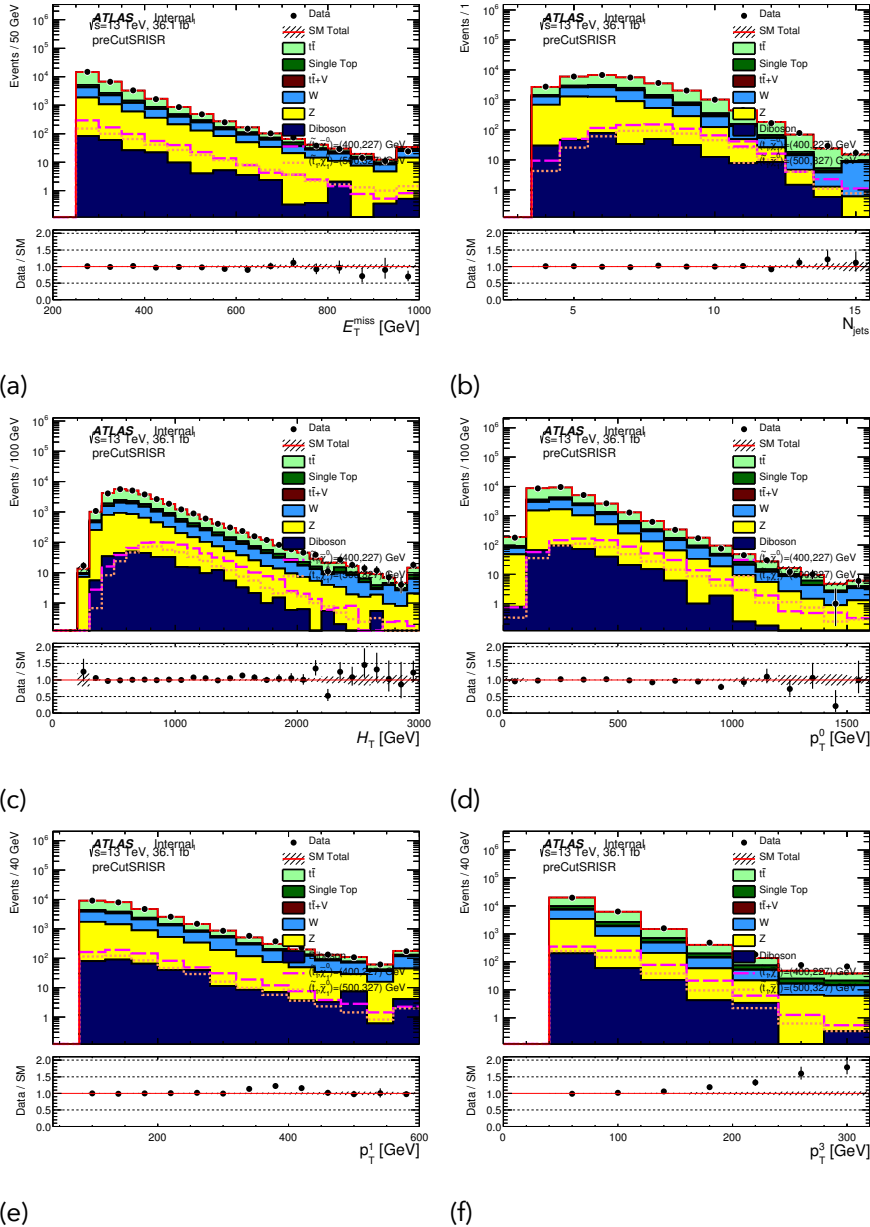


Figure 10.1: Kinematic variable distributions after the zero-lepton preselection; (a) E_T^{miss} (b) number of jets (c) H_T (d) p_T of the highest p_T jet (e) p_T of the 2nd highest p_T jet (f) p_T of the 4th highest p_T jet. SM backgrounds are displayed as the solid stacked histograms. Stop signals with $(m_{\tilde{t}}, m_{\tilde{\chi}_1^0}) = (400 \text{ GeV}, 227 \text{ GeV})$ and $(500 \text{ GeV}, 327 \text{ GeV})$ are shown as dashed histograms. The data/MC ratio is shown in the lower panel.

11

Signal Region Definition

The kinematic selections in the signal region are designed to maximize signal acceptance and reject SM $t\bar{t}$ events. SM $t\bar{t}$ is the dominant background for this analysis and comprises 70% of backgrounds in the signal region. The signal region selections are also effective at rejecting subdominant backgrounds, including $W+jets$, single-top, $Z+jets$ and QCD multijet backgrounds.

This chapter first builds physical intuition on the dominant SM $t\bar{t}$ in section 11.1 and explains how the signal region selections reject background. The signal region kinematic selections are defined in section 11.3. A back-of-the-envelope estimation of the signal region background rejection power and an order-of-magnitude estimation of how the signal over background ratio improves with the signal region selections is given in section 11.2. Lastly, the signal region yields and background composition are covered in sections 11.4 and 12.1.

11.1 Physical Intuition on how Signal Region Selections Reject Background

The zero-lepton signal region is designed specifically to reject the dominant $t\bar{t}$ background while maximizing signal acceptance. The signal region design and the signal and $t\bar{t}$ kinematics are summarized in this section. The signal region selections' effects on subdominant backgrounds are also described near the end of the section. More detail on each SM background, including background estimation techniques, can be found in chapter 12.

We find that 95% of all $t\bar{t}$ which survive the signal region selections decay via the single hadronic tau, single electron, or single muon decay channels. SM $t\bar{t}$ that decays via the fully hadronic decay channel generates little intrinsic E_T^{miss} and is negligible in the signal region. The SM $t\bar{t}$ dileptonic decay branching ratio is a factor of 5 lower than the single lepton decay channel. Plus, di-leptonic $t\bar{t}$ has a higher proba-

bility of being rejected by the lepton veto. A pie chart of the branching fractions for different $t\bar{t}$ decay channels is shown in Figure 11.1.

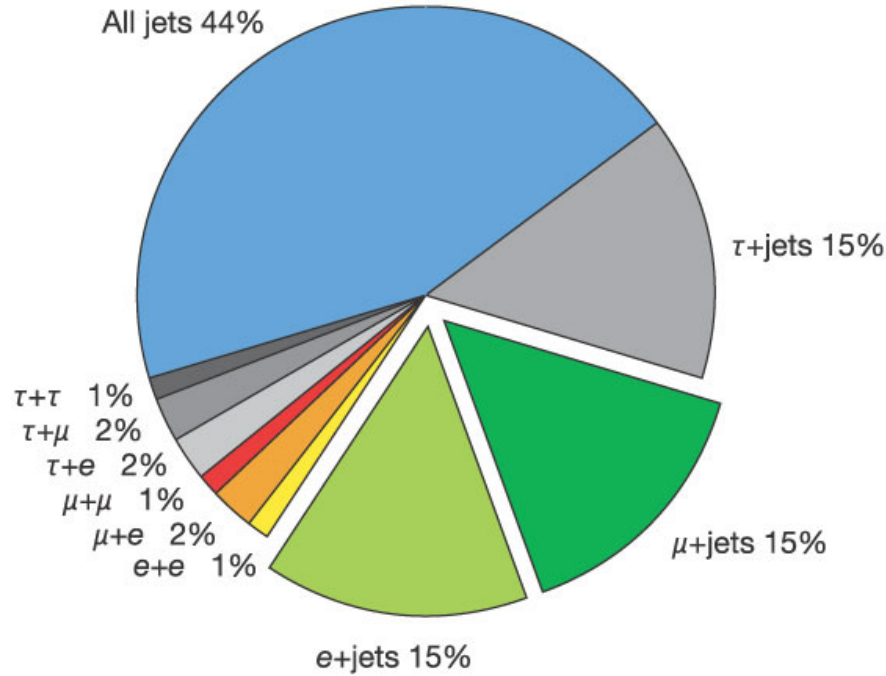


Figure 11.1: Pie chart of the branching fractions for different $t\bar{t}$ decay channels.

The E_T^{miss} and $R_{\text{ISR}} = E_T^{\text{miss}}/p_T^{\text{ISR}}$ distributions after the zero-lepton preselection for stop signal and SM backgrounds can be seen in Figure 11.2 and 11.3.

The E_T^{miss} distribution is very similar between stop signal and SM background, but the signal peaks in the R_{ISR} distribution. The R_{ISR} peak in signal is wide because we have not made a requirement for high ISR p_T at the preselection level. This signal peak will sharpen with the additional signal region selections.

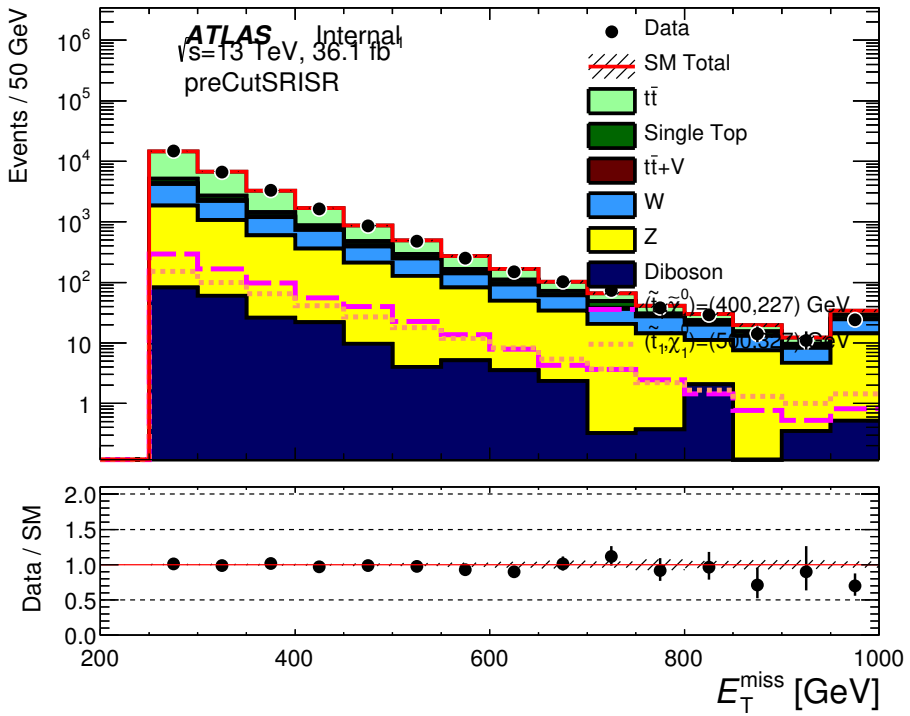


Figure 11.2: The E_T^{miss} distributions after the zero-lepton preselection. SM backgrounds are displayed as the solid stacked histograms. Stop signals with $(m_{\tilde{t}}, m_{\tilde{\chi}_1^0}) = (400 \text{ GeV}, 227 \text{ GeV})$ and $(500 \text{ GeV}, 327 \text{ GeV})$ are shown as dashed histograms.

The $t\bar{t}$ R_{ISR} distribution peaks at ~ 0.75 . This corresponds to $t\bar{t}$ events without hard ISR which gives a high $E_T^{\text{miss}}/p_T^{\text{ISR}}$ ratio. Again, no requirement on p_T^{ISR} has been made at the preselection level. After placing more signal region requirements on events with high ISR p_T , the $t\bar{t}$ events with high R_{ISR} ratio will be rejected. The rest of this section will be devoted to explaining why the $t\bar{t}$ background initially peaks at ~ 0.75 and how the signal region selections reject these high R_{ISR} $t\bar{t}$ events.

First, it is important to note that the top decay cannot generate a 250 GeV p_T

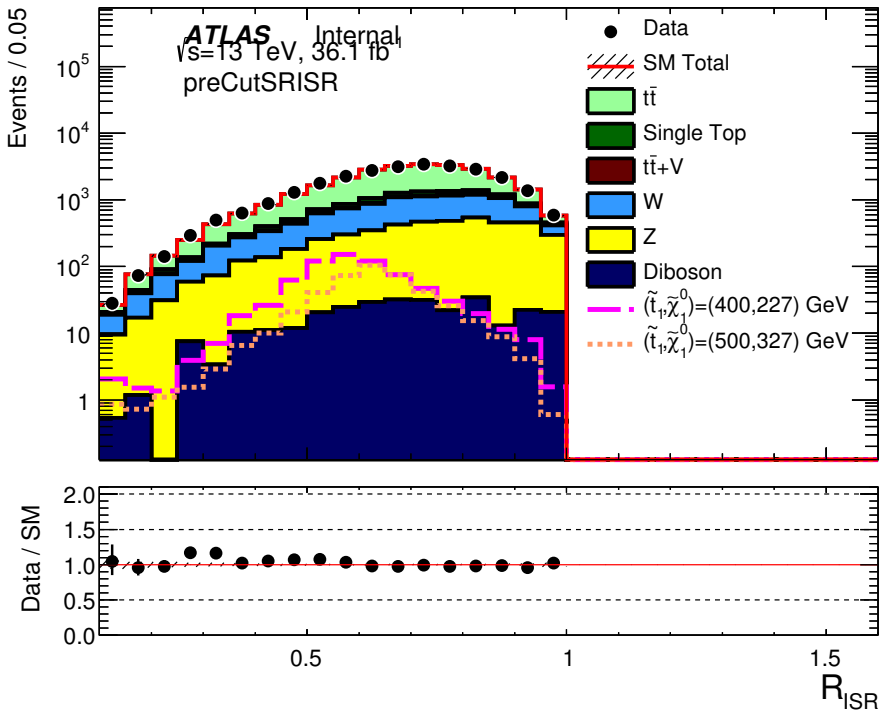


Figure 11.3: The R_{ISR} distribution after preselection. SM backgrounds are displayed as the solid stacked histograms. Stop signals with $(m_{\tilde{t}}, m_{\tilde{\chi}_1^0}) = (400 \text{ GeV}, 227 \text{ GeV})$ and $(500 \text{ GeV}, 327 \text{ GeV})$ are shown as dashed histograms.

neutrino if the top decays at rest. Therefore, the $E_T^{\text{miss}} > 250 \text{ GeV}$ requirement in preselection selects mainly for $t\bar{t}$ with a boosted leptonic top.

The leptonic top can only gain boost in one of two ways. Either the leptonic top recoils against the hadronic top in a back-to-back fashion, or both tops recoil against hard ISR. This break-down of SM $t\bar{t}$ into two kinematically distinct populations is covered in more detail in section 12.3. A schematic representation of these two distinct $t\bar{t}$ kinematic populations can be found in Figure 12.2.

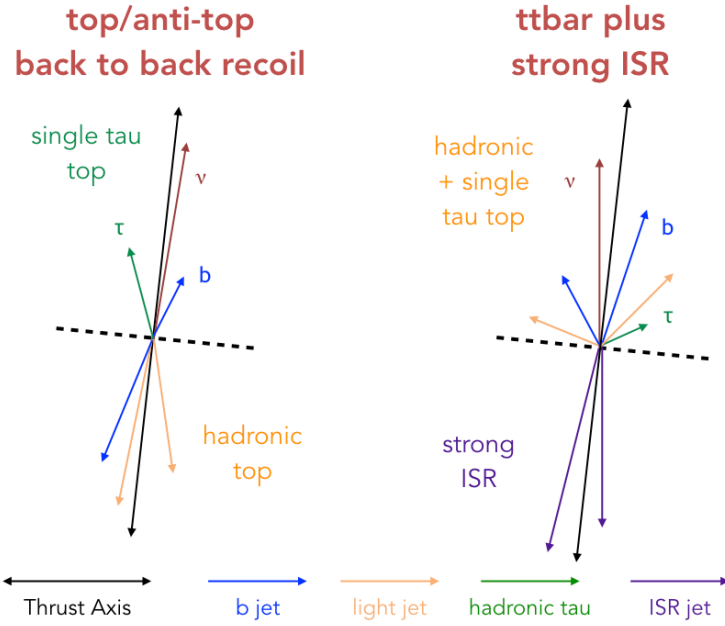


Figure 11.4: Depiction of the kinematics of the $t\bar{t}$ back-to-back population and the $t\bar{t}$ +hard ISR population that exists after the zero-lepton pre-selection. The two example events' thrust axis are aligned. The hemisphere containing E_T^{miss} has significantly higher jet multiplicities and total energy in $t\bar{t}$ +hard ISR events.

The thrust axis or the axis that maximizes the amount of back-to-back p_T along it contains important information in both populations. In the $t\bar{t}$ back-to-back population, the thrust axis aligns along the top/anti-top back-to-back boost. In the $t\bar{t}$ +hard ISR population, the thrust axis aligns along the ISR/ $t\bar{t}$ back-to-back boost.

After preselection, 90% of all $t\bar{t}$ events belong to the $t\bar{t}$ back-to-back population.

Boosting one top against the other top simply requires less center-of-mass energy than boosting both tops with additional hard ISR.

In the $t\bar{t}$ back-to-back population, the hadronic top's decay products will be mainly

in the hemisphere not containing E_T^{miss} . The reconstructed ISR p_T will therefore be approximately the hadronic top p_T . The leptonic top and hadronic top have roughly equal p_T because the two tops are back-to-back. The leptonic top will have its p_T split between its decay products. For this reason, we would expect the R_{ISR} to be approximately 1/3 as the neutrino would be expected to carry about 1/3 the leptonic top p_T if no selections were applied. Some $t\bar{t}$ events will have a high R_{ISR} ratio because the neutrino carries a higher fraction of the leptonic top p_T because of specific alignments between the top boost and the decay axes. However, the $E_T^{\text{miss}} > 250 \text{ GeV}$ requirement preferentially selects for neutrinos that gain a large fraction of the top p_T . This leads to a higher R_{ISR} peak at ~ 0.75 for the $t\bar{t}$ back-to-back population.

Figure 11.5 illustrates example events from the two $t\bar{t}$ populations alongside a stop signal event for comparison. We line up all three events according to their thrust axis and the hemisphere containing the E_T^{miss} is displayed in the upper half of the figure.

We can immediately see that the signal has significantly higher jet multiplicity and total energy in the hemisphere with the E_T^{miss} than the $t\bar{t}$ back-to-back population in $t\bar{t}$. The signal has six jets originating from the two hadronic top decays in the hemisphere plus the E_T^{miss} from two neutralinos in the same hemisphere. In comparison, the $t\bar{t}$ back-to-back event only has decay products from a single leptonic top in the hemisphere containing E_T^{miss} . The $t\bar{t}+\text{hard ISR}$ population has higher jet multiplicity

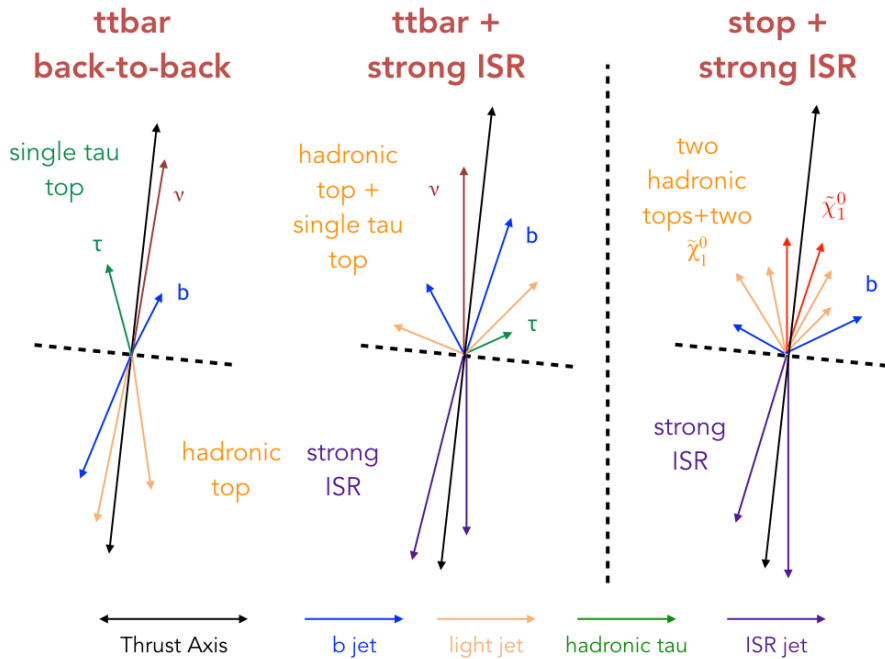


Figure 11.5: Schematic depiction of example events from the $t\bar{t}$ back-to-back population, the $t\bar{t}$ +hard ISR population, and the stop+hard ISR signal after the zero-lepton preselection. All three events are aligned with one another according to their thrust axis. The hemisphere containing E_T^{miss} is located in the upper half of the figure. The stop signal has much higher jet multiplicity and total energy in the hemisphere containing E_T^{miss} than the $t\bar{t}$ back-to-back population.

and energy in the E_T^{miss} hemisphere. However, it still has on average less total energy and jet multiplicity than the stop signal.

By placing requirements on the jet multiplicity and total energy in the hemisphere with E_T^{miss} , the signal region selections are able to reject over 99.5% of $t\bar{t}$ events with less than 400 GeV of true ISR p_T . The acceptance of $t\bar{t}$ events increases with true ISR p_T but only asymptotically. Even at 1200 GeV of true ISR p_T , a $t\bar{t}$ event which already passed zero-lepton preselection only has an 8% chance of passing the additional

signal region selection.

The signal region selection efficiency for $t\bar{t}$ as a function of ISR p_T is shown in Figure 11.1.

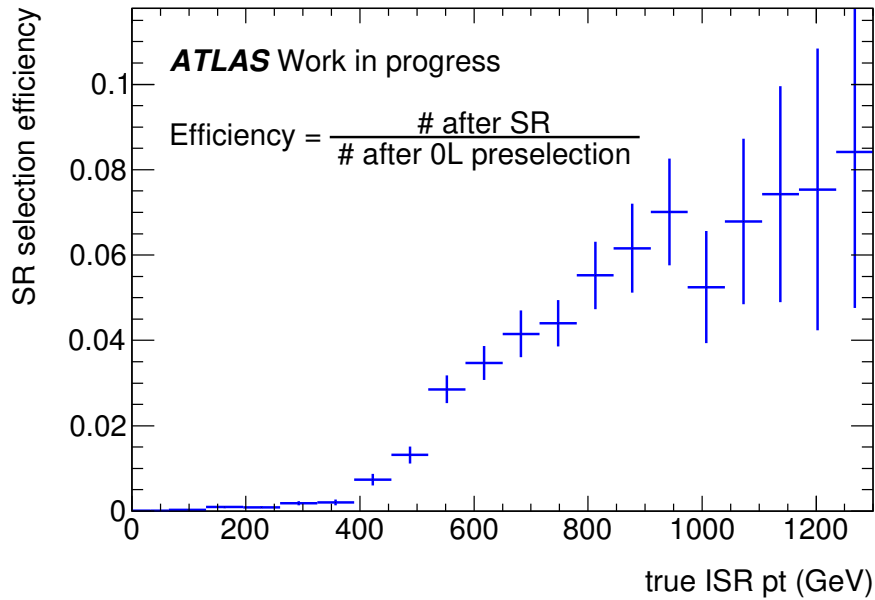


Figure 11.6: The selection efficiency for $t\bar{t}$ as a function of ISR p_T for $t\bar{t}$ after the zero-lepton preselection and after all signal region selections. The selections overwhelmingly reject $t\bar{t}$ with low ISR p_T , rising to around 8% for $t\bar{t}$ with 1 TeV of ISR p_T .

After signal region selections, only approximately 10% of all $t\bar{t}$ events have true ISR p_T less than 400 GeV. A back-of-the-envelope calculation shows that $t\bar{t}$ events need around 600 GeV of ISR p_T in order to boost the neutrino past the 250 GeV E_T^{miss} selection if both tops started at rest. Such high ISR p_T is required because the neutrino must share the total $t\bar{t}$ p_T with the 5 other particles in the $t\bar{t}$ decay. This completely agrees with the true ISR p_T distribution in the signal region which peaks

around 550-600 GeV for $t\bar{t}$ background.

The $t\bar{t}$ true ISR p_T distribution after the zero-lepton preselection and after signal region selections can be seen in Figure 11.7.

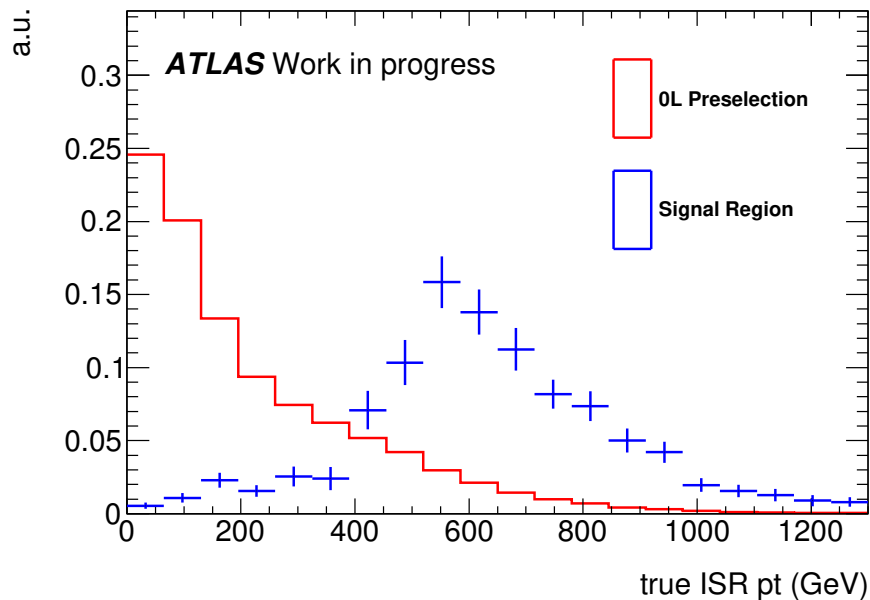


Figure 11.7: Distribution of true ISR p_T for $t\bar{t}$ after the zero-lepton preselection and after all signal region selections. Both distributions have been normalized to unit area.

11.2 Order of Magnitude Estimation of how Signal Region Selections Improve Signal over Background Ratio

The signal region selects for $t\bar{t}$ with at least 550 GeV of ISR p_T . In comparison, the stop signal with $m_{\tilde{t}} = 400$ GeV requires only 440 GeV of ISR p_T to pass the $E_T^{\text{miss}} > 250$ GeV requirement and the signal region selections due to the $E_T^{\text{miss}} \sim m_{\tilde{\chi}_1^0}/m_{\tilde{t}} \times$

p_T^{ISR} relationship.

The normalized $t\bar{t}$ differential cross section as a function of $p_T^{t\bar{t}}$ can be seen in Figure 11.8. $p_T^{t\bar{t}}$ is equal to the true p_T^{ISR} because anything that the $t\bar{t}$ recoils against is considered “ISR” by the ISR identification algorithm. By extrapolating the $t\bar{t}$ differential cross section measurement to high $p_T^{t\bar{t}}$ we can see that there is approximately an order of magnitude increase in differential cross section if we decrease the ISR p_T requirement by 150 GeV. Therefore, the signal has a order of magnitude larger normalized differential cross section than the SM $t\bar{t}$ background because the signal requires less ISR p_T . This equals an increase in the signal over background ratio (S/B) by a factor of ~ 10 .

In addition, the stop signal has an higher probability of having high ISR p_T than SM $t\bar{t}$. This is because 440 GeV of ISR p_T is relatively small when compared to the two 400 GeV stops. In comparison, 440 GeV is large relative to the mass of two top quarks at ~ 172.5 GeV each. This means the gain in S/B from the lower signal ISR p_T requirement is even larger than what Figure 11.8 suggests.

At the same time, we gain another factor of 5 improvement in S/B simply by working in the zero-lepton channel. In the signal region, the stops decay mainly via the all-hadronic decay channel with a 44% branching fraction. In comparison in the signal region, 80% of $t\bar{t}$ background decay via the hadronic tau channel with a branching fraction of approximately 10%. The $t\bar{t}$ single tau decay has a branching fraction of approximately 15% but only about 65% of taus decay hadronically. The $t\bar{t}$ decay

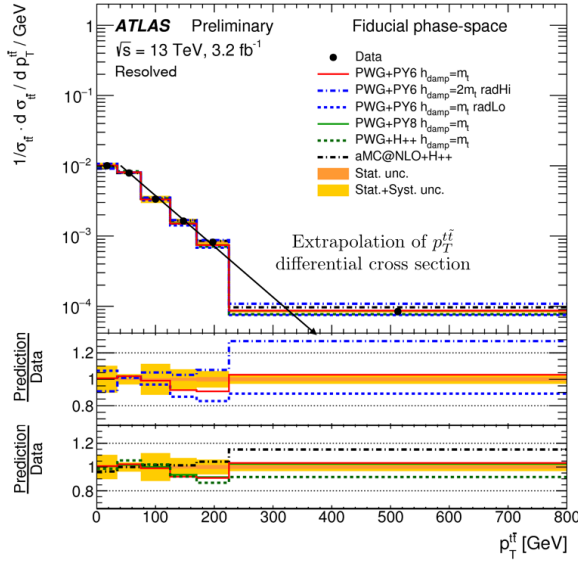


Figure 11.8: Normalized $t\bar{t}$ differential cross-section as a function of $p_T^{t\bar{t}}$.¹⁸ $p_T^{t\bar{t}}$ is equal to the p_T^{ISR} because our ISR identification algorithm reconstructs anything that recoils against the $t\bar{t}$ as ISR. $p_T^{t\bar{t}}$ distribution falls exponentially and can be modeled by a straight-line in the log plot. Assuming the straight-line extrapolation holds, we would expect roughly an order of magnitude increase in differential cross section if the ISR p_T required decreased by ~ 150 GeV.

branching fraction is shown in Figure 11.1.

The E_T^{miss} and ISR correlations in both direction and magnitude further improve the S/B ratio by another factor of 5 to 10 depending on the stop mass. The distribution of $\Delta\phi_{\text{ISR}, E_T^{\text{miss}}}$ with all other signal region selections applied is shown in Figure 11.11. The R_{ISR} distribution after all signal selections including the $\Delta\phi_{\text{ISR}, E_T^{\text{miss}}} > 3.0$ requirement is shown in Figure 11.12

With all these effects combined, we are able to overcome the original 300 times difference in production cross section between the 400 GeV stop and SM $t\bar{t}$.

As the stop mass increases, the required ISR p_T in signal decreases according to

$m_{\tilde{t}}/m_{\tilde{\chi}_1^0}$, further increasing the accepted signal differential cross section, even if the signal production cross section is dropping. At the same time, the signal will peak at higher R_{ISR} ratios where background contributions are lower. In this way, the analysis is able to maintain sensitivity across a wide range of stop masses despite rapidly dropping signal production cross section at high stop masses.

After zero-lepton preselection, the S/B ratio is 1:40 for a stop mass of 400 GeV. After signal region selection, the S/B ratio improves to approximately 2:1 for the same mass point. A quantitative breakdown of signal region selections and yields is given in sections 11.3 and 11.4.

At the same time, the same kinematic selections on jet multiplicity and total energy are also difficult for subdominant backgrounds to satisfy. In general, it is difficult for processes such as $W+\text{jets}$, $Z+\text{jets}$, single-top and QCD multijets to produce such high jet multiplicity and total energy in the same half of the event as the E_T^{miss} . Processes such as $W+\text{jets}$ and $Z+\text{jets}$ normally have the E_T^{miss} recoiling against other energetic jets. Therefore, energetic jets in these processes tend to lie in the hemisphere opposite the E_T^{miss} . After the signal region selections, the total subdominant background contribution is around 20 to 40% depending on R_{ISR} region.

11.3 Signal Region Kinematic Selection

The signal region kinematic selections are defined in Table 11.1.

The kinematic variables used are reconstructed using the Recursive Jigsaw method. A detailed description of this method and variable defined can be found in section 8.1. In short, the Recursive Jigsaw method separates the event into two hemispheres according to the thrust axis. The thrust axis, the axis that maximizes the amount of back-to-back p_T along it, approximates the axis of back-to-back recoil between the sparticle and ISR. The hemisphere containing the E_T^{miss} is considered the sparticle hemisphere, and the hemisphere opposite the E_T^{miss} is considered the ISR hemisphere. All jets in the sparticle hemisphere are considered to have originated from one of the stop decays. All jets in the ISR hemisphere are considered ISR jets. The performance of this ISR identification algorithm can be found in section 8.2.

We also construct variables that measure kinematic properties of both the ISR and sparticle hemispheres. These include N_{jet}^S and $N_{\text{b-jet}}^S$, the number of jets and b-tagged jets in the sparticle system. m_T^S , $p_T^{4,S}$, and $p_{T,b}^{0,S}$ are all related to the total energy in the sparticle system. m_T^S is the total transverse mass of the sparticle system. $p_T^{4,S}$ is the p_T of the fourth highest p_T jet in the sparticle system. $p_{T,b}^{0,S}$ is the p_T of the highest p_T b-tagged jet in the sparticle system. p_T^{ISR} corresponds to the total p_T of the ISR system. Finally $R_{\text{ISR}} = E_T^{\text{miss}} / p_T^{\text{ISR}}$ and $\Delta\phi_{\text{ISR}, E_T^{\text{miss}}}$ quantify the correlation between the ISR system and E_T^{miss} in both magnitude and direction.

The selections on $N_{\text{jet}}^S \geq 5$ and $N_{\text{b-jet}}^S \geq 1$ ensure that the hemisphere with E_T^{miss} has a high amount of jet multiplicity. These requirements are naturally satisfied in

Table 11.1: Signal region definitions, in addition to the preselection requirements presented in Table 10.1.

Variable	SRC-1	SRC-2	SRC-3	SRC-4	SRC-5
$N_{b\text{-jet}}^S$			≥ 1		
N_{jet}^S			≥ 5		
p_T^{ISR}			$> 400 \text{ GeV}$		
$p_{T,b}^{0,S}$			$> 40 \text{ GeV}$		
$p_T^{4,S}$			$> 50 \text{ GeV}$		
m_T^S			$> 300 \text{ GeV}$		
$\Delta\phi_{\text{ISR}, E_T^{\text{miss}}}$			> 3.00		
R_{ISR}	0.30-0.40	0.40-0.50	0.50-0.60	0.60-0.70	0.70-0.80

signal events because the six jets from the two stop decays are boosted by ISR toward the same direction as the two neutralinos. However, this requirement is more difficult to satisfy for the $t\bar{t}$ back-to-back population since these events contain only a single leptonic or hadronic tau top in the same hemisphere as the E_T^{miss} .

The $t\bar{t}$ +hard ISR population is able to pass this selection as both the leptonic and hadronic tops are in the sparticle hemisphere. For this reason, the main background is comprised of $t\bar{t}$ +hard ISR events after the sparticle jet multiplicity and the $p_T^{\text{ISR}} > 400 \text{ GeV}$ requirements. The S/B ratio is around 1:5 after these selections.

The R_{ISR} distribution for signal and background is shown after the requirements on p_T^{ISR} , N_{jet}^S , and $N_{b\text{-jet}}^S$ in Figure 11.9.

The signal peaks in the R_{ISR} distribution after the selections on p_T^{ISR} , N_{jet}^S and $N_{b\text{-jet}}^S$

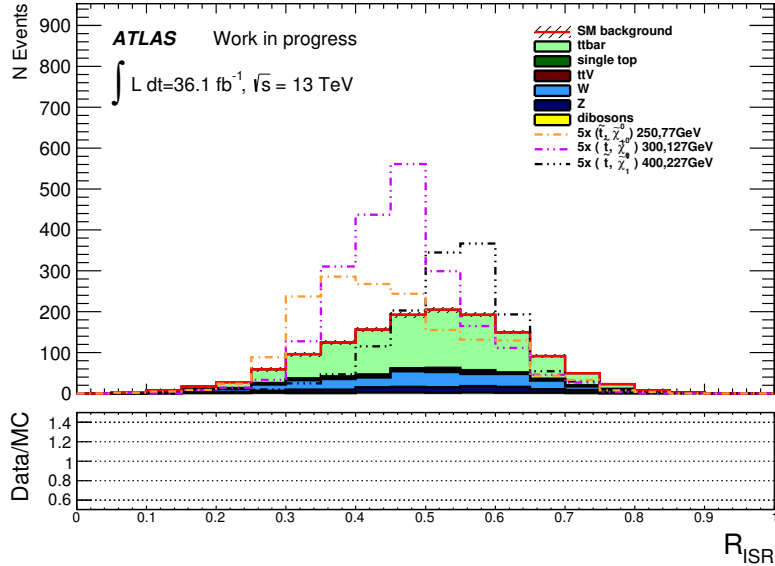


Figure 11.9: R_{ISR} distribution for signal and background after preselection plus $p_T^{ISR} > 400 \text{ GeV}$, $N_{jet}^S \geq 5$, and $N_{b-jet}^S \geq 1$ selections. Stop signal rate is increased by a factor of 5 for better visibility. The hashed area in both the top and lower panel represent the uncertainty due to MC statistics. QCD background estimation is not included.

(in Figure 11.9) are much sharper when compared to the R_{ISR} distribution after preselection in Figure 11.3. The high N_{jet}^S and p_T^{ISR} requirements select for signal events with good correlations between ISR and E_T^{miss} . In this way, the selections on p_T^{ISR} , N_{jet}^S , and N_{b-jet}^S increase the background rejection power of the later requirements on R_{ISR} and $\Delta\phi_{ISR, E_T^{\text{miss}}}$.

The $t\bar{t}$ background distribution now peaks at approximately ~ 0.55 . The $t\bar{t}$ events with a high R_{ISR} of ~ 0.75 which dominated the $t\bar{t}$ R_{ISR} distribution after the zero-lepton preselection in Figure 11.3 have been rejected. The high R_{ISR} $t\bar{t}$ events correspond to $t\bar{t}$ with hard $t\bar{t}$ back-to-back boost but little ISR p_T . The events with lower

$R_{\text{ISR}} \sim 0.5$ values correspond to $t\bar{t}$ with high ISR p_T because $R_{\text{ISR}} = E_T^{\text{miss}}/p_T^{\text{ISR}}$. The rejection of $t\bar{t}$ with $R_{\text{ISR}} \sim 0.75$ is evidence that the selection is selecting mainly $t\bar{t}$ events with high ISR p_T .

Next, we make a requirement on the total energy of the sparticle system. The total transverse mass of the sparticle system, m_T^S , must be greater than 300 GeV and $p_T^{4,S}$, p_T of the 4th highest p_T jet in the sparticle system, must be greater than 50 GeV. $p_{T,b}^{0,S}$, the highest p_T b-jet in the sparticle system, must also be greater than 40 GeV. The distributions of m_T^S , $p_T^{4,S}$ and $p_{T,b}^{0,S}$ after the $N_{\text{jet}}^S \geq 5$, $N_{\text{b-jet}}^S \geq 1$ and $p_T^{\text{ISR}} > 400$ GeV selections are shown in Figure 11.10.

In general, the signal with two fully hadronic tops has higher energy jets and more total energy in the sparticle hemisphere than SM $t\bar{t}$. The $t\bar{t}$ back-to-back population is nearly eliminated by these selections as they only have a single leptonic top in the same hemisphere as E_T^{miss} . In $t\bar{t}$ events with hard ISR, the ISR boosts both tops toward the hemisphere containing E_T^{miss} . However, the combined energy of the hadronic and leptonic tops is still less on average than the energy of two hadronic tops plus two neutralinos in the stop signal. The $m_T^S > 300$ GeV, $p_T^{4,S} > 50$ GeV and $p_{T,b}^{0,S} > 40$ GeV requirements improve the S/B ratio to around 1:2.

Lastly, we make selections based on the correlations between the E_T^{miss} and ISR systems. $\Delta\phi_{\text{ISR}, E_T^{\text{miss}}} > 3.0$ ensures the E_T^{miss} and ISR systems are back-to-back. The ISR system and E_T^{miss} must be nearly back-to-back in signal because the neutralino gains momentum mainly from ISR. On the other hand, the neutrino in SM $t\bar{t}$ gains

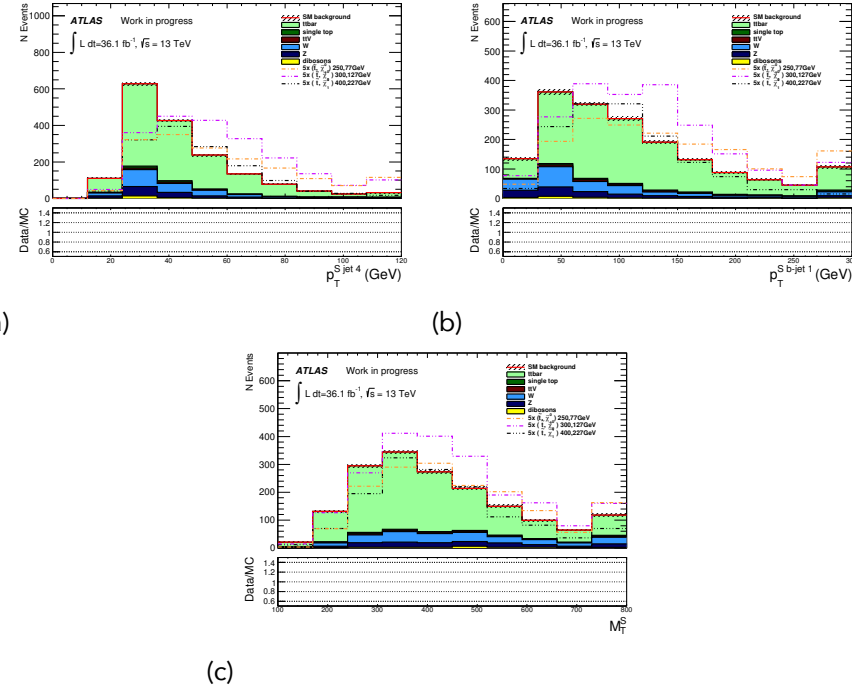


Figure 11.10: m_T^S , $p_T^{4,S}$, and $p_{T,b}^{0,S}$ distributions for signal and background after preselection plus $p_T^{\text{ISR}} > 400 \text{ GeV}$, $N_{\text{jet}}^S \geq 5$, and $N_{\text{b-jet}}^S \geq 1$ selections. Stop signal rate is increased by a factor of 5 for better visibility. The hashed area in both the top and lower panel represent the uncertainty due to MC statistics. QCD background estimation is not included.

significant momentum from the top decay and its correlation with ISR is not as strong.

This is also true for subdominant backgrounds including $W+\text{jet}$ and single-top.

The distribution of $\Delta\phi_{\text{ISR}, E_T^{\text{miss}}}$ with all previous selections on $p_T^{\text{ISR}} > 400 \text{ GeV}$, sparticle hemisphere jet multiplicity, and sparticle hemisphere energy is shown in Figure 11.11.

The final R_{ISR} distribution after all signal selections is shown in Figure 11.12. This R_{ISR} distribution is then separated into 5 bins from 0.3 to 0.8. The 5 signal region

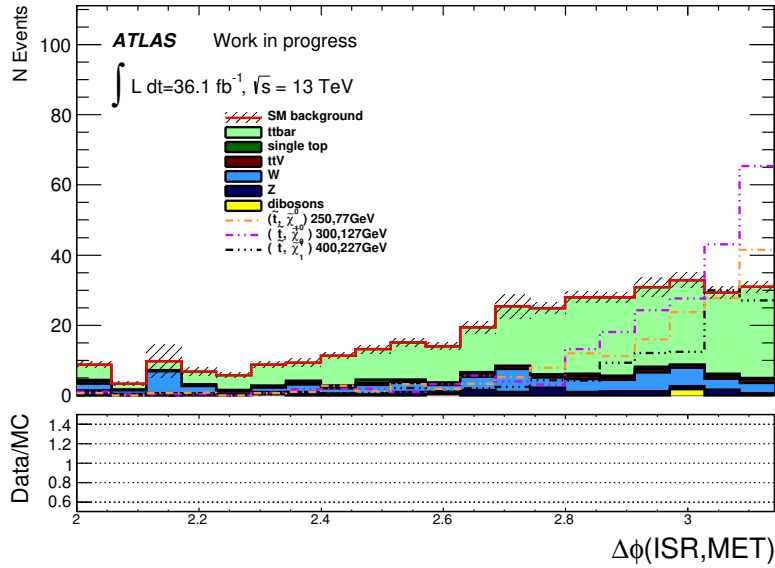


Figure 11.11: $\Delta\phi_{ISR,E_T^{\text{miss}}}$ distribution after the zero-lepton preselection, $p_T^{\text{ISR}} > 400$ GeV, sparticle hemisphere jet multiplicity and sparticle hemisphere energy requirements. The solid stacked histogram represents the expected SM background rates. The dashed histogram represent the expected number of signal events for several stop and neutralino masses. The hashed area in both the top and lower panel represents the uncertainty due to MC statistics.

bins are fitted simultaneously to extract the signal strength. We expect very few signal events in the R_{ISR} region below 0.3. The same region is also dominated by QCD background. As such, the R_{ISR} region below 0.3 is not included in the final signal region fit.

Stop samples with different stop and neutralino masses will peak in different locations in R_{ISR} with a S/B ratio of approximately 2:1 under the peak. The simultaneous fit to all 5 bins captures this peaking feature in R_{ISR} for any stop mass.

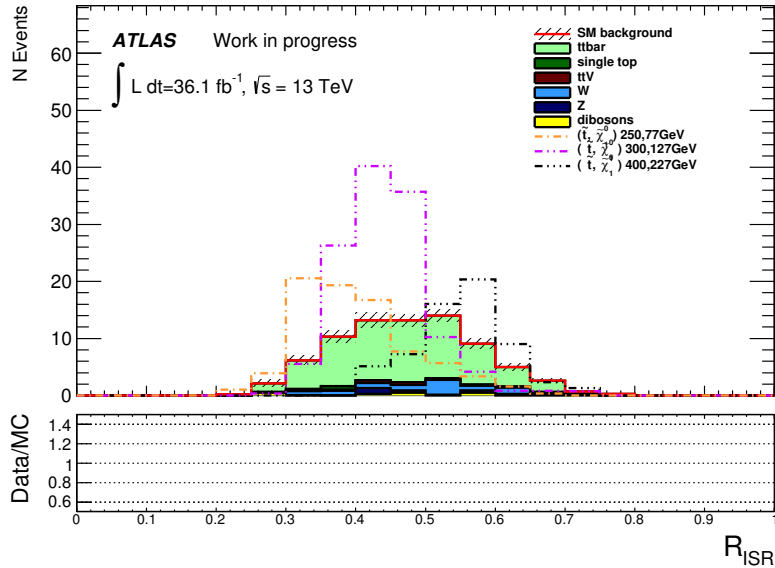


Figure 11.12: R_{ISR} distribution after signal region selection corresponding to 36.07 fb^{-1} of data. The solid stacked histogram represents the expected SM background rates. The dashed histogram represent the expected number of signal events for several stop and neutralino masses. The hashed area in both the top and lower panel represents the uncertainty due to MC statistics.

11.4 Signal Region Expected Yields and Kinematic Distributions

The expected yields in the signal region are given in Table 11.2. Signal yields for three example signal samples with stop, neutralino masses of (300, 127 GeV), (400, 227 GeV), and (500, 327 GeV) are also shown for comparison. We achieve a 1:1 to 2:1 S/B ratio under the signal R_{ISR} peak in the signal region.

All expected background rates in the signal region are normalized to control regions defined in chapter 12. The control regions are designed to mimic the background kinematics in the signal region but are orthogonal to the signal region and

have low expected signal rate. We directly measure the background rate using data in the control regions and use simulation to extrapolate background predictions from the control region to the signal region.

Table 11.2: SR expected background yields after normalization to background CRs using integrated luminosity of 36.07 fb^{-1} . The uncertainties include both statistical and systematic uncertainties. Expected stop signal yields are also shown for comparison.

SRC yields	SRC1	SRC2	SRC3
Expected bkg events	21.02 ± 6.62	28.42 ± 4.89	19.60 ± 3.53
Expected TTbar events	12.85 ± 5.87	22.05 ± 4.19	14.57 ± 3.23
Expected Wjets events	0.81 ± 0.37	1.93 ± 0.48	1.91 ± 0.63
Expected Zjets events	0.46 ± 0.09	0.90 ± 0.13	0.74 ± 0.15
Expected TtbarV events	0.29 ± 0.18	0.59 ± 0.38	0.56 ± 0.31
Expected SingleTop events	$1.67^{+2.02}_{-1.67}$	$1.18^{+1.81}_{-1.18}$	$1.22^{+1.37}_{-1.22}$
Expected Diboson events	0.39 ± 0.33	0.21 ± 0.11	0.29 ± 0.18
Expected Multijets events	4.56 ± 2.38	1.58 ± 0.77	0.32 ± 0.17
$(m_{\tilde{t}} = 300, m_{\tilde{\chi}^0} = 127) \text{ GeV}$	30.68 ± 4.17	72.20 ± 7.29	14.80 ± 2.56
$(m_{\tilde{t}} = 400, m_{\tilde{\chi}^0} = 227) \text{ GeV}$	1.57 ± 0.45	10.81 ± 1.00	30.01 ± 1.67
$(m_{\tilde{t}} = 500, m_{\tilde{\chi}^0} = 327) \text{ GeV}$	0.11 ± 0.06	1.42 ± 0.26	6.90 ± 0.56
SRC yields	SRC4	SRC5	
Expected bkg events	8.14 ± 1.39	0.99 ± 0.71	
Expected TTbar events	4.92 ± 0.98	$0.63^{+0.69}_{-0.63}$	
Expected Wjets events	1.93 ± 0.45	0.21 ± 0.12	
Expected Zjets events	0.45 ± 0.24	0.09 ± 0.04	
Expected TtbarV events	0.08 ± 0.08	0.06 ± 0.03	
Expected SingleTop events	$0.72^{+0.77}_{-0.72}$	0.00 ± 0.00	
Expected Diboson events	0.00 ± 0.00	0.00 ± 0.00	
Expected Multijets events	0.04 ± 0.02	0.00 ± 0.00	
$(m_{\tilde{t}} = 300, m_{\tilde{\chi}^0} = 127) \text{ GeV}$	0.80 ± 0.57	0.55 ± 0.39	
$(m_{\tilde{t}} = 400, m_{\tilde{\chi}^0} = 227) \text{ GeV}$	8.95 ± 0.86	0.43 ± 0.17	
$(m_{\tilde{t}} = 500, m_{\tilde{\chi}^0} = 327) \text{ GeV}$	10.53 ± 0.68	1.19 ± 0.22	

Distributions of kinematic variables in the signal region are shown in Figure 11.13 and 11.14.

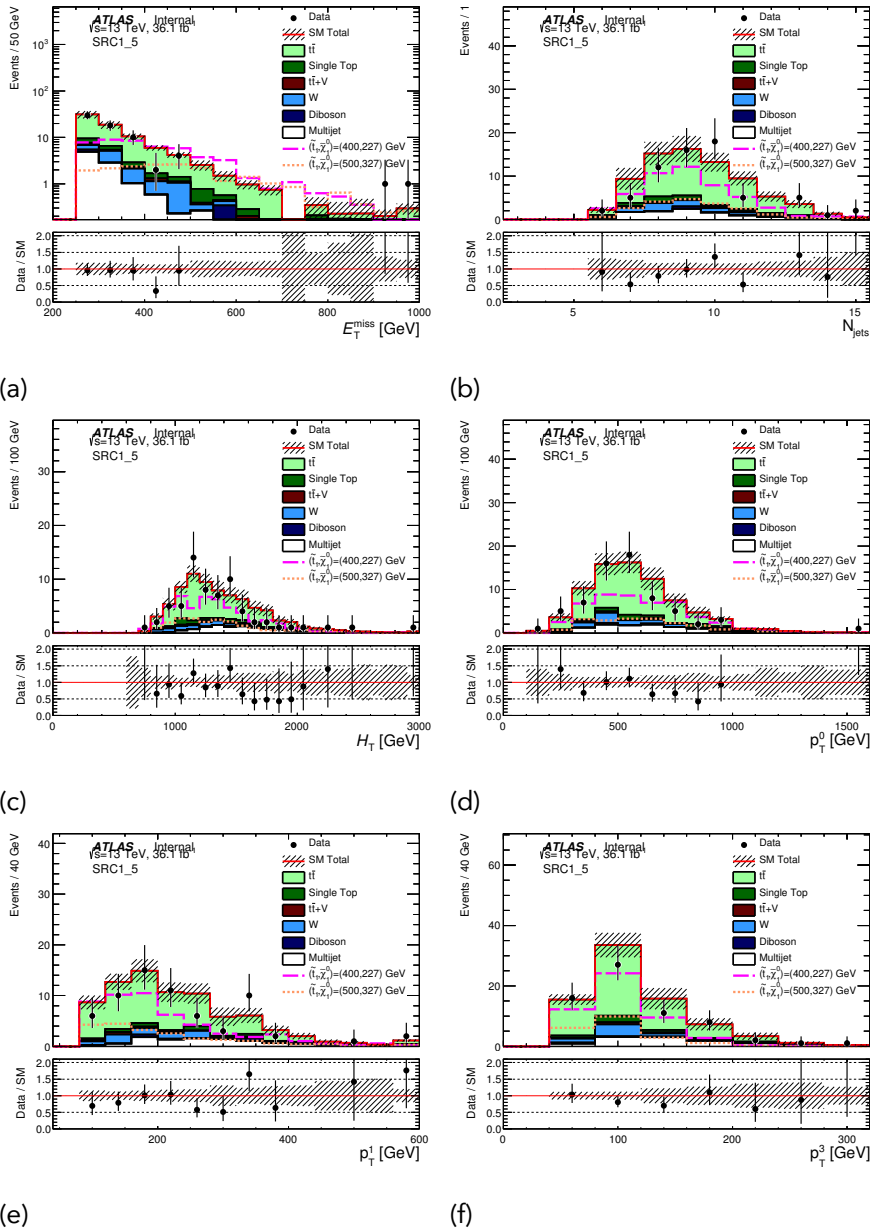


Figure 11.13: Distributions of kinematic variable after the signal region selection; (a) $E_{\text{miss}}^{\text{miss}}$ (b) number of jets (c) H_T (d) p_T of the highest p_T jet (e) p_T of the 2nd highest p_T jet (f) p_T of the 4th highest p_T jet. The solid stacked histogram represents the expected SM background rates. The dashed histogram represent the expected number of signal events for $m_{\tilde{t}} = 400, 500$ GeV. The hashed bars represent the size of the systematic uncertainty on the background. The data/MC ratio is shown in the lower panel.

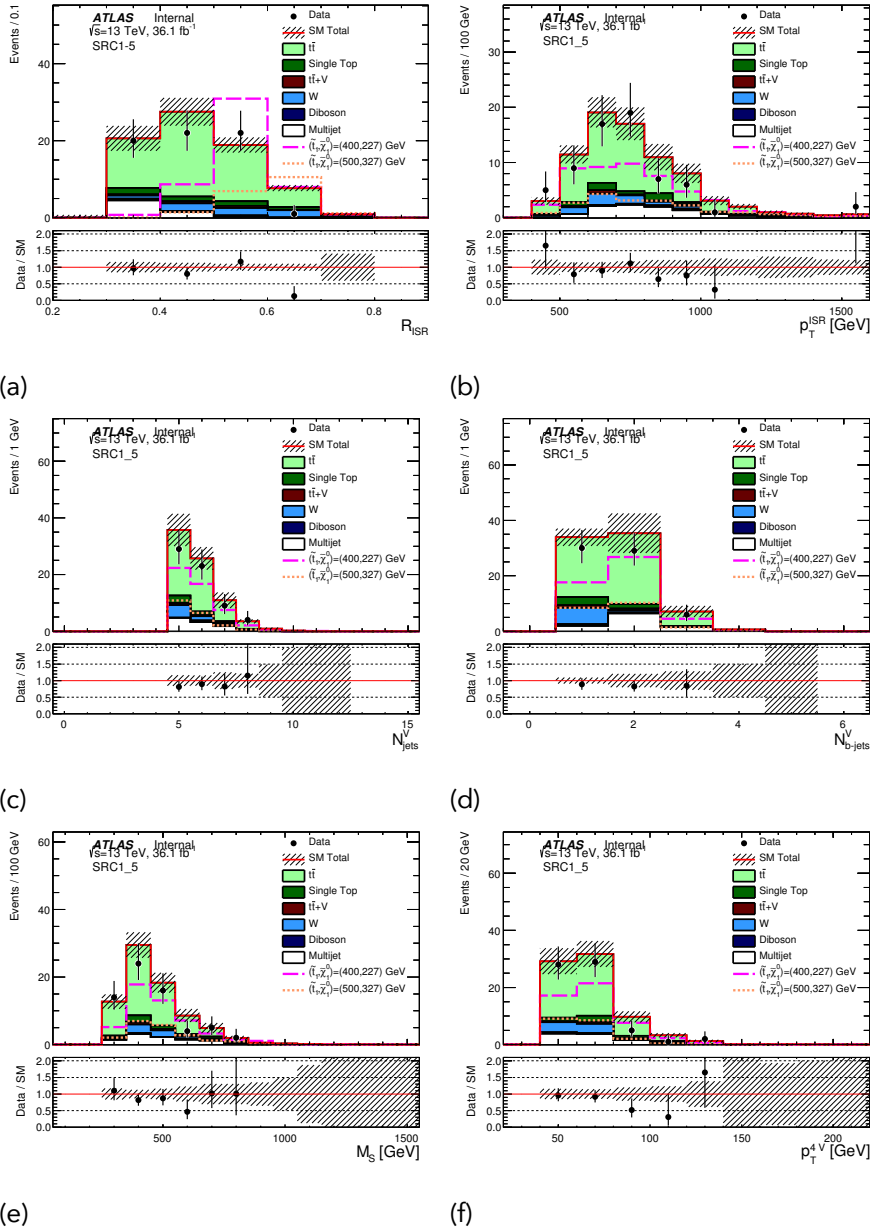


Figure 11.14: Distributions of Recursive Jigsaw kinematic variable after the signal region selection; (a) R_{ISR} (b) p_T^{ISR} (c) N_{jet}^S (d) $N_{b-\text{jet}}^S$ (e) m_T^S (f) $p_T^{4,S}$. The solid stacked histogram represents the expected SM background rates. The dashed histogram represent the expected number of signal events for $m_{\tilde{t}} = 400, 500 \text{ GeV}$. The hashed bars represent the size of the systematic uncertainty on the background. The data/MC ratio is shown in the lower panel.

12

Standard Model Backgrounds

12.1 Signal Region Background Composition

The dominant background in all signal region bins is SM $t\bar{t}$, accounting for 70 percent of all backgrounds in the signal region. The next most prevalent background is W+jets, which accounts for 9% of all signal region backgrounds but can reach up to 24% percent in high R_{ISR} bins. The breakdown of background composition is given

in Table 12.1.

Table 12.1: Standard Model background composition in the signal region. The signal region selections are defined in Table 11.1.

R_{ISR} Range	0.3-0.4	0.4-0.5	0.5-0.6	0.6-0.7	0.7-0.8
$t\bar{t}$	61%	78%	74%	60%	64%
$W+\text{jets}$	4%	7%	10%	24%	21%
$Z+\text{jets}$	2%	3%	4%	6%	9%
Single top	2%	4%	6%	9%	6%
$t\bar{t} + W/Z$	1%	2%	3%	1%	0%
QCD	22%	5%	2%	0%	0%
dibosons	8%	1%	1%	0%	0%

12.2 Using Control and Validation Regions to Estimate Background in the Signal Region

We use both data and MC based background estimation techniques for estimating background rates in the signal region. A common partially data driven technique directly measures the amount of background in kinematically similar control regions in data. Once we know the background rates in the control region in data, we can then extrapolate to the signal region using MC predictions.

We determined the background rate through a combined fit to all control and signal regions when setting limits or calculating discovery significances. The back-

ground rate will be mainly constrained by the control regions because the control regions have significantly higher statistics than the signal region.

We also perform a fit to only the control regions to estimate the background rates. The fit, called a background only fit, extracts normalization factors for backgrounds by simultaneously fitting all control regions but not the signal region. The normalization factors are then applied to the expected background rates in the signal region. The fitted background rates may differ from the rate given by the combined fit to both signal and control regions. However the predicted rates from the different fits should be similar because the control regions are designed to have a much higher constraining power on background than the signal region. A more detailed explanation of the control regions, signal region and fitting procedures are covered in the statistical analysis chapter 13.

We use control regions to estimate the dominant $t\bar{t}$ background and subdominant $W+jet$, single top, and tV backgrounds. A detailed explanation of the $t\bar{t}$ background kinematics and estimation techniques can be found in section 12.3.

$Z+jets$ and dibosons contribute less than 5 percent of all backgrounds in the signal region. Therefore these backgrounds are estimated using MC alone and we apply an additional 50 percent theory uncertainty to these two samples. Finally QCD multijet background is estimated using the Jet Smearing method described in section 12.4.6. Details on the treatment of each subdominant background can be found in section 12.4.

12.3 Dominant Background: Standard Model $t\bar{t}$

The dominant background in this analysis is SM $t\bar{t}$. After signal selection $t\bar{t}$ still accounts for 60 – 80% of the background depending on R_{ISR} range. This section covers in detail the properties and treatment of SM $t\bar{t}$ in this analysis. The section 12.3.1 demonstrates that there exist two kinematically distinct populations of SM $t\bar{t}$, each with unique characteristics and observables. Section 12.3.2 describes how we are able to directly measure the amount of $t\bar{t}$ in the signal region using a one-lepton control region.

12.3.1 Two Kinematically Distinct Populations of $t\bar{t}$

The $t\bar{t}$ production and decay is shown in Figure 12.1. Each top decays to a W boson and b quark and then in turn the W can decay into two quarks or a lepton and a neutrino. Depending on the number of leptons produced in the two W boson decays, the $t\bar{t}$ decay channels are referred to as the zero-lepton, the single-lepton, or the dilepton channels. The zero-lepton decay channel is also called the all-hadronic decay channel because all $t\bar{t}$ decay products are quarks in this channel.

The decay channels that produce leptons are further categorized by the type of lepton produced. For example, the single tau $t\bar{t}$ decay channel has one W that decays leptonically to a tau and a neutrino and the second W decays hadronically into two quarks. The single muon decay channel has one W that decays leptonically to a

muon and a neutrino and the second W decays hadronically into two quarks.

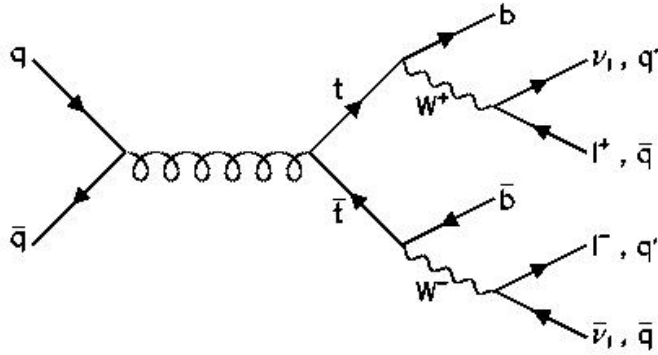


Figure 12.1: The Feynman diagram for the $pp \rightarrow t\bar{t} \rightarrow W^+ b + W^- \bar{b} \rightarrow ffb + ffb$ process. The $t\bar{t}$ decay channels are classified according to the number and type of leptons produced. The different decay channels are referred to as the zero-lepton, the single-lepton, or the dilepton channels. The zero-lepton decay channel is also called the all-hadronic decay channel because all $t\bar{t}$ decay products are quarks. Decay channels that also produce leptons are further separated by the types of lepton produced. For example, the single tau $t\bar{t}$ decay channel has one W that decays leptonically to a tau and a neutrino and the second W decays hadronically into two quarks.

After the zero-lepton preselection, $\sim 80\%$ of $t\bar{t}$ events decay via the single tau channel. $\sim 15\%$ of $t\bar{t}$ events decay via the single electron or single muon channels. The electron and muon either doesn't pass the p_T selection or the lepton is removed because it is too close to another jet or is misreconstructed as a jet. The final $\sim 5\%$ are due to dileptonic decays. Fully hadronic $t\bar{t}$ is negligible after signal region selections because fully hadronic $t\bar{t}$ produces little intrinsic E_T^{miss} .

The $E_T^{\text{miss}} > 250$ GeV requirement in preselection selects for $t\bar{t}$ with a boosted leptonic top. A top at rest simply does not have enough energy to produce a neutrino with 250 GeV of p_T . The leptonic top can gain boost mainly through one of two

ways. Either the leptonic top recoils in a back-to-back fashion against the hadronic top or both tops can recoil against strong ISR.

In both situations the thrust axis, the axis of maximum back-to-back p_T , contains important information. In the case where the leptonic top is recoiling against the hadronic top, the thrust axis lines up along the two tops' axis of back-to-back boost. In the case where both tops are boosted by strong ISR, the thrust axis approximates the $t\bar{t}$ and ISR axis of back-to-back recoil. An artistic representation of the role of the thrust axis in each $t\bar{t}$ population can be seen in Figure 12.2.

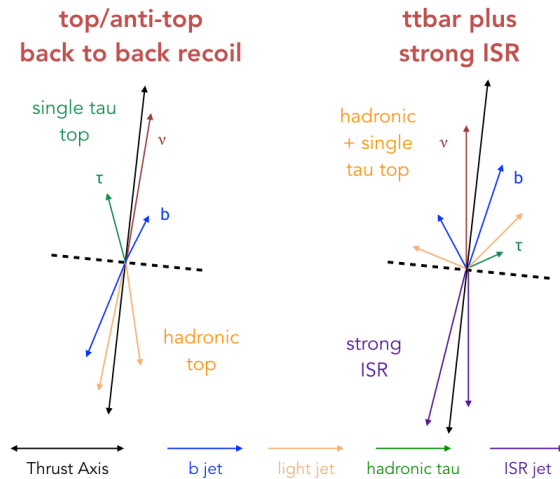


Figure 12.2: Schematic depiction of the $t\bar{t}$ back-to-back $t\bar{t}$ population and the $t\bar{t}$ +hard ISR population after the zero-lepton preselection. The two example events' thrust axes are aligned. The hemisphere containing E_T^{miss} has significantly higher jet multiplicities and total energy in $t\bar{t}$ +hard ISR events.

Only the leptonic top is boosted towards the same hemisphere as the E_T^{miss} when the top and anti-top are back-to-back to one another. In comparison, both tops are

boosted towards the hemisphere containing E_T^{miss} in the $t\bar{t}$ with strong ISR. Therefore the $t\bar{t}$ +hard ISR population has a much higher jet multiplicity and total energy in the E_T^{miss} hemisphere. Hence, we can use observables such as N_{jet}^S and m_T^S to distinguish $t\bar{t}$ plus large ISR events from $t\bar{t}$ back-to-back recoil events.

12.3.2 Predicting the amount of $t\bar{t}$ in Signal Region using a One-Lepton Control Region

The stop signal is expected to have higher jet multiplicities and total energy in the hemisphere containing E_T^{miss} than both $t\bar{t}$ populations. The stringent signal region requirements on the jet multiplicities and total energy of the sparticle hemisphere effectively eliminate the $t\bar{t}$ back-to-back $t\bar{t}$ population and also reject approximately 2/3 of the $t\bar{t}$ plus large ISR population. A detailed explanation of the signal region design and performance can be found in chapter 11.

Approximately 90% of the $t\bar{t}$ events in the signal region have at least 400 GeV of real ISR p_T . A back of the envelope calculation shows that we need around 550-600 GeV of ISR p_T to boost the $t\bar{t}$ neutrino to above 250 GeV of p_T . The neutrino must share the total $t\bar{t}$ p_T with the five other $t\bar{t}$ decay products and is not particularly efficient at absorbing ISR p_T .

Figure 12.3 shows that the true ISR p_T distribution for $t\bar{t}$ in the signal region peaks at approximately 550 GeV. In comparison, the true ISR p_T distribution after prese-

lection peaks at zero and rapidly falls with increasing ISR p_T . This demonstrates that the additional signal region requirements select mainly for $t\bar{t}$ with high ISR p_T .

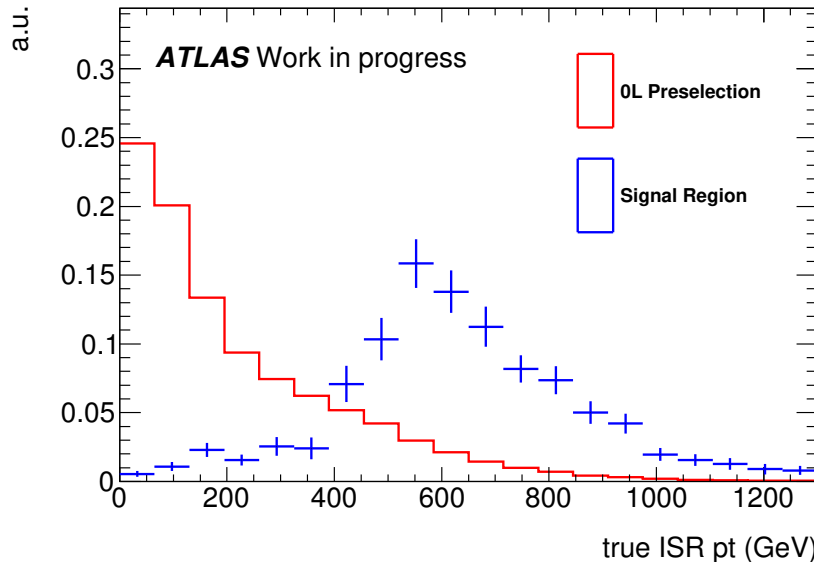


Figure 12.3: Distribution of true ISR p_T for $t\bar{t}$ after the zero-lepton preselection and after all signal region selections. Both distributions have been normalized to unit area.

A direct consequence of selecting for only high ISR $t\bar{t}$ events is that the predicted $t\bar{t}$ background rates in the signal region are directly related to the amount of ISR/FSR in the MC. The next-to-leading order (NLO) Powheg+PYTHIA6 $t\bar{t}$ MC has a $\sim 30\%$ ISR/FSR systematic uncertainty in the signal region. The ISR/FSR uncertainty would dominate the systematic uncertainty in this analysis if we relied on MC alone to predict the $t\bar{t}$ background in the signal region.

In order to decrease the ISR/FSR uncertainty, we directly measure the $t\bar{t}$ +hard ISR rate in data using a one-lepton $t\bar{t}$ control region (CRTopC). The lepton refers only to

an electron or muon in this context because they can be reconstructed with much greater purity than taus. The control region CRTopC selections are defined in Table 12.2. All variables used are defined in section 8.3.

Table 12.2: One-lepton $t\bar{t}$ control region (CRTopC) definitions. The one-lepton preselections defined in Table 10.2 are also applied.

Variable	1 lepton $t\bar{t}$ control region
1 Lepton Preselection	
N_{lep}	1
$m_T(\ell, E_T^{\text{miss}})$	$< 80 \text{ GeV}$
$\Delta R(b_{0,1}, \ell)_{\min}$	< 2.0
N_{jet}^S	≥ 5
$N_{\text{b-jet}}^S$	≥ 1
$p_T^{4,S}$	$> 40 \text{ GeV}$
p_T^{ISR}	≥ 400

In the one-lepton control region, the lepton is included as a “jet” in the Jigsaw ISR algorithm and will be counted as a sparticle jet or an ISR jet depending on which hemisphere it falls in. The lepton is meant to play the role of a hadronic tau jet in the zero-lepton signal region. This approximation is justified since $\sim 80\%$ of all $t\bar{t}$ events in the signal region decay via the hadronic tau channel.

The control region CRTopC uses similar selections on the same kinematic variables as the signal region. In this way, the control region CRTopC captures the same kinematic features as the signal region by also targeting $t\bar{t}$ with high ISR p_T . Some

signal region requirements such as the correlations on ISR and E_T^{miss} are removed to increase statistics and lower signal contamination. For example, the signal region $\Delta\phi_{\text{ISR}, E_T^{\text{miss}}} > 3.0$ requirement is removed. The $\Delta\phi_{\text{ISR}, E_T^{\text{miss}}}$ variable specifies the direction of neutrino relative to the direction of the ISR. A requirement of $\Delta\phi_{\text{ISR}, E_T^{\text{miss}}} > 3.0$ essentially selects specific alignments between the $t\bar{t}$ decay axis and the $t\bar{t}$ vs ISR boost axis. Removing this requirement opens up more phase space for $t\bar{t}$ to decay but does not change the requirement on high ISR p_T .

The $p_T^{4,S} > 50 \text{ GeV}$ requirement is relaxed to $p_T^{4,S} > 40 \text{ GeV}$ in order to increase statistics in the CR. The $p_T^{4,S}$ requirement specifies the p_T of the 4th jet in the sparticle system. The $p_T^{4,S}$ variable is correlated with amount of ISR/FSR in the MC because there is a chance that the 4th most energetic jet in the sparticle system is from radiation and not from a top decay. However it is more important to accurately gauge the amount of hard ISR of order hundred or more GeV that boosts the entire $t\bar{t}$ system than the amount of additional radiation in the same hemisphere as $t\bar{t}$. We found that loosening the $p_T^{4,S}$ requirement to 40 GeV does not result in a large difference between the control and signal regions' true ISR p_T distributions .

A $m_T(\ell, E_T^{\text{miss}})$ less than 80 GeV requirement selects events with a transverse mass that is consistent with a W boson. The $m_T(\ell, E_T^{\text{miss}})$ increases $t\bar{t}$ purity and removes signal contamination. A $\Delta R(b_{0,1}, \ell)_{\text{min}}$ less than 2.0 requirement is also added to increase $t\bar{t}$ purity and ensure orthogonality to the W+jets control region. $m_T(\ell, E_T^{\text{miss}})$ is defined in equation 12.1 and $\Delta R(b_{0,1}, \ell)_{\text{min}}$ is defined in equation 12.2.

$$m_T(\ell, E_T^{\text{miss}}) = (E_T^{\text{lep}} + E_T^{\text{miss}})^2 - (\vec{p}_T^{\text{lep}} + \vec{E}_T^{\text{miss}})^2 = m_{\text{lep}}^2 + 2(E_T^{\text{lep}} E_T^{\text{miss}} - \vec{p}_T^{\text{lep}} \cdot \vec{E}_T^{\text{miss}}) \quad (12.1)$$

$$\Delta R(b_{0,1}, \ell)_{\min} = \min_{\text{jets with two highest } b\text{-tagging values}} \sqrt{\Delta\eta(b\text{jet}, \text{lep})^2 + \Delta\phi(b\text{jet}, \text{lep})^2} \quad (12.2)$$

Figure 12.4 shows the true ISR p_T distribution for $t\bar{t}$ in the control region and the signal region. Both distributions peak at roughly 550 GeV and have similar shapes. We use the one-lepton control region to measure the amount of $t\bar{t}$ plus high ISR p_T events using data. By normalizing $t\bar{t}$ background rates to the control region, we are able to limit the ISR/FSR uncertainty to below 10% for all R_{ISR} regions.

The similar kinematic selection between the control region CRTopC and the signal region cancels many systematic uncertainties. For example, the 6% uncertainty on jet energy resolution is partial due to the similar jet p_T requirements between the control region and the signal region. A more detailed discussion of systematics can be found in chapter 14

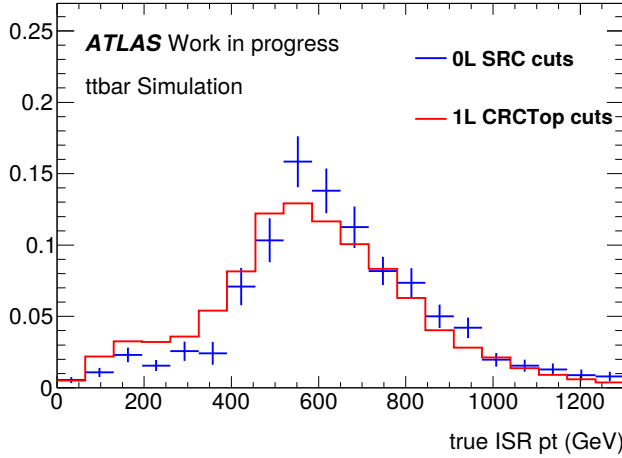


Figure 12.4: The true ISR p_T distribution for $t\bar{t}$ events after signal region and $t\bar{t}$ control region (CRCTopC) selections. Both control and signal region distributions peak at roughly 550 GeV demonstrating that the one-lepton control region and the zero-lepton signal region select for the same $t\bar{t}$ +hard ISR events. Therefore, the one-lepton control region is able to directly measure the amount of $t\bar{t}$ with high ISR p_T directly from data. This lets us predict the $t\bar{t}$ background rate in the signal region with minimal extrapolation between the control region and the signal region.

Control Region CRCTopC Signal Contamination

The control regions are designed to have low expected signal rates. If stop events are present in the control region then they can be misinterpreted as additional SM background. In this way, a high expected signal rate in the control region decreases signal sensitivity. The fractional signal contamination can be quantified as the signal over background (S/B) ratio in the control region.

Signal contamination in the control region CRCTopC ranges from 1% at high stop masses to 12% at low stop masses for all stop masses that we are sensitive to and are not already excluded by previous stop experiments.

The largest signal contamination occurs at a stop mass of 225 to 250 GeV. Here, the signal contamination approaches 12% due to the large stop production cross section. Lower stop masses result in higher signal contamination but our search does not have sensitivity to regions below 225 GeV.

The fact that the control region CRTopC can attain such low signal contamination while selecting for $t\bar{t}$ background with similar kinematic features to the signal region is impressive. The signal region has a S/B ratio of approximately 2.1 for stop masses between 250 GeV and 400 GeV. In comparison, the control region CRTopC is able to achieve the fractional signal contamination of around 5 to 12% for the same stop masses.

The control region CRCTop has a factor of 20-40 lower S/B ratio when compared to the signal region because of mainly two reasons. First, the CRCTop is a one-lepton region while the signal region is a zero-lepton region.

The signal region primarily selects for stops that decay fully hadronically with a $\sim 44\%$ branching fraction. However, the $t\bar{t}$ background in the signal region mainly decays via the single hadronic tau decay channel with only a 10% decay fraction. The signal region therefore gains a factor of 5 in S/B ratio because of the difference in stop and $t\bar{t}$ branching fractions.

Meanwhile, the one-lepton control region primarily selects events that decay via the single muon and single electron decay channels in both stop signal and $t\bar{t}$ background. Signal and background therefore has similar decay fractions in the control

region CRTopC. This means the control region CRTopC has a factor of 5 less S/B ratio than the signal region simply because of branching fractions.

The signal region also gains in S/B ratio by requiring strong correlations between the ISR system and E_T^{miss} . The signal region separates the signal and background into 5 bins in R_{ISR} . This targets the signal's peak in R_{ISR} . In contrast, the control region CRTopC does not have separate R_{ISR} bins. Integrating over all R_{ISR} instead of specifically targeting the bins under the signal region peak decreases the S/B ratio by a factor of 2-5 depending on the stop mass and location of the signal R_{ISR} peak.

At the same time, removing the $\Delta\phi_{\text{ISR}, E_T^{\text{miss}}} > 3.0$ requirement in the control region decreases the S/B ratio by another factor of 3. Removing the requirements on the ISR and E_T^{miss} correlations open up more phase space but do not change the requirement on strong $t\bar{t}$ ISR p_T .

These factors combine to make up the factor of ~ 40 decrease in the S/B ratio between the signal region and the control region CRTopC; all the while preserving the agreement in the true $t\bar{t}$ ISR p_T distribution shown in Figure 12.4.

$t\bar{t}$ Control Region Yields and Distributions

Distribution of important variables after a background-only fit to 36.07 fb^{-1} of data are shown for the control region CRTopC in Figure 12.5 and 12.6. There is a noticeable trend in the data over MC comparison in the CRTopC p_T^{ISR} distribution. The disagreement is not surprising given that a priori we have a 30% uncertainty due to the

ISR/FSR uncertainty. This further demonstrates the need for a control region that directly measures the amount of $t\bar{t}$ with strong ISR using data.

The fitted normalization scale factor for $t\bar{t}$ is 0.707. This scale factor is quite different from 1.0 which indicates that the $t\bar{t}$ MC does a poor job of modeling the high ISR p_T phase space. Again, this difference is not unexpected given the 30% ISR/FSR uncertainty on $t\bar{t}$ MC in this high ISR p_T region.

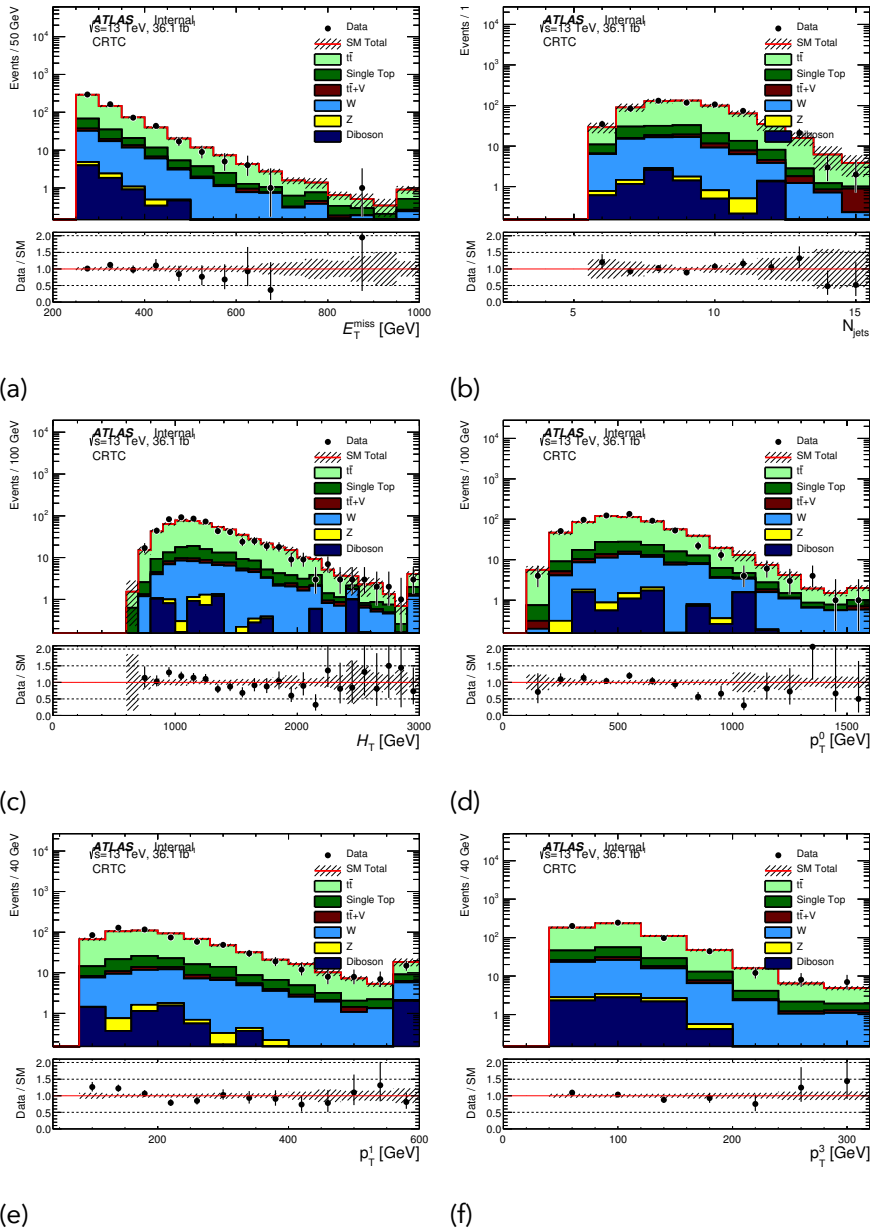


Figure 12.5: One-lepton $t\bar{t}$ control region (CRCTop) distributions for 36.07 fb^{-1} of data. The kinematic variables shown include (a) $E_{\text{T}}^{\text{miss}}$ (b) number of jets (c) H_{T} (d) p_{T} of the highest p_{T} jet (e) p_{T} of the 2nd highest p_{T} jet (f) p_{T} of the 4th highest p_{T} jet.

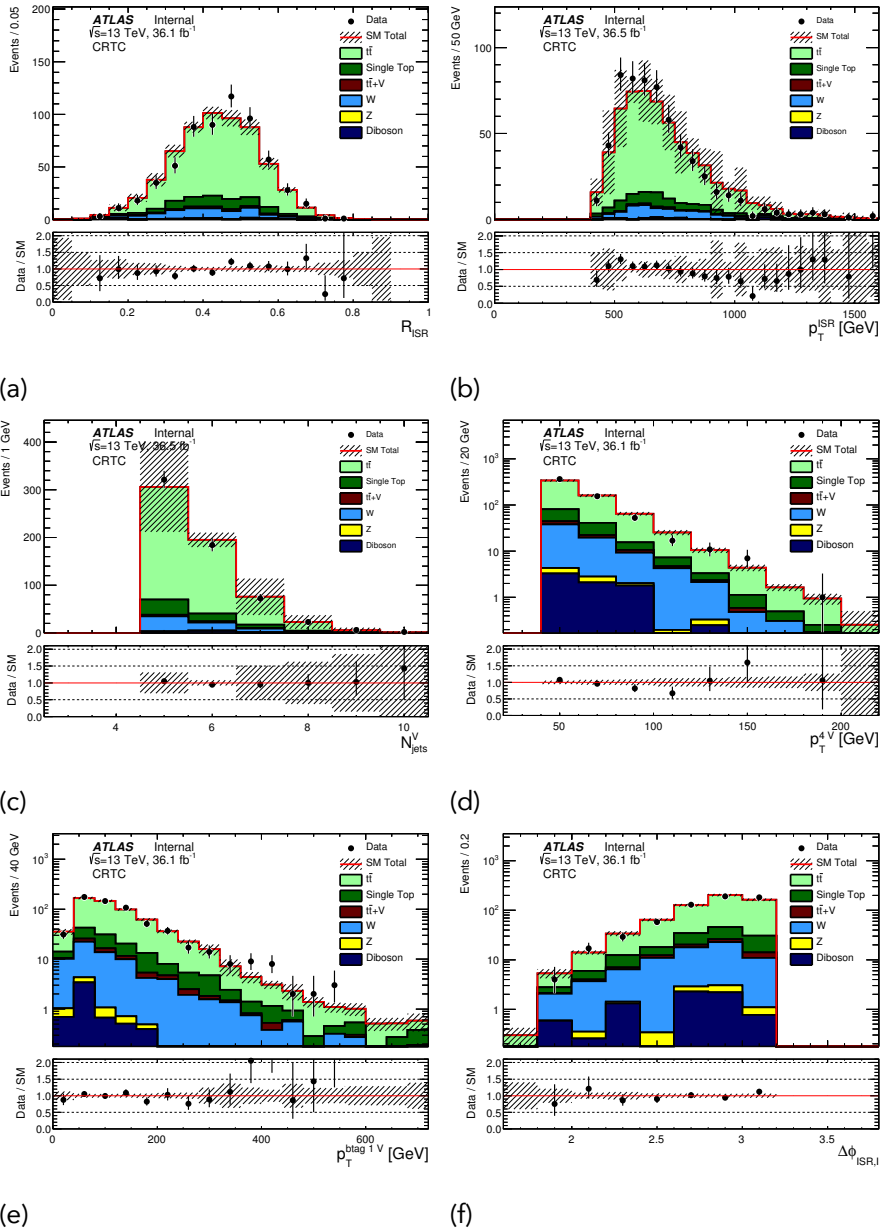


Figure 12.6: One-lepton $t\bar{t}$ control region (CRCTop) distributions for 36.07 fb^{-1} of data. The kinematic variables shown include (a) R_{ISR} (b) p_T^{ISR} (c) N_{jet}^S (d) $p_T^{4,S}$ (e) $p_T^{0,S}$ (f) $\Delta\phi_{\text{ISR}, E_T^{\text{miss}}}$.

There seems to be no significant slope in the data over MC comparison in the

CRCTop $p_T^{4,S}$ distribution. This is further evidence that the extrapolation from 40 to 50 GeV across $p_T^{4,S}$ is allowed. No strong trends outside of statistical and systematic uncertainties are observed for any other distributions.

The control region CRTopC yields from before and after the background-only fit can be found in Table 12.3.

Table 12.3: CRTopC MC Yield and background-only fit results for 36.07 fb^{-1} of data. MC exp. events are expected background rates directly from MC predictions. Fitted background event rates are the expected background rates after normalizing the MC to data by simultaneously fitting all control regions using a background only fit. The fitted $t\bar{t}$ normalization scale factor is equal to (Fitted $t\bar{t}$ events)/(MC exp. $t\bar{t}$ events). The quoted uncertainties include statistical and systematic uncertainties.

Yields	CRTopC
Observed data events	611
Fitted SM bkg events	610.96 ± 24.72
Fitted $t\bar{t}$ events	461.47 ± 31.85
Fitted Wjets events	64.94 ± 12.12
Fitted Zjets events	2.15 ± 0.90
Fitted TtbarV events	11.32 ± 2.19
Fitted SingleTop events	63.49 ± 20.36
Fitted Diboson events	7.58 ± 2.84
Fitted Multijets events	0.00 ± 0.00
MC exp. SM events	777.01 ± 14.91
MC exp. $t\bar{t}$ events	652.93 ± 7.35
MC exp. Wjets events	51.34 ± 6.02
MC exp. Zjets events	1.84 ± 0.58
MC exp. TtbarV events	8.78 ± 0.90
MC exp. SingleTop events	54.53 ± 5.03
MC exp. Diboson events	7.58 ± 2.87
MC exp. Multijets events	0.00 ± 0.00
Fitted $t\bar{t}$ normalization scale factor	0.707 ± 0.050

12.3.3 Validating $t\bar{t}$ Predictions in Signal Region using a Zero-Lepton Validation Region

We also define a zero-lepton $t\bar{t}$ validation region to validate the predicted background rates in the signal region. The $t\bar{t}$ validation region (VRTopC) is kinematically similar but completely orthogonal to the signal region. In addition, the validation region must have limited signal contamination and high $t\bar{t}$ purity.

The $\Delta\phi_{\text{ISR}, E_T^{\text{miss}}} > 3.0$ selection in the signal region is inverted in the validation region to limit signal contamination. In signal, the neutralinos and the ISR tend to be back-to-back in ϕ . The neutralinos gain most of their momenta by recoiling against ISR and the correlation is strong.

In contrast, $\Delta\phi_{\text{ISR}, E_T^{\text{miss}}}$ has a different physical interpretation in SM $t\bar{t}$ events. In $t\bar{t}$ events, $\Delta\phi_{\text{ISR}, E_T^{\text{miss}}}$ specifies the neutrino direction relative to the direction of the ISR. Inverting the $\Delta\phi_{\text{ISR}, E_T^{\text{miss}}}$ selection selects for $t\bar{t}$ events with a different decay axis relative to $t\bar{t}$ vs ISR boost axis but does not change the requirements on strong ISR p_T .

For this reason, the $\Delta\phi_{\text{ISR}, E_T^{\text{miss}}} < 3.0$ requirement in the validation region rejects $\sim 50\%$ of signal events while retaining $\sim 80\%$ of background.

The requirement on m_T^S is reduced in the validation region to 100 GeV (vs. 300 GeV in the signal) and the N_{jet}^S selection is relaxed to ≥ 4 (vs. $N_{\text{jet}}^S \geq 5$ in the signal region). Relaxing both requirements enhances the background yields in the valida-

tion region.

Similar to the control region CRTopC, the $p_T^{4,S} > 50$ GeV selection is also relaxed to $p_T^{4,S} > 40$ GeV to increase the validation region statistics.

Finally, a requirement of $m_V/m_T^S < 0.6$ is added to reduce signal contamination and reject QCD multijet background.

Table 12.4: Zero-lepton $t\bar{t}$ +ISR validation region definitions, in addition to the zero lepton preselection requirements listed in Table 10.1.

Variable	0 lepton $t\bar{t}$ validation region
N_{jet}^S	≥ 4
$N_{\text{b-jet}}^S$	≥ 1
$p_{T,b}^{0,S}$	≥ 40
p_T^{ISR}	≥ 400
m_T^S	> 100 GeV
m_V/m_T^S	< 0.6
$\Delta\phi_{\text{ISR}, E_T^{\text{miss}}}$	< 3.00

The distributions of select variables in VRTopC are shown in Figure 12.7 and 12.8. The background rates have been normalized to control regions through the use of a background-only fit to 36.07 fb^{-1} of data.

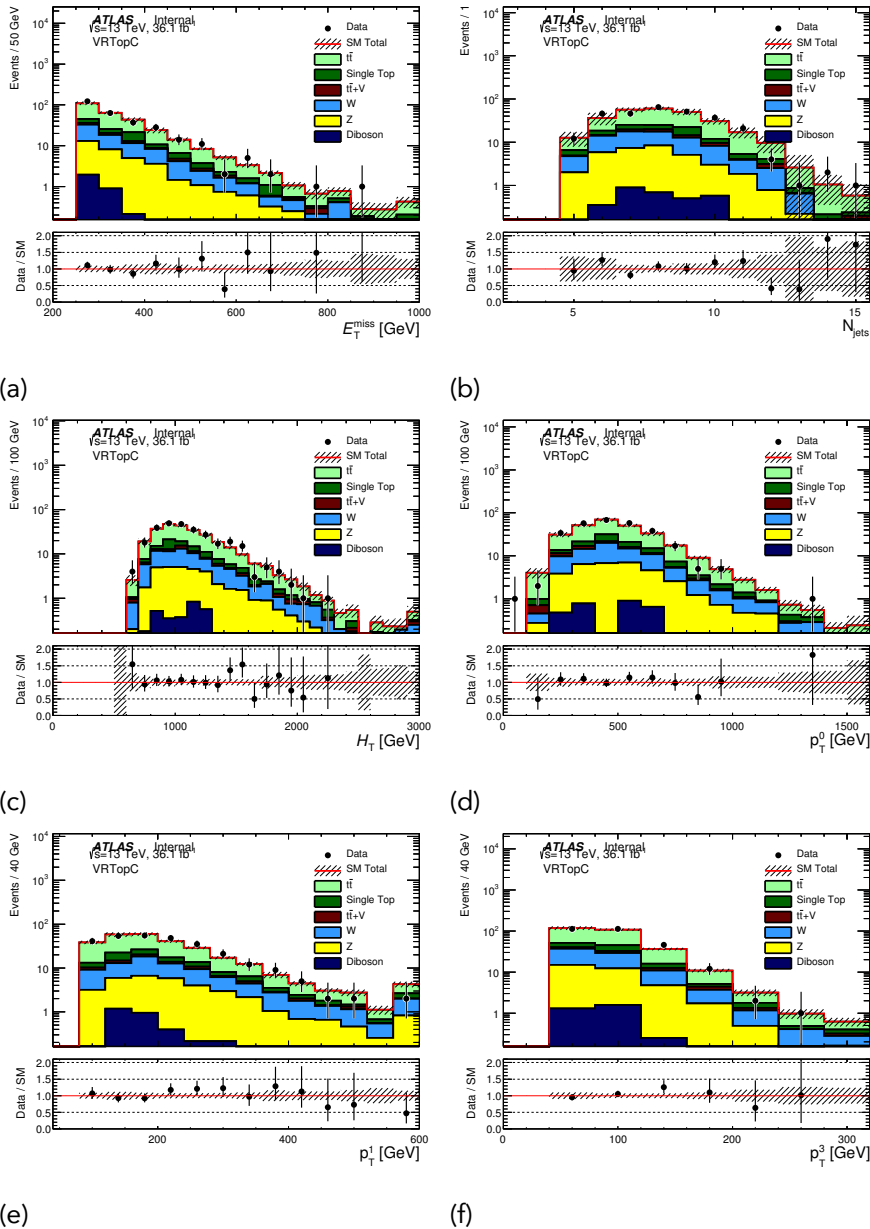


Figure 12.7: Distribution of select variables in the zero-lepton $t\bar{t}$ validation region. The kinematic variables shown include (a) E_T^{miss} (b) number of jets (c) H_T (d) p_T of the highest p_T jet (e) p_T of the 2nd highest p_T jet (f) p_T of the 4th highest p_T jet.

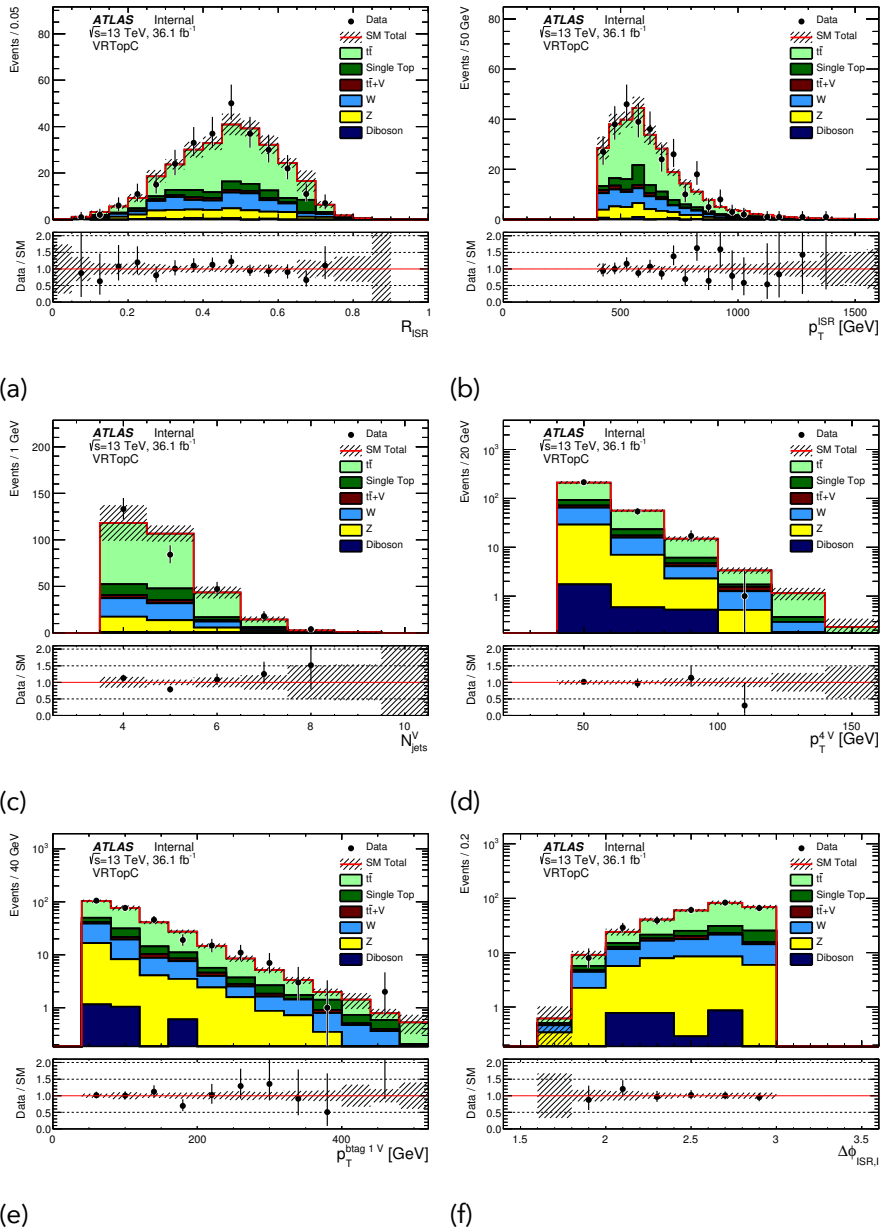


Figure 12.8: Distribution of select variables in the zero-lepton $t\bar{t}$ validation region. The kinematic variables shown include (a) R_{ISR} (b) p_T^{ISR} (c) N_{jet}^S (d) $p_T^{4,S}$ (e) $p_T^{0,S}$ (f) $\Delta\phi_{ISR, E_T^{\text{miss}}}$.

The predicted background rate in the VRTopC agrees with data to within 1σ . This

demonstrates that the control region CRTopC is an effective predictor of $t\bar{t}$ background rates in the validation region and the signal region. The R_{ISR} shape is well modeled as we see no distinct trends in the data vs MC ratio in R_{ISR} .

Similar to the control region CRTopC, there is a noticeable trend in the data over MC comparison in the VRTopC p_T^{ISR} distribution. Again this is expected because the MC has a $\sim 30\%$ ISR/FSR uncertainties in the high ISR p_T region and is a poor predictor of ISR p_T rates.

The MC and data yields in VRTopC is given in Table 12.5. The background MCs have already been normalized to their respective control regions using a background-only fit. The validation region has the 0.707 ± 0.050 $t\bar{t}$ normalization scale factor applied to its expected $t\bar{t}$ MC rates. The fact that data in VRTopC agrees with the post-fit predicted background rate is evidence that the control region CRTopC can predict the background rate in the signal region.

12.4 Subdominant Backgrounds

12.4.1 Standard Model W+Jets

A W boson produced in conjunction with QCD jets (W +jets) is our largest subdominant background. W +jets comprises 9% of the total background in the signal region. However the distribution of W +jets is not uniform across R_{ISR} . W +jets can reach 20-25% of all backgrounds in signal region bins with the largest R_{ISR} . This means the

Table 12.5: VRTopC expected background and data yields with 36.07 fb^{-1} of data. MC exp. events are expected background rates directly from MC predictions. Fitted background events correspond to the expected background rates after simultaneously fitting all control regions using a background only fit. The backgrounds are normalized to the data in control regions and the fitted $t\bar{t}$ normalization scale factor derived from the fit is 0.707 ± 0.050 . The fitted normalization scale factors are then applied to the expected MC yields giving the fitted expected background rate. The agreement between the fitted expected background yield and data in VRTopC is evidence that CRTopC is correctly measuring the amount of $t\bar{t}$ with high ISR p_T . The quoted uncertainties include statistical and systematic uncertainties.

VRTop yields	VRTopC
Observed events	286
Fitted bkg events	289.20 ± 34.10
Fitted TTbar events	162.19 ± 18.77
Fitted Wjets events	47.37 ± 10.17
Fitted Zjets events	36.13 ± 10.26
Fitted TtbarV events	8.89 ± 1.68
Fitted SingleTop events	$28.67^{+30.30}_{-28.67}$
Fitted Diboson events	3.00 ± 1.86
Fitted Multijets events	2.96 ± 2.33
MC exp. SM events	335.18 ± 31.37
MC exp. TTbar events	229.37 ± 19.56
MC exp. Wjets events	37.46 ± 5.92
MC exp. Zjets events	30.88 ± 4.18
MC exp. TtbarV events	6.90 ± 1.16
MC exp. SingleTop events	24.60 ± 24.60
MC exp. Diboson events	3.01 ± 1.88
MC exp. Multijets events	2.96 ± 2.33
Fitted $t\bar{t}$ normalization scale factor	0.707 ± 0.050

$W+jets$ contribution mostly affects high stop mass samples because those signal samples peak at high R_{ISR} .

We estimate $W+jets$ using an one-lepton control region defined in Table 12.6.

The one-lepton W +jet control region is designed to ensure high W +jet purity. All one-lepton control regions are mutually exclusive including the $t\bar{t}$, W +jets and single-top control region.

Table 12.6: Summary of the selections for the one-lepton W +jets control region. The one-lepton preselections defined in Table 10.2 are also applied.

Variables	W +jets control region
Number of leptons	1
Number of jets (incl. lepton)	≥ 4
p_T of jets (incl. lepton)	(80,80,40,40) GeV
$\min \left \Delta\phi \left(\text{jet}^{0-1}, E_T^{\text{miss}} \right) \right $	> 0.4
E_T^{miss}	> 250 GeV
$m_T(\ell, E_T^{\text{miss}})$	($> 30, < 100$ GeV)
Number of b -jets	= 1
$m_{\text{jet}, R=1.2}^0$	< 60 GeV
$\Delta R(b_{0,1}, \ell)_{\text{min}}$	> 2.0

The lepton is treated as a jet for the jet multiplicity and the jet p_T requirements.

Similar to the one-lepton $t\bar{t}$ control region, the lepton is meant to play the role of a hadronic tau jet in the zero-lepton signal region.

$m_T(\ell, E_T^{\text{miss}})$ is defined in equation 12.1 as the transverse mass of the lepton and the E_T^{miss} . The $m_T(\ell, E_T^{\text{miss}})$ selection ensures that the transverse mass is consistent with those originating from a W boson.

Orthogonality between the W +jet control region and the single-top control region is ensured by the requirement on the number of b -jets. Orthogonality between $t\bar{t}$ control region and W +jet control region is ensured by the selection on $\Delta R(b_{0,1}, \ell)_{\text{min}}$.

$\Delta R(b_{0,1}, \ell)_{\min}$ is defined in equation 12.2 as the minimum ΔR between the two jets with the highest b-tag value and the selected lepton.

$m_{\text{jet}, R=1.2}^0$ is defined as the mass of an $\text{anti}-k_t$ jet built with a distance parameter of $R = 1.2$ instead of regular $R = 0.4$. The $\text{anti}-k_t$ algorithm clusters calorimeter energy into a jet according to the distance metric R and is covered in detail in section 4.3.1. The $\text{anti}-k_t$ algorithm will form a perfectly conical jet of radius R if no other hard objects are found within a cone of $2R$. If two hard objects exist within $R < \Delta R < 2R$ of one another then two jets will be formed splitting the energy cells between them.

The large $R=1.2$ jet is designed to cluster all the energy of a boosted top quark into a single jet. If the jet contains a boosted top, the invariant mass of jet should be close to $\sim m_t$. The $m_{\text{jet}, R=1.2}^0 < 60$ GeV is designed to reject events with boosted top quarks.

Distributions of select kinematic variables in the $W + \text{jets}$ control region are shown in Figure 12.9 and 12.10. The MC background has been normalized to data by performing a simultaneous fit to all control regions. The hashed bands on the total SM background correspond to the total experimental systematical uncertainty plus the MC statistical uncertainty. The yield in the $W + \text{jets}$ control region is given in Table 12.7.

The fitted $W+\text{jets}$ normalization scale factor is 1.27 ± 0.15 . Data and MC are compatible to within statistical uncertainty. No strong trends are observed in the data to

MC ratios in any of the distributions.

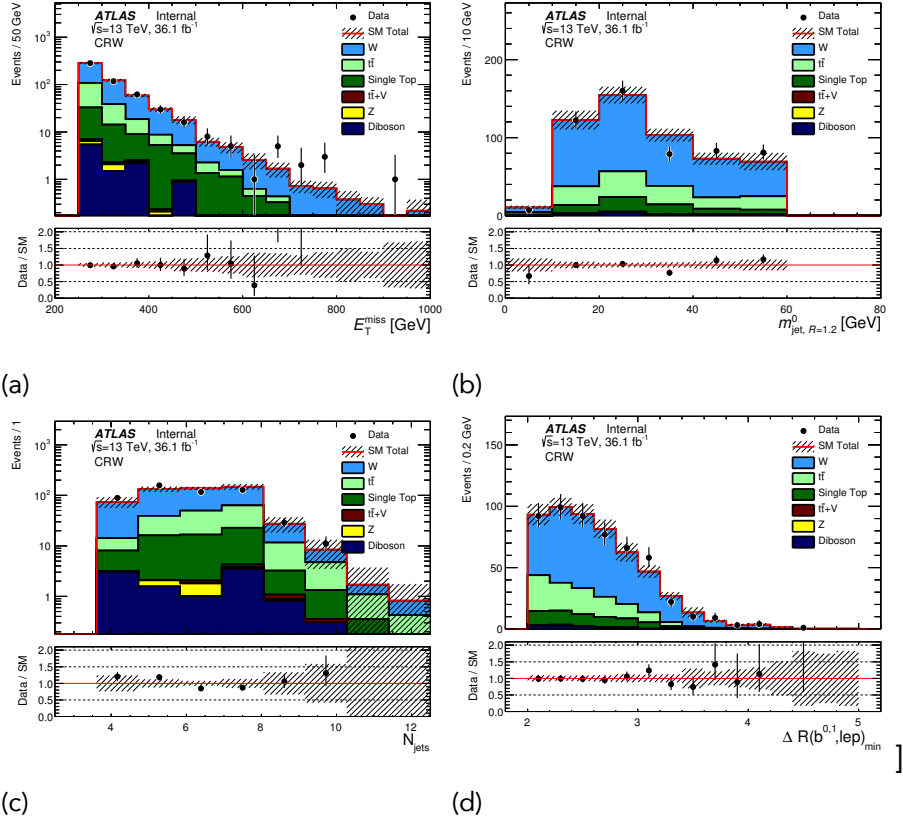


Figure 12.9: Kinematic distributions in the $W + \text{jets}$ control region after the background only fit to 36.07 fb^{-1} of data. From left to right and top to bottom, the variables shown are E_T^{miss} , $m_T(\ell, E_T^{\text{miss}})$, $m_{\text{jet}, R=1.2}^0$ and the number of jets and $\Delta R(b_{0,1}, \ell)_{\min}$. The expected SM background has been normalized to the data by performing a simultaneous fit to all control regions. The hatched band on the total SM background corresponds to the total experimental systematic uncertainty plus the MC statistical uncertainty.

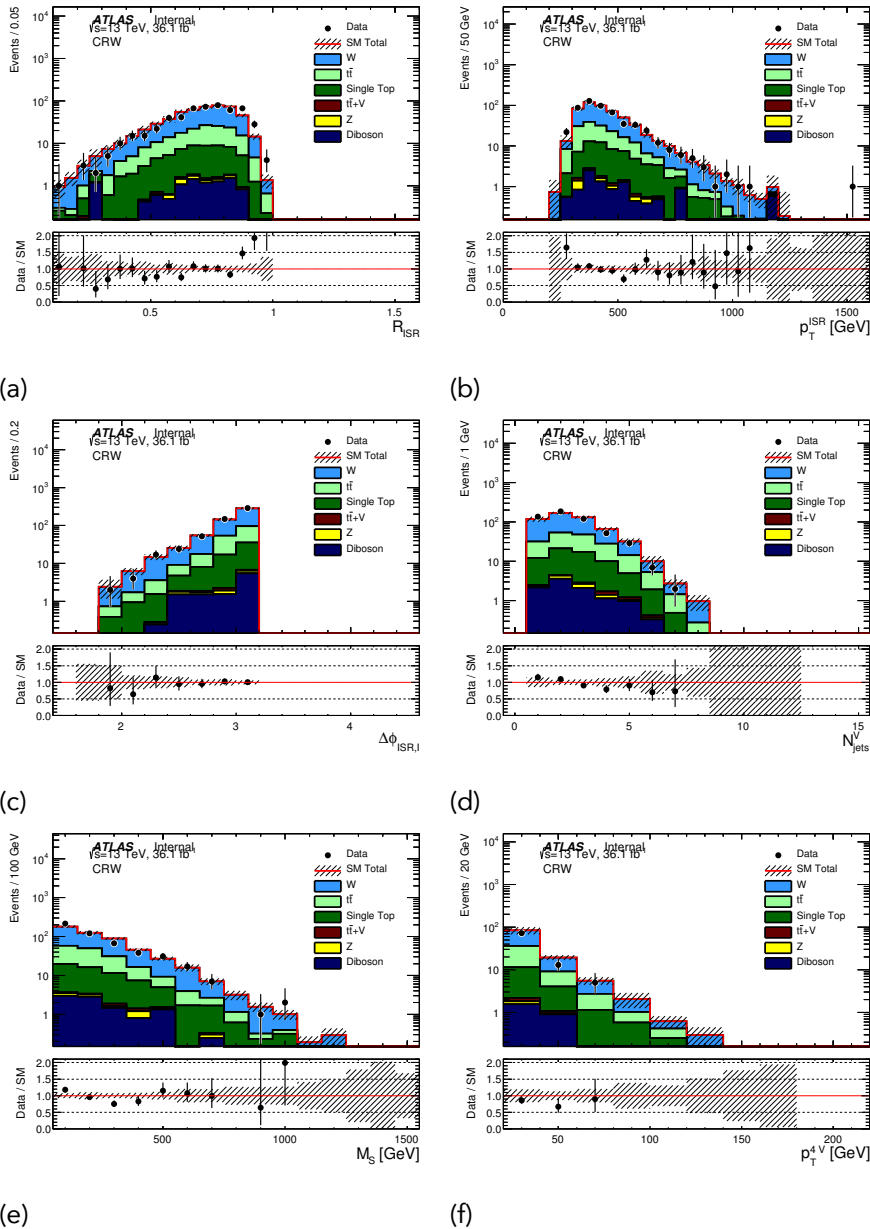


Figure 12.10: Kinematic distributions in the $W + \text{jets}$ control region after the background only fit to 36.07 fb^{-1} of data. The variables shown are (a) R_{ISR} (b) p_T^{ISR} (c) $\Delta\phi_{\text{ISR}, E_T^{\text{miss}}}$ (d) N_{jet}^S (e) m_T^S (f) $p_T^{4,S}$.

Table 12.7: W +jets control region MC Yield and background-only fit results for 36.07 fb^{-1} of data. MC exp. events are expected background rates directly from MC predictions. Fitted background event rates are the expected background rates after normalizing the MC to data by simultaneously fitting all control regions using a background only fit. The fitted W +jets normalization scale factor is equal to (Fitted W + jets events)/(MC exp. W + jets events). The quoted uncertainties include statistical and systematic uncertainties.

CRW yields	CRW
Observed events	533
Fitted bkg events	533.23 ± 23.09
Fitted TTbar events	115.60 ± 18.76
Fitted Wjets events	349.54 ± 38.87
Fitted Zjets events	1.86 ± 0.63
Fitted TtbarV events	1.15 ± 0.43
Fitted SingleTop events	54.76 ± 20.41
Fitted Diboson events	10.31 ± 2.34
Fitted Multijets events	0.00 ± 0.00
MC exp. SM events	458.28 ± 21.31
MC exp. TTbar events	122.28 ± 15.29
MC exp. Wjets events	276.00 ± 5.53
MC exp. Zjets events	1.79 ± 0.52
MC exp. TtbarV events	0.89 ± 0.35
MC exp. SingleTop events	47.00 ± 5.70
MC exp. Diboson events	10.31 ± 2.35
MC exp. Multijets events	0.00 ± 0.00
Fitted W +jets normalization scale factor	1.27 ± 0.15

12.4.2 Standard Model Single-Top

Standard Model single-top consists of 6% of the total background in the signal region. This rate varies between 2-9% for any one signal region R_{ISR} bin. A one-lepton

single-top control region is defined in Table 12.8. The single-top control region is orthogonal to both the one-lepton W +jets control region and $t\bar{t}$ control region.

Table 12.8: Selection for the one-lepton single-top control region. The one-lepton preselection defined in Table 10.2 is also applied.

Variables	Single-top 1 lepton control region
Number of leptons	1
Number of jets (incl. lepton)	≥ 4
p_T of jets (incl. lepton)	(80,80,40,40) GeV
$\min \left \Delta\phi \left(\text{jet}^{0-1}, E_T^{\text{miss}} \right) \right $	> 0.4
E_T^{miss}	$> 250 \text{ GeV}$
$m_T(\ell, E_T^{\text{miss}})$	$> 30, < 100 \text{ GeV}$
Number of b -jets	≥ 2
$m_{\text{jet}, R=1.2}^0$	$v > 120 \text{ GeV}$
$m_T^{b,\text{min}}$	$> 200 \text{ GeV}$
$\Delta R(b_{0,1}, \ell)_{\text{min}}$	> 2.0
$\Delta R(b, b)$	> 1.5

The lepton is treated as a jet for the jet multiplicity and the jet p_T requirements as well as for the top reconstruction. Similar to the one-lepton $t\bar{t}$ control region, the lepton is meant to play the role of a hadronic tau jet in the zero-lepton signal region.

$m_T(\ell, E_T^{\text{miss}})$ is defined in equation 12.1 as the transverse mass of the lepton and the E_T^{miss} . The $m_T(\ell, E_T^{\text{miss}})$ selection ensures that the transverse mass is consistent with a W decay.

The $\Delta R(b, b)$ variable is defined in equation 12.3 as the ΔR between the two b -jets with the highest b -tagging values. $\Delta R(b, b) > 1.5$ isolates single-top events and rejects $t\bar{t}$. This gives the single-top control region a purity of $\sim 50\%$.

$$\Delta R(b_{0,1}, \ell)_{\min} = \sqrt{\Delta\eta(b_1, b_2)^2 + \Delta\phi(b_1, b_2)^2} \quad (12.3)$$

The $m_{\text{jet}, R=1.2}^0 > 120 \text{ GeV}$ requirement selects for events with reconstructed boosted tops and ensures orthogonality with the $W + \text{jets}$ control region. $m_{\text{jet}, R=1.2}^0$ is defined as the mass of an $\text{anti}-k_t$ jet built with a distance parameter of $R = 1.2$ instead of the regular $R = 0.4$. The $\text{anti}-k_t$ algorithm clusters calorimeter energy into a jet according to the distance metric R and is covered in detail in section 4.3.1. The large $R = 1.2$ jet is designed to cluster all the energy of a boosted top quark into a single jet. If the jet contains a boosted top, the invariant mass of jet should be close to $\sim m_t$.

$\Delta R(b_{0,1}, \ell)_{\min}$ is defined in equation 12.2 as the minimum ΔR between the two jets with the highest b-tag value and the selected lepton. The $\Delta R(b_{0,1}, \ell)_{\min}$ selection ensures orthogonality with the $t\bar{t}$ control region.

Kinematic distributions in the single control region are shown in Figure 12.11 and 12.12. The MC background has been normalized to data by performing a simultaneous fit to all control regions. The hashed bands on the total SM background correspond to the total experimental systematical uncertainty plus the MC statistical uncertainty. The yield in the single-top control region is given in table 12.9.

Data and MC are compatible to within statistical uncertainty. No strong trends are observed in the data to MC ratios in any of the distributions.

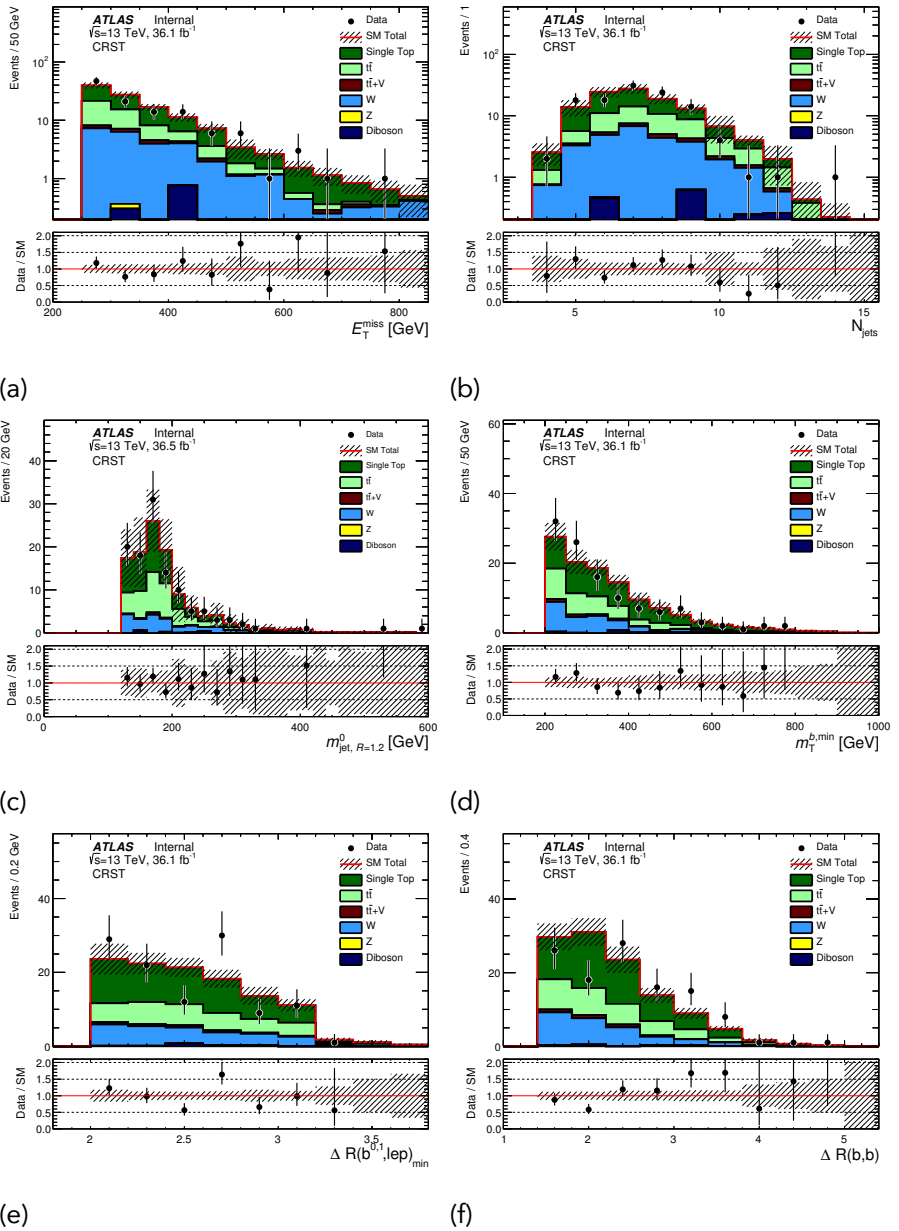


Figure 12.11: Single-top control region distributions for 36.07 fb^{-1} of data after a simultaneous fit to all control regions. The kinematic variables include (a) E_T^{miss} (b) number of jets (c) $m_{\text{jet}, R=1.2}^0$ (d) $m_T^{b,\text{min}}$ (e) $\Delta R(b_{0,1}, \ell)_{\text{min}}$ (f) $\Delta R(b, b)$.

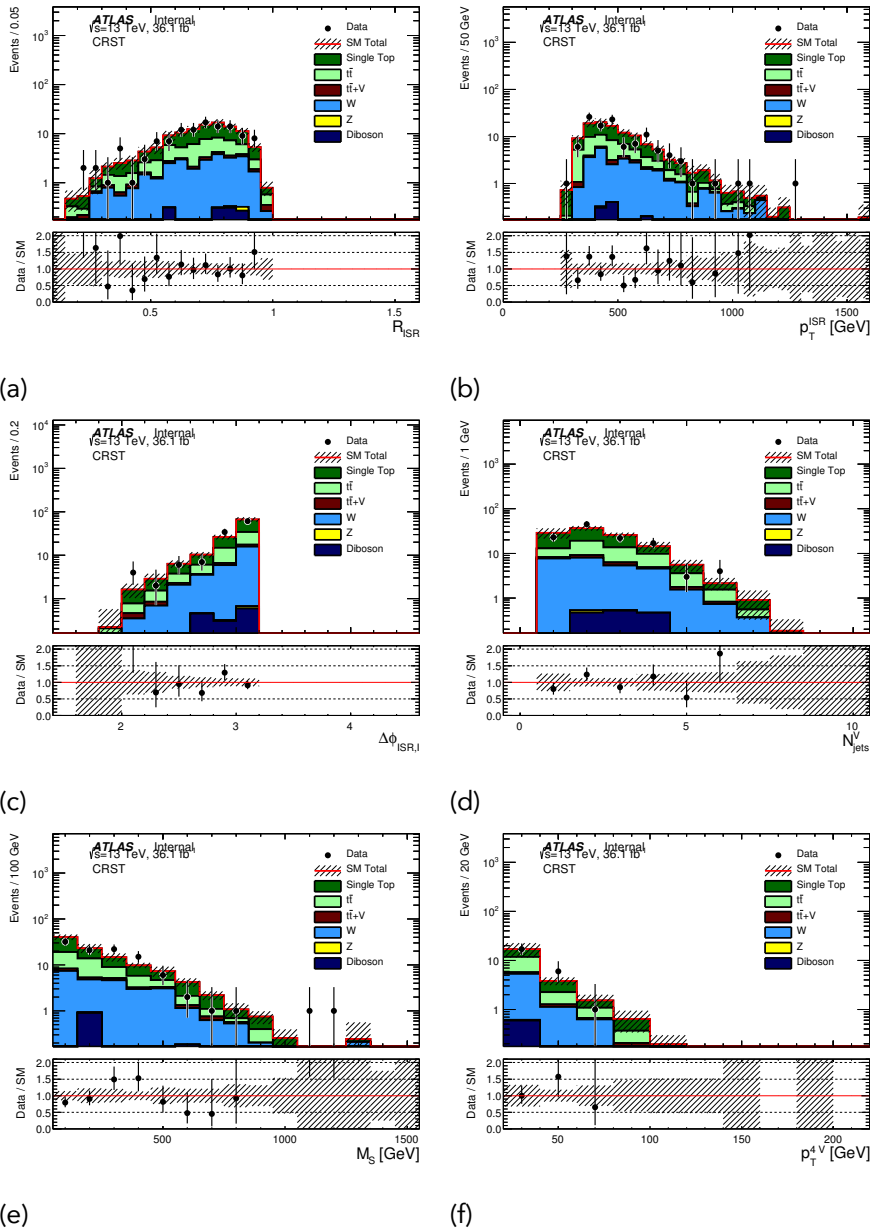


Figure 12.12: Single-top control region distributions for 36.07 fb^{-1} of data after a simultaneous fit to all control regions. The kinematic variables include (a) R_{ISR} (b) p_T^{ISR} (c) $\Delta\phi_{\text{ISR}, E_T^{\text{miss}}}$ (d) N_{jet}^S (e) m_T^S (f) $p_T^{4,S}$.

Table 12.9: Single top control region MC Yield and background-only fit results for 36.07 fb^{-1} of data. MC exp. events are expected background rates directly from MC predictions. Fitted background event rates are the expected background rates after normalizing the MC to data by simultaneously fitting all control regions using a background only fit. The fitted $W+\text{jets}$ normalization scale factor is equal to (Fitted single top events)/(MC exp. single top events). The quoted uncertainties include statistical and systematic uncertainties.

CRother yields	CRST
Observed events	114
Fitted bkg events	113.93 ± 10.65
Fitted TTbar events	29.80 ± 10.52
Fitted Wjets events	26.36 ± 5.82
Fitted Zjets events	0.10 ± 0.07
Fitted TtbarV events	3.14 ± 0.73
Fitted SingleTop events	52.95 ± 17.45
Fitted Diboson events	1.59 ± 0.79
Fitted Multijets events	0.00 ± 0.00
MC exp. SM events	102.60 ± 12.42
MC exp. TTbar events	32.24 ± 11.17
MC exp. Wjets events	20.83 ± 3.02
MC exp. Zjets events	0.09 ± 0.06
MC exp. TtbarV events	2.44 ± 0.42
MC exp. SingleTop events	45.42 ± 1.32
MC exp. Diboson events	1.58 ± 0.79
MC exp. Multijets events	0.00 ± 0.00
Fitted single top normalization scale factor	0.707 ± 0.050

12.4.3 Standard Model $t\bar{t}+Z$

$t\bar{t}$ produced in conjunction with a Z boson consists of about 1% of the background in the signal region. We estimate the amount of $t\bar{t}+Z$ using a $t\bar{t}+\gamma$ control region.

Using the charged leptonic Z boson decays to design a control region to estimate the $t\bar{t} + Z$ background would produce a control region with small systematic uncertainty. However, such a control region tends to have low statistics because $Z \rightarrow ee/\mu\mu$ has a lower branching fraction than $Z \rightarrow \nu\nu$. A dilepton control region also contains a large contribution from SM $t\bar{t}$ and $Z + \text{jets}$.

We take another data driven approach by building a one-lepton control region for $t\bar{t} + \gamma$. $t\bar{t} + \gamma$ mimics $t\bar{t} + Z$ as the photon is in many ways like a lighter Z boson. The control region is designed to minimize theoretical uncertainties due to the extrapolation from the γ in the control region to the Z in the signal region.

We require exactly one Signal photon and one Signal lepton. The lepton is not treated as a jet for the purpose of jet multiplicity and jet p_T requirements unlike in the other one-lepton control regions. We also trigger on leptons instead of E_T^{miss} in this region. The lepton triggers used are defined in Table 12.10.

We require the photon p_T be greater than 150 GeV. The high p_T photon ensures that we are in a region of phase space where the γp_T shape will mimic the heavier $Z p_T$ distribution. The true γp_T and the $Z p_T$ distributions are shown in Figure 12.13 after selecting for a boson p_T with greater than 150 GeV. We add a systematic uncertainty to account for the difference between the γ and $Z p_T$ spectrum.

Table 12.10: Single Lepton triggers used in the $t\bar{t} + \gamma$ control region. The electron triggers correspond to the a p_T threshold of 24, 26, 60, 120, and 140 GeV respectively. The muon triggers correspond to p_T thresholds of 20, 26 and 50 GeV.

Channel	Trigger
Data 2015	
Electron	HLT_e24_lhmedium_L1EM20VH HLT_e60_lhmedium HLT_e120_lhloose
Muon	HLT_mu20_iloose_L1MU15 HLT_mu50
Data 2016	
Electron	HLT_e26_lhtight_nod0_ivarloose HLT_e60_lhmedium_nod0 HLT_e140_lhloose_nod0
Muon	HLT_mu26_ivarmedium HLT_mu50

The $t\bar{t} + \gamma$ control region is defined in Table 12.11. The expected background and data yields in the $t\bar{t} + \gamma$ control region is given in Table 12.12.

Kinematic distributions in the $t\bar{t} + \gamma$ control region are shown in Figure 12.14. The MC background has been normalized to data by performing a simultaneous fit to all the control regions. The hashed bands on the total SM background correspond to the total experimental systematical uncertainty plus the MC statistical uncertainty.

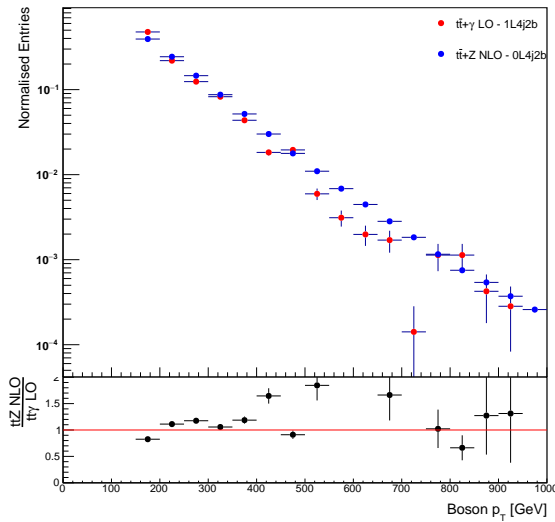


Figure 12.13: γ and Z p_T distributions in MC simulation with no detector resolution effects. A selection of $p_T > 150$ GeV has been applied.

Table 12.11: Selections for the $t\bar{t} + \gamma$ one-lepton control region. The single lepton triggers as described in Table 12.10

Selection	Requirement
Event selection	Event cleaning
Trigger	1L Triggers
Leptons	= 1
Lepton p_T	28 GeV
Photons	exactly 1
jet multiplicity	≥ 4
Jet p_T	(80,80,40,40) GeV
b-jet multiplicity	≥ 2
γp_T	> 150 GeV

Table 12.12: $t\bar{t} + \gamma$ control region MC Yield and background-only fit results for 36.07 fb^{-1} of data. MC exp. events are expected background rates directly from MC predictions. Fitted background event rates are the expected background rates after normalizing the MC to data by simultaneously fitting all control regions using a background-only fit. The fitted $t\bar{t} + \gamma$ normalization scale factor is equal to (Fitted $t\bar{t} + \gamma$ events)/(MC exp. $t\bar{t} + \gamma$ events). The quoted uncertainties include statistical and systematic uncertainties.

CRTTgamma yields	CRTTGamma
Observed events	161
Fitted bkg events	161.19 ± 14.03
Fitted TTbar events	$4.75^{+9.52}_{-4.75}$
Fitted Wjets events	0.05 ± 0.01
Fitted Zjets events	0.75 ± 0.19
Fitted TtbarV events	3.01 ± 0.42
Fitted TtbarGamma events	143.96 ± 13.37
Fitted SingleTop events	2.40 ± 0.84
Fitted Diboson events	0.00 ± 0.00
Fitted VGamma events	6.27 ± 1.63
MC exp. SM events	128.31 ± 18.89
MC exp. TTbar events	$5.14^{+11.21}_{-5.14}$
MC exp. Wjets events	0.04 ± 0.01
MC exp. Zjets events	0.66 ± 0.13
MC exp. TtbarV events	2.34 ± 0.37
MC exp. TtbarGamma events	111.77 ± 13.41
MC exp. SingleTop events	2.07 ± 0.40
MC exp. Diboson events	0.00 ± 0.00
MC exp. VGamma events	6.29 ± 1.64
Fitted $t\bar{t} + \gamma$ normalization scale factor	1.29 ± 0.20

12.4.4 Standard Model Z+Jets

Z+jets consist of 3% of all backgrounds in the signal region. We only use the MC prediction for Z+jets because the rate of Z+jet is so low. We assign a 50 percent

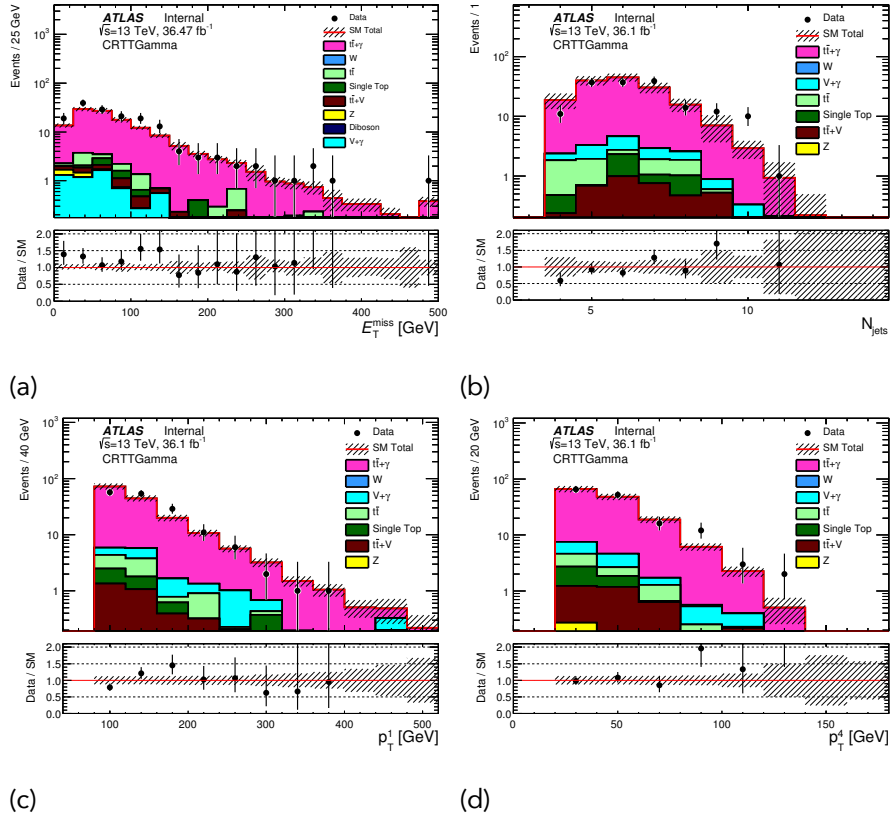


Figure 12.14: Distributions of select kinematic variables in the $t\bar{t} + \gamma$ control region. Kinematic variables shown include (a) E_T^{miss} (b) number of jets (c) p_T of the 2nd highest p_T jet (d) p_T of the 5th highest p_T jet. The hashed area in both the top and lower panel represents the uncertainty due to MC statistics.

theory uncertainty to the $Z+\text{jets}$ MC predictions.

12.4.5 Standard Model Diboson

Standard Model dibosons consist of approximately 1% of the background in the signal region. The background is negligible and we only use MC predictions for background estimation. We assign a 50% theory uncertainty to the MC estimation.

12.4.6 Standard Model QCD Multijet

QCD multijet events form a significant contribution to background rates in signal region bins with $R_{\text{ISR}} < 0.4$. The QCD multijet process creates little intrinsic E_T^{miss} from actual neutrinos. Instead, misreconstructed jets are the primary reason why some QCD multijet events are able to pass the $E_T^{\text{miss}} > 250 \text{ GeV}$ requirement and the signal region selections. Misreconstructed jets can cause an imbalance in the total event E_t and lead to events with a large reconstructed E_T^{miss} even if the event has little intrinsic E_T^{miss} . We estimate the QCD background using the data driven Jet Smearing method.

More details on the Jet Smearing method can be found in reference [65]. A detailed description of how the Jet Smearing method is used to estimate the QCD background in the signal region of this analysis is given in this section.

The Jet Smearing Method of Estimating QCD Background

The Jet Smearing method first selects seed events from data with well reconstructed jets and little E_T^{miss} . We then repeatedly smear the seed events' jets with a predetermined jet energy response. The resulting pseudo-data events can have potentially large E_T^{miss} due to the smeared jets. A schematic demonstrating the jet smearing method is shown in Figure 12.15.

The Jet Smearing methods have a number of inherent assumptions about the

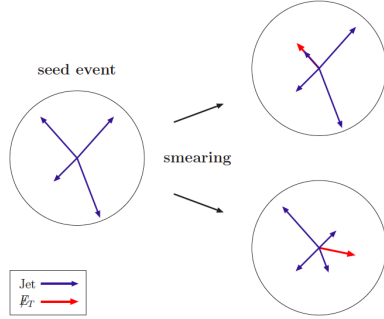


Figure 12.15: Schematic diagram demonstrating the Jet Smearing method of estimating rate of QCD background. Seed events with good jet energy measurements are repeatedly smeared with predetermined jet energy resolutions. The new E_T^{miss} is calculated as the difference between the seed event's and smeared event's jet momentum plus the original seed event's E_T^{miss} .⁶⁵

generation of E_T^{miss} in QCD multijet background. These assumptions include:

- The jet response captures all sources of jet p_T measurement fluctuations
- The E_T^{miss} in multijet events result predominately from mis-measured jets
- Jet response is independent on the presence of other jets and jet smearing can be applied on a jet-by-jet basis

These assumptions seem to be well satisfied in the high E_T^{miss} , high jet multiplicity environment of the signal region. Other sources of E_T^{miss} not taken into account by the jet smearing method include E_T^{miss} from pile-up jets, a mis-reconstructed soft term of the E_T^{miss} and object overlap removal. All such additional sources of E_T^{miss} are assumed to be negligible in the high $E_T^{\text{miss}} > 250$ GeV signal region.

We then define a QCD control region that is kinematic similar to the signal region but dominated by QCD background. We normalize the predicted QCD rate to the

amount of data in the control region. The normalization factor is then applied to predicted QCD rates in the signal region. We also validate the QCD predictions using a QCD validation region. The QCD control and validation regions are covered in greater details in section 12.4.6.

Jet Smearing Seed Event Selection and Jet Response Function

We select for events with multiple well reconstructed jets and no leptons as seed events. Because QCD multijet events have low intrinsic E_T^{miss} , seed events must have low E_T^{miss} relative to the total reconstructed E_T in the event.

Some E_T^{miss} is expected even in well reconstructed multijet events because both the electromagnetic and hadronic calorimeters at ATLAS are sampling calorimeters. The energy deposited in the absorber material is effectively lost because the absorber does not actively record a signal. Therefore the energy measured using the active material must be scaled up to compensate for this loss. The statistical nature of the sampling process means the uncertainty, σE_T , for jets depend on the total E_T .

The quantity $E_T^{\text{miss}}\text{sig.} = \frac{E_T^{\text{miss}} - 8 \text{ GeV}}{\sum E_T}$ measures the significance of E_T^{miss} relative to total hadronic activity in an event. An event with low $E_T^{\text{miss}}\text{sig.}$ has a low amount of E_T imbalance relative to the total amount of calorimeter activity in the event. In this case, the amount of E_T imbalance is consistent with the expected uncertainty on calorimeter energy measurements. If $E_T^{\text{miss}}\text{sig.}$ is high then the E_T^{miss} is inconsistent with the expected uncertainty on calorimeter measurements and the probability of

having energetic weakly interacting particles in the event is high.

QCD multijet events are expected to produce very few energetic neutrinos and therefore, we select for well reconstructed seed events by requiring low $E_T^{\text{miss}}\text{sig.}$.

Seed events are selected according to the criteria listed in Table 12.13.

Table 12.13: Jet Smearing seed event preselection

Selection
$n_{\text{prim.vertices}} > 0$
Jet trigger
Bad jet veto
Cosmic muon veto
Bad muon veto
Baseline lepton veto
≥ 4 jets
≥ 1 b-jets
$E_T^{\text{miss}}\text{sig.} < 0.3 + 0.1 \cdot n_{\text{n-bjets}}$

The $E_T^{\text{miss}}\text{sig.} < 0.3 + 0.1 \cdot n_{\text{n-bjets}}$ requirement depends on the number of b-jets because b-quarks can emit significant portions of their energy in the form of neutrinos. We therefore expect larger $E_T^{\text{miss}}\text{sig.}$ in events with more b-jets. B-jets also have a different jet response function than light quark jets to account for this effect.

The jet response function used in Jet Smearing includes contributions from the following effects:

- Limited calorimeter granularity.
- Hadronic energy falling outside of the jet radius or failing to be clustered correctly by jet reconstruction.

- Additional energy clustered into the jet that results from other sources.
- Energetic jet punching through the calorimeter.
- Dead material in the calorimeter.
- b-quark generating real E_T^{miss} through decay to neutrinos.

QCD multijet Control Region and Validation Region

The QCD control region is designed to be similar to the signal region except the

$\min |\Delta\phi(\text{jet}^{0-1}, E_T^{\text{miss}})|$ is required to be between 0.05 to 0.1 instead of greater than 0.04. $\min |\Delta\phi(\text{jet}^{0-1}, E_T^{\text{miss}})|$ is defined in equation 12.4 as the separation in ϕ between E_T^{miss} and the two highest p_T jets in the event.

If the E_T^{miss} mainly results from a single misreconstructed energetic jet then we would expect the E_T^{miss} and jet to be collinear in ϕ . The $\min |\Delta\phi(\text{jet}^{0-1}, E_T^{\text{miss}})| > 0.4$ selection rejects such events in the signal region. The QCD control region selects for events with $0.05 < \min |\Delta\phi(\text{jet}^{0-1}, E_T^{\text{miss}})| < 0.1$ which is dominated by QCD.

$$|\Delta\phi(\text{jet}^{0,1}, E_T^{\text{miss}})| = \min_{2 \text{ highest } p_T \text{ jets}} \Delta\phi(\text{jet}, E_T^{\text{miss}}) \quad (12.4)$$

The pseudo-data resulting from the Jet Smearing processes is then normalized to data using the QCD control region defined in Table 12.14.

Data vs QCD pseudo-data distributions for the p_T^{ISR} , $\Delta\phi_{\text{ISR}, E_T^{\text{miss}}}$ and m_T^S variables

Table 12.14: QCD control region selections, in addition to the zero-lepton preselection in Table 10.1.

Variable	QCD control region
$\min \Delta\phi(\text{jet}^{0-1}, E_T^{\text{miss}}) $	[0.05,0.1]
$N_{\text{b-jet}}^S$	≥ 1
N_{jet}^S	≥ 5
p_T^{ISR}	$> 150 \text{ GeV}$
$p_{T,b}^{0,S}$	$> 40 \text{ GeV}$
$p_T^{4,S}$	$> 50 \text{ GeV}$
$\Delta\phi_{\text{ISR}, E_T^{\text{miss}}}$	> 2.00
R_{ISR}	< 0.4

in the QCD control region can be seen in Figure 12.16. We extrapolate over these variables between the control and signal regions.

The QCD multijet prediction after normalizing to the control region can be checked in the QCD validation region defined in Table 12.15. The QCD validation region has the exact same kinematic selection as the signal region except a lower $\min |\Delta\phi(\text{jet}^{0-1}, E_T^{\text{miss}})|$ requirement of between 0.1 and 0.2. R_{ISR} is also required to be below 0.4 as we don't expect significant QCD contribution at higher R_{ISR} .

Data vs QCD pseudo-data distribution for the R_{ISR} and $\Delta\phi_{\text{ISR}, E_T^{\text{miss}}}$ variables in the QCD validation region can be seen in Figure 12.16. A good agreement is found between data and pseudo-data predictions.

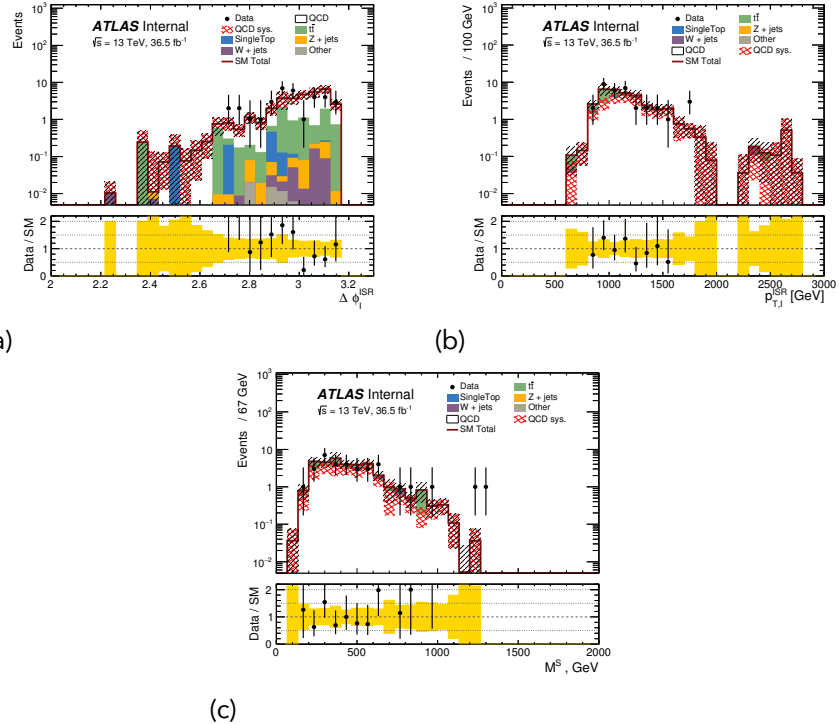


Figure 12.16: p_T^{ISR} , $\Delta\phi_{\text{ISR}, E_T^{\text{miss}}}$ and m_T^S distributions in the QCD control region

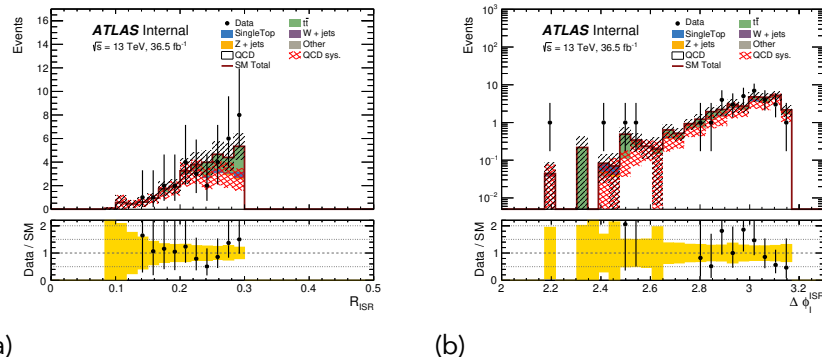


Figure 12.17: R_{ISR} and $\Delta\phi_{\text{ISR}, E_T^{\text{miss}}}$ distributions in the QCD validation region.

Table 12.15: QCD validation region selections, in addition to the zero-lepton preselection in Table 10.1.

Variable	QCD Validation Region
$\min \Delta\phi(\text{jet}^{0-1}, E_T^{\text{miss}}) $	[0.1,0.2]
$N_{\text{b-jet}}^S$	≥ 1
N_{jet}^S	≥ 5
p_T^{ISR}	$> 400 \text{ GeV}$
$p_{T,b}^{0,S}$	$> 40 \text{ GeV}$
$p_T^{4,S}$	$> 50 \text{ GeV}$
m_T^S	$> 300 \text{ GeV}$
$\Delta\phi_{\text{ISR}, E_T^{\text{miss}}}$	> 3.00
R_{ISR}	< 0.4

QCD prediction in the Signal Region

The predicted amount of QCD in the signal region is given by the amount of QCD pseudo-data that passes the signal region selections after normalizing to the QCD control region. The systematic uncertainty on the signal region QCD prediction is given by repeating the Jet Smearing process with a tighter and looser set of seed event selections.

An upward error corresponds to using seed events requiring $E_T^{\text{miss}} \text{sig.} < 0.6 + 0.2 \cdot n_{\text{n-bjets}}$ and a lower error corresponds to using seed events requiring $E_T^{\text{miss}} \text{sig.} < 0.2 + 0.05 \cdot n_{\text{n-bjets}}$. QCD multijet events with better reconstructed jets tend to have

a smaller E_T^{miss} sig.

The expected QCD yield and uncertainty in the signal region is given in Table 12.16.

Table 12.16: Expected yields of the QCD multijet backgrounds in the signal region.

SR R_{ISR} Region	0.3-0.4	0.4-0.5	0.5-0.6
QCD expected yield	4.56 ± 2.38	1.58 ± 0.77	0.32 ± 0.17

SR R_{ISR} Region	0.6-0.7	0.7-0.8
QCD expected yield	0.04 ± 0.02	0.00 ± 0.00

13

Statistical Analysis

13.1 Introduction to Log Likelihood Fitting

We check the consistency of data and expected SM background and extract information on any potential signal using log likelihood fitting. In log likelihood fitting, we select for parameter values that maximize the total likelihood defined in equation 13.1.

$$\mathcal{L}(\vec{z}) = \prod_{i=1}^n P(x_i|\vec{z}) \quad (13.1)$$

x_i are data points and \vec{z} is a list of parameters. $P(x|\vec{z})$ is the fitted probability density function (PDF). In log-likelihood fitting, the PDF $P(x|\vec{z})$ has the highest probability of producing the dataset x_i when the likelihood is maximized.

Maximizing the likelihood is equivalent to minimizing the negative log likelihood or NLL since logarithms are monotonically increasing functions. Therefore, we can instead minimize the NLL M defined in equation 13.2

$$M(\vec{z}) = -\ln((\mathcal{L}(\vec{z})) = -\sum_{i=1}^n \ln(P(x_i|\vec{z})) \quad (13.2)$$

In collider physics we do not know the total number of observed events a priori. Instead, we have an expected value of events proportional to the cross-section times the luminosity. The actual number of measured events can vary according to a Poisson distribution. We include the uncertainty on the number of observed events by multiplying the log likelihood and a Poisson distribution with expected rate λ ; resulting in equation 13.3.

$$\mathcal{L}(\vec{z}) = \left\{ \frac{\exp^{-\lambda} \lambda^n}{n!} \right\} \prod_{i=1}^n P(x_i|\vec{z}) \quad (13.3)$$

For this particular analysis we perform a binned fit to the R_{ISR} distribution in the

signal region. Therefore the fitted PDF ($x_i|\vec{z}$) is not a continuous function but a series of expected values in discrete bins. The binned $P(x|\vec{z})$ can be written as equation 13.4.

$$P_{b_i} = P(x_i|\vec{z}) = \int_{b_{i-1}}^{b_i} f(x|\vec{z}) \, dx \quad (13.4)$$

$f(x|\vec{z})$ represents the continuous PDF and b_i and b_{i-1} are the bin edges for the i th bin. Assuming a Poisson distribution of events in each bin, the extended likelihood and NLL become equation 13.5 and 13.6.

$$\mathcal{L}(N_{b_i}^{\text{data}}|\vec{z}) = \prod_{k=1}^{n_{\text{bins}}} \frac{(\lambda P_{b_i})^{N_{b_i}^{\text{data}}} e^{-\lambda P_{b_i}}}{N_{b_i}^{\text{data}}!} \quad (13.5)$$

$$M(\vec{z}) = -\ln(\mathcal{L}(\vec{z})) = -\sum_{i=1}^{n_{\text{bins}}} (N_{b_i}^{\text{data}} \ln(\lambda P_{b_i}) - \lambda P_{b_i} - \ln N_{b_i}^{\text{data}}!) \quad (13.6)$$

$N_{b_i}^{\text{data}}$ is the number of data in the i th bin, λ is the expected rate in the region, P_{b_i} is the probability of an event being in the i th bin if it is in the signal region and \vec{z} represents a list of fitted parameters such as the signal cross-section. Both λ and P_{b_i} can depend on the fitted parameters as the normalization and shape of the PDF can change with the fitted parameters.

We can also rewrite equation 13.5 and 13.6 as 13.7 and 13.8. In this interpretation, $\lambda P_{b_i} = N_{b_i}^{\text{MC}}$ is simply the expected number of events in a particular bin.

$$\mathcal{L}(N_{b_i}^{data} | \vec{z}) = \prod_{k=1}^{n_{bins}} \frac{(N_{b_i}^{MC})^{N_{b_i}^{data}} e^{-N_{b_i}^{MC}}}{N_{b_i}^{data}!} \quad (13.7)$$

$$M(\vec{z}) = -\ln((\mathcal{L}(\vec{z})) = -\sum_{i=1}^{n_{bins}} (N_{b_i}^{data} \ln(N_{b_i}^{MC}) - N_{b_i}^{MC} - \ln N_{b_i}^{data}!) \quad (13.8)$$

In this analysis we perform a simultaneous fit to multiple control and signal regions to extract the best fit signal strength. We do this by maximizing the total NLL of all fitted regions where the total NLL is simply a sum of the individual NLL for each region.

13.2 Overview of Fitting to Control Regions and Signal Regions

In this analysis we use a signal region to isolate signal from background. At the same time, we use multiple control regions that are kinematically similar to the signal region but have high background purity to estimate the background. The signal strength and expected background rate are both extracted through a simultaneous fit to all control regions and signal regions.

The amount of MC background in both the control and signal regions will vary with experimental and theoretical systematics before the fit. However, after the fit, the total amount of background will be normalized to the control. If the MC yield for background has a downward variation for a given systematic then the normaliza-

tion scale factor will increase. The increased normalization scale factor will compensate for any simultaneous drops in signal region MC yield. This partial cancellation of variations between control and signal regions can lead to smaller systematic uncertainties. In summary, the control regions reduce the systematic uncertainty by directly measuring the amount of background in data instead of relying solely on MC simulations.

The more kinematically similar the definition of the control region to the signal region, the better the cancellation. Any extrapolation between control and signal region must be across well modeled variables. Otherwise, large systematic uncertainties can arise and the background predictions in the signal region may be wrong.

We can also check the result of our background predictions without unblinding the signal region in validation regions. Validation regions receive the background normalization scale factors from the fit to control regions but do not participate in the fit. Validation regions are designed to be kinematically similar to the signal regions while keeping signal contaminations low. In this way, validation regions serve as a mid-point to check the extrapolation between the control and signal regions.

The relationship between control, validation and signal regions is graphically depicted in Figure 13.1.

The data in the signal region is originally blinded to avoid any bias for or against discovery. We first check the agreement between MC simulation and background predictions in the control and validation regions. We unblind the signal region only

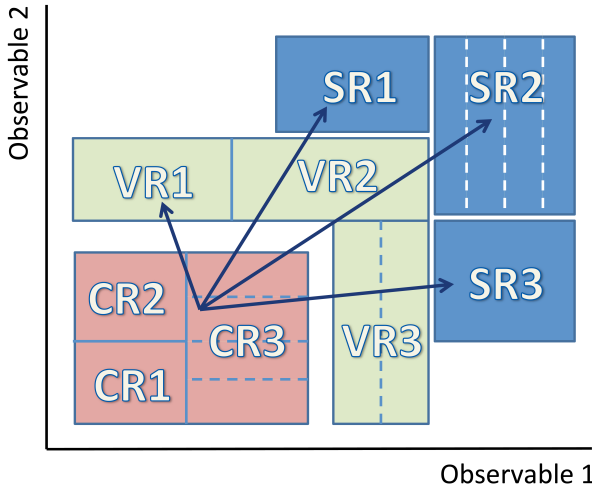


Figure 13.1: Schematic representation of the data driven background estimation technique which uses control regions to estimate background rates in the signal region and uses validation regions to validate those estimates. We define control regions (CR) that are dominated by background and have little signal. We can estimate the amount of background we expect in the signal region by measuring the amount of background in the control region. We then use MC simulation to extrapolate between the control region and the signal region. Validation regions are in between control regions and the signal regions and serve to validate the extrapolation between the control and signal regions.

after we decide the background prediction in the signal region is well understood based on these observations in the control regions and validation regions.

If an excess exists in the signal region, a simultaneous fit to all control and signal regions is performed to calculate the statistical significance of any potential excess (discovery fit). If no excess is found, then a simultaneous fit to all control and signal regions is also performed to quantify the smallest signal cross-section that can be excluded (exclusion fit).

We also quantify the expected background rate and the systematic uncertainty

in the signal region by performing a background only fit. In this case, only the control regions are fitted. The signal region acts like another validation region, receiving the fitted background normalization but not participating in the fit. The background only fit may give a different predicted background rate from the exclusion or discovery fit because the signal region is not simultaneously fitted. However, the difference is expected to be small because the control regions are designed to have much greater constraining power on background rates than the signal region.

These three types of fits, the background only fit, the discovery fit and the exclusion fit are covered in more detail in sections 13.4 to 13.5. The parameterization of systematics as constrained nuisance parameters is covered in section 13.3.

We use the software package `HistFitter` (version `HistFitter-00-00-53`) to perform the statistical analysis.³⁴ At its core, `HistFitter` is still performing log likelihood fitting based on the principle introduced in section 13.1, but `HistFitter` provides many tools to easily manage and integrate multiple control region, validation region, signal region, signal samples, backgrounds, and systematics. `HistFitter` is built upon other statistical analysis software including `RooFit`.⁷²

13.3 Parameterization of Systematics as Gaussian Constraints

Systematics uncertainties are parameterized as fitted parameters called nuisance parameters. In general, the nuisance parameter α is constrained to a particular value

by a constraint function $C(\alpha)$. The constraint function $C(\alpha)$ is multiplied by the likelihood as shown in equation 13.9. The fitted PDF $P(x|\vec{z}, \alpha)$ can depend on the unconstrained fitted parameters \vec{z} and the constrained α .

$$\mathcal{L}(\vec{z}, \alpha) = \prod_{i=1}^n P(x_i|\vec{z}, \alpha) C(\alpha) \quad (13.9)$$

We pay a penalty on the total likelihood if the nuisance parameter α deviates from the value with maximum $C(\alpha)$. In summary, the fit simultaneously optimizes the agreement between the PDF and the data while minimizing the constraint function on α .

We use Gaussians as the constraint function for all systematics. The nominal value corresponds to $\alpha = 0$ and the $\pm 1\sigma$ deviation corresponds to $\alpha = \pm 1$.

13.4 Background Only Fit and Background Estimation

The background rates are normalized to data through a simultaneous fit to all control regions for the background only fit. The fitted background normalizations derived from the fit are then applied to the signal region but the signal region is not simultaneously fitted. No signal sample is included in the fit and any potential signal contamination in the control regions are ignored. This fit has the advantage of being able to quantify the expected background rate and systematic uncertainties while the signal region is blinded.

The background normalizations predicted in the background only fit may differ from the discovery and exclusion fits because the signal region is simultaneously fitted in the latter two fits. This difference should be small as long as the control regions have high background purity and significantly higher statistics than the signal region.

13.5 Exclusion Fit and Exclusion Limit Calculation

The exclusion fit is performed as a simultaneous fit to all control regions and all five R_{ISR} bins in the signal region. The signal sample is included in both the control and signal regions and normalized to the fitted signal strength parameter.

The best fit signal strength is found when the negative log likelihood (NLL) is at a minimum after fitting to data. As the signal strength deviates from the best fit value, the NLL increases and we are more confident that the signal strength is not supported by data. We use the difference in NLL as our test statistic. The relationship between the test statistic and statistical significance is approximated by a parabola in the asymptotic high statistics case.

We can calculate the NLL corresponding to the nominal signal strength of each signal model and compare it with the fitted minimum NLL. The difference in the two NLLs can be converted into the statistical significance using the parabolic relationship between the two. The statistical significance is quantified as the exclusion confidence level.

dence limit (CL_s). If the CL_s is below 5% then the signal model has been excluded to 95% confidence.

We calculate the CL_s values corresponding to a grid of signal models each with a different \tilde{t} and $\tilde{\chi}_1^0$ mass. The CL_s are plotted in a 2D graph with the \tilde{t} mass along the x-axis and the $\tilde{\chi}_1^0$ mass along the y-axis. These CL_s are then interpolated over to form a 2D contour plot. The contour corresponding to the 95% CL_s defines the parameter space excluded by the search.

We can also find the 95% confidence limit on the observed signal cross-section in each R_{ISR} bin. The observed signal cross-section is defined as the number of signal events predicted to exist in signal region for any particular signal model and is equivalent to selection efficiency times the signal production cross-section. The limit on the observed cross-section is completely theory independent. It is simply a statement on the maximum additional BSM rate that can exist in the signal without being ruled out to 95% confidence.

13.6 Discovery Fit and Discovery Significance Calculation

The discovery fit is also performed as a simultaneous fit to all control and signal regions. The signal sample is included only in the signal but not to the control in the fit. Excluding the signal sample from the control regions gives a more conservative estimate. If a signal is present in nature, the signal contamination would still con-

tribute to the control region yield in data. The higher data yield will in turn increase background normalizations in the control region. Hence, any potential signal contamination is considered essentially as additional background in the control regions.

Again, a well designed control region has little signal contamination so the difference between this approach and exclusion fit should be small. Our signal contamination is less than 12% for all relevant signal samples. The signal contamination drops to below 10% for all \tilde{t} masses above 300 GeV.

We do not statistically combine the 5 R_{ISR} bins for the discovery fit. The single R_{ISR} bin with the best significance is used to calculate the discovery significance. Again this is a conservative approach and gives us lower discovery significances but it makes the analysis less sensitive to potential shape uncertainties in signal.

We also use the difference in NLL as the test statistic for our discovery fit. The signal strength and background normalization that best fit the data is found at the minimum NLL. Then we calculate the NLL with a signal strength of zero. The difference between the zero signal strength NLL and the best fit NLL is our test statistic. The relationship between the test statistic and statistical significance is given by a parabola in the asymptotic high statistics case.

The statistical significance of the zero signal strength fit is the p-value of the no signal hypothesis test. This p-value quantifies the discovery significance for the analysis. If the discovery significance is above 5 sigma then discovery can be claimed.

14

Systematic Uncertainties

Systematic uncertainties can be separated into two categories, experimental uncertainties and theoretical uncertainties. Experimental systematics result from uncertainties in physics object reconstruction, calibration, the understanding of the detectors and the amount of additional pile-up interactions. Theoretical systematics result from uncertainties in PDFs, interaction scales, and theoretical calculations.

Experimental uncertainties such as jet energy resolution are assumed to be 100 percent correlated across different background sources. On the other hand, theoretical uncertainties are assumed to be uncorrelated from one another.

In general systematic uncertainties are parameterized as independent parameters with gaussian constraints. These parameters are called “nuisance” parameters and normally denoted by the symbol α . The systematic errors on backgrounds are evaluated through a simultaneous fit to the control and signal regions. An estimate of the systematic uncertainties on backgrounds in the signal region can be made by fitting to the control region alone and extrapolating the result to the signal region. It is important to note that the fit can also lead to correlations between initially independent systematics uncertainties.

A control region that is kinematically similar to the signal region leads to cancellations of systematic uncertainties. Because of this, designing a control region that is kinematically similar to the signal region is crucial to mitigating systematic uncertainties. More detail on control region design and systematic uncertainties can be found in chapter 12.2 on background estimation and chapter 13 on statistical analysis.

The total background systematic uncertainty is $\sim 20\%$ in the signal region. The dominant background systematic uncertainties in the first four signal region R_{ISR} bins, between $0.3 < R_{ISR} < 0.7$, include uncertainty on the $t\bar{t}$ ISR/FSR, uncertainty on the $t\bar{t}$ matrix element and parton shower calculation, and uncertainty on the jet energy resolution. Each of these dominant systematic uncertainties contributes 5-

10% to the total uncertainty on background rate in the signal region. The theoretical uncertainty on the amount of interference between SM $t\bar{t}$ and single top at NLO is also significant.

The large systematic uncertainty in the highest R_{ISR} bin between 0.7 – 0.8 is completely due to low MC statistics caused by the low expected yield. However the 0.7 – 0.8 R_{ISR} region is completely statistically dominated for the same reason, with only 0.7 expected background events.

The dominant background uncertainties in each signal region bin is given in Table 14.1.

The post background only fit pull is given in Figure 14.1. All nuisance parameters, α , are close to zero with uncertainties close to plus/minus one. No profiling of any systematics is observed.

A summary of the experimental and theoretical uncertainties relevant to this analysis is given in the sections below.

14.1 Experimental Uncertainties

14.1.1 Uncertainties on the Jet Energy Scale and Jet Energy Resolution

The two main uncertainties affecting jet measurements are the uncertainties from jet energy scale and jet energy resolution calibrations. The jet reconstruction and calibration process is described in section 4.3. Uncertainty in the calibration process

Table 14.1: Breakdown of the dominant systematic uncertainties on background estimates. Note that the individual uncertainties can be correlated, and do not necessarily add up quadratically to the total background uncertainty. The percentages show the size of the uncertainty relative to the total expected background.

Uncertainty of channel	SRC1	SRC2	SRC3
Total background expectation	20.56	27.54	18.86
Total statistical ($\sqrt{N_{\text{exp}}}$)	± 4.53	± 5.25	± 4.34
Total background systematic	± 6.62 [32.18%]	± 4.89 [17.75%]	± 3.53 [18.72%]
ttbar ME/PS uncertainty	± 4.86 [23.6%]	± 1.91 [6.9%]	± 2.39 [12.7%]
ISR/FSR uncertainty	± 2.64 [12.8%]	± 2.19 [8.0%]	± 1.06 [5.6%]
Single Top Theory Uncertainty	± 1.66 [8.1%]	± 1.18 [4.3%]	± 1.21 [6.4%]
MC statistics in SR bin	± 1.29 [6.3%]	± 1.42 [5.1%]	± 0.96 [5.1%]
ttbar CR normalization factor	± 0.91 [4.4%]	± 1.55 [5.6%]	± 1.03 [5.4%]
Jet energy resolution	± 0.81 [3.9%]	± 2.70 [9.8%]	± 1.14 [6.0%]
QCD Jet Smearing Uncertainty	± 2.38 [11.6%]	± 0.77 [2.8%]	± 0.17 [0.91%]
Uncertainty of channel	SRC4	SRC5	
Total background expectation	7.69	0.90	
Total statistical ($\sqrt{N_{\text{exp}}}$)	± 2.77	± 0.95	
Total background systematic	± 1.37 [17.77%]	± 0.71 [78.68%]	
ttbar ME/PS uncertainty	± 0.68 [8.8%]	± 0.63 [69.1%]	
ISR/FSR uncertainty	± 0.46 [6.0%]	± 0.13 [14.8%]	
Single Top Theory Uncertainty	± 0.71 [9.3%]	± 0.00 [0.00%]	
MC statistics in SR bin	± 0.54 [7.0%]	± 0.21 [23.0%]	
ttbar CR normalization factor	± 0.35 [4.5%]	± 0.04 [4.9%]	
Jet Energy Resolution	± 0.35 [4.6%]	± 0.09 [9.7%]	
QCD Jet Smearing Uncertainty	± 0.02 [0.26%]	± 0.00 [0.15%]	

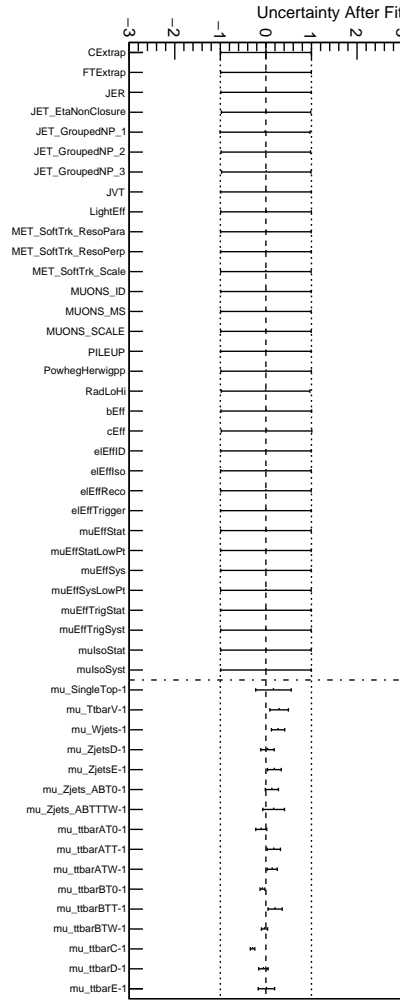


Figure 14.1: Post-fit pull plot for the background-only fit. All nuisance parameters (α) are close to zero after the fit with a fit uncertainty close to plus/minus 1. No profiling of any systematics is observed. The background normalization factors to background control regions, μ , are also shown. Most background normalization factors are statistically consistent with the nominal value of 1.0 but μ_{ttbarC} , the $t\bar{t}$ normalization in the $t\bar{t}$ +hard ISR control region, has a central value of 0.707 and is inconsistent with 1.0. This is because the $t\bar{t}$ MC overestimates the amount of $t\bar{t}$ +hard ISR.

leads to uncertainty in the calorimeter response.

Jet energy scale uncertainties are derived from different in-situ techniques by the ATLAS Jet/ E_T^{miss} group. These techniques exploit the transverse momentum balance between a jet and a reference object such as a photon, a Z boson, or another jet.^{6,7}. The jet energy scale uncertainty depends on η and p_T of the jet. Uncertainties related to jet flavor composition and pile-up are also included.

The $t\bar{t}$ control region requires similar jet multiplicity and jet energy as the signal region. Therefore, much of the jet energy scale and jet energy resolution uncertainties are canceled out in the transfer factor between the control and signal regions. Even after the cancelations, the jet energy scale uncertainty contributes a $\sim 10\%$ uncertainty to background yields and is one the major systematic uncertainties in this analysis.

The fractional jet energy scale uncertainty as a function of η and p_T for 2016 data can be seen in Figures 14.2 and 14.3.

Uncertainties on the jet energy resolution are derived from dijet balance techniques.⁶ The fractional uncertainty on jet energy resolution as a function of η and p_T can be seen in Figures 14.4 and 14.5.

14.1.2 Uncertainty on b -tagging Efficiency

The b -tagging uncertainty is derived by the ATLAS flavor-tagging working group. A separate set of weights are applied for each set of b -tagging variations. These

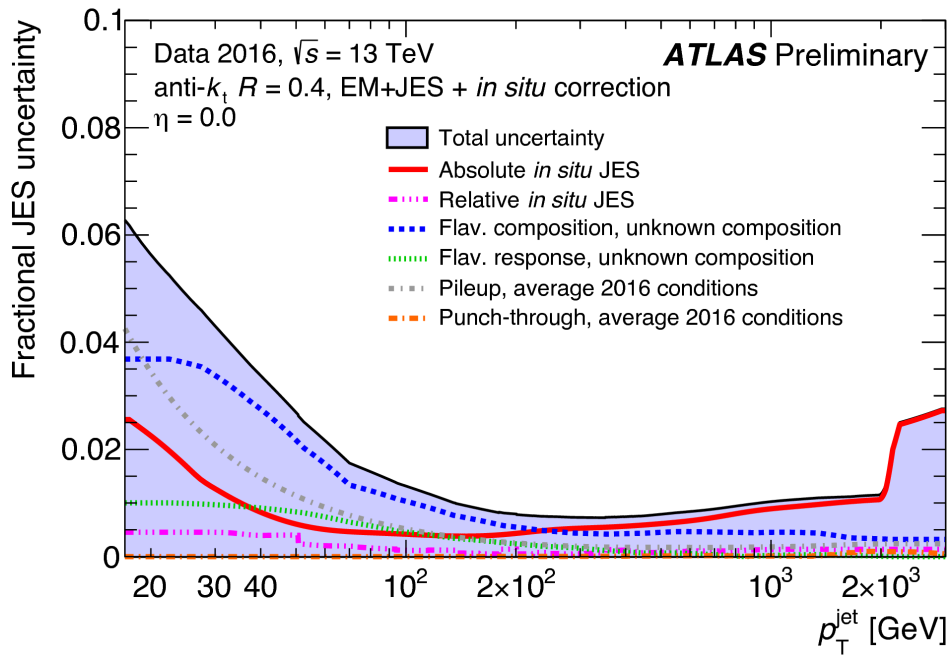


Figure 14.2: The fractional uncertainty on the jet energy scale as a function of jet p_T . The total uncertainty is shown as the solid shaded distribution. The different solid and dashed lines represent different sources of uncertainty on the jet energy scale. This distribution is for central jets with $\eta = 0.0$ and the uncertainties are averaged over ϕ .

include scale factors on b -tagging efficiencies and the rate of mis-tagging of c -jets and light-flavored jets. The b -tagging efficiency uncertainty as a function of jet p_T in $t\bar{t}$ is shown as the green shaded region in Figure 14.6.

The uncertainty on b -tagging does not contribute a large systematic uncertainty to our analysis because we only require one b -tagged jet with $p_T > 40$ GeV. The $p_T > 40$ GeV requirement avoids the large uncertainty on b -tagging efficiency at low p_T .

At the same time, there is little extrapolation between background control re-

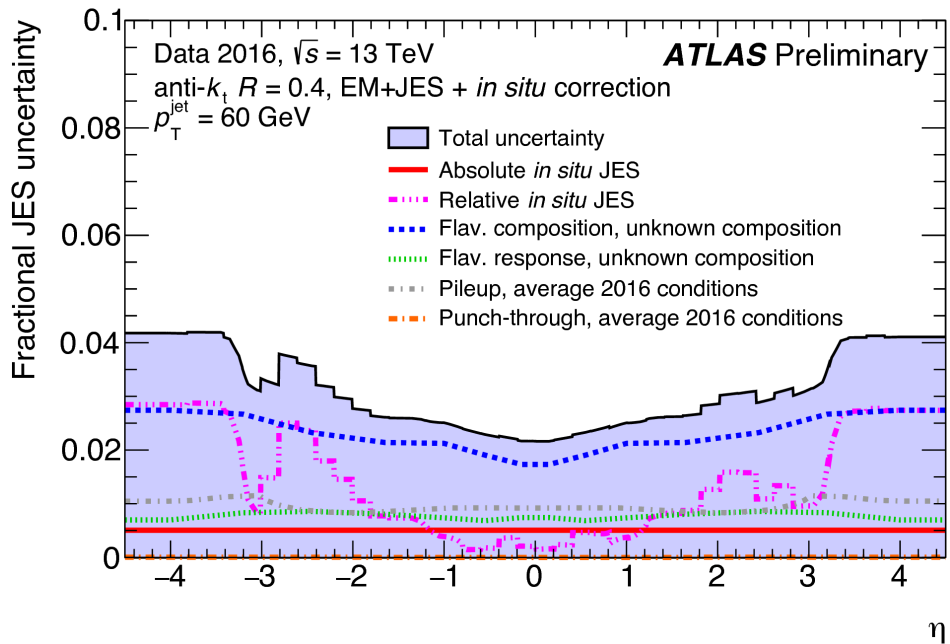


Figure 14.3: The fractional uncertainty on the jet energy scale as a function of jet η . The total uncertainty is shown as the solid shaded distribution. The different solid and dashed lines represent different sources of uncertainty on the jet energy scale. This distribution is for jets with $p_T = 60$ GeV and the uncertainties are averaged over ϕ .

gions and the signal region. The $t\bar{t}$, $W+jets$ and QCD multijets all use control regions that also require one b -tagged jet. After fitting to control regions, b -tagging systematics amount to only a 1-3% uncertainty on the total background rate in the signal region.

14.1.3 Uncertainty on the E_T^{miss} Soft Term

The E_T^{miss} is defined in equation 14.1 as the negative vector sum of all hard reconstructed objects and a “soft term”. Hard objects include reconstructed electrons,

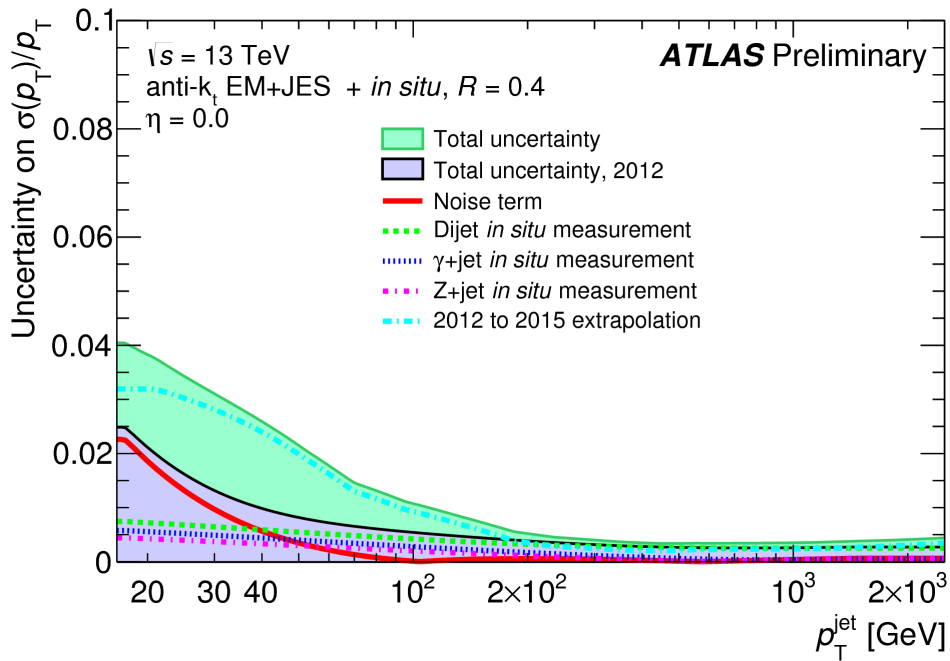


Figure 14.4: The fractional uncertainty on the jet energy scale as a function of jet p_T . The total uncertainty is shown as the solid shaded distribution. The different solid and dashed lines represent different sources of uncertainty on the jet energy scale. This distribution is for central jets with $\eta = 0.0$ and the uncertainties are averaged over ϕ .

photons, jets, and muons. The soft term is determined by summing over the p_T of all ID tracks that aren't associated with any hard objects and is intended to estimate all the energy not associated with any hard reconstructed objects. Although the soft term only registers the p_T from charged objects, it is able to effectively reject any energy deposited by pile-up interactions because ID tracks can be associated with the hard interaction primary vertex.

$$E_T^{\text{miss}} = - \left(\sum_{\text{hard objects}} E_T + \sum_{\text{soft}} E_T \right) \quad (14.1)$$

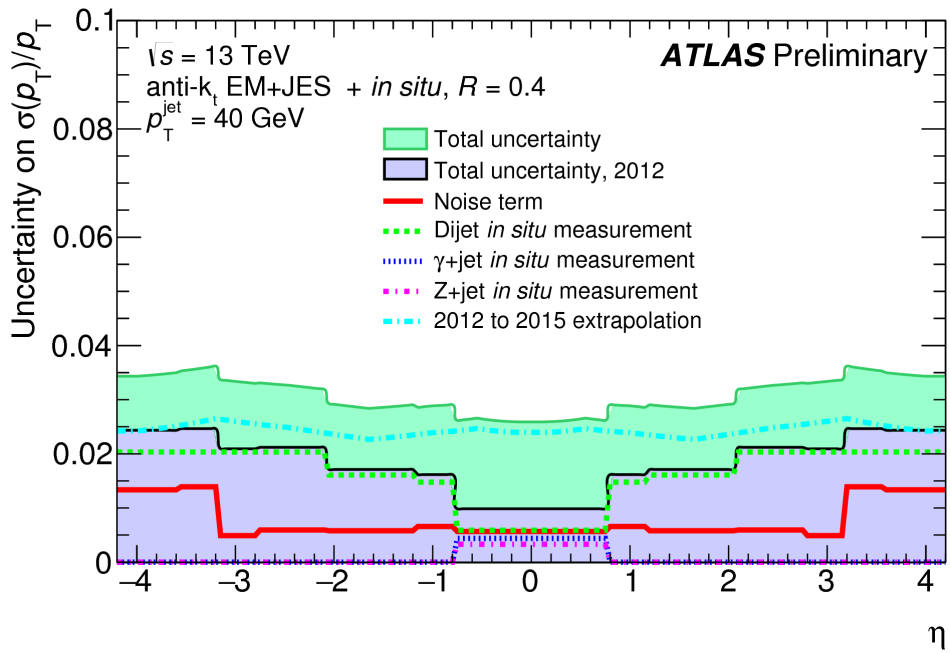


Figure 14.5: The fractional uncertainty on the jet energy scale as a function of jet η . The total uncertainty is shown as the solid shaded distribution. The different solid and dashed lines represent different sources of uncertainty on the jet energy scale. This distribution is for jets with $p_T = 60$ GeV and the uncertainties are averaged over ϕ .

The majority of the uncertainty on E_T^{miss} has already been accounted for by systematics on other reconstructed objects because the E_T^{miss} is built mostly out of fully calibrated and reconstructed physics objects. However, there is one term in the E_T^{miss} reconstruction that is independent of any hard reconstructed object; the E_T^{miss} soft term or $\sum_{\text{soft}} E_T$. The purpose of the E_T^{miss} soft term is to take into account the E_T from objects that are too soft to be reconstructed. Therefore, the uncertainty on the E_T^{miss} soft term forms an independent systematic uncertainty.

The uncertainty on the E_T^{miss} soft term resolution and scale is derived by the AT-

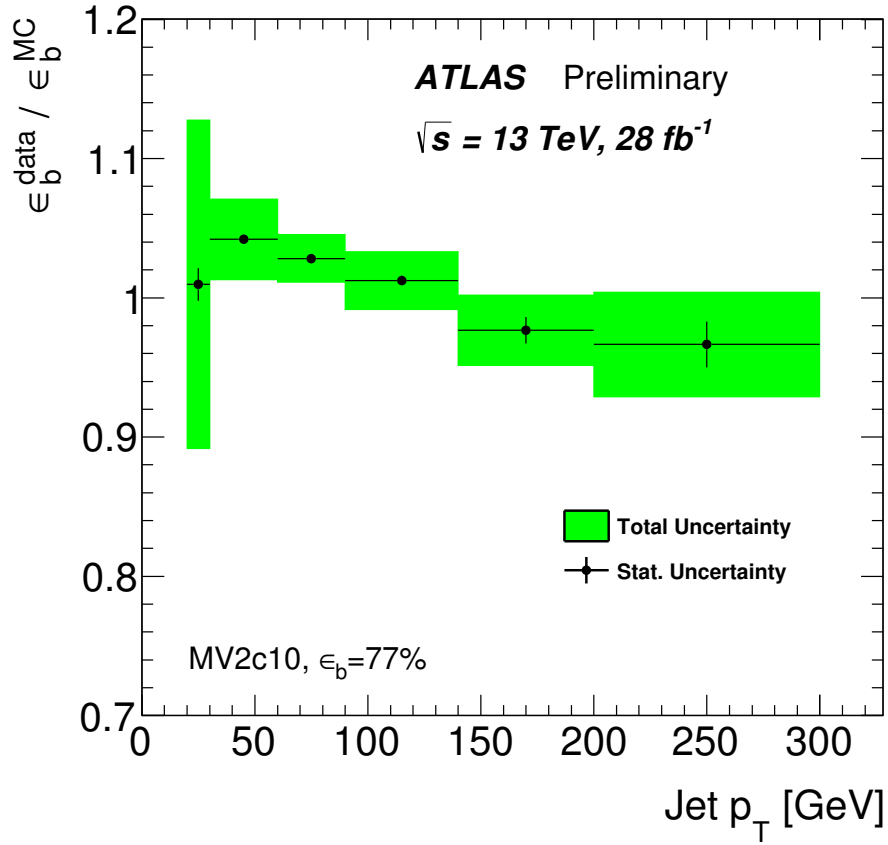


Figure 14.6: Ratio of b-tagging efficiency in data and Monte Carlo for the MV2c10 b-tagging algorithm at the 77% working point as a function of jet p_T . The b-tagging efficiency was extracted from a $t\bar{t}$ enriched region. Statistical errors (black lines) and total errors (green shaded region) are shown. The bin below a p_T of 30 GeV has large uncertainties.

LAS Jet/ E_T^{miss} group from two in-situ methods. Both methods measures the amount of E_T^{miss} in $Z \rightarrow \mu\mu$ events which are expect to contain little intrinsic E_T^{miss} .¹² Hence, the reconstructed E_T^{miss} is expected to come from mainly the E_T^{miss} soft term, instead of an imbalance in hard reconstructed objects.

The uncertainty on the E_T^{miss} track soft term (TST) vs the number of reconstructed

primary vertexes in $t\bar{t}$ simulation is shown in Figure 14.7.

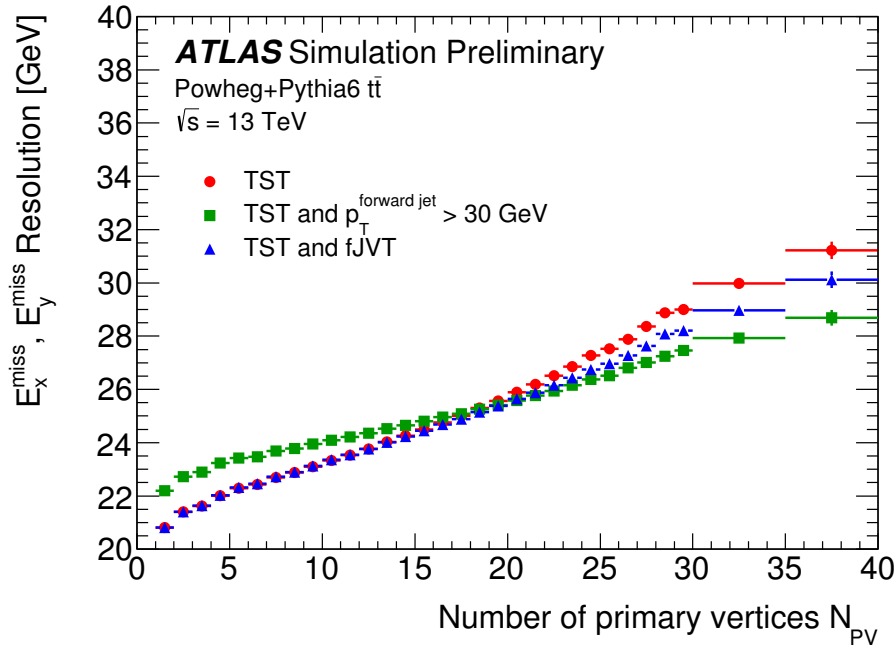


Figure 14.7: Uncertainty on the E_T^{miss} track soft term as a function the number of reconstructed vertexes. More reconstructed vertexes means more pile-up interactions are in the event.

The E_T^{miss} soft term resolution and scale uncertainty contribute a 1 – 2% uncertainty on the total background yield. The small uncertainty result from the high E_T^{miss} requirement of at least 250 GeV and little to no extrapolation across E_T^{miss} between the control and signal regions for all major backgrounds.

14.1.4 Uncertainties on Lepton Reconstruction and Resolution

Uncertainties on lepton reconstruction and identification propagate to uncertainties on control and signal region yields. These uncertainties include uncertainties on e/γ resolution, energy scale, and reconstruction efficiency and muon momentum and reconstruction efficiency. Lepton trigger scale factors are also taken into account for the $t\bar{t} + \gamma$ control region.

These uncertainties are derived by the ATLAS E/γ and muon combined performance groups and result in sub 1% uncertainty on signal region yields.^{41,17}

14.1.5 Pile-up Uncertainty

The uncertainty on the amount of pile-up in 2015 and 2016 ATLAS data is estimated using a two sided variation in event weights. One set of weights simulates a lower rates of pile-up interactions and the other set simulates a higher rate. Pile-up uncertainty contributes a 1-2% uncertainty on the total background yield in the signal region.

14.2 Theoretical Uncertainties

Theoretical uncertainties quantify the uncertainty associated with MC generation including different scale parameters such as QCD renormalization, factorization scales and calculations on the matrix element and parton shower. We vary MC generation

with respect to the default setting and get different MC yields in the control and signal regions. Because the background rate is normalized to the data in the control region, only differences in the transfer factor (defined in equation 14.2) will result in a different signal region background prediction.

$$T = \frac{N_{MC}^{SR}}{N_{MC}^{CR}} \quad (14.2)$$

N_{MC}^{SR} is the MC yield in the signal region and N_{MC}^{CR} is the MC yield in the control region.

We determine the variation in the signal region background prediction according to the variation in the transfer factor as defined in equation 14.3. All theoretical uncertainties for different backgrounds are assumed to be independent of one another.

$$\Delta_x = \frac{T_f^{\text{up}} - T_f^{\text{down}}}{T_f^{\text{up}} + T_f^{\text{down}}} \quad (14.3)$$

T_f^{up} (T_f^{down}) is the transfer factor defined in equation 14.2 for the upward (downward) variation in the systematics and Δ_x is the uncertainty due to parameter X in the signal region.

14.2.1 $t\bar{t}$ Theoretical Uncertainty

Theoretical uncertainties on $t\bar{t}$ production include uncertainties on the hard scattering matrix element calculation, uncertainties on the parton shower, and uncertainty on the amount of ISR/FSR produced in association with $t\bar{t}$.

The $t\bar{t}$ ISR/FSR uncertainty is estimated by producing *PowHegPYTHIA* MC samples with a different amount of radiation than the nominal MC sample. These ISR/FSR variation samples are called the radHi and radLo samples. In general, the radHi (radLo) sample generates a higher (lower) differential cross-section for $t\bar{t}$ that is produced in conjunction with hard ISR.

The radHi and radLo samples are produced with different renormalization and factorization scales compared to the nominal sample (x0.5 to radHi and x2 to radLo). The radHi sample also increase the h_{damp} parameter which controls the matching between the parton shower and matrix element calculations. The h_{damp} parameter is increased from the nominal m_t to $2 \times m_t$ for the radHi sample.

The $t\bar{t}$ ISR/FSR uncertainty ($\Delta_{t\bar{t}ISR/FSR}$) is estimated using equation 14.4 where

T_f^{radHi} (T_f^{radLo}) is the transfer factor corresponding to the radHi (radLo) sample.

$$\Delta_{t\bar{t}ISR/FSR} = \frac{T_f^{\text{radHi}} - T_f^{\text{radLo}}}{T_f^{\text{radHi}} + T_f^{\text{radLo}}} \quad (14.4)$$

Uncertainties on the hard scattering and parton shower are calculated by comparing the nominal *PowHegPYTHIA* $t\bar{t}$ sample with the *PowHegHERWIG ++* $t\bar{t}$ and *SHERPA* 2.2.1 $t\bar{t}$ samples. The *PowHegHERWIG ++* sample has the same matrix element calculation as the nominal sample but uses *HERWIG ++* to perform a different set of parton shower calculation with a distinct parton shower tune. The *SHERPA* 2.2.1 $t\bar{t}$ sample perform a different matrix element and parton shower calculation using a different PDF set and parton shower tune. More details on the different $t\bar{t}$ MC generation can be found in section 7.4.

We take an envelope of the *SHERPA* and *PowHegHERWIG ++* variations as the combined $t\bar{t}$ hard scattering and parton shower uncertainty. This is because the *PowHegHERWIG ++* and *SHERPA* samples both vary the parton shower calculations. Taking an envelope of both variations instead of summing the two in quadrature avoids double counting the parton shower uncertainty. The total hard scattering plus parton shower uncertainty is defined as the maximum of equation 14.5 and 14.6.

$$\Delta_{\text{hard scatter}} = \frac{T_f^{\text{PowHegPYTHIA}} - T_f^{\text{SHERPA}}}{T_f^{\text{PowHegPYTHIA}}} \quad (14.5)$$

$$\Delta_{\text{PS}} = \frac{T_f^{\text{PowHegPYTHIA}} - T_f^{\text{PowHegHERWIG++}}}{T_f^{\text{PowHegPYTHIA}}} \quad (14.6)$$

$T_f^{\text{PowHegPYTHIA}}$, $T_f^{\text{PowHegHERWIG++}}$ and T_f^{SHERPA} correspond to the transfer factors derived by using the nominal *PowHegPYTHIA* $t\bar{t}$ MC, the *PowHegHERWIG++* $t\bar{t}$ MC and the *SHERPA* $t\bar{t}$ MC. $\Delta_{\text{hard scatter}}$ is the uncertainty on the hard scattering calculation and Δ_{PS} is the uncertainty on the parton shower calculation.

The MC $t\bar{t}$ yields in the control region, validation region and signal region for the different $t\bar{t}$ samples and the $t\bar{t}$ theory uncertainties are given in Table 14.2.

Table 14.2: MC yields and theory uncertainties for the $t\bar{t}$ background for the control, validation and signal regions. MC yields are quoted for before any fitting to the data in the control region. Uncertainties are derived using variations in the transfer factor according to equations 14.4, 14.5 and 14.6. The uncertainties are symmetrical and are quantified as percentage of total background yield.

	CRTopC	VRTopC	SRC1	SRC2
$t\bar{t}$ (nominal)	668 ± 9	232 ± 5	16.7 ± 1.6	31.7 ± 2.1
$t\bar{t}$ (rad up)	872 ± 11	293 ± 7	25.2 ± 2.3	39.5 ± 2.3
$t\bar{t}$ (rad down)	521 ± 9	187 ± 5	10.1 ± 1.0	19.2 ± 1.6
$t\bar{t}$ (Powheg+H++)	621 ± 10	206 ± 5	16.3 ± 1.8	27.8 ± 1.8
$t\bar{t}$ (Sherpa)	840 ± 40	297 ± 30	30 ± 8	42 ± 9
Transfer factors (in %)				
ISR/FSR		3.3	20	10
PS		4	5	6
Generator (Sherpa)		2	40	5
	SRC3	SRC4	SRC5	
$t\bar{t}$ (nominal)	21.7 ± 1.6	6.3 ± 0.8	0.60 ± 0.23	
$t\bar{t}$ (rad up)	28.7 ± 2.1	8.6 ± 1.0	1.05 ± 0.33	
$t\bar{t}$ (rad down)	15.8 ± 1.5	6.3 ± 1.2	0.7 ± 0.4	
$t\bar{t}$ (Powheg+H++)	18.0 ± 1.5	6.5 ± 0.9	0.46 ± 0.18	
$t\bar{t}$ (Sherpa)	22 ± 5	7.4 ± 3.2	< 0.01	
Transfer factors (in %)				
ISR/FSR	4	10	5	
PS	11	11	20	
Generator (Sherpa)	19	10	100	

14.2.2 $W +$ jets Theoretical Uncertainty

The *SHERPA* generator is used to estimate $W +$ jets theory uncertainties. Variations of the renormalization and factorization scales are included. The uncertainty for each variation is quantified as the uncertainty on the transfer factor according to

equation 14.3. The total W +jets theory uncertainty is the combination of all uncertainties summed in quadrature.

The total theory uncertainty on $W +$ jets in the signal region is given in Table 14.3. Values are given as percent uncertainties on $W +$ jets yields in the signal region. The uncertainties are symmetrical.

Table 14.3: Summary of the theory uncertainties (in percent) on W production obtained using variations on transfer factors. The uncertainties are symmetrical and are quantified as percentage of total background yield.

SR	uncertainty (%)
SRC1	12.5
SRC2	11.8
SRC3	10.7
SRC4	9.5
SRC5	11.3

14.2.3 Single-top Theoretical Uncertainty

Single-top theoretical uncertainties include the uncertainties on the parton shower, ISR/FSR, and the interference between $t\bar{t}$ and single-top in the Wt channel. Single-top uncertainties are evaluated for the Wt subprocess because the Wt subprocess dominates the single-top background in the signal region. A Feynman diagram for Wt production is given in Figure 14.8.

The single-top parton shower uncertainty is modeled by comparing the nominal *PowHegPYTHIA* sample with a *PowHegHERWIG ++* single-top sample in a similar

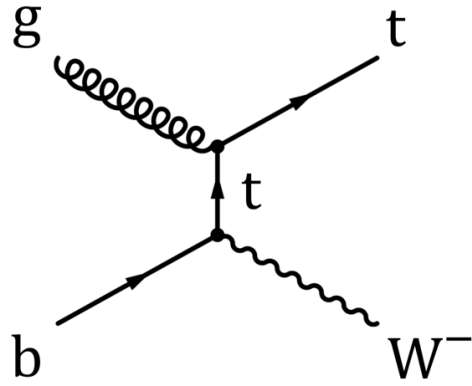


Figure 14.8: Single top production Feynman diagram for the Wt channel.

fashion to the $t\bar{t}$ parton shower uncertainty in section 14.2.1.

The single-top ISR/FSR uncertainty is also modeled by comparing the radHi and radLo PowHegPYTHIA single-top samples to the nominal PowHegPYTHIA samples. This method is completely analogous to the modeling of the $t\bar{t}$ ISR/FSR uncertainty.

The single-top interference uncertainty refers to the fact that there is an uncertainty in how to treat the interference between single-top and SM $t\bar{t}$. The NLO calculation of the $pp \rightarrow Wt$ process will include contributions from $pp \rightarrow t\bar{t} \rightarrow t + b + W$ process which is already included in the SM $t\bar{t}$. In order to avoid double counting with SM $t\bar{t}$, we can subtract out the $pp \rightarrow t\bar{t} \rightarrow t + b + W$ contribution.

However, it is uncertain whether this subtraction should be done at either the amplitude level (DR scheme) or at the matrix element level (DS scheme). Subtracting at the matrix element level also removes any potential interference between the single-top $pp \rightarrow Wt$ and the $pp \rightarrow t\bar{t} \rightarrow t + b + W$ processes. Subtracting at the amplitude level does not remove those interferences.

Both the DR and DS schemes violate formal gauge invariance and there is no consensus on the correct procedure to treat the single-top and $t\bar{t}$ interference. We quantify the interference uncertainty by taking the difference between the DR and DS schemes. At the moment we take an 100% interference uncertainty because of the low MC statistics in DS scheme.

The single-top MC yields and theory uncertainties are given in Table 14.4. The MC yields corresponding to different single-top MC samples are given for control, validation and signal regions. The single-top theory uncertainties are derived using transfer factors.

14.2.4 $t\bar{t} + W/Z$ Theoretical Uncertainty

The $t\bar{t} + W/Z$ theoretical uncertainty include scale variations and variations on the underlying event tuning. An additional uncertainty on the difference between the $t\bar{t}\gamma$ and $t\bar{t}Z$ vector boson p_T differential cross sections is added to the total $t\bar{t} + W/Z$ uncertainty due to the procedure of using $t\bar{t}+\gamma$ to estimate $t\bar{t}+W/Z$. The *SHERPA+OpenLoops* program³⁹ is used to calculate $t\bar{t}\gamma$ and $t\bar{t}Z$ vector boson differential cross-sections to

Table 14.4: Summary of the single-top (ST) theory uncertainties obtained in each of the signal regions. The uncertainties are computed according to the variation on the transfer factor defined in equation 14.3. The uncertainties are symmetrical and are quantified as percentage of total background yield.

	CRST	VRTopC	SRC1	SRC2
ST (nominal)	41.7 ± 1.1	19.9 ± 0.8	0.66 ± 0.14	1.14 ± 0.18
ST (radHi)	50.4 ± 1.3	21.9 ± 0.8	0.60 ± 0.14	1.26 ± 0.20
ST (radLo)	34.9 ± 1.0	16.9 ± 0.7	0.57 ± 0.13	0.77 ± 0.15
ST (Powheg+H++)	39.2 ± 1.0	18.7 ± 0.7	0.62 ± 0.13	0.84 ± 0.16
ST (DS)	6.8 ± 0.4	4.39 ± 0.31	0.12 ± 0.05	0.30 ± 0.09
Transfer factors (in %)				
ISR/FSR		5.4 ± 3.4	16 ± 17	6 ± 13
PS		0 ± 7	0 ± 30	22 ± 22
Interference (DR vs DS)		35 ± 13	10 ± 50	60 ± 50
	SRC3	SRC4	SRC5	
ST (nominal)	0.99 ± 0.17	0.39 ± 0.11	0.12 ± 0.06	
ST (radHi)	1.33 ± 0.21	0.57 ± 0.14	0.25 ± 0.09	
ST (radLo)	0.77 ± 0.15	0.37 ± 0.10	0.09 ± 0.05	
ST (Powheg+H++)	0.79 ± 0.15	0.38 ± 0.10	0.08 ± 0.05	
ST (DS)	0.23 ± 0.08	0.16 ± 0.06	0.020 ± 0.020	
Transfer factors (in %)				
ISR/FSR	9 ± 13	3 ± 18	32 ± 32	
PS	15 ± 24	0 ± 40	30 ± 70	
Interference (DR vs DS)	40 ± 50	150 ± 110	0 ± 110	

NLO accuracy. The difference between *SHERPA+OpenLoops* and the nominal MadGraph5_aMC@NLO cross-sections is combined in quadrature with the variations on the scale and the underlying event tune to give the total $t\bar{t} + W/Z$ theoretical uncertainty.

The $t\bar{t} + W/Z$ theoretical uncertainty is given in Table 14.5. The systematic uncer-

tainty maybe large for $t\bar{t} + W/Z$ production in the signal region but $t\bar{t} + W/Z$ comprise about 1% of our expected background. Therefore uncertainties on the $t\bar{t} + W/Z$ process do not contribute significantly to the total background uncertainty in the analysis.

Table 14.5: Summary of the theory uncertainties (in percent) on $t\bar{t} + W/Z$ production obtained on the transfer factor. The uncertainties are symmetrical and are quantified as percentage of total background yield.

SR	uncertainty (%)
SRC1	95.5
SRC2	20.6
SRC3	21.4
SRC4	36.6
SRC5	30.9

14.2.5 Dibosons Theoretical Uncertainty

A 50% theory uncertainty is applied to the dibosons MC estimate.

14.2.6 Z+jets Theoretical Uncertainty

A 50% theory uncertainty is applied to the Z + jets MC estimate.

15

Results and Conclusion

The signal region R_{ISR} distribution after unblinding is shown in Figure 15.1. The solid stacked histogram corresponds to the expected SM background rate. The expected background rates have been normalized to all control regions using the background-only fitting procedure described in section 13.4. The hashed bars correspond to the systematic uncertainty on the total SM background rate.

The observed data is shown as black data points. The dashed histograms correspond to the expected signal rates for stop signals with $(m_{\tilde{t}}, m_{\tilde{\chi}_1^0}) = (400 \text{ GeV}, 227 \text{ GeV})$ and $(500 \text{ GeV}, 327 \text{ GeV})$ with a 100% branching fraction to the $\tilde{t} \rightarrow t\tilde{\chi}_1^0$ decay channel.

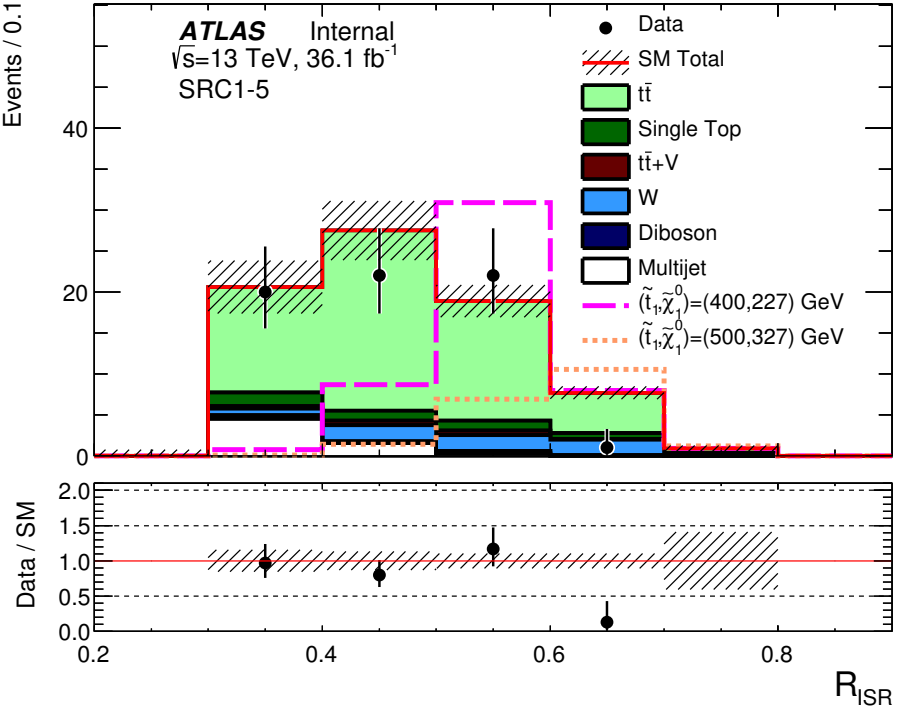


Figure 15.1: Unblinded R_{ISR} distributions for SRC1-5 for 36.07 fb^{-1} . The solid stacked histogram corresponds to the expected SM background rate. The expected background rates have been normalized to all control regions using the background-only fitting procedure. The hashed bars correspond to the systematic uncertainty on the total SM background rate. The observed data is shown as black data points. The dashed histograms correspond to the expected signal rates for stop signals with $(m_{\tilde{t}}, m_{\tilde{\chi}_1^0}) = (400 \text{ GeV}, 227 \text{ GeV})$ and $(500 \text{ GeV}, 327 \text{ GeV})$ with a 100% branching fraction to the $\tilde{t} \rightarrow t\tilde{\chi}_1^0$ decay channel

The peaking feature of the signal can be clearly seen in Figure 15.1. The width of

the signal peak in R_{ISR} is $\sim 8\%$ for all signal masses as long as the $\Delta m = m_{\tilde{t}} - m_{\tilde{\chi}_1^0} = m_t$.

Signal region yields with 36.07 fb^{-1} of data can be seen in Table 15.1. No significant excess is observed in any region. Only 1 data event is observed in the R_{ISR} bin between $0.6 - 0.7$ compared to the ~ 8 expected events due to SM background. However, this disagreement is not statistically significant due to the low number of expected events.

95% upper confidence limits on the number of signal events (S_{obs}^{95}) and on the observed cross section ($\langle\epsilon\sigma\rangle_{\text{obs}}^{95}$) in each R_{ISR} bin is shown in Table 15.2. The limit on the number of signal events is a statement on the maximum BSM event rate that can exist in the signal region without being ruled out at the 95% confidence level. The limit remains the same regardless of the particular BSM physics process used to produce the signal events. As such, the limit on the number of signal events is mostly theory independent.

The observed signal cross section is defined as the number of BSM events predicted to exist in the signal region. The observed signal cross section is equivalent to the signal region selection efficiency times the signal production cross section for any particular BSM physics model. The limit on the observed signal cross section is also equivalent to the limit on the number of signal events divided by the integrated luminosity.

Observed limits are derived using the discovery fit procedure described in section

Table 15.1: The observed data rate and the expected background rate in the signal region for an integrated luminosity of 36.07 fb^{-1} . The quoted uncertainties include both statistical and systematic uncertainties.

SRC yields	SRC1	SRC2	SRC3
Observed events	20	22	22
Expected bkg events	21.02 ± 6.62	28.42 ± 4.89	19.60 ± 3.53
Expected TTbar events	12.85 ± 5.87	22.05 ± 4.19	14.57 ± 3.23
Expected Wjets events	0.81 ± 0.37	1.93 ± 0.48	1.91 ± 0.63
Expected Zjets events	0.46 ± 0.09	0.90 ± 0.13	0.74 ± 0.15
Expected TtbarV events	0.29 ± 0.18	0.59 ± 0.38	0.56 ± 0.31
Expected SingleTop events	$1.67^{+2.02}_{-1.67}$	$1.18^{+1.81}_{-1.18}$	$1.22^{+1.37}_{-1.22}$
Expected Diboson events	0.39 ± 0.33	0.21 ± 0.11	0.29 ± 0.18
Expected Multijets events	4.56 ± 2.38	1.58 ± 0.77	0.32 ± 0.17
SRC yields	SRC4	SRC5	
Observed events	1	0	
Expected bkg events	8.14 ± 1.39	0.99 ± 0.71	
Expected TTbar events	4.92 ± 0.98	$0.63^{+0.69}_{-0.63}$	
Expected Wjets events	1.93 ± 0.45	0.21 ± 0.12	
Expected Zjets events	0.45 ± 0.24	0.09 ± 0.04	
Expected TtbarV events	0.08 ± 0.08	0.06 ± 0.03	
Expected SingleTop events	$0.72^{+0.77}_{-0.72}$	0.00 ± 0.00	
Expected Diboson events	0.00 ± 0.00	0.00 ± 0.00	
Expected Multijets events	0.04 ± 0.02	0.00 ± 0.00	

13.6. Discovery p-values ($p(s = 0)$) are calculated using the discovery fit and are also shown in Table 15.2.

Table 15.2: The first two column show the 95% CL upper limits on the observed signal cross section ($\langle\epsilon\sigma\rangle_{\text{obs}}^{95}$) and on the number of signal events (S_{obs}^{95}). The third column, (S_{exp}^{95}), shows the 95% confidence limit on the number of signal events, for the expected number of background events. The last two columns shows the confidence level observed for the background-only hypothesis (CL_B , and the discovery p -value ($p(s = 0)$).

Signal channel	$\langle\epsilon\sigma\rangle_{\text{obs}}^{95} [\text{fb}]$	S_{obs}^{95}	S_{exp}^{95}	CL_B	$p(s = 0) (Z)$
SRC1	0.44	16.0	$16.3^{+5.8}_{-4.2}$	0.47	0.50 (0.00)
SRC2	0.35	12.6	$15.5^{+5.9}_{-4.2}$	0.26	0.50 (0.00)
SRC3	0.44	15.8	$12.8^{+4.7}_{-2.7}$	0.69	0.30 (0.54)
SRC4	0.09	3.1	$6.5^{+3.3}_{-2.1}$	0.02	0.50 (0.00)
SRC5	0.06	2.2	$2.8^{+2.0}_{-1.1}$	0.32	0.49 (0.02)

15.1 Interpretation of Results on Different Stop Models

Since no significant excesses were observed in the signal region, the results are interpreted as exclusions on the stop parameter space. The 95% confidence limit is shown in Figure 15.2. The maroon curve corresponds to the observed 95% confidence limit on the $\Delta m = m_{\tilde{t}} - m_{\tilde{\chi}_1^0}$, $m_{\tilde{t}}$ plane derived from 36.07 fb^{-1} of ATLAS p-p collision data. The solid blue curve corresponds to the expected 95% confidence limit. The expected limit quantifies the expected sensitivity of the search if the background predictions are correct and no signal were present.

The exclusion confidence limit values (CL_s) are derived using the exclusion fit procedure described in section 13.5 where all 5 bins in R_{ISR} and all control regions are simultaneously fitted. The simultaneous fit to all 5 R_{ISR} bins is designed to capture the feature of a sharp signal peak against a broad background in R_{ISR} .

Stop exclusion limits from previous ATLAS searches on 8 TeV p-p collision dataset
are shown in blue for comparison.

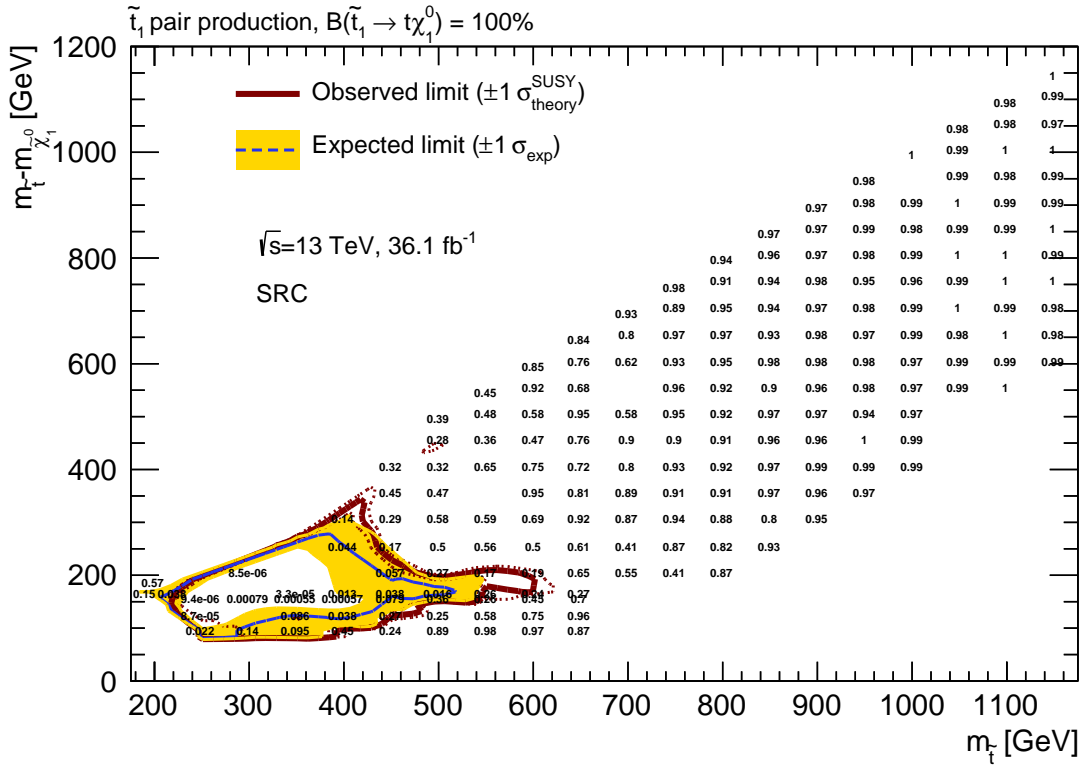


Figure 15.2: 95% confidence limit curves in the stop, neutralino parameter space from a simultaneous fit to the compressed stop analysis control regions and signal region (SRC). Y-axis correspond to the mass splitting between stops and neutralinos, with $\Delta m = m_{\tilde{t}} - m_{\tilde{\chi}_1^0}$, and x-axis is the stop mass, $m_{\tilde{t}}$. The solid blue and maroon curve correspond to the expected and observed 95% confidence limit curve in the Δm , $m_{\tilde{t}}$ plane. The region enclosed by the curves are excluded. The dashed red line is the 95% confidence limit on stop signal with a 1σ increase/decrease in signal production cross section. The shaded yellow region correspond to the 1σ variation on the expected limit curve. The best sensitivity is along the $\Delta m = m_t$ horizontal line. 95% confidence limits extend to a wide range of Δm , close to the $\Delta m = m_W + m_b$ line at the bottom and upwards of $\Delta m > m_t + 30$ GeV. We are able to exclude stop masses between 225 GeV and 600 GeV if $\Delta m = m_t$. The expected sensitivity of the analysis, quantified in terms of expected CL_s values for different stop samples, are the numbers written on the histogram. The location of the number on the Δm , $m_{\tilde{t}}$ plane corresponds to the stop, neutralino mass point for the expected CL_s value.

The compressed stop analysis fills in the gap in exclusion along the $\Delta m = m_t$ diagonal line left unconstrained by previous ATLAS searches for stops using the 8 TeV p-p collision dataset. The analysis is able to exclude stops from 225 GeV to 600 GeV in the $\Delta m = m_t$ region with expected CL_s values below 5×10^{-4} for stop mass between 250 and 400 GeV. The analysis also extends the zero lepton sensitivity far into the 3 body decay region almost to the $\Delta m = m_W + m_b$ line.

Figure 15.3 shows the compressed stop analysis exclusion limit (SRC) combined with the bulk region stop zero-lepton analysis exclusion limit (SRA+SRB) using 36.07 fb^{-1} of 13 TeV ATLAS p-p collision data.

The bulk region stop zero-lepton analysis targets the high stop mass parameter space with large mass splitting between stop and neutralino masses. In this region of phase space, the stop decay gives a large amount of momentum to the resulting neutralinos. The bulk region analysis selects events with high E_T^{miss} to separate signal from background. Because of this, the bulk region analysis's strategy loses sensitivity as Δm approaches m_t . A detailed description of the bulk region stop zero-lepton analysis can be found in reference [21].

The bulk region analysis is sensitive to stop masses up $\sim 900 - 1000$ GeV if the neutralino mass is below ~ 350 GeV. The compressed region analysis adds sensitivity to the $\Delta m = m_t$ diagonal region where the bulk region analysis and previous ATLAS stop searches lack sensitivity. The exclusion limit for the compressed analysis and the bulk region analysis are combined by simply selecting the lowest CL_s value

at each stop and neutralino mass. No statistical combinations are made between the two analyses because the two analyses signal regions are not orthogonal to one another.

Figure 15.4 show how the exclusion limit changes for stops with different branching fractions to the $\tilde{t} \rightarrow t + \tilde{\chi}_1^0$ decay channel and the $\tilde{t} \rightarrow b + \tilde{\chi}_1^\pm$ decay channel. As the $\tilde{t} \rightarrow t + \tilde{\chi}_1^0$ branching fraction decreases, the $\tilde{t} \rightarrow b + \tilde{\chi}_1^\pm$ branching fraction increases with total branching ratio of the two channels summing to 100%. Sensitivity from another signal region (SRD) that directly targets the mixed decay channel is combined with the compressed analysis (SRC) and the bulk region analyses (SRA+SRB). Detailed documentation on the mixed decay analysis can also be found in reference [²¹]. Again the compressed analysis is responsible for the exclusion of stop parameter space along the $\Delta m = m_t$ diagonal line when branching fraction to $\tilde{t} \rightarrow t + \tilde{\chi}_1^0$ is high.

15.2 Broader Applications of the ISR Identification Algorithm

This analysis serves as a demonstration of the general strategy of using events with hard ISR to search for other BSM signatures with E_T^{miss} . The correlations between E_T^{miss} and ISR in compressed regions are mainly dictated by special relativity. If the new BSM particle has a small mass splitting between it and its decay products, its decay products will gain little momenta from the decay. In events with hard ISR, the

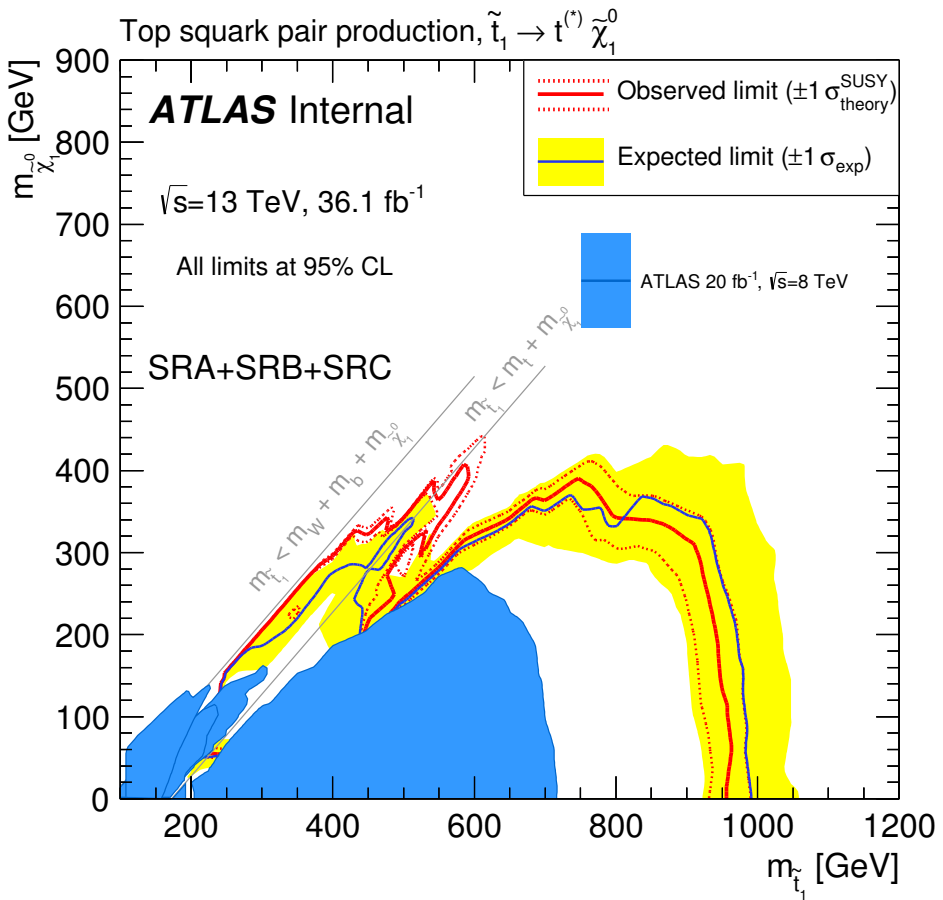


Figure 15.3: 95% confidence limit curves in the stop, neutralino mass parameter space for the compressed stop analysis (SRC) and the bulk region stop 0L analysis (SRA+SRB). The solid red (black) line correspond to the 95% confidence observed (expected) limit curve from all three analysis combined. All regions below the curve has been excluded to the 95% confidence level. The dashed red line is the 95% confidence limit on stop signal with a 1σ increase/decrease in signal production cross section. The shaded yellow region correspond to the 1σ variation on the expected limit curve. The variation on the expected limit curve is derived by fitting independent toy experiments and deriving an envelope of confidence limits. 95% confidence limits from previous ATLAS stop searches using the 8 TeV collision dataset are shown as the shaded blue region for comparison. The SRA and SRB analyses target high stop masses with large Δm and medium amount of Δm . Together these two analyses are sensitive to stop masses up $\sim 900 - 1000$ GeV if the neutralino mass is below ~ 350 GeV. SRC correspond to the compressed region analysis and adds sensitivity to the $\Delta m = m_t$ diagonal region where SRA, SRB and the 8 TeV ATLAS stop searches lack sensitivity.

correlations between ISR and the decay products will be strong because the decay products are gaining the majority of their momenta from the ISR boost.

The ISR identification algorithm is also completely generalizable. The thrust axis will mimic the axis of back-to-back recoil between ISR and hard scattering particles so long as the ISR is energetic enough to be the single largest back-to-back kick in the event. This ISR based approach has potential applications to other searches for SUSY including searches for Higgsinos and Charginos.

Other ISR assisted searches such as the mono-jet/mono-photon searches for dark-matter can also benefit from such an accurate ISR identification algorithm. Even in situations where the thrust-based ISR identification algorithm doesn't improve separation power between signal and background, using the thrust based algorithm can still significantly reduce ISR/FSR uncertainties. The thrust based ISR algorithm identifies entire ISR systems and is insensitive to uncertainties associated with a single hard ISR parton splitting into multiple jets.

At the same time, the accurate ISR identification algorithm can also be used to measure the Standard Model production of hard ISR. The thrust based algorithm is able to effectively separate $t\bar{t}$ produced with around 550 GeV of ISR p_T from $t\bar{t}$ with low ISR p_T as demonstrated by the $t\bar{t}$ +hard ISR control region. Current $t\bar{t}$ ISR p_T differential cross section measurements at ATLAS identify ISR by first attempting to reconstruct tops and then identifying all non-top jets as ISR jets.¹⁸ Hadronic top reconstruction efficiency is extremely correlated with top p_T with a top reconstruction

efficiency of only 30% at top $p_T = 200$ GeV. This means that $t\bar{t}$ ISR p_T measurements that require the reconstructed tops are inherently biased towards events with high hadronic top p_T .

Because the ISR algorithm primarily uses the thrust axis and properties of the entire $t\bar{t}$ system, we can avoid reconstructing individual tops but still identify a region with high purity of $t\bar{t}$ +hard ISR. This means we can independently measure the $t\bar{t}$ ISR p_T and the $t\bar{t}$ top p_T distributions and without being biased by one or the other. Plus we can avoid any top reconstruction inefficiencies leading to a higher acceptance of $t\bar{t}$ events.

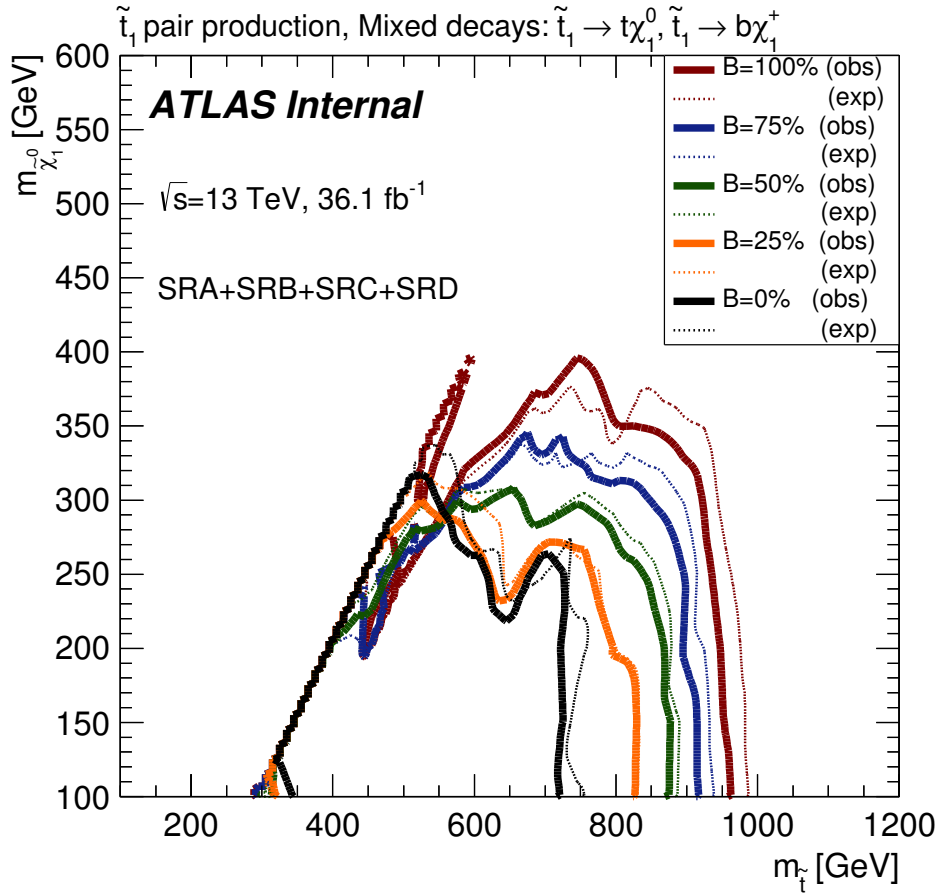


Figure 15.4: 95% confidence limit curves in the stop, neutralino mass plane for different branching ratios between the $\tilde{t} \rightarrow t\tilde{\chi}_1^0$ decay channel and the $\tilde{t} \rightarrow b\tilde{\chi}_1^\pm \rightarrow bW^{(*)}\tilde{\chi}_1^0$ decay channel. The different curves correspond to different branching ratio values of the $\tilde{t} \rightarrow t\tilde{\chi}_1^0$ decay channel: 0%, 25%, 50%, 75% and 100%. $m(\tilde{\chi}_1^\pm)$ is assumed to be $m(\tilde{\chi}_1^0) + 1\text{ GeV}$ which is a good assumption for some wino and Higgsino LSP SUSY models. The chargino and neutralino LSP should have a small mass difference if the LSP is a wino or a Higgsino because of the SU(2) symmetry in the weak interaction. The results are based on a combination of the compressed stop analysis (SRC) targeting $\tilde{t} \rightarrow t\tilde{\chi}_1^0$ with $\Delta m = m_{\tilde{t}} - m_{\tilde{\chi}_1^0} = m_t$, the bulk region stop zero-lepton search (SRA+SRB) targeting $\tilde{t} \rightarrow t\tilde{\chi}_1^0$ with $\Delta m >> m_t$ region, and the mixed decay stop search (SRD) targeting stops that decays via both the $\tilde{t} \rightarrow t\tilde{\chi}_1^0$ and $\tilde{t} \rightarrow b\tilde{\chi}_1^\pm$ decay channels. We combine the different analysis by selecting for the best expected CL_s value at each stop and neutralino mass for the specific branching ratio. The compressed analysis SRC adds sensitivity to the $\Delta m = m_t$ line when the branching fraction is mostly to $\tilde{t} \rightarrow t\tilde{\chi}_1^0$.

References

- [1] (2010). *Properties of Jets and Inputs to Jet Reconstruction and Calibration with the ATLAS Detector Using Proton-Proton Collisions at $\sqrt{s} = 7$ TeV*. Technical Report ATLAS-CONF-2010-053, CERN, Geneva.
- [2] (2012). Observation of a new particle in the search for the standard model higgs boson with the {ATLAS} detector at the {LHC}. *Physics Letters B*, 716(1), 1 – 29.
- [3] (2013). *Pile-up subtraction and suppression for jets in ATLAS*. Technical Report ATLAS-CONF-2013-083, CERN, Geneva.
- [4] (2014). *ATLAS Run 1 Pythia8 tunes*. Technical Report ATL-PHYS-PUB-2014-021, CERN, Geneva.
- [5] (2014). *Tagging and suppression of pileup jets with the ATLAS detector*. Technical Report ATLAS-CONF-2014-018, CERN, Geneva.
- [6] (2015a). *Data-driven determination of the energy scale and resolution of jets reconstructed in the ATLAS calorimeters using dijet and multijet events at $\sqrt{s} = 8$ TeV*. Technical Report ATLAS-CONF-2015-017, CERN, Geneva.
- [7] (2015b). *Determination of the jet energy scale and resolution at ATLAS using Z/γ -jet events in data at $\sqrt{s} = 8$ TeV*. Technical Report ATLAS-CONF-2015-057, CERN, Geneva.
- [8] (2015a). *Expected performance of missing transverse momentum reconstruction for the ATLAS detector at $\sqrt{s} = 13$ TeV*. Technical Report ATL-PHYS-PUB-2015-023, CERN, Geneva.
- [9] (2015). *Expected performance of the ATLAS b-tagging algorithms in Run-2*. Technical Report ATL-PHYS-PUB-2015-022, CERN, Geneva.

- [10] (2015). *Jet global sequential corrections with the ATLAS detector in proton-proton collisions at $\sqrt{s} = 8$ TeV.* Technical Report ATLAS-CONF-2015-002, CERN, Geneva.
- [11] (2015). *Monte Carlo Calibration and Combination of In-situ Measurements of Jet Energy Scale, Jet Energy Resolution and Jet Mass in ATLAS.* Technical Report ATLAS-CONF-2015-037, CERN, Geneva.
- [12] (2015b). *Performance of missing transverse momentum reconstruction for the ATLAS detector in the first proton-proton collisions at $\sqrt{s} = 13$ TeV.* Technical Report ATL-PHYS-PUB-2015-027, CERN, Geneva.
- [13] (2015). *Properties of Jets and Inputs to Jet Reconstruction and Calibration with the ATLAS Detector Using Proton-Proton Collisions at $\sqrt{s} = 13$ TeV.* Technical Report ATL-PHYS-PUB-2015-036, CERN, Geneva.
- [14] (2015). *Selection of jets produced in 13TeV proton-proton collisions with the ATLAS detector.* Technical Report ATLAS-CONF-2015-029, CERN, Geneva.
- [15] (2015). *Vertex Reconstruction Performance of the ATLAS Detector at $\sqrt{s} = 13$ TeV.* Technical Report ATL-PHYS-PUB-2015-026, CERN, Geneva.
- [16] (2016). *Electron and photon energy calibration with the ATLAS detector using data collected in 2015 at $\sqrt{s} = 13$ TeV.* Technical Report ATL-PHYS-PUB-2016-015, CERN, Geneva.
- [17] (2016). *Electron efficiency measurements with the ATLAS detector using the 2015 LHC proton-proton collision data.* Technical Report ATLAS-CONF-2016-024, CERN, Geneva.
- [18] (2016). *Measurements of top-quark pair differential cross-sections in the lepton+jets channel in pp collisions at $\sqrt{s} = 13$ TeV using the ATLAS detector.* Technical Report ATLAS-CONF-2016-040, CERN, Geneva.
- [19] (2016). *Optimisation of the ATLAS b-tagging performance for the 2016 LHC Run.* Technical Report ATL-PHYS-PUB-2016-012, CERN, Geneva.
- [20] (2016). *Photon identification in 2015 ATLAS data.* Technical Report ATL-PHYS-PUB-2016-014, CERN, Geneva.

- [21] (2017). *Search for a Scalar Partner of the Top Quark in the Jets+ E_{miss} Final State at $\sqrt{s} = 13$ TeV with the ATLAS detector.* Technical Report ATLAS-CONF-2017-020, CERN, Geneva.
- [22] (2017). *Search for squarks and gluinos in final states with jets and missing transverse momentum using 36 fb^{-1} of $\sqrt{s} = 13$ TeV pp collision data with the ATLAS detector.* Technical Report ATLAS-CONF-2017-022, CERN, Geneva.
- [23] (2017). *Trigger Menu in 2016.* Technical Report ATL-DAQ-PUB-2017-001, CERN, Geneva.
- [24] Adams, T. (2008). SUSY Searches at the Tevatron. In *Hadron collider physics. Proceedings, 19th Symposium, HCP2008, Galena, USA, May 27-31, 2008.*
- [25] Agostinelli, S. et al. (2003). GEANT4: A Simulation toolkit. *Nucl. Instrum. Meth.*, A506, 250–303.
- [26] Alioli, S., Moch, S.-O., & Uwer, P. (2012). Hadronic top-quark pair-production with one jet and parton showering. *Journal of High Energy Physics*, 2012(1), 137.
- [27] Alioli, S., Nason, P., Oleari, C., & Re, E. (2009). NLO single-top production matched with shower in POWHEG: s- and t-channel contributions. *JHEP*, 09, 111. [Erratum: JHEP02,011(2010)].
- [28] Alwall, J., Frederix, R., Frixione, S., Hirschi, V., Maltoni, F., Mattelaer, O., Shao, H.-S., Stelzer, T., Torrielli, P., & Zaro, M. (2014). The automated computation of tree-level and next-to-leading order differential cross sections, and their matching to parton shower simulations. *Journal of High Energy Physics*, 2014(7), 79.
- [29] An, H. & Wang, L.-T. (2015). Opening up the compressed region of top squark searches at 13 tev lhc. *Phys. Rev. Lett.*, 115, 181602.
- [30] Artoisenet, P., Frederix, R., Mattelaer, O., & Rietkerk, R. (2013). Automatic spin-entangled decays of heavy resonances in monte carlo simulations. *Journal of High Energy Physics*, 2013(3), 15.

- [31] Bähr, M., Gieseke, S., Gigg, M. A., Grellscheid, D., Hamilton, K., Latund-Dada, O., Plätzer, S., Richardson, P., Seymour, M. H., Sherstnev, A., & Webber, B. R. (2008). Herwig++ physics and manual. *The European Physical Journal C*, 58(4), 639–707.
- [32] Ball, R. D., Bertone, V., Carrazza, S., Deans, C. S., Del Debbio, L., Forte, S., Guffanti, A., Hartland, N. P., Latorre, J. I., Rojo, J., & Ubiali, M. (2015). Parton distributions for the lhc run ii. *Journal of High Energy Physics*, 2015(4), 40.
- [33] Barberio, E., Boudreau, J., Butler, B., Cheung, S. L., Dell'Acqua, A., Simone, A. D., Ehrenfeld, W., Gallas, M. V., Glazov, A., Marshall, Z., Mueller, J., Plačakytė, R., Rimoldi, A., Savard, P., Tsulaia, V., Waugh, A., & Young, C. C. (2008). Fast shower simulation in the atlas calorimeter. *Journal of Physics: Conference Series*, 119(3), 032008.
- [34] Besjes, G. J., Baak, M., Côté, D., Koutsman, A., Lorenz, J. M., & Short, D. (2015). Histfitter: a flexible framework for statistical data analysis. *Journal of Physics: Conference Series*, 664(7), 072004.
- [35] Borschensky, C., Krämer, M., Kulesza, A., Mangano, M., Padhi, S., Plehn, T., & Portell, X. (2014). Squark and gluino production cross sections in pp collisions at $\sqrt{s} = 13, 14, 33$ and 100 tev. *Eur. Phys. J.*, C74(12), 3174.
- [36] Cacciari, M., Salam, G. P., & Soyez, G. (2008a). The anti-kt jet clustering algorithm. *Journal of High Energy Physics*, 2008(04), 063.
- [37] Cacciari, M., Salam, G. P., & Soyez, G. (2008b). The catchment area of jets. *Journal of High Energy Physics*, 2008(04), 005.
- [38] Capeans, M., Darbo, G., Einsweiller, K., Elsing, M., Flick, T., Garcia-Sciveres, M., Gemme, C., Pernegger, H., Rohne, O., & Vuillermet, R. (2010). ATLAS Insertable B-Layer Technical Design Report. Technical Report CERN-LHCC-2010-013. ATLAS-TDR-19.
- [39] Cascioli, F., Maierhöfer, P., & Pozzorini, S. (2012). Scattering amplitudes with open loops. *Phys. Rev. Lett.*, 108, 111601.
- [40] Collaboration, A. (2014). Electron and photon energy calibration with the atlas detector using lhc run 1 data. *The European Physical Journal C*, 74(10), 3071.

- [41] Collaboration, A. (2016a). Muon reconstruction performance of the atlas detector in proton–proton collision data at $\sqrt{s} = 13$ tev. *The European Physical Journal C*, 76(5), 292.
- [42] Collaboration, A. (2016b). *Performance of the ATLAS Trigger System in 2015*. Technical Report arXiv:1611.09661. CERN-EP-2016-241, CERN, Geneva. Comments: 76 pages in total, author list starting page 60, 50 figures, 1 table. Submitted to Eur. Phys. J. C. All figures including auxiliary figures are available at <http://atlas.web.cern.ch/Atlas/GROUPS/PHYSICS/PAPERS/TRIG-2016-01/>.
- [43] Collaboration, C. (2012). Observation of a new boson at a mass of 125 gev with the {CMS} experiment at the {LHC}. *Physics Letters B*, 716(1), 30 – 61.
- [44] Collaboration, T. A. (2008). The atlas experiment at the cern large hadron collider. *Journal of Instrumentation*, 3(08), S08003.
- [45] Cornelissen, T., Elsing, M., Fleischmann, S., Liebig, W., Moyse, E., & Salzburger, A. (2007). *Concepts, Design and Implementation of the ATLAS New Tracking (NEWT)*. Technical Report ATL-SOFT-PUB-2007-007. ATL-COM-SOFT-2007-002, CERN, Geneva.
- [46] Czakon, M. & Mitov, A. (2014). Top++: A Program for the Calculation of the Top-Pair Cross-Section at Hadron Colliders. *Comput. Phys. Commun.*, 185, 2930.
- [47] Djouadi, A. (2008). The anatomy of electroweak symmetry breaking: Tome i: The higgs boson in the standard model. *Physics Reports*, 457(1–4), 1 – 216.
- [48] Donoghue, J. F., Golowich, E., & Holstein, B. R. (1992). *Dynamics of the Standard Model*. Cambridge Monographs on Particle Physics, Nuclear Physics and Cosmology. Cambridge University Press.
- [49] Englert, F. & Brout, R. (1964). Broken symmetry and the mass of gauge vector mesons. *Phys. Rev. Lett.*, 13, 321–323.
- [50] et al., R. A. (2008). The atlas level-1 calorimeter trigger. *Journal of Instrumentation*, 3(03), P03001.
- [51] Evans, L. & Bryant, P. (2008). LHC Machine. *JINST*, 3, S08001.

- [52] Fruhwirth, R., Waltenberger, W., & Vanlaer, P. (2007). Adaptive vertex fitting. *J. Phys.*, G34, N343.
- [53] Gianotti, F. (2002). Searches for supersymmetry at high-energy colliders: the past, the present and the future. *New Journal of Physics*, 4(1), 63.
- [54] Gleisberg, T., Hoeche, S., Krauss, F., Schonherr, M., Schumann, S., Siegert, F., & Winter, J. (2009). Event generation with SHERPA 1.1. *JHEP*, 02, 007.
- [55] Higgs, P. W. (1964). Broken symmetries and the masses of gauge bosons. *Phys. Rev. Lett.*, 13, 508–509.
- [56] Higgs, P. W. (1966). Spontaneous symmetry breakdown without massless bosons. *Phys. Rev.*, 145, 1156–1163.
- [57] Hoecker, A., Speckmayer, P., Stelzer, J., Therhaag, J., von Toerne, E., Voss, H., Backes, M., Carli, T., Cohen, O., Christov, A., Dannheim, D., Danielowski, K., Henrot-Versille, S., Jachowski, M., Kraszewski, K., Krasznahorkay, Jr., A., Kruk, M., Mahalalel, Y., Ospanov, R., Prudent, X., Robert, A., Schouten, D., Tegenfeldt, F., Voigt, A., Voss, K., Wolter, M., & Zemla, A. (2007). TMVA - Toolkit for Multivariate Data Analysis. *ArXiv Physics e-prints*.
- [58] Hugging, F. (2011). The ATLAS Pixel Insertable B-Layer (IBL). *Nucl. Instrum. Meth.*, A650, 45–49.
- [59] Illingworth, J. & Kittler, J. (1988). A survey of the hough transform. *Computer Vision, Graphics, and Image Processing*, 44(1), 87 – 116.
- [60] Jackson, P., Rogan, C., & Santoni, M. (2017a). Sparticles in motion: Analyzing compressed susy scenarios with a new method of event reconstruction. *Phys. Rev. D*, 95, 035031.
- [61] Jackson, P., Rogan, C., & Santoni, M. (2017b). Sparticles in motion: Analyzing compressed susy scenarios with a new method of event reconstruction. *Phys. Rev. D*, 95, 035031.
- [62] Lai, H.-L., Guzzi, M., Huston, J., Li, Z., Nadolsky, P. M., Pumplin, J., & Yuan, C.-P. (2010). New parton distributions for collider physics. *Phys. Rev. D*, 82, 074024.

- [63] Macaluso, S., Park, M., Shih, D., & Tweedie, B. (2016). Revealing compressed stops using high-momentum recoils. *Journal of High Energy Physics*, 2016(3), 151.
- [64] Martin, S. P. (1997). A Supersymmetry primer. [Adv. Ser. Direct. High Energy Phys.18,1(1998)].
- [65] Owen, S. (2012). *Data-driven estimation of the QCD multijet background to SUSY searches with jets and missing transverse momentum at ATLAS using jet smearing*. Technical Report ATL-PHYS-INT-2012-008, CERN, Geneva.
- [66] Peskin, M. E. & Schroeder, D. V. (1995). An introduction to quantum field theory.
- [67] Pumplin, J., Stump, D. R., Huston, J., Lai, H.-L., Nadolsky, P., & Tung, W.-K. (2002). New generation of parton distributions with uncertainties from global qcd analysis. *Journal of High Energy Physics*, 2002(07), 012.
- [68] Re, E. (2011). Single-top Wt-channel production matched with parton showers using the POWHEG method. *Eur. Phys. J.*, C71, 1547.
- [69] Sjostrand, T., Ask, S., Christiansen, J. R., Corke, R., Desai, N., Ilten, P., Mrenna, S., Prestel, S., Rasmussen, C. O., & Skands, P. Z. (2015). An introduction to pythia 8.2. *Computer Physics Communications*, 191, 159 – 177.
- [70] Sjostrand, T., Mrenna, S., & Skands, P. (2006). Pythia 6.4 physics and manual. *Journal of High Energy Physics*, 2006(05), 026.
- [71] Skands, P. Z. (2010). Tuning monte carlo generators: The perugia tunes. *Phys. Rev. D*, 82, 074018.
- [72] Verkerke, W. & Kirkby, D. (2003). The roofit toolkit for data modeling. *eConf*, C0303241, MOLT007.